Lehrstuhl für Computerunterstützte Klinische Medizin
der Medizinischen Fakultät Mannheim
Direktor: Prof. Dr. rer. nat. Lothar Schad

EFFICIENT QUANTIFICATION OF IN-VIVO ^{23}NA MAGNETIC RESONANCE IMAGING

Inauguraldissertation
zur Erlangung des Doctor scientiarum humanarum (Dr. sc. hum.)
der
Medizinischen Fakultät Mannheim
der Ruprecht-Karls-Universität
zu
Heidelberg

vorgelegt von
ANNE ADLUNG
aus
BERLIN

2022

DEKAN: Prof. Dr. med. Sergij Goerdt
REFERENT: Prof. Dr. rer. nat. Lothar R. Schad

ABSTRACT

The tissue sodium concentration (TSC) can be obtained from quantitative sodium (^{23}Na) magnetic resonance imaging (MRI). It provides valuable information about tissue physiology, and cell vitality and viability that cannot be derived from conventional hydrogen (^{1}H) MRI. However, even after decades of research, quantitative ^{23}Na MRI is still facing crucial challenges such as its long measurement times and elaborate measurement setups. Thus, its clinical establishment is still pending. This thesis aimed to explore data acquisition and post-processing techniques, which could make quantitative ^{23}Na MRI more efficient for its clinical applications. It intended to obtain further knowledge about TSC in exemplary pathologies.

For the absolute TSC quantification, usage of external reference phantoms is state of the art. However, it requires additional efforts and carries the risk of introducing errors, e.g., because of the phantoms' spatial distance to the region of interest. In this thesis, the absolute TSC quantification was performed by considering internal instead of external quantification references in the ^{23}Na MR image of the brain from patients with ischemic stroke. The results indicated a reliable TSC quantification based on an internal reference within the vitreous humor. Prospectively, this could allow for an easier measurement setup whilst maintaining robust absolute TSC quantification.

Measurement time is a crucial parameter for MRI sequences, and ^{23}Na MRI takes substantially longer than ^{1}H MRI. A convolutional neural network was optimized, trained, and tested with the purpose of reducing the required measurement time for quantifiable ^{23}Na MR images. The results showed that a multiple-fold undersampling might be possible for ^{23}Na MR images when applying a properly adjusted network to the post-processing algorithm, prospectively allowing for substantially shorter data acquisition times.

Two prospective in-vivo studies were conducted to obtain further knowledge about TSC alterations: One study investigated TSC in the brain of patients with brain metastases undergoing stereotactic radiosurgery. The study included ^{23}Na MR images pre- and post-irradiation. The results indicated that TSC might be able to quantify radiation-induced tissue changes. The other study investigated TSC in the human prostate. The results showed differences between TSC in the prostate of patients diagnosed with cancerous lesions and those with clinically inconspicuous findings. The findings indicate the additional diagnostic information that quantitative ^{23}Na MRI could be able to provide if being established for clinical applications.

The thesis aimed to contribute to quantitative ^{23}Na MRI overcoming its obstacles. It proposes how to enable faster, easier, and thus more efficient data acquisition. Furthermore, it gives insights into the significance of TSC, which was exemplary explored within patients with ischemic stroke, brain metastases and prostate cancer.

ZUSAMMENFASSUNG

Die Natriumkonzentration im Gewebe (TSC) kann aus der quantitativen Natrium (^{23}Na) Magnetresonanztomographie (MRT) abgeleitet werden. Sie liefert wertvolle Informationen über die Gewebephysiologie und die Zellvitalität, die nicht aus der herkömmlichen Wasserstoff (^{1}H) MRT erlangt werden können. Nach jahrzehntelanger Forschung steht die ^{23}Na MRT noch immer vor entscheidenden Herausforderungen, wie zum Beispiel den aufwendigen Vorbereitungen für die Messungen und die lange Messzeit. Daher ist ihre Etablierung im klinischen Alltag noch ausstehend. Ziel dieser Arbeit war es, Techniken zur Datenerfassung und Nachbearbeitung zu erforschen, die die quantitative ^{23}Na MRT für ihre klinische Anwendung effizienter machen können. Des Weiteren sollten mehr Informationen gewonnen werden über die Aussagekraft von TSC in beispielhaften Pathologien.

Die Verwendung externer Referenzphantome entspricht dem Stand der Technik für die absolute TSC Quantifizierung, auch wenn sie zusätzlichen Aufwand erfordert. In dieser Arbeit wurde die absolute TSC Quantifizierung im Kopf von Patienten mit ischämischem Schlaganfall durchgeführt, indem interne anstelle von externen Quantifizierungsreferenzen in dem ^{23}Na MR Bild berücksichtigt wurden. Die Ergebnisse deuteten auf eine zuverlässige TSC Quantifizierung bei Verwendung des Glaskörpers im Auge als interne Referenz. Perspektivisch könnte dies die Natrium MRT Messungen vereinfachen, wobei eine robuste TSC Quantifizierung beibehalten wird.

Die Messzeit ist ein kritischer Parameter von MRT Sequenzen und sie ist wesentlich länger für ^{23}Na MRT als für die ^{1}H MRT. Daher wurde ein künstliches neuronales Netzwerk optimiert, trainiert und getestet mit dem Ziel die erforderliche Messzeit für quantifizierbare ^{23}Na MR Bilder zu reduzieren. Die Ergebnisse zeigten, dass eine mehrfache Unterabtastung der ^{23}Na MR Bilder von Patienten mit einem ischämischen Schlaganfall möglich ist, wenn ein entsprechend angepasstes Netzwerk auf den Nachbearbeitungsalgorithmus angewendet wird. Dies könnte eine signifikant kürze Messzeit ermöglichen.

Um weitere Erkenntnisse über die Aussagekraft von TSC zu erhalten, wurden zwei prospektive in-vivo Studien durchgeführt: Eine Studie untersuchte die TSC im Gehirn von Patienten mit Hirnmetastasen, die stereotaktisch bestrahlt wurden. ^{23}Na MR Bilder wurden vor und nach der Bestrahlung aufgenommen. Die Ergebnisse wiesen darauf hin, dass die TSC in der Lage sein könnte strahleninduzierte Veränderungen im Gewebe zu quantifizieren. Die andere Studie untersuchte die TSC in der menschlichen Prostata. Die Ergebnisse zeigten Unterschiede zwischen der TSC in der Prostata von Patienten mit einer diagnostizierten Krebsläsion und von solchen mit klinisch unauffälligen Befunden. Diese Erkenntnisse weisen auf den diagnostischen Mehrwert hin, den die ^{23}Na MRT in klinischen Anwendungen liefern könnte.

Diese Thesis sollte einen Beitrag dazu leisten, dass die ^{23}Na MRT einige ihrer aktuellen Hindernisse überwinden kann. Sie liefert Vorschläge wie eine schnellere, einfachere und somit effizientere Datenerfassung ermöglicht werden kann. Des Weiteren liefert sie Erkenntnisse über die Bedeutung des TSC, was beispielhaft in Patienten mit ischämischem Schlaganfall, Hirnmetastasen und Prostatakarzinom untersucht wurde.

CONTENTS

LIST OF FIGURES

LIST OF TABLES

ACRONYMS

ACC	Adaptive coil combination
ADC	Apparent diffusion coefficient
BM	Brain metastasis
CSF	Cerebrospinal fluid
CI	Artificially up-sampled ^{23}Na MR image
CT	Computer tomography
DWI	Diffusion-weighted imaging
ESC	Extra-cellular sodium concentration
FBV	Femoral blood vessel
EVF	Extra-cellular volume fraction
FFT	Fast fourier transformation
FI	MR image that was reconstructed using the full $k-space$ data
FLAIR	Fluid-attenuated inversion recovery
FoV	Field of view
GDL	Gradient difference loss
GM	Grey matter
GTV	Gross tumor volume
HC	Healthy control, healthy volunteer
HR	Healthy ROI
ISC	Intra-cellular sodium concentration
IVF	Intra-cellular volume fraction
LPF	Low-pass filter
mpMRI	multi-parametric magnetic resonance imaging
MPRAGE	Magnetization prepared rapid gradient-echo
MR	Magnetic resonance
MRI	Magnetic resonance imaging
NMR	Nuclear magnetic resonance
NAWM	Normal-appearing white matter

PTT	Peritumoral tissue
PVE	Partial volume effects
PWI	Perfusion-weighted imaging
PZ	Peripheral zone
RI	Artificial under-sampled ^{23}Na MR image
ROI	Region of interest
rTSC	Relative tissue sodium concentration
sd	Standard deviation
SI	Signal intensity
SNR	Signal-to-noise ratio
SRS	Stereotactic radiosurgery
SSC	Blood serum sodium concentration
SSIM	Structural similarity index
TSC	Tissue sodium concentration
TZ	Transitional zone
VH	Vitreous humor
WM	White matter
WMH	White matter hyperintensities
WML	White matter lesions
WP	Whole prostate

1 INTRODUCTION

Magnetic resonance imaging (MRI) is a well-established, non-invasive medical imaging technique based on the physical phenomenon of nuclear magnetic resonance (NMR) [Haa+99; Levo8]. It is broadly used and finds applications in the area of diagnosis, progress control, and treatment decision and planning [Cha+07; Win+07; Kan+10; Dic+11; Dev12; WT18]. Nowadays, magnetic resonance (MR) images can be acquired of any body part with various different contrasts [BKZ04; Lu+05; Ayd+12]. Conventional MRI measures the hydrogen (^{1}H) nucleus in the human body, resulting in images of the human anatomy with a particularly good contrast of soft tissues. Due to the varying NMR properties of different tissues and the great number of possibilities in MRI sequence design, various MRI techniques have evolved beyond aiming to depict only the human anatomy but also showing the functional and physiological processes in the human body [Oga+90; Bano7; Nel11; Ban12], e.g. diffusion-weighted imaging, perfusion-weighted imaging, or arterial spin labeling.

In addition to the ^{1}H nucleus, there are also other nuclei with NMR properties [MR13; KS14; SWL16; Thu18; BSJ19; Hu+20]. In 1985, the first human in-vivo brain MR image was acquired that measured the sodium (^{23}Na) nucleus instead of ^{1}H [Hil+85]. With ^{23}Na playing an essential and irreplaceable role in the cell metabolism [SE92; Fal+94; Som04; Som02], ^{23}Na MRI aims to provide information about cell vitality, viability and activity, which cannot be provided by ^{1}H MRI alone.

1.1 STATE OF THE ART

Great milestones have been achieved since the first ^{23}Na MR image acquisition.

Hardware developments, with increased available magnetic field strengths and double resonant (^{1}H/^{23}Na) radiofrequency coils allow for image acquisition within a conventional clinical setup [MR13; Hu+20]. The higher magnetic field strengths enable a better signal-to-noise ratio (SNR) without an excessive increase in data acquisition times [Red98; Ben+13]. Today, 3 Tesla MRI scanners are common; they are available in any university hospital or larger radiological center. Even 7 T MRI scanners have received approval (within Europe and within the USA) for clinical applications in 2017, although, they are still not broadly available [Sch+04; The+08; Mad+12a]. Research presented in this thesis will be entirely focused on ^{23}Na MRI at 3 T, which is broadly established.

Double-resonant ^{1}H/^{23}Na coils make it possible to acquire conventional ^{1}H MR images and ^{23}Na MR images with the same coil, thus, enabling to add ^{23}Na MRI after a standard of care ^{1}H MRI protocol, without having to burden the patient with a coil change in between, saving time and resources [JL89; Mag+18; Mal+19a; Mal+19b]. Within the area of radiofrequency coils, developments include various combinations of transmit and receive channels for both nuclei. In this thesis, data acquisition with two different double resonant coils – for applications in the human head and in the abdomen – will be explored.

Decades of sequence developments and optimization have shown the ability to generate different contrast images, e.g. sodium-weighted imaging, aiming for the quantification of the depicted tissue's sodium concentration [MR13; Par+97]. A 3D radial sequence, first suggested by Nielles et al. in 2007, is the most common implementation [NV+07], and it was further optimized using various approaches [Boa+97b; GHN06; Lu+10; Pip+11]. In this thesis, ^{23}Na MR images were acquired with a sequence, which uses a density-adapted read-out, enabling a more homogeneous data acquisition [Nag+09].

Based on sodium-weighted imaging, the idea of quantifying the tissue sodium concentration (TSC) was introduced and fast established [Boa+94; Thu+99; Ouw+03; Ouw+07; Lot+19; Moh+21a]. TSC is of high interest because of sodium's crucial role in cell metabolism, which is defined by a sharp gradient between intra- and extra-cellular ^{23}Na concentration [SE92; Fal+94; Som02; Som04]. Consequently, TSC is influenced by any changes in sodium concentration or the respective volume fraction of the extra- or intra-cellular compartment. Therefore, TSC is able to provide valuable information about tissue vitality and viability. To obtain the absolute TSC, it is currently considered state of the art to place reference phantoms – typically vials filled with NaCl and agarose – within the field of view, next to the patient [MR13; Ouw+07; Han+11; Zaa+12]. Precise positioning of the vials is crucial as image signal intensity within the vials determines the quantified TSC values of the whole image, which might be impacted by less careful positioning or by misplacement due to (involuntary) movements of the patient.

Data acquisition of ^{23}Na MRI is long compared to ^{1}H MRI, which is mainly caused by the physical and biological properties of the nuclei [KS14; Hu+20]. The substantially lower natural abundance of the ion and its less favorable gyromagnetic ratio reduce SNR and image quality, and increase the required measurement time. Convolutional neural networks (CNNs) are part of machine learning and they are on the rise for medical image pre- and post-processing and have been applied to various image modalities, including ^{1}H MRI [KJS17; FA+18]. They have already been suggested for image reconstructions with the purpose of improving SNR, potentially enabling the reduction of measurement time [Sch+17a; Ber+19; LL19].

1.2 MOTIVATION

Until today, ^{23}Na MRI is still facing various challenges, which have hampered its clinical establishment so far; despite the developments in hardware and software, its well-known advantages and the additional diagnostic information that ^{23}Na MRI could be able to provide.

One of the most prominent reasons for ^{23}Na MRI not being used in the clinical routine is the long and rather complicated data acquisition.

Data acquisition time is a crucial parameter when deciding on whether a sequence can be integrated into clinical measurements: An MRI exam might be uncomfortable for the patient because of the noise and possible claustrophobia. Furthermore, in some cases, particularly when considering acute diseases, fast treatment decisions need to be made to reduce further risks to the patient. For example, for patients

with an ischemic stroke, "time is brain" is a common phrase, meaning that patients need treatment (and therefore a diagnosis) as fast as possible to minimize the loss of functioning brain cells and improve the patient's outcome substantially [Sav06; Gon06]. Additionally, MRI scanners are still expensive imaging tools, making long data acquisitions a costly investment.

Under-sampling is an approach of acquiring less data whilst generating images with the same field of view and resolution. It reduces data acquisition time but introduces noise and artifacts, also reducing the image quality. The might lead to the image being considered as not providing sufficient information for image diagnosis. CNNs are already able to improve ^{1}H MR image post-processing and reconstruction algorithms. Thus, an CNN optimized for the application on ^{23}Na MR images could become a valuable tool.

Considering the ^{23}Na MRI measurement setup for TSC quantification, positioning of the above mentioned reference phantoms carries the hazard of not being sufficiently accurate or even being forgotten. This might be less problematic within the setup of a study protocol but could become relevant within a hectic clinical routine, which can be assumed for any MRI measurement of an acute disease. With the quantification depending on the signal intensity within the reference phantoms, measurements with no properly placed phantoms become unusable. Consequently, other references, which do not depend on external factors and which cannot be forgotten, would be desirable. With relative TSC (relative to contra-lateral tissue) already having been explored, the accuracy of absolute TSC quantification based on internal references with a known sodium concentration would be of high interest.

Additionally, further insights are warranted into TSC changes in certain pathologies to enable proper interpretation of the data acquired with ^{23}Na MRI.

During an ischemic stroke, cells in the affected area of the brain experience an insufficient supply of blood, leading to cell swelling and death [BB00; Sav06; WG07]; affecting the TSC. Quantifying the occurred cell damage – through TSC – with the aim of optimizing treatment decisions, has been suggested previously. While it seems promising, it still requires further insights and research.

Ionizing radiation from radiation therapy aims to destroy cells within tumorous tissue whilst minimizing the harm within healthy tissue and stereotactic radiosurgery (SRS) optimizes radiation distribution by using sharp gradients [Lek83; WK04; Mil+21]. The following cell death is hypothesized to initially increase the extra-cellular volume fraction, and consequently TSC. Afterwards, the onset of tissue regeneration could reverse the process. Therefore, changes in TSC might be an early biomarker for tissue response to radiation.

The prostate carcinoma is one of the most prevalent tumor diseases worldwide, and its diagnosis with multi-parametric MRI maintains uncertainties despite well-established standards [Wei+16; Ken+18; Tol+21]. With TSC having shown to correlate with tumor malignancies in research about other cancers, it might also be able to contribute to a more precise diagnosis of lesions within the prostate.

1.3 OUTLINE

This thesis aims to pave the way for a more efficient data acquisition of ^{23}Na MR images and to contribute to its establishment in the clinical routine for various diseases. Therefore, it will cover the following:

1. Various TSC quantification techniques are compared, aiming to simplify the measurement setup for quantitative ^{23}Na MRI.

2. An optimized, applied and tested CNN is introduced as a potential post-processing technique to reduce ^{23}Na MR image data acquisition time.

3. Two prospective human in-vivo studies are presented, evaluating TSC changes within brain metastases and their surrounding tissue introduced by SRS (1) and within the prostate and its possibly tumorous tissue (2).

In this thesis, the application of ^{23}Na MRI was explored and investigated exemplary in patients with three different pathologies: ischemic stroke, brain metastases and prostate carcinoma.

Data was used from the clinical study "^{23}Na MRI in ischemic stroke", which provided ^{23}Na MR images of patients with an acute ischemic stroke. The data was used to evaluate various image post-processing techniques:

TSC QUANTIFICATION Absolute and relative TSC quantification were performed according to the current state of the art techniques and they were compared between each other and tested for plausibility based on the results of TSC in the region of the ischemic stroke and in the patients' white matter and by considering the patients' pre-existing small vessel diseases (in form of white matter lesions, WML) as well as previously reported findings. These investigations have been published in [Adl+21b] by Karger Publishers.

Furthermore, absolute TSC quantification was also performed based on internal references (namely, the cerebrospinal fluid and the vitreous humor), and the feasibility, simplicity, and accuracy of the different absolute quantification techniques were compared.

DATA ACQUISITION TIME REDUCTION Aiming to prospectively reduce the data acquisition time, a CNN was optimized, trained, and tested with the available ^{23}Na MR image data, which was artificially under-sampled, meaning that data was simulated that would have been acquired with substantially shorter measurement time. Different network architectures and parameters were considered to obtain an optimal network configuration for the specific application. The network's training and initial tests were conducted with the data from patients with ischemic stroke from the above mentioned study. This study has been published in [Adl+21a] by John Wiley & Sons Ltd. Eventually, the network was also applied and tested on real under-sampled data, meaning data that was actually acquired with a fraction of the initially suggested data acquisition time.

Furthermore, two prospective human in-vivo studies were conducted:

TSC AFTER STEREOTACTIC RADIOSURGERY One of the studies aimed to investigate TSC changes within brain metastases and their surrounding peritumoral tissue caused by irradiation. For that purpose, ^{23}Na MR images were acquired from patients with brain metastases from different primary tumors undergoing SRS. The ^{23}Na MR images were acquired pre- and post-irradiation and TSC evolution was observed within the metastases and within the surrounding tissues.

TSC IN THE HUMAN PROSTATE WITH SUSPECTED PROSTATE CARCINOMA The second study investigated the TSC within the human prostate with a clinically suspected prostate carcinoma. ^{23}Na MR images were acquired in addition to a ^{1}H multi-parametric MRI protocol and TSC quantification was performed within the prostate's peripheral zone, transitional zone and – if presented – the lesions.

2

THEORETICAL BACKGROUND

Magnetic resonance imaging (MRI) utilizes the physical phenomenon Nuclear Magnetic Resonance (NMR) and is a diagnostic modality within radiological imaging. This chapter will provide a brief explanation of the physical background of hydrogen (^{1}H) and sodium (^{23}Na) MRI and of the vital role of ^{23}Na ions in the human physiology. It intends to describe the potential of quantifying tissue sodium concentration from ^{23}Na MRI.

2.1 NUCLEAR MAGNETIC RESONANCE

Otto Stern [GS24], Isidor Isaac Rabi [RC33], Felix Bloch [Blo46] and Edward Mills Purcell [PTP46] have all been awarded with cumulatively four Nobel prices for their contribution in the field of NMR [Boe04]. This section will provide a brief overview of the fundamental physical concepts of NMR, based on their findings. The here given explanations follow the books by E. Mark Haacke [Haa+99] and Malcolm H. Levitt [Lev08].

2.1.1 *Nuclear spin*

Nucleons, which are protons and neutrons, possess a physical property that is called spin ($\hat{I}$). The total angular momentum of the nucleon is the sum over its spin and orbital angular momentum. The total angular momentum of a nucleus is calculated by the sum over its angular momentum of its nucleons.
The spin describes the nucleus' rotation around its own axis and it is given as a unit-less number with a definite magnitude and projection. Only nuclei with an odd number of protons or neutrons or both have a non-zero spin and exclusively those nuclei can be used for NMR which is due to the Pauli exclusion principle [Pau25]. The reduced Planck constant $\hbar$ is defined as

$$\hbar = \frac{h}{2\pi} = \frac{6.626 \cdot 10^{-34}\,\mathrm{Js}}{2\pi} \tag{2.1}$$

and is used to describe the eigenvalue equations

$$\hat{I} = \hbar\sqrt{I(I+1)} \tag{2.2}$$

with I being the nuclear spin quantum number. I is zero when the nucleus consists of an even number of neutrons and protons and I is a full-integer value when the nucleus consists of an odd number of protons and an odd number of neutrons. It is a half-integer value when the nucleus consists either of an odd number of protons or of an odd number of neutrons which applies for ^{1}H ($I = 1/2$) and ^{23}Na ($I = 3/2$). A non-zero spin generates a magnetic momentum, enabling magnetization.

The gyromagnetic ratio γ is an isotope-specific constant describing the ratio of its angular momentum (spin) and its magnetic moment $\vec{\mu}$, with

$$\vec{\mu} = \gamma \vec{I} \tag{2.3}$$

where

$$\gamma = g \cdot \frac{\mu_N}{\hbar} \tag{2.4}$$

with g being the nucleus-specific g-factor and μ_N being the nuclear magneton, which is defined as

$$\mu_N = \frac{e\hbar}{2m_p} \tag{2.5}$$

with e being the electric charge and m_p being the intrinsic mass of a proton. The gyromagnetic ratio indicates the element's sensitivity to NMR. Its unit is rad per second per Tesla. Although, NMR mostly uses $\frac{\gamma}{2\pi}$ in MHz per Tesla, e.g. $\gamma_{^1H} = 2.68 \cdot 10^8$ rad/sT $= 42.58$ MHz/T and $\gamma_{^{23}Na} = 7.08 \cdot 10^7$ rad/sT $= 11.27$ MHz/T. Multiple nuclei with NMR properties are listed with in Table 2.1.

All nuclei are, at any given point, in a quantifiable energy state. With no applied external magnetic field, all nuclei of one element will possess the same energy level and the spins are randomly oriented. The spins are equally distributed in all directions and, therefore, the net magnetization is zero.

With the application of an external magnetic field, the spins will form a preference of an orientation parallel or anti-parallel to the direction of the magnetic field, with slightly more spins being in the parallel orientation. The spin energy levels of the nuclei split up in an external magnetic field. Therefore, the nuclei's spin forms the basis of NMR. The splitting into different levels is called *Zeeman effect*[1].

The magnetic quantum number m_I of the spin can take numbers between $-I$ and I in full integer steps. The number of possible angular momentum states m_I is $2I + 1$. Consequently, ^{1}H with $I = 1/2$ has two spin states with $m_I = -1/2$ or $m_I = +1/2$ whereas ^{23}Na with its $I = 3/2$ has four spin states with $m_I = -3/2$, $m_I = -1/2$, $m_I = 1/2$, and $m_I = 3/2$. The Zeeman effect is depicted in Figure 2.1 for the ^{1}H and the ^{23}Na nuclei with their different energy states m_I.

The magnetic flux density is described by magnitude and direction, as it is a vector. In NMR, it is commonly labeled as B-field. The coordinate system of the MRI scanner defines its B_0 field as exclusively pointing into z-direction, thus

$$\vec{B} = \begin{bmatrix} 0 \\ 0 \\ B_0 \end{bmatrix}. \tag{2.6}$$

The energy of nuclei within such B_0 field is calculated by considering the magnetic energy of the system that is associated with the Hamiltonian operator $\mathcal{H}$, which is defined by

$$\mathcal{H} = -\vec{\mu}\vec{B} = \gamma \vec{I} \begin{bmatrix} 0 \\ 0 \\ B_0 \end{bmatrix}. \tag{2.7}$$

1 The Zeeman effect is named after its discoverer, the Dutch physicist Pieter Zeeman. He was awarded with the Nobel prize in physics in 1902 [ZB97]

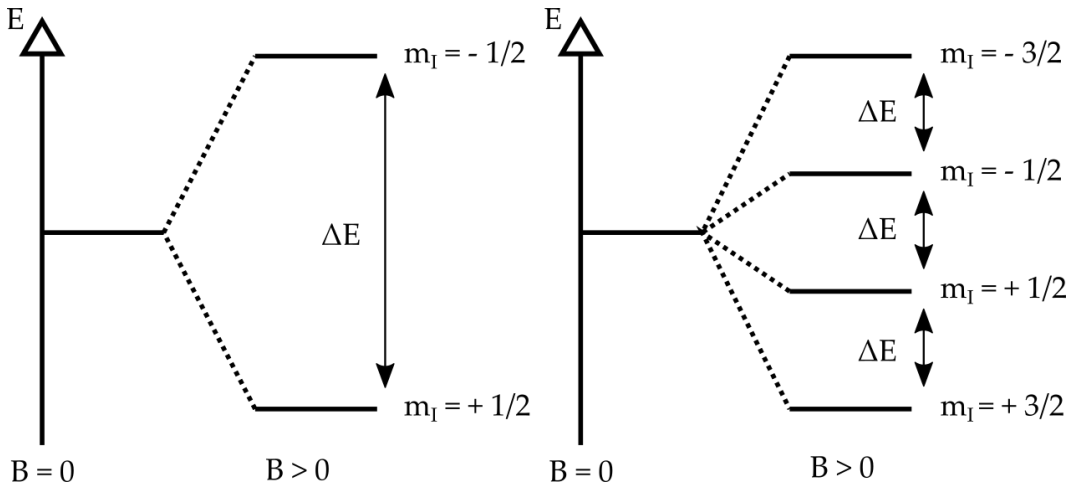

Figure 2.1: The Zeeman effect on nuclei with a spin of $I = 1/2$ (left) and $I = 3/2$ (right).

As it is time-independent, the time-independent Schrödinger equation applies with

$$\mathcal{H}\Psi = E\Psi, \tag{2.8}$$

where Ψ is the Eigenfunction. The corresponding energy Eigenvalues are

$$E_m = -\gamma\hbar m_I B_0, \tag{2.9}$$

with the difference of energy therefore depending on the considered nucleus' property (γ), its magnetic quantum number (m_I), and the applied magnetic field strength (B). As m_I is in full integer steps, two neighboring energy levels, have the energy difference of:

$$\Delta E = \gamma\hbar B_0. \tag{2.10}$$

2.1.2 *Macroscopic magnetization*

The orientation of the spins within the $\vec{B}$-field (parallel or anti-parallel) is not equally distributed with more nuclei being oriented parallel to B_0 and therefore favoring the lower energy level. The Boltzmann distribution describes the number of nuclei possessing a certain energy level. The ratio of two Boltzmann distributions of neighboring energy levels is therefore the ratio of the population density of the respective energy levels, which can be described by

$$\frac{N_{upper}}{N_{lower}} = e^{-\Delta E/k_B T}, \tag{2.11}$$

with k_B being the Boltzmann constant ($k_B = 1.381 \cdot 10^{-23}$ J/K) and T being the temperature in Kelvin. Considering, for example, the human body with a temperature of 310 K being exposed to the common magnetic field strength of 3 T, the ratio of the number of protons in the higher energy level to the number of protons in the lower energy level is

$$\frac{N_{upper}}{N_{lower}} = 0.999980. \tag{2.12}$$

Considering the number of all spins within a defined volume being N, one can derive

$$\Delta N = N \tanh\left(\frac{\hbar\gamma B_0}{2k_B T}\right) \tag{2.13}$$

for the absolute population difference ΔN. Conclusively, the number of spins which are parallel to the magnetic field exceed the number of anti-parallel spins by 20 per million at 3 T, when considering the ^{1}H nucleus. However, for the ^{23}Na nucleus, the number of spins which are parallel to the magnetic field exceed the number of anti-parallel spins by only 5 per million at 3 T with the difference deriving from the different gyromagnetic ratio. Those 20 or 5 excess spins per million generate the net magnetization M_0 along the $\overrightarrow{B}$ field with the magnitude M_0. In the human brain, ^{1}H has an approximate concentration c of ≈ 80 mol/liter (M) and ^{23}Na has a concentration of $\approx 20-60$ mmol/liter (mM) within the brain matter. Considering the Avogadro constant of $N_A = 6.022 \cdot 10^{23}$ 1/mol, one can calculate the nuclei density. For ^{1}H, one yields

$$\begin{aligned} N_{^1H} = N_A \cdot 80\ ^{\text{mol}}/_{\text{liter}} &= N_A \cdot 80\ ^{\text{mol}}/_{10^6 \text{mm}^3} \\ &= 4.8176 \cdot 10^{19}\ ^1/_{\text{mm}^3} \end{aligned} \tag{2.14}$$

protons in the human brain and for ^{23}Na, one yields

$$\begin{aligned} N_{^{23}Na} = N_A \cdot 40 \cdot 10^{-3}\ ^{\text{mol}}/_{\text{liter}} &= N_A \cdot 40 \cdot 10^{-3}\ ^{\text{mol}}/_{10^6 \text{mm}^3} \\ &= 2.4088 \cdot 10^{16}\ ^1/_{\text{mm}^3} \end{aligned} \tag{2.15}$$

sodium ions in the human brain. Thus, the proton density is by a factor of $\approx 2,000$ larger than the ^{23}Na ion density in brain matter with the NMR signal intensity (SI) directly depending on it.

Considering the magnetization being the sum of all spin's magnetic moments over the total volume, it is defined by

$$\overrightarrow{M} = \frac{1}{V}\sum_{s=1}^{N} \overrightarrow{\mu}_s = \frac{1}{V}\sum_{s=1}^{N} \gamma I. \tag{2.16}$$

Thus, its magnitude M_0 depends on the body's volume V, the number of particles N, and the nuclear gyromagnetic ratio γ. The sum of all energy levels (Zeeman) m_I includes their population probability (given by the Boltzmann distribution) p_m which is described by

$$p_m = \frac{1}{Z} e^{-E_m/kT}, \tag{2.17}$$

where Z is the partition function, and is described by the sum of all Zeeman states with

$$Z = \sum_{m_I} e^{-E_m/kT}, \tag{2.18}$$

including E_m from Equation 2.9. The magnitude of the magnetization is consequently described by

$$M_0 = \frac{N}{V}\gamma\hbar \sum_{m_I=-I}^{I} p_m m_I \tag{2.19}$$

in $\overrightarrow{B}$-direction, which is known as the Curie law. Due to the magnetization, the magnetic moment will rotate around the magnetic B-field and its direction, which is called precession.

The Larmor equation describes the precession frequency of the nucleus with its gyromagnetic ratio γ while being exposed to a magnetic field with the strength B by

$$\omega_0 = \gamma B. \tag{2.20}$$

The transition between two Zeeman states is only possible by stimulated emission causing emission of a photon at Larmor frequency. Assuming thermal equilibrium and no influence of additional, external forces (magnetic fields), the spins will remain at the state of lowest energy with net magnetization being exclusively along B_0 parallel to the z-axis.

2.1.3 *Signal excitation, relaxation, and detection*

To obtain an NMR signal, a time-varying radiofrequency (RF)-field, commonly refereed to as B_1-field, must be applied in addition to the B_0-filed.

EXCITATION The B_1-field is perpendicular to B_0 and can be defined as

$$\overrightarrow{B_1} = B_1 \begin{pmatrix} \cos(\omega_1) \\ -\sin(\omega_1) \\ 0 \end{pmatrix} \tag{2.21}$$

with ω_1 being the oscillation frequency in xy-plane, which will impact the direction of the magnetization. Assuming no relaxation processes, the effect on the net magnetization will then be described as

$$\frac{d}{dt}\overrightarrow{M} = \gamma M \times \overrightarrow{B}_{eff} \tag{2.22}$$

with the effective magnetic field

$$\overrightarrow{B}_{eff} = \overrightarrow{B}_0 + \overrightarrow{B}_1 \tag{2.23}$$

where the B_0-field is the longitudinal magnetic field B_z, and the B_1-field is the transverse magnetic field with $B_{xy} = B_x + iB_y$, in the resting frame.

In the rotational frame of reference, when assuming rotation around the z-axis, the effective magnetic field comes to:

$$\overrightarrow{B}_{eff} = \begin{pmatrix} B_1 \\ 0 \\ B_0 - \frac{\omega_1}{\gamma} \end{pmatrix} \tag{2.24}$$

The temporal evolution of the net magnetization is described by

$$\frac{d}{dt}\vec{M} = \gamma\vec{M} \times \begin{pmatrix} B_1 \\ 0 \\ B_0 - \frac{\omega_1}{\gamma} \end{pmatrix}, \tag{2.25}$$

which means that the z component of the magnetization vanishes if the frequency of the B_1-field (ω_1) equals the Larmor frequency. Only the transverse component of B_1 magnetization persists with

$$\frac{d}{dt}\vec{M} = \gamma\vec{M} \times \begin{pmatrix} B_1 \\ 0 \\ 0 \end{pmatrix}, \tag{2.26}$$

where the magnetization derives from $\vec{M}$, precessing around the x-axis. The effect of B_1 on the spin is called signal excitation.

With no relaxation being present and an exclusively longitudinal magnetic field B_0, one yields

$$\begin{aligned} \frac{dM_{xy}(t)}{dt} &= -i\gamma M_{xy} B_0 \\ \frac{dM_z(t)}{dt} &= 0 \end{aligned} \tag{2.27}$$

with the solution

$$\begin{aligned} M_{xy}(t) &= M_{xy} e^{-i\gamma B_0 t} \\ M_z(t) &= 0. \end{aligned} \tag{2.28}$$

FLIP ANGLE The net magnetization can be rotated by the application of an RF-pulse with a duration τ and direction along $\vec{B}_1$ in the xy-plane. The RF-pulse causes a 'flipping' of the net magnetization out of its thermal equilibrium. The rotation away from the z-plane occurs with an angle α which is therefore being called flip angle and is defined as

$$\alpha = \gamma \int_\tau B_1(t)\, dt, \tag{2.29}$$

which is can be simplified for a rectangular pulse to

$$\alpha = \gamma\tau B_1. \tag{2.30}$$

The magnetization and its direction can be changed by the application of B_1. After application of an RF-pulse, the magnetization returns to equilibrium due to relaxation effects, which cause the equilibrium magnetization in $\vec{B_0}$ direction. The process of the spins returning to their state that is only affected by B_0 is called relaxation. The effect occurs parallel to B_0 as well as transverse to B_0. Therefore, one distinguishes between the relaxation times T1 (parallel) and T2 (transverse).

SPIN-LATTICE RELAXATION The longitudinal relaxation is parallel to B_0 and is called spin-lattice relaxation. The relaxation occurs because the spins are returning to the most favorable state of energy. Thus, energy – in the form of heat – needs to be released from the nuclei to the surrounding tissue through rotation. Therefore, the spin-lattice relaxation not only depends on the applied field strength and the considered nucleus but also on the surrounding tissue and its properties which determine the efficiency of energy exchange. The spin-lattice relaxation uses the time constant T1, which can be derived based on the differential equation of the magnetization in z-direction (M_z), with the initial magnetization $M(0)$, by

$$\frac{dM_z}{dt} = \frac{M_0 - M_z}{T1}, \tag{2.31}$$

with the solution of the exponential equation being

$$M_z(t) = M_z(0) \cdot e^{-t/T1} + M_0 \cdot (1 - e^{-t/T1}). \tag{2.32}$$

Here, $M_z(0)$ is the net magnetization in z-direction at $t = 0$, which comes to zero when assuming an RF-pulse with $\alpha = 90°$, which allows the simplification to

$$M_z(t) = M_0 \cdot (1 - e^{-t/T1}) \tag{2.33}$$

showing that T1 relaxation after a 90° pulse is at 63% after $1 \cdot T1$ and above 99% after $5 \cdot T1$. For $\alpha = 180°$ the equation can be solved with

$$M_z(t) = M_0 \cdot (1 - 2e^{-t/T1}) \tag{2.34}$$

as M_z equals $-M_0$ at $t = 0$. Figure 2.2 shows the exponential recovery of the spin-lattice relaxation.

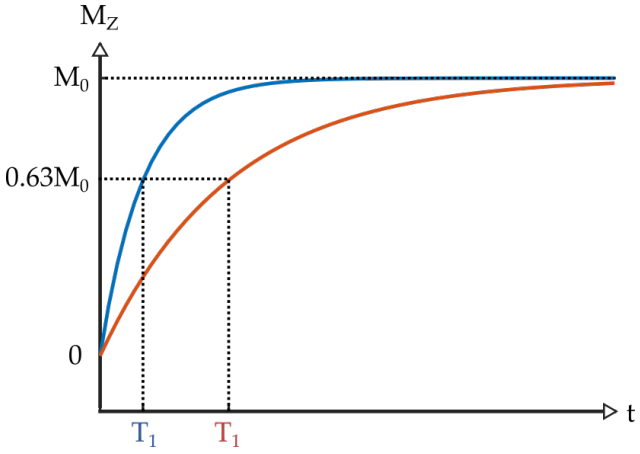

Figure 2.2: Spin-lattice relaxation after a 90° RF-pulse. The figure depicts the increasing longitudinal magnetization over time of two tissues with different T1-times. The blue blue curve depicts the longitudinal magnetization of a tissue with a shorter T1-time than the tissue that is depicted with the red curve.

SPIN-SPIN RELAXATION The transverse relaxation decays after elimination of $\overrightarrow{B_1}$ influences and it is called spin-spin relaxation. It uses the time constant T2.

Right after signal excitation, all spins are in phase and with the same precession which causes the transversal magnetization M_{xy}. The magnetic field strength that is

applied to each nucleus depends on the B_0 field and on the magnetic moment of their neighboring atoms which have an impact because of the dipole-dipole interactions. The Brownian motion describes random movements of atoms causing the magnetic field strength to be locally dependent. Thus, each spin experiences a different field causing a change in freqeuncy and an accumulation of phase differences. The differential equation of the transverse magnetization is therefore

$$\frac{dM_{xy}}{dt} = -\frac{M_{xy}}{T2} \tag{2.35}$$

and can be solved with an exponential decay of

$$M'_{xy}(t) = M'_{xy}(0) \cdot e^{-t/T2}, \tag{2.36}$$

where $M'_{xy}(0)$ is the transverse net magnetization at the beginning of the relaxation process and T2 is the time constant describing the spins' irreversible dephasing process. The equation can be simplified for $\alpha = 90°$ to

$$M'_{xy}(t) = M_0 \cdot e^{-t/T2} \tag{2.37}$$

as transverse net magnetization M_{xy} is at M_0 when the relaxation process starts according to Equation 2.25. After $1 \cdot T2$ the dephasing of the spins is at 63% and it reaches over 99% at $5 \cdot T2$, when $\alpha = 90°$. Figure 2.3 shows the exponential decay of the transverse magnetization.

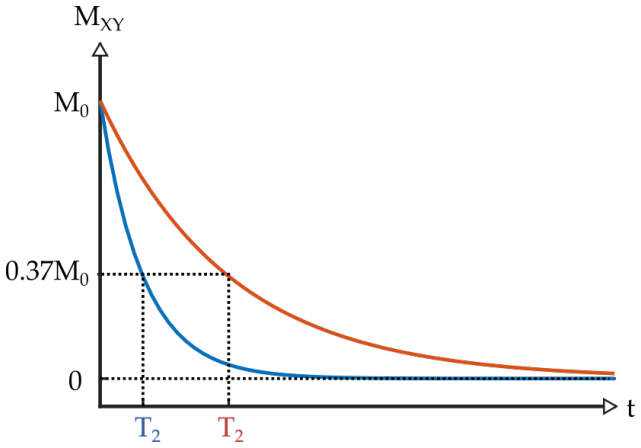

Figure 2.3: Spin-spin relaxation after a ang90 RF-pulse. The figure depicts the decreasing transverse magnetization over time of two tissues with different T2-times. The blue blue curve depicts the transverse magnetization of a tissue with a shorter T2-time than the tissue that is depicted with the red curve.

With dipole fields being more dynamic in liquids and more static in solids, the spin's fluctuations are more prevalent in fluids and thus the T2 times are longer. The spin-spin relaxation does not involve energy transfer (heat) like T1 relaxation and can occur independently, whereas the spin lattice relaxation will always cause dephasing and thus there is no T1 relaxation without T2 relaxation.

T2, like T1 also depends on the surrounding tissue and is considered a tissue property. However, as T2 generally arises from the locally fluctuating magnetic field strengths, which are not only caused by the surrounding spins but can also be influenced by possible inhomogeneities of the B_0-field, those will consequently also affect the dephasing process with a measurable impact on T2, resulting in $T2^*$.

With increasing B_0 inhomogeneities, transverse relaxation will be accelerated and the measured $T2^*$ will be shortened. T2 is a tissue property that is independent of the magnetic field., whereas the observed transverse relaxation time $T2^*$ is defined as

$$\frac{1}{T2^*} = \frac{1}{T2} + \frac{1}{T2'} \tag{2.38}$$

where $T2'$ is the reversible component of the observed relaxation process deriving from the macroscopic B_0 inhomogeneities. The $T2^*$ relaxation damps the free induction decay. Considering the field inhomogeneities to be static, the $T2'$ effects can be eliminated by applying a 180° RF-pulse after a 90° excitation pulse. The additional 180° pulse generates a *spin-echo*[2] which enables determination of the actual tissue property T2. [BPP48]

BLOCH EQUATIONS The Bloch equations were derived by Felix Bloch in 1946. They combine the above described macroscopic magnetization with the signal excitation and the relaxation processes, which applies for the $I = \frac{1}{2}$ spin of ^1H in homogeneous media.

The three-dimensional components are described by:

$$\begin{aligned}
\frac{dM_x}{dt} &= \gamma \left(\vec{M} \times \vec{B}\right)_x - \frac{M_x}{T2} \\
\frac{dM_y}{dt} &= \gamma \left(\vec{M} \times \vec{B}\right)_y - \frac{M_y}{T2} \\
\frac{dM_z}{dt} &= \gamma \left(\vec{M} \times \vec{B}\right)_z - \frac{M_z - M_0}{T1}
\end{aligned} \tag{2.39}$$

This can be simplified, when assuming $\vec{B}$ to be a longitudinal magnetic field in z-direction, to

$$\begin{aligned}
\frac{dM_x}{dt} &= \omega_0 M_y - \frac{M_x}{T2} \\
\frac{dM_y}{dt} &= -\omega_0 M_x - \frac{M_y}{T2} \\
\frac{dM_z}{dt} &= \frac{M_0 - M_z}{T1},
\end{aligned} \tag{2.40}$$

where ω_0 is the Larmor frequency defined according to Equation 2.20.

The x and y component of the equation can be solved by considering the definition of the $\vec{B}$-field and come to

$$\begin{aligned}
M_x(t) &= e^{-t/T2}(M_x(0)\cos(\omega_0 t) + M_y(0)\sin(\omega_0 t)) \\
M_y(t) &= e^{-t/T2}(M_y(0)\cos(\omega_0 t) - M_x(0)\sin(\omega_0 t)),
\end{aligned} \tag{2.41}$$

which can be combined to:

$$\begin{aligned}
M_{xy}(t) &= M_x(t) + iM_y(t) \\
&= e^{i\omega_0 t} \cdot e^{-t/T2} M_{xy}(0)
\end{aligned} \tag{2.42}$$

2 The spin-echo was discovered by Erwin Hahn in 1950 [Hah50].

SIGNAL DETECTION Faraday's law of induction (also: Maxwell-Faraday equation) describes the interaction of a magnetic field $\vec{B}$ with an electric circuit. It explains the phenomenon of electromagnetic induction stating that the change of the magnetic flux Φ in a coil induces an induction voltage U_{ind} that is defined as

$$\begin{aligned} U_{ind} &= -\frac{d\Phi}{dt} \\ &= -\frac{d}{dS}\int_S \vec{B}\, d\vec{S} \end{aligned} \tag{2.43}$$

with $\vec{S}$ being the surface of the coil and the magnetic flux being described with the Stokes theorem

$$\begin{aligned} \Phi(t) &= \int_S \vec{B}(S,t)\, dS \\ &= \int_V \vec{M}_{xy}(\vec{r},t)\,\vec{B}_1^-(\vec{r})\, d^3rtext, \end{aligned} \tag{2.44}$$

where $\vec{r}$ indicates the location within the magnetic field and $\vec{B}_1^-$ is the coil's receive field. When the *principle of reciprocity*[3] applies, B_1^- corresponds to the magnetic flux created by the coil (B_1^+, also called the transmit field). With Equation 2.43 and Equation 2.44, one can derive

$$U_{ind} = -\frac{d}{dt}\int_V \vec{M}(\vec{r},t)\,\vec{B}_1^-(\vec{r})\, d^3r \tag{2.45}$$

The magnetization $\vec{M}$ is constant in longitudinal direction with only B_0 being present but the magnetic flux experiences changes with the introduction of B_1 when $\vec{M}$ is flipped away from the z-axis into the transverse xy-plane by the angle α. With Equation 2.26 and Equation 2.45, one can derive

$$U_{ind} \propto \gamma B_0 B_1 V M_0 \sin(\alpha)\sin(\omega_0 t + \phi) \tag{2.46}$$

as a homogeneous B_1 caused $M_{xy} = M_0 \sin(\alpha)$. Assuming the magnetic field to be perfectly homogeneous and neglecting all relaxation effects, it follows

$$U_{ind} \propto S = \gamma^3 I(I+1)c \tag{2.47}$$

with S being the physical sensitivity of the nucleus and c being the natural, relative abundance of the isotope. Table 2.1 lists multiple commonly used NMR nuclei ($I \neq 0$) which may also be present in the human body. The physical sensitivity S is given relative to the sensitivity of ^1H [Har+01].

However, the NMR SI does not only depend on the signal sensitivity but also on the natural abundance of the nucleus in the examined substance, which was exemplary calculated for ^1H and ^{23}Na in the human brain in Equation 2.14 and Equation 2.15.

2.1.4 *Quadrupolar interactions*

The above-explained dipole-dipole interactions occur for all nuclei with a spin of $I \geqslant 1/2$, like ^1H. All nuclei with a spin $I > 1/2$, like ^{23}Na with $I = 3/2$, experience additional

3 The principle of reciprocity describes how to determine an RF coil's receive sensitivity from its transmit field. It was introduced by David I. Hoult et al. in 1976 [HR76].

Table 2.1: Physical NMR properties of some nuclei in the human body according to [Har+01].

Isotope	Spin I	μ/μ_N	$\gamma/2\pi \left[\frac{MHz}{T}\right]$	c [%]	S
^{1}H	$1/2$	4.84	42.58	99.99	1.0
^{17}O	$5/2$	−2.24	−5.77	0.04	$1.11 \cdot 10^{-5}$
^{19}F	$1/2$	4.55	40.08	100	$8.3 \cdot 10^{-1}$
^{23}Na	$3/2$	2.86	11.27	100	$9.3 \cdot 10^{-2}$
^{31}P	$1/2$	1.96	17.25	100	$6.7 \cdot 10^{-2}$
^{39}K	$3/2$	0.51	1.99	93.26	$4.8 \cdot 10^{-4}$

electrical quadrupolar interactions. They possess a nuclear electric-quadrupole moment Q that can be calculated with the quadrupolar coupling constant

$$C_Q = \frac{e^2 qQ}{\hbar} \tag{2.48}$$

and the quadrupolar frequency

$$\omega_Q = \frac{e^2 qQ}{2I(2I-1)\hbar}, \tag{2.49}$$

where the system can be described by the quadrupolar Hamiltonian

$$\mathcal{H}_Q = \frac{\omega_Q}{2}(3I_z^2 - I(I+1)) \tag{2.50}$$

when assuming human tissue where the quadrupolar interactions are significantly smaller than the Zeeman interactions ($\mathcal{H}_Q \ll \mathcal{H}_z$) and when assuming a perfect ellipsoid shape of the charge distribution. [MR13]

For ^{1}H, the quadrupole moments are zero due to its $I = 1/2$ spin. ^{23}Na, with its $I = 3/2$ spin, has a quadrupolar moment but all higher-order moments are zero, which become non-zero for nuclei with higher spins.

With no quadrupolar moment (for all nuclei with $I \leqslant 1/2$), the electrical charge distribution is spherical and thus symmetrical so it does not interact with electric field gradients. With a quadrupolar moment of the nucleus, the nuclear electrical charge distribution becomes elliptical and thus asymmetrical. Different charge orientations which do not correspond to the same energy level become possible. The nucleus can take the more or less favorable energetic state. Examples of different charge distributions are illustrated in Figure 2.4.

The rotation of the nucleus can change the orientation of the asymmetrical charge distribution in reference to the electric field gradient, causing the asymmetrical charge distribution to interact with the electric field gradients.

The quadrupolar interactions depend on the surrounding tissue, which influences the rotational correlation time τ_C that is defined as the time it takes for a molecule to rotate 1 rad around an arbitrary axis. The consideration of the rotational correlation time allows the separation into different motional regimes of the quadrupolar interactions, depending on τ_C and $\bar{\omega_Q}$. Furthermore, the time-averaged value of ω_Q, which is $\bar{\omega}_Q$ needs to be considered with macroscopic anisotropy causing $\bar{\omega}_Q \neq 0$ because of a resulting shift of the energy levels.

Considering the interaction of ^{23}Na within different surrounding media, one yields different spectra according to Rooney et al. [RS91]:

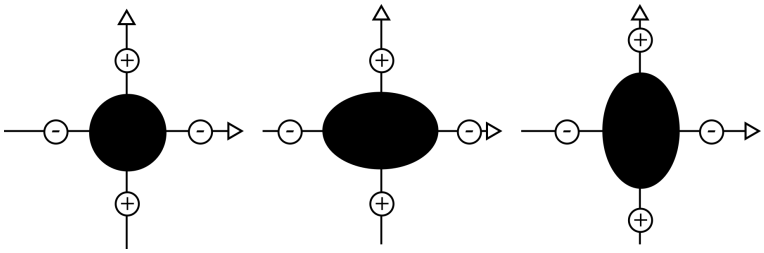

Figure 2.4: The charge distribution of a nucleus being placed in an electric field with two negative charges on the x-axis and two positive charges on the y-axis. The figure on the left depicts the spherical electric charge of an $I = 1/2$ spin. The other two figures depict the ellipsoid charge distribution of an $I = 3/2$ spin with the figure on the right showing the energetically less favorable state compared to the state that is shown in the middle figure.

1. $\omega_0\tau_C \ll 1 \rightarrow$, $\bar{\omega}_Q = 0 \rightarrow$ extreme narrowing motion regime
   - Type d spectrum, e.g. NaCl solution
2. $\omega_0\tau_C > 1$, $\bar{\omega}_Q = 0 \rightarrow$ intermediate motion regime, bi-exponential relaxation
   - Type c spectrum, e.g. human tissue (interaction with macromolecules such as proteins)

This is illustrated in Figure 2.5. Rooney et al. further mention type b (e.g. inhomogeneous powder) and type a (e.g. crystalls) spectra, which will not be further explained here and are not depicted in Figure 2.5 as they are not relevant for the work presented in this thesis.

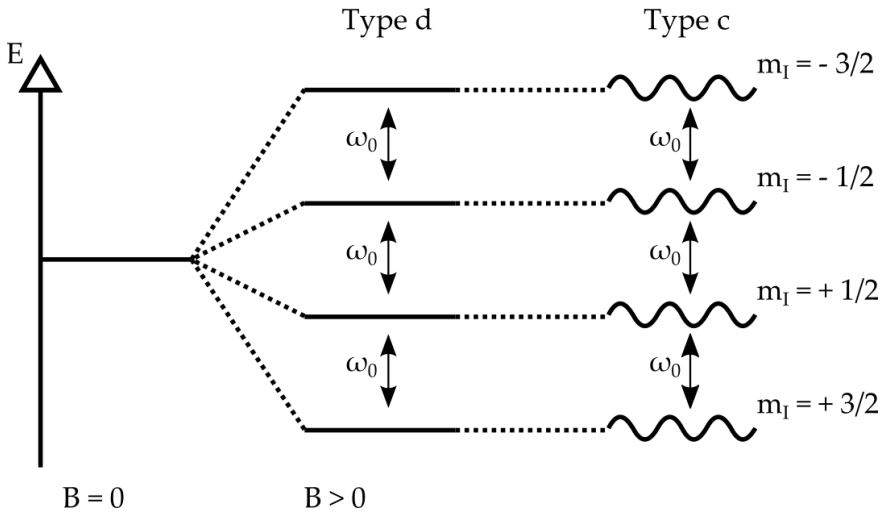

Figure 2.5: NMR spectra of $I = 3/2$ under the influence of no magnetic field (left) and under the influence of a magnetic B-field (right), which results in different spectra depending on the tissue type. The figure is adapted from [RS91].

Quadrupolar interactions have an additional impact on both (spin-lattice and spin-spin) relaxation times and thus cause a bi-exponential signal decay with two components of each relaxation for type c spectra but not for type d spectra. Therefore, the relaxation times T1 and T2 will be split into one fast (index: f) and one slow (index: s) component that are defined by

$$
\begin{aligned}
T1_f &= \frac{1+(\omega_0\tau_C)^2}{4C\tau_C} \\
T1_s &= \frac{1+(2\omega_0\tau_C)^2}{4C\tau_C} \\
T2_f &= \frac{1}{C\left(2\tau_C + \frac{2\tau_C}{1+\omega_0^2\tau_C^2}\right)} \\
T2_s &= \frac{1}{C\left(\frac{2\tau_C}{1+(2\omega_0\tau_C)^2} + \frac{2\tau_C}{1+(\omega_0\tau_C)^2}\right)}
\end{aligned}
\tag{2.51}
$$

where C is the coupling rate

$$
C = \frac{1}{40}\left(\frac{e^2qQ}{\hbar}\right)^2\left(1+\frac{\eta^2}{3}\right) \tag{2.52}
$$

with η being a parameter of the field gradient asymmetry. The model is an extension of the Bloch equations. It is named after Nicolaas Bloembergen, Edward Mills Purcell, and Robert Pound [BPP48] and is thus called the Bloembergen-Purcell-Pound (or short BPP) theory. It applies exclusively to pure substances.

For T2, the fast component is responsible for 60% and the slow component is responsible for 40% of the transverse relaxation, when considering one specific medium. The two T2 components of ^{23}Na have been measured and a bi-exponential decay was observed in a way that both components were distinguishable. For T1, the fast component takes 20% of the total longitudinal relaxation and the slow component takes 80%. Here, the bi-exponential decay for ^{23}Na is challenging to measure as the values of $T1_f$ and $T1_s$ are similar. Thus, for T1, both components are difficult to distinguish from each other and a mono-exponential T1 decay is a common assumption. Assuming very short correlation times with $\omega_0\tau_C \ll 1$, T1 and T2 become mono-exponential again and yield similar values. Thus,

$$
T1_f = T1_s = T2_f = T2_s = \frac{1}{4C\tau_C} \tag{2.53}
$$

applies.

2.2 MAGNETIC RESONANCE IMAGING

In 2003, the Nobel prize in medicine was awarded to Paul C. Lauterbur [Lau73] and Sir Peter Mansfield [MG73], who are considered pioneers in the field of MRI, which uses the NMR phenomenon for medical imaging and diagnosis.
MRI enables the representation of the internal anatomy without exposure to ionizing radiation. MRI is considered to be a safe and non-invasive imaging technique, as (opposite to computer tomography, CT) it does not use ionizing radiation. MRI has been used in the clinical routine since the nineteen eighties[4]. It is well-established and state of the art for the diagnosis of many conditions and diseases. This section will provide a brief overview of the basic concepts of MRI physics and applications.

4 In 1971, Raymond Damadian was the first to suggest in-vivo NMR for cancer detection [Dam71].

2.2.1 *k-space and spatial encoding*

Any acquired NMR data can be understood to be in the Fourier space, which is here called k-space, thus being the *Fourier transform*[5] of the magnetic resonance (MR) image. Consequently, the inverse Fourier transform needs to be applied to obtain the image. As NMR signals have magnitude and phase, all k-space data are complex with a real and imaginary part. The SI in k-space over the time τ is determined by the transverse magnetization and the applied gradient by

$$SI = \iiint M'_{xy}(x,y,z) \cdot e^{-i\gamma\left(\int_\tau G_x(t)x\,dt + \int_\tau G_y(t)y\,dt + \int_\tau G_z(t)z\,dt\right)}\,dx\,dy\,dz \tag{2.54}$$

which can be simplified to

$$SI(\vec{k}) = \iiint M'_{xy}(x,y,z) \cdot e^{-i(xk_x + yk_y + zk_z)} \tag{2.55}$$

when introducing the wave number k with

$$k_i = \gamma \int_\tau G_i(t)\,dt \tag{2.56}$$

The signal intensities $SI(\vec{k})$ can therefore be transformed from k-space into image space through the Fourier transform $\mathcal{F}$. Thus, information from k-space defines the resulting MR image.

MR image reconstruction depends on the localization of the acquired NMR signal in k-space in image space, which is called spatial encoding. It is enabled by the introduction of magnetic field gradients $\vec{G}$ that are superimposed on the magnetic field. Considering the Larmor frequency ω_0 depending on the field strength according to Equation 2.20, the introduction of a field gradient

$$\vec{G} = \begin{pmatrix} G_x \\ G_y \\ G_z \end{pmatrix} = \begin{pmatrix} \frac{dB}{dx} \\ \frac{dB}{dy} \\ \frac{dB}{dz} \end{pmatrix} \tag{2.57}$$

will impact ω_0 by

$$\begin{aligned} \omega(\vec{r}) &= \gamma B(\vec{r}) \\ &= \gamma(B_0 + \vec{r}\,\vec{G}), \end{aligned} \tag{2.58}$$

resulting in each spatial point corresponding to one specific frequency. Considering two-dimensional imaging, the information of the location is encoded via three different processes: slice selection, phase encoding, and frequency encoding. The spatial encoding process is graphically illustrated in figure Figure 2.6

5 The Fourier transform is a mathematical function, translating a time- or space-dependent function to frequency dependency, which was described by the French mathematician Jean-Baptiste J. Fourier [Fou22].

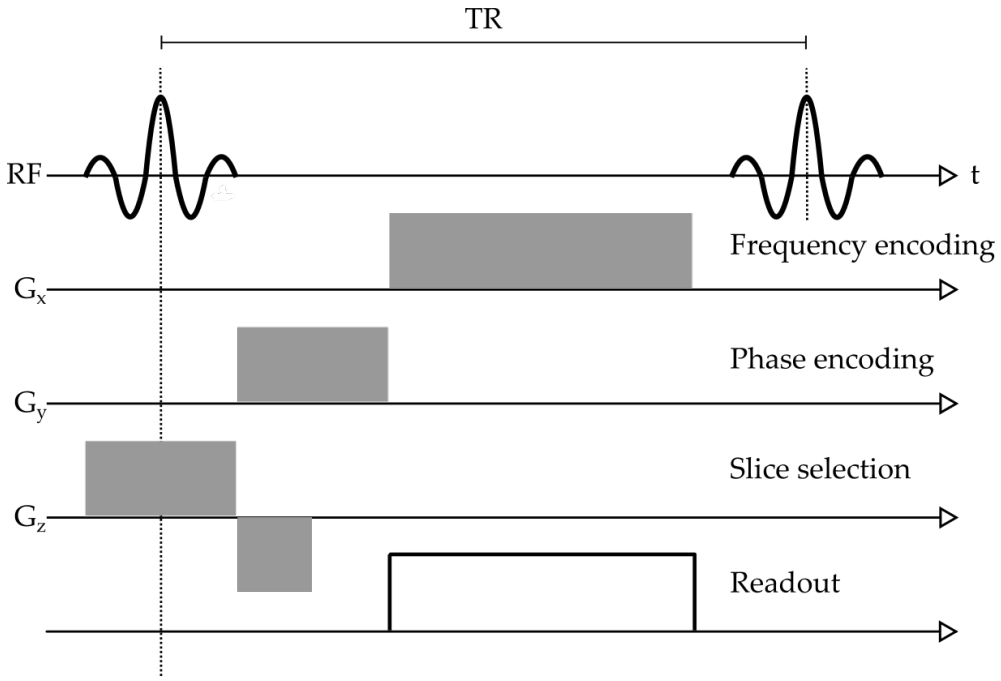

Figure 2.6: Spatial encoding of the NMR signal for the localization of the signal to enable MR image reconstruction.

SLICE SELECTION The application of a gradient parallel to the main magnetic field with $G_z \neq 0$ will cause a dependency of the Larmor frequency on the longitudinal location with

$$\omega_0(z) = \gamma(B_0 + zG_z) \tag{2.59}$$

and is thus called *slice selection* when applied parallel to the RF-pulse. The gradient is activated during the RF-pulse. The frequency varies along the z-axis. The application of an RF-pulse will only excite spins with resonance frequencies within the RF bandwidth $\Delta\omega$ which are thus in local proximity to each other. The spatial width Δz of the excited slice depends on the RF bandwidth by

$$\Delta z = \frac{\Delta\omega}{\gamma G_z} \tag{2.60}$$

with the slice thickness linearly increasing with $\Delta\omega$. After the RF-pulse, a second gradient is applied in z-direction. It has opposite direction and half the area under the curve of the first gradient. Its purpose is the compensation of the dephasing of the spins.

Slice selection is mostly relevant for two-dimensional imaging. For three-dimensional data acquisition, no slice selection is needed as all spins within the coil's reach are excited at the same time, requiring an additional phase encoding z-direction, which is described below. While two-dimensional imaging commonly uses a sinc-pulse for the signal excitation (Figure 2.6), three-dimensional imaging mostly uses a rectangular pulse.

PHASE ENCODING The second dimension of spatial encoding is the G_y gradient along the y-axis, which is applied after the RF-pulse but before the readout window. The G_y gradient changes the frequency along the y-axis for a limited time τ. After deactivation of G_y, the spins have the same frequency again but were shifted in

phase along their location on the y-axis. Therefore, this encoding step is called *phase encoding*. The shift can be described with

$$\Delta\phi(y) = \gamma G_y(y)\tau \tag{2.61}$$

and is repeated with varying G_y causing different phase shifts and thus precise localization of the y-axis based on the signals' phase shifts.

FREQUENCY ENCODING The gradient along the x-axis G_x is applied during the readout window. The precession frequency of the spin is therefore depending on their location on the x-axis during readout with

$$\omega(x) = \gamma \overrightarrow{B}(x) = \gamma(B_0 + G_x(x)) \tag{2.62}$$

and the last encoding step is therefore called *frequency encoding*.

IMAGE RESOLUTION AND FIELD OF VIEW All points in k-space do not change continuously but discrete. This is because of the sampling with an analogue to digital converter with the time difference Δt_x in frequency encoding direction and gradient difference t_y in phase encoding direction. It results in a total amount of N_i points that were sampled in the respective direction, with the distance between two neighboring points in k-space being defined as Δk_i. The most common k-space sampling is with a *Cartesian*[6] trajectory resulting in a cuboid k-space. In two-dimensional imaging, the slice thickness is defined by G_z and pulse bandwidth. Using Cartesian imaging, Δk_i can be described with

$$\begin{aligned} \Delta k_x &= \frac{\gamma}{2\pi} G_x \Delta t_x \\ \Delta k_y &= \frac{\gamma}{2\pi} t_y \Delta G_y. \end{aligned} \tag{2.63}$$

The field of view (FoV) of the MR image depends on that distance between two k-space points with

$$\begin{aligned} FoV_x &= \frac{1}{\Delta k_x} \\ FoV_y &= \frac{1}{\Delta k_y} \end{aligned} \tag{2.64}$$

and the resolution of an MR image is defined by the distance between two image points, depending on the maximum values k_{max} and $-k_{max}$ in that direction with

$$\begin{aligned} \Delta x &= \frac{1}{2k_{max,x}} = \frac{1}{N_x \gamma G_x \Delta t_x} \\ \Delta y &= \frac{1}{2k_{max,y}} = \frac{1}{N_y \gamma t_y \Delta G_y}. \end{aligned} \tag{2.65}$$

The *Nyquist criterion*[7] requires a sampling rate of at least twice the highest frequency to be sampled, thus setting an upper limit for Δt_x and ΔG_y with

6 Cartesian sampling means acquisition of regularly spaced data points, enabling the Fast Fourier Transformation.

7 The Nyquist criterion was defined by the electrical engineer Harry Nyquist. It determines a sampling rate for the stability of a dynamic system [Nyq32].

$$\begin{aligned} \Delta t_x \leqslant \frac{1}{2\omega_{max,x}} = \quad & \frac{1}{N_x \gamma G_x \Delta x} \\ \Delta G_y \leqslant \quad & \frac{1}{N_y \gamma t_y \Delta y}. \end{aligned} \tag{2.66}$$

SIGNAL-TO-NOISE RATIO The quality of an MR image can be quantified by consideration of the signal-to-noise ratio (SNR).

The SNR is a commonly-used parameter to evaluate the power of the measured signal compared to the unintentionally recorded additional background noise. It is defined as the fraction of the mean SI to the standard deviation of the background noise, which is expressed by

$$SNR = \frac{\mu_{Signal}}{\sigma_{Noise}}. \tag{2.67}$$

The noise in MR images derives from the hardware (MRI scanner and RF coils) or from artifacts that are caused by the investigated body. The acquired noise can be assumed to be *Gaussian*[8] in k-space. To derive the MR image, one uses the complex Fourier transform and mostly only regards the absolute values of the image points instead of considering the real and imaginary part. After this operation, the noise in image space follows the Rician distribution [Mac96; GP95; Ric44].

The SNR is proportional to the voxel volume and the square root of the MRI acquisition time (TA), thus

$$SNR \propto \Delta x \Delta y \Delta z \sqrt{TA} \tag{2.68}$$

applies.

2.2.2 *Sequences and contrasts*

MRI sequences are defined by their sequential RF-pulses, the set of gradients, and the related parameters which determine the MRI contrast that eventually defines the visibility of the depicted structures. Human tissues have different relaxation times and therefore different contrasts are best suited for the diagnosis of differing pathologies within differing types of tissues.

IMAGE CONTRASTS The most common MRI sequences aim for one of the three main contrasts:

1. T1-weighted
2. T2-weighted
3. ρ-weighted

Those can be less or more prevalent within an MR image by adjusting the echo time (TE) and the repetition time (TR) when using a spin-echo sequence. Both parameters are crucial for sequence design. The repetition time is the time between two RF excitation pulses and the echo time is the time from the middle of the RF excitation pulse to the peak of the received signal which is graphically illustrated in Figure 2.6.

8 Gaussian noise is noise with its probability density function being the normal (Gaussian) distribution.

A T1-weighted (T1w) image is acquired when using short TR (TR $\ll$ T1) and a short TE (TE $\ll$ T2*). The T2-weighted (T2w) contrast is caused by a long TR (TR $>$ 3T1) and a long TE (TE $> 3 - 5 \cdot$ T2*). The spin-density or ρ-weighted contrast depends on the investigated nucleus and is also called proton-weighted or sodium-weighted contrast. It can be obtained by using a long TR and a short TE. When using a short TR and a long TE, the contrast will be generally poor. The contrasts are graphically illustrated in Figure 2.7.

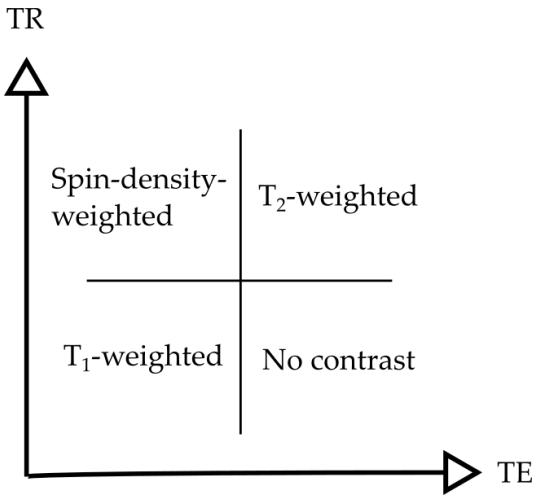

Figure 2.7: The effect of long and short TR and TE on the resulting MRI contrast: T1-weighted, T2-weighted, and spin-density-weighted.

GRADIENT-ECHO There are many different MRI sequences that are used and established in the clinical routine. Different MRI scanner vendors use company-specific names for their sequences but one of the most basic and relevant sequence is the gradient-echo sequence. It uses only one RF-pulse before the readout. Thus, signal relaxation follows the free induction decay. The x-gradient can be applied in the opposite direction to dephase the spins which enables the sampling to start at higher frequency instead of the k-space center. The excitation angle α can be adjusted for the specific tissue that is investigated with

$$\alpha_E = \arccos\left(e^{-TR/T1}\right), \tag{2.69}$$

where α_E is the Ernst angle that allows to generate the maximal SI.

The MR image SI is proportional to TR and TE, which can be described by

$$SI = \rho \sin(\alpha) \frac{1 - e^{-TR/T1}}{1 - \cos(\alpha) e^{-TR/T1}} e^{-TE/T2^*} \cdot K \tag{2.70}$$

when a flip angle ($\alpha \leqslant 90°$) is chosen, where K is the transmit/receive coil sensitivity. In that case, the sequence is also called fast low-angle shot, or short FLASH. Equation 2.70 shows a linear dependency between SI and the spin-density ρ for gradient-echo sequences, which enables the below describes quantification processes.

SPIN-ECHO The spin-echo sequence uses, compared to the gradient-echo, an additional 180° pulse after the 90° RF excitation pulse. The purpose is to correct for $\vec{B}_0$-field inhomogeneities and thus eliminating the T2* effects, which enables the

measurement of T2. The 180° pulse is applied exactly in between the excitation pulse and the readout window. Thus, at $t = \frac{TE}{2}$ after the first RF-pulse.

After the excitation pulse, dephasing occurs due to B_0 inhomogeneities with $T2^*$. The 180° pulse reverses the spin's phase, which also reverses the dephasing processes (this is called rephasing). Therefore, at readout, the spin's dephasing due to field inhomogeneities has occurred in two opposite directions and was thus erased. Thus, at readout, the spin's phase is only depending on T2 rather than $T2^*$. This is why T2 is also called the irreversible transverse relaxation whereas the transverse relaxation due to field inhomogeneities is considered reversible.

INVERSION RECOVERY The inversion recovery sequence uses an additional 180° pulse before the RF excitation pulse. Thus, the longitudinal magnetization is inverted before it is flipped by the excitation pulse. The time between the inversion pulse and the excitation pulse is called inversion time TI.

This sequence is commonly used when one aims to determine T1-times. The longitudinal magnetization is flipped to $-M_0$ and depends on TI and T1 with

$$S \propto \left| M_0 \left(1 - 2e^{TI/T1} \right) \right| \tag{2.71}$$

and passes zero during the relaxation process. The signal of tissues can thus be eliminated with

$$TI = \ln(2)T1. \tag{2.72}$$

Eliminating the signal of certain tissues can be useful for the more detailed diagnosis of the surrounding tissue.

2.2.3 *Quantification*

Conventional MRI sequences will provide images with a contrast that was impacted by T1, T2, and spin-density ρ. The signal intensity further depends on coil positioning, measurement time and also on placement within the MRI scanner due to field inhomogeneities. Inhomogeneities may also arise from the RF coil, which are either from the transmit (B_1^+)- or the the receive (B_1^-)-field. Therefore, the MRI technique is considered not to be a quantitative imaging technique – opposite to CT, which uses the Hounsfield unit with absolute numbers.

Even though, various MRI quantification techniques have been implemented and established like the apparent diffusion coefficient (ADC) from diffusion-weighted imaging (DWI), or T1- and $T2^*$-maps.

For gradient-echo sequences, the MR SI linearly depends on the spin-density as was shown in Equation 2.70. Further considering the coil's inhomogeneities, the equation can be adjusted by its dependency on the location r and can thus be expressed by

$$SI(r) \propto \rho(r) \cdot \left(C_{B1^-} \cdot C_{B1^+} \cdot C_{T1} \cdot C_{T2^*} \right)^{-1}, \tag{2.73}$$

where $\rho(r)$ describes the spin density at location r. C_{B1^+} and C_{B1^-} are the correction factors for the transmit / receive field, respectively. C_{T1} and C_{T2^*} are correction factors for T1- and $T2^*$-weighting with C_{T2^*} changing depending on whether the considered medium can be assumed to have a mono- or a bi-exponential $T2^*$ relaxation.

The B_1^+ correction factor exclusively depends on the flip angle α with

$$C_{B1^+} = \sin \alpha, \tag{2.74}$$

which becomes 1 and thus obsolete when a homogeneous $\alpha = 90°$ can be applied. The relaxation time correction factors can be calculated with:

$$\begin{aligned} C_{T1} &= \frac{1 - \cos \alpha e^{-TR/T1}}{1 - e^{-TR/T1}} \\ &\approx \frac{1}{1 - e^{-TR/T1}} \\ C_{T2^*,mono} &= \frac{1}{e^{-TE/T2^*}} \\ C_{T2^*,bi} &= \frac{1}{0.6e^{-TE/T2^*_f} + 0.4e^{-TE/T2^*_s}} \end{aligned} \tag{2.75}$$

The approximation for C_{T1} is valid when $\alpha \approx 90°$.

The B_1^--field and its correction factor mainly depend on the used coil's sensitivity. Inhomogeneities in the B_1^--field can be assumed to occur mainly within low frequencies. There are common approaches to correct for B_1^- inhomogeneities. One is to scan a homogeneous phantom (for ^{23}Na MRI a saline phantom is required), acquiring the coil's sensitivity map, which can then serve as correction map. Another approach is to use the assumption of B_1^- inhomogeneities to occur mainly within low frequencies and to apply a low-pass filter (LPF) to obtain the correction map. The method using a LPF was used in this thesis and is explained in more detail in subsubsection 3.4.2.2.

2.3 ^{23}Na MRI

Sodium (^{23}Na) yields, after ^{1}H, the second strongest NMR signal of all nuclei in the human body and ^{23}Na is the only stable sodium isotope in the human body, thus, having a relative abundance of 100%. The NMR sensitivity of ^{23}Na is $\approx 9.3\%$ (see Table 2.1) relative to the ^{1}H NMR sensitivity. Additionally, the ion's concentration in the human body is $\approx 20 - 60$ mM compared to ≈ 80 M ^{1}H, yielding a ^{23}Na MRI signal that is around 20,000-times lower compared to the ^{1}H MRI signal.

First in-vivo ^{23}Na MR images in the human head were performed in 1985 by Hilal et al. [Hil+85]. Ever since, applications, sequences, and acquisition techniques have evolved and been adapted [LHC86; Per+86; Kol+87; RHO89; Win90; Boa+97b; Boa+97a; Thu+99]. Along with rising magnetic field strengths in research and in the clinical routine, ^{23}Na MRI has evolved and can nowadays provide valuable information for a variety of pathologies that cannot be derived from ^{1}H MRI alone [MR13; SWL16; KS14; Thu18; BSJ19; Hu+20].

2.3.1 *Physiology*

In the human body, ^{23}Na plays an essential role in many cellular processes and functions. It occurs extra- and intra-cellular with a respective concentration of ≈ 145 mM and $\approx 10 - 15$ mM. The concentration gradient is maintained by the Na^+/K^+ ATP-ase, a trans-membrane protein pumping Na^+ and K^+-ions across the plasma membrane against their concentration gradient [SE92; Fal+94; Som02; Som04]. The mechanism is depicted in Figure 2.8.

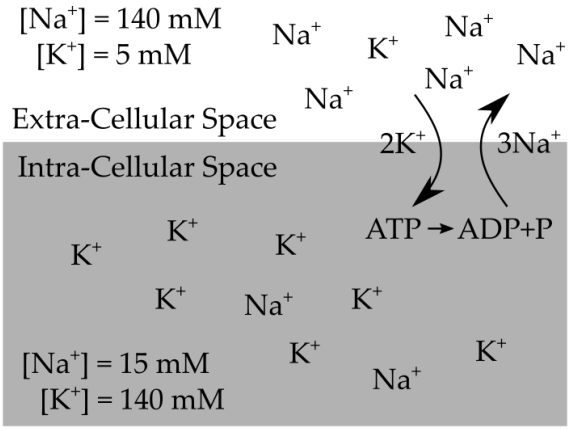

Figure 2.8: Graphical illustration of the Na^+/K^+-ATPase pumping Na^+ and K^+ ions against their concentration gradients.

The protein moves three Na^+-ions from the cytoplasm into the extra-cellular space and exchanges those for two K^+-ions whilst requiring energy in the form of adenosine triphosphate (ATP). An insufficient ATP supply will restrain the ATPase from maintaining the Na^+/K^+ gradient. This will lead to an influx of Na^+-ions into the cell and thus an increased intra-cellular sodium concentration (ISC). Because of osmosis, excessive amounts of water will enter the cell, leading to osmotic swelling and eventually causing cell death [MR13; Hu+20].

The tissue sodium concentration (TSC) is the volume-weighted average of the ISC, and extra-cellular sodium concentration (ESC) [Boa+94; Thu+99; BSJ19]. In the human body, ESC is apparently relatively constant around 145 mM, whereas the ISC might undergo changes depending on cell properties [GG82]. In healthy tissue, the intra- and extra-cellular volume fraction (IVF/EVF) are at about 20% (IVF) and 80% (EVF). Consequently, TSC will be impacted by alterations in ISC or ESC or by changes in the IVF to EVF ratio[9], with those factors possibly changing independently of each other [Roo+15; Bai+18; BSJ19].

Vice-versa, changes in the TSC can indicate changes in cell density, vitality or viability or can be caused by a restricted energy supply of the Na^+/K^+-ATPase. A variety of pathologies have been shown to be associated with changes in TSC.

The earliest ^{23}Na MR images have started investigating the cerebral stroke, which remains of high interest until today [SNS93; Lin+01; Thu+05; Hus+09; Kim+14; Lef+20]. Other investigated diseases in the brain involved glioblastomas and tumor diseases [Thu+99; Ouw+03], multiple sclerosis [Zaa+12; Eis+21; Web+21], and neurodegenerative diseases such as dementia or amyotrophic lateral sclerosis [Gra+19; Hae+20; Moh+21b]. Furthermore, the TSC was investigated, e.g., in musculoskeletal diseases [Con+00; Sha+02; Web+11; Ger+20], in various tumor diseases beyond the brain [Ouw+07; Jac+10; Pok+21] and in different applications within abdominal imaging [Gra+13; Han+14; Jam+15; Mal+19a].

9 The principle of TSC being influenced by the independent factors of ESC, ISC and IVF to EVF ratio, which might be competing with each other is referred to as 'Hilal-ambiguity' [BSJ19].

2.3.2 *Hardware*

^{23}Na MRI requires signal excitation and acquisition at ^{23}Na's Larmor frequency, thus requiring MRI scanners and RF coils to cover additional frequencies.

^{23}NA MRI SCANNERS MRI scanners can be enabled for X-Nuclei MRI (MRI of other than the ^{1}H nucleus) by an additional bandwidth filter, meaning a broadband transmitter and receiver, covering the respective nucleus' Larmor frequency. In this thesis, data acquisition was performed with two clinical MRI scanners of 3 Tesla, where ^{23}Na's Larmor frequency is at 33.81 MHz (assuming exactly 3 T), which is almost four times lower compared to the ^{1}H's Larmor frequency (127.72 MHz at 3 T) [KS14; Hu+20].

^{23}NA MRI COILS For X-Nuclei MRI, the RF coils' transmit and receive frequencies are, analogue to the MRI scanners, also required to be tuned for the respective nucleus' Larmor frequency. Therefore, ^{23}Na MR images cannot be acquired with every standard clinically available coil but require dedicated ^{23}Na coils [VG12]. For human MRI scanners, dual-tuned coils, which can acquire ^{1}H and ^{23}Na MR images, are mostly used, whereas ^{23}Na-only coils are less common [JL89; Mag+18; Mal+19a; Mal+19b]. This offers the great advantage of acquiring clinically required ^{1}H MR images and ^{23}Na MR images within the same measurement session, and with no repositioning of the patient [NP+15]; making image co-registration between both MRI modalities easier and more reliable and the overall data acquisition process faster. The possibility of faster data acquisition makes ^{23}Na MRI substantially more practicable in the clinical setup. With no required coil change, the data acquisition also becomes more tolerable for the patient as MRI – even if it is non-invasive and does not expose the patient to ionizing radiation – can cause discomfort for the patient because of the small space and the restricted possibility of movements combined with loud noise [MB97; Ozt+20]. Additionally, MRI scanners are still expensive medical imaging tools. Thus, faster data acquisition times, with no long periods between two image acquisitions, can also make ^{23}Na MRI more profitable for the respective hospital or radiological center.

The development of dual-tuned coils was an indispensable contribution for the perspective establishment of ^{23}Na MRI in the clinical routine.

For applications in the human head, transmit/receive (Tx/Rx) birdcage coils are commonly used, which may be one- or multi-channel coils [JL89; Ibr+01; WBL16]. For Tx/Rx birdcage coils, the principle of reciprocity can be assumed, meaning that the coil's transmit and receive fields (B_1) can be directly derived from each other [HR76; Hou00]. In this thesis, the B_1-fields are assumed to be homogeneous when using a one channel Tx/Rx ^{1}H/^{23}Na birdcage head coil, which was based on previously reported findings [Isa+90; Ibr+01; Gio+02; Pas20].

In the human abdomen, multi-channel surface coils are more common, although birdcage coils are also available. When using surface coils or any coils where transmit and receive coils are not analogue, the principle of reciprocity does not apply and B_1^+ and B_1^- need to be considered separately. For the image reconstruction of data acquired with multi-channel coils, it is common practice to reconstruct all channels individually, resulting in as many images as RF receive channels were used. The channels' individual images can be combined using different approaches.

A common and robust approach is the sum-of-squares method. It takes the absolute square of each channel's image and combines them by taking the square root of their sums. It aims to suppress any spatial weighing, as it assumes spatial uniformity for the sum of the absolute squares. However, the assumption is – usually – not justified for surface coils [Roe+90; BLH02; She+10].

Another approach for a multi-channel coil combination is an adaptive coil combination (ACC), which optimizes the coil weights for their combination by calculating the statistically expected signal and noise covariances [WGM00; Ben+16; Lac+20].

2.3.3 *Sequences and quantification*

Decades of MRI sequence developments and optimization have shown the ability to generate different contrast images. Sequences for sodium-weighted imaging, as well as for ^{23}Na T1w or T2w imaging were introduced. Furthermore, also multi-quantum imaging techniques have been explored, which aim to use the nucleus' quadrupole interactions to distinguish between ISC and ESC [Ben+13; Fie+13; BBN14; Sch19; HSR20; Hu+20]. This thesis will exclusively consider sodium-weighted imaging, focusing on the TSC.

SODIUM-WEIGHTED IMAGING For sodium-weighted imaging, developments have resulted in rapid pulse imaging with ultra-short echo times as the most favorable sequences, which are now well-established [Par+97; MR13].

A 3D radial sequence is the most common implementation of a ^{23}Na MRI sequence with ultra-short echo times [NV+07], and it is broadly used as it allows for very short TE because of the read-out starting within the k-space center. The short echo times are crucial, as they enable the suppression of the T2*-weighting. 3D radial sequences were further optimized using various pulse and projection patterns [Boa+97b; GHN06; Lu+10; Pip+11; KN14]. In this thesis, a sequence was used, which was introduced by Nagel et al. in 2009. It uses a density-adapted read-out, enabling a more homogeneous data acquisition [Nag+09]. Its resolution is determined based on the full width at half maximum of the point-spread function. The suppression of T1-weighting can be obtained by choosing a sufficiently long TR, which – ideally – would exceed $5 \times$ T1 of the investigated tissues. The point-spread function and the relatively large voxel size that is used in ^{23}Na MRI make it sensitive to partial volume effects (PVE) [Nie+15; GN15; Kim+21].

For radial sequences, sampling is defined by the number of acquired radial spokes and by the number of samples per spoke. The number of spokes necessary for stable acquisition of a 'fully-sampled' image can be determined with the Nyquist criterion, which depends on the image's FoV and its resolution. However, data acquisition time depends linearly on the number of acquired spokes, thus, under-sampling is one common approach for reducing data acquisition time. Under-sampling means acquiring less data (fewer radial spokes) than what is required according to the Nyquist criterion without reducing the FoV or the image's resolution. However, it

can lead to a reduction in image quality (SNR) and might introduce artifacts, such as *Gibbs ringing*[10], for example [PGF87].

TSC QUANTIFICATION Quantification of the absolute tissue sodium concentration is performed on images with a sodium-weighted contrast, and – according to the current state of the art – by placing reference phantoms within the FoV, next to the patient. The reference phantoms are required to contain a known sodium concentration, which is obtained by adding NaCl to pure water. Furthermore, they are usually composed to obtain relaxation times, which correspond approximately to an estimation of the relaxation times of the investigated tissue. This is achieved by adding between 2 and 7% of agarose to the phantoms. It carries the advantage of avoiding or reducing the necessity for relaxation time corrections [Mit+86; Wol+21; Bau+21]. The absolute TSC-map is then calculated by applying a linear regression based on the SI within the phantoms. Usually, multiple phantoms with different sodium concentrations are used, stabilizing the linear regression.

Another approach is to consider the relative TSC instead of absolute TSC values, meaning that the SI within the investigated tissue on a sodium-weighted MR image is considered relative to the SI of another tissue within the same image, e.g. the contra-lateral tissue [WAH12; NP+15].

2.4 CONVOLUTIONAL NEURAL NETWORKS

A convolutional neural network (CNN) is a deep learning algorithm, which is part of machine learning and can be considered to belong to the broad area of artificial intelligence [GBC16]. Imaging and image analysis are within the most common and original applications for CNNs [MJU17]. Here, the network takes one image as input and assigns weights and biases to different aspects of the depicted objects in the image [Sah18]. CNNs have found a broad spectrum of applications in the area of image segmentation, e.g. in the medical context, where they are well-established. The main building blocks of CNNs are convolutional layers. They have weights, which are learned throughout the CNN training process.

Today, CNNs are emerging for various applications in medical imaging with pre- and post-processing techniques [KJS17; FA+18]. They have already proven to enable robust ^{1}H MR image reconstruction [Sch+17a; Ber+19; LL19]. Furthermore, CNNs successfully improved image quality with post-processing of highly under-sampled ^{1}H MRI data and have been proposed for acquisition time reduction [Ple+12; Eo+18].

CNNs were inspired by the physiological process of neuron connectivity, particularly in the visual cortex. Modern CNNs are based on Fukushima's [Fuk88] model of the visual system, which was based on Hubel and Wiesel's [HW62] representation of neuron architecture, and findings of cell types in the visual cortex [Lin21; RW17; SMB10]. There is a wide variety of network architectures using different parameters, which can be applied and tested.

For the CNN implementation, multiple architectures and parameters can be considered, tested, and optimized for speed or accuracy depending on the application [Hua+17].

10 Gibbs ringing presents itself as multiple parallel lines on the MR image and is caused by the Fourier transform of a discontinuous signal. It is named after Josiah W. Gibbs [Gib99].

2.4.1 *Network architecture*

One broadly used and well-established CNN architecture is the U-Net architecture that was initially developed by Ronneberger et al., aiming for fast image segmentation [RFB15]. U-Nets have previously provided promising results for medical imaging post-processing [Ber+19]. U-Nets are based on fully convolutional networks, which were first introduced by Long et al. [LSD15], and they consist of an encoding and a decoding path. The encoding path of a CNN consists of convolutions of a specific size with a certain number of filters, generating feature maps. Those are further reduced in size (down-sampled) via max-pooling. Max-pooling is the extraction of the singular maximum value of patches within the feature map whilst disregarding the remaining values of the regarded patch [MP14; Gra14].

The decoding path consists of deconvolutions of the same size as the previous convolutions with the same number of filters. U-Nets have obtained their name because of their u-shaped architecture, which is caused by the symmetrical de- and encoding path.

A novelty with U-Nets were the additionally introduced skip connections, meaning connections between the layers of the encoding and the decoding paths that skipped parts of the de- and encoding algorithms and were added to the decoding path via concatenation.

Another network architecture is the ResNet [He+16] (where Res stands for residual) implementation. The ResNet-based CNN, which will be tested in this thesis, uses – in contrast to the U-Net – residual connections only and no skip connections. Thus, connections were only present within the layers of the decoding or the encoding path, but there were no connections between both paths, no connections that skipped some of the layers. ResNets are supposed to be easier to optimize with smaller training errors [He+16].

2.4.2 *Network parameters*

LOSS FUNCTION The loss function of a CNN defines according to which metric the CNN optimizes its output [Zha+16; Wan+18]. Two well established loss functions are L1 and L2, with both loss functions optimizing by minimizing their respective parameters, which are:

L1: Absolute difference

L2: Mean squared error

BATCH NORMALISATION Generally, CNNs use normalization during training to avoid biases towards higher value parameters, meaning that input is normalized to be within a pre-defined range. Batch normalization means rescaling the input mean and variance for every batch, which is commonly defined to be in between convolutional layers. Its purpose is to prevent shifts in the distribution of the input, to reduce over-fitting – meaning not to depend too closely on the limited input data – thus making the training easier, faster, and consequently, more robust [IS15; LC16; Osa+19].

FILTER The CNN optimizes its filters, which are composed of filter kernels, within each convolutional layer. Optimization depends on the application the training process. The filters are not pre-set, which defines the automated learning character of CNNs. Due to the down-sampling of patches, feature map size decreases with the increasing order of the layers. With bigger feature maps requiring fewer filters, the number of filters usually increases with an increasing depth of the layer. The number of applied filters per convolutional layer can be varied for the purpose of optimizing feature extraction [Ioa+15; ZAP16; AM20].

2.5 PHYSIOLOGICAL BACKGROUND

In this thesis, data is presented from ^{23}Na MRI of the human brain, investigating the ischemic stroke, white matter lesions (WML) and brain metastases. Furthermore, data of ^{23}Na MRI of the male pelvis is presented, which aims to investigate the prostate and possibly cancerous lesions. The observed anatomical regions have already been investigated with quantitative ^{23}Na MRI, and the previously found TSC values and respective T1 and T2-times are listed in Table 2.2. The values were obtained from various publications, such as the findings by Ouwerkerk et al. [Ouw+03; Ouw11], Tsang et al. [TSB12], Madelin and Regatte [MR13], and Liao et al. [Lia+19] (brain), Kokavec et al. [Kok+16] (vitreous humor), Hausmann et al. [Hau+12] and Farag et al. [Far+15] (prostate), Ouwerkerk et al. [OWB05], Konstandin and Schad [KS13] and Lott et al. [Lot+19] (blood), and from approximations, which were previously performed by Wenz et al. [Wen+18] (vitreous humor) and Paschke [Pas20] (prostate). Many publications are based on different data acquisition and quantification techniques; thus, the range of reported values is large. For some tissue types, no reliable data was available, and approximations were made based on previously studied similar tissue types. If TSC, T1- or T2-times are used in this thesis for TSC quantification or correction of relaxation times; the used value is displayed parenthesis.

2.5.1 *Tissue sodium concentration in the human brain*

The brain was the first region that was explored with in-vivo ^{23}Na MRI in humans [Hil+85], and it remains of high interest for ^{23}Na MRI research [Thu+99; KS14; Thu18; BSJ19; Hu+20].

Table 2.2: Tissue sodium concentration and ^{23}Na relaxation times in human in-vivo tissues.

Anatomical Region	TSC [mM]	T1 [ms]	$T2_f^*$ [ms]	$T2_s^*$ [ms]
Brain				
White matter	20 – 60	15 – 35	0.8 – 3	15 – 30
Gray matter	30 – 70	15 – 35	0.8 – 3	15 – 30
Cerebrospinal fluid	140 – 150 (145)	50 – 55 (50)	-	55 – 65 (55)
Vitreous humor	145 – 148 (145)	(50)	-	(55)
Prostate tissue	24 – 98	(38.8)	(6.8)	(14.8)
Blood (full blood)	71 – 85 (81)	20 – 40 (31.9)	-	12 – 20.1 (20.1)

There have been a large number of studies, investigating with ^{23}Na MRI the sodium concentrations and the ^{23}Na relaxation times in healthy brain tissue and in various pathologies in the human brain [Ouw11; Mad+14; GNM17; Rid+18]. In the healthy brain matter, absolute TSC values were reported in the range of $20-60$ mM (WM) and $30-70$ mM (GM). The broad range might be explainable because of the various data acquisition and quantification techniques, emphasizing the importance of further research to obtain a gold standard for those techniques.

CEREBROSPINAL FLUID The CSF is a body fluid, which surrounds brain matter and the spinal cord. The fluid does not contain vital cells, explaining the correlation between ESC and TSC within CSF, which are assumed to be in equilibrium [OR55; Har+10]. Results from previous ^{23}Na MRI studies support this assumption as TSC within CSF was found to be between 140 and 150 mM. The strong dependency of TSC in CSF on the ESC also indicates a correlation with the blood serum sodium concentration (SSC). SSC is usually in the range of $135-145$ mM, although it might be influenced by various pathologies and has already been linked to pre-deposition of, e.g., the ischemic stroke [LP86; Wan+94; Gao+17]. The ventricles in the brain are filled with CSF and they expand with age, which leads to an increase in CSF [Mat+96; Zha+05].

On most MRI contrast images, CSF is well distinguishable because of its differing ^{1}H and ^{23}Na concentration and its different relaxation times compared to brain tissue. Therefore, and because of its apparently stable concentration, TSC quantification based on the SI within CSF was proposed previously [Han+13], which will be further explored within this thesis.

VITREOUS HUMOR The vitreous humor (VH) is a gel-like material occupying the vitreous chamber, which is a spherical body in the space between lens and retina of the human eye with a diameter of ≈ 16 mm. The VH has a volume of ≈ 4 ml [RWB06; SE12; MA14].

Like CSF, the VH does not contain any vital cells and can be assumed to be exclusively extra-cellular space; an extra-cellular matrix [SLG20]. It is also referred to as trans-cellular fluid in the eyeball [SSZ14; MMI16]. Therefore, a sodium concentration equivalent to the ESC would be assumed, which is supported by findings of 145 to 148 mM ^{23}Na (with a mean of 146.7 ± 3.3 mM) by Kokavec et al. [Kok+16; Pig+20]. Because of the VH being purely extra-cellular, its sodium concentration is assumed to be maintained constant by the natural regularization of electrolytes in the human body [Som02; Wol13]. Furthermore, because of its gel-like consistency, similar ^{23}Na relaxation times compared to CSF are assumed, which are in the range of $T1 = 50$ ms and $T2^* \geqslant 55$ ms [MR13], as was assumed in a previous publication by Wenz et al. [Wen+18]. In this thesis, the VH is considered as a possible reference for TSC quantification.

STROKE Of all pathologies that were investigated with ^{23}Na MRI, the ischemic stroke is one of the – if not the single – best-explored one. There are numerous publications about animal models and in-vivo human studies.

An ischemic stroke is defined by a restricted blood supply in areas of the brain. It is usually caused by blood clots blocking the blood vessel or other forms of narrowing of the blood vessel. Because of the insufficient supply of oxygen and nutrients, brain cells start dying fast. Thus, it requires immediate treatment [BB00; WG07].

The ischemic stroke is commonly diagnosed with radiological imaging, using CT or MRI. On the one hand, a CT scan carries the great advantage of being faster with measurement time being a crucial parameter when diagnosing an ischemic stroke. "Time is brain" is a commonly used phrase in the context of ischemic strokes, emphasizing the irreversible loss of functioning cells in the brain tissue, which increases with an increasing time until treatment [Sav06; Gon06]. However, various studies have shown the higher accuracy of diagnosing and defining the affected ischemic region with multi-parametric MRI (mpMRI) compared to CT [Kar+99; Cha+07; Win+07; Kid+13; VR17].

Studies exploring additional ^{23}Na MRI for patients with ischemic stroke have suggested improved *penumbra*[11] detection or even possible correlations between TSC and the stroke onset time were suggested, which would be interesting for patients with a wake-up stroke, where onset time is not known [SNS93; Lin+01; Thu+05; Hus+09; Kim+14; NP+15; Wet+15].

In this thesis, data was used that was acquired from patients with ischemic stroke. Different quantification techniques were explored.

SMALL VESSEL DISEASE Small vessel diseases are, e.g., microbleeds, perivascular spaces, or the lacunar stroke [Pan10; WSD13]. They may cause WML, which present themselves as white matter hyperintensities (WMH) on MR images with a T2w contrast [Pan10; DM10; WSD13; Man+15]. They have been associated with dysfunctions in the blood-brain barrier [War+03; Sch+13; Bri+14].

WMH indicate, e.g., demyelination leading to axonal loss, overall changes in the water content or degeneration of the white matter integrity [WVHMM15; Man+15; MC19] and they have been shown to correlate with various neuropathological diseases, such as cognitive impairment, dementia, or depression [YHK08; PS15; Faz+93; Bok+06].

2.5.2 *Stereotactic radiosurgery for brain metastases*

Malignant brain tumors and metastases (BM) have previously been investigated with quantitative ^{23}Na MRI and they have presented an elevated TSC compared to healthy brain tissue [Has+91; Ouw+03; Boa+04; Nag+11; Ell+14]. The increase in TSC might derive from an increase in ISC, which strongly depends on the cells' energy metabolism, which is highly impaired in tumorous cells [Ouw+07]. A higher ISC has been linked to tumor malignancy [Ign83; Cam+80; Nag+83; Mad+14; Bil+16; Reg+20]. Tumor *angiogenesis*[12] could also contribute to a TSC increase due to the resulting increase in EVF [Ouw07].

Furthermore, changes in TSC of BM have been associated with applied chemotherapy or radiation therapy [Sch+05; Bab+05; Bab+07; Lup+09], which is why ^{23}Na MRI has been suggested for the prognosis of tumor treatment responses [Pok+21; Pae+21]. Recently, the effect of SRS on TSC in the vestibular schwannoma microenvironment was published by Lewis et al. [Lew+21], who found SRS to cause an increase in TSC.

11 The ischemic penumbra is defined as perfused brain tissue with the capacity to recover. It was first described in 1981 by Jens Astrup [ASS81].

12 Tumor angiogenesis is defined by a substantial increase in blood vessels, triggered by the tumor's excessive need of nutrients [LRD20].

Stereotactic radiosurgery (SRS) aims for an effective and localized radiation therapy of tumors or BM, defined by the gross tumor volume (GTV), which is the visible extent of the lesion, with potential addition of safety margins, yielding the planning target volume. It uses a single, heavy, ablative dose of radiation [Lek83] and sharp dosage gradients, enabling a high precision. Consequently, it reduces the radiation dose in the peritumoral tissue (PTT), yielding better neurocognitive outcomes [Cha+09] and significantly reducing the risk of radionecrosis compared to whole-brain radiation therapy, particularly when treating patients with only a relatively small number of metastases [LAr90; WK04; Kur+14; Mil+21]. At the same time, similar treatment response and overall survival is maintained [Yam+14; Bro+16; Che+17] and the irradiated lesions show a fast reduction in volume [DS+09; Goe+20]. Today, SRS is also suggested for repeated treatments of recurring BM [McK+16; Jab+20].

Anatomical ^{1}H MR images, such as contrast-enhanced T1w images, or PWI and DWI are state of the art for treatment planning and evaluation of tumor response to SRS [Kan+10; Pat+11; Dev12; Lee+14; Lin+15; Sha+17; Saw+19]. However, it remains challenging to distinguish between tumor progression, pseudo-progression [HZ12; Sha+21], and radionecrosis (RN) [Sug+00; Koh+15; Meh+19]. Previous studies have already aimed for early response prediction with ^{1}H MRI modalities [Des+17; Sha+21] but optimization of the MRI protocols is still warranted, suggesting the addition of another imaging technique for a more reliable tumor response assessment [Haw+97; Sto+12; Tau+18].

SRS does not affect the isolated BM but also its surrounding area, the PTT [Jak+15; Win+18]; even if dosage in that area is minimized by the high precision and sharp gradients of the radiation beam. SRS-induced vascular damage and molecular response to radiation [Par+12; Sia+20] suggest that changes in the sodium concentration will occur. The effect of radiation dose on TSC was explored previously in the human kidney [Han+15]. Consequently, TSC might be able to quantify the effect of SRS on BM and PTT – the tumorous and the healthy tissue. Previously, it was reported that massive vascular damage, causing apoptosis and cell death, occurs with radiation dosage above 5 or 8 to 10 Gy, whereas, with lower dosages, only mild vascular damages were reported [GB+03; Par+12; Son+20].

In this thesis, a prospective in-vivo study was conducted that investigated tissue response to SRS. The aim was to monitor possible TSC changes in healthy and in cancerous tissue after the exposure to radiation with SRS. The study aimed to quantify the tissue response; prospectively enabling the possibility of establishing an early outcome prediction of SRS treatment.

2.5.3 *Prostate carcinomas*

The Prostate Imaging-Reporting and Data System (PI-RADS) guidelines from the American College of Radiology describe a mpMRI, including ^{1}H T1w, T2w, DWI, and PWI as the gold standard for the detection, localization, and characterization of prostate carcinoma (PCa) [Dic+11; Wei+16; WB+19; Tol+21]. The combination of multiple different MRI techniques is recognized to yield a higher accuracy for the diagnosis of PCa [Kur+08; Ken+18].

PCa are characterized by high cell densities, impairing the motion of ^{1}H molecules and consequently showing themselves by lowered values on the ADC-map and the diagnosis of tumorous tissue based on ADC-maps has shown high accuracies

[Yos+08; Ren+08]. A correlation was found between the extent of diffusion restriction (reduction of the ADC) and tumor aggressiveness [Now+16]. Furthermore, PCa usually present themselves by a lowered SI on the T2w MR image [Sch+93; DV+10]. The PI-RADS guidelines have established a scoring system, grading lesions between 1 (most likely not cancer) and 5 (very suspicious), based on how they present themselves on the MRI.

Even though, to date, prostatitis, benign prostate hyperplasia and other benign diseases as well as cancer mimics impair the diagnostic accuracy and reduce the specificity as they may present themselves similar to malignant lesions [Tur+10; Hau+12; Not+15].

At the same time, PCa is the most common tumor disease in men, and it is worldwide the second most often cancer-related cause of death in men [Jen+02; Mur+13], thus, justifying research for a more specific diagnosis of malignant tumors.

If receiving a biopsy, a PCa is commonly graded according to the histopathological *Gleason score*[13], which is a grading system for quantifying the tumor's aggressiveness. The score describes the tumor's resemblance with healthy tissue or cancerous tissue, with higher scores indicating malignant degeneration. Each patient receives a primary and a secondary grade (each ranging from 1 to 5), that sum up the total Gleason score. In prostatectomy specimen, which will be considered in this thesis, the most and the second most prevalent Gleason grades are reported [GM74; Gle92; Ege+02].

Due to the high gradient of ESC and ISC, TSC is highly sensitive to changes in cell density, which were observed in PCa. Consequently, ^{23}Na MRI might have the potential of closing the research gap for characterization of tumor aggressiveness and differentiation from benign diseases. The aim is to provide information about cellular processes in addition to the existing and established mpMRI protocols [Hau+12; Bar+18; Bro+19; Bar+20; Pok+21].

For abdominal ^{23}Na MRI, precise TSC quantification is crucial and requires references with a known sodium concentration. It is commonly based on external reference phantoms, placed within the FoV, which is well-established and considered state of the art, analogue to the imaging of the brain [MR13; Dee+19]. At the same time, quantification accuracy decreases with an increasing distance between reference and investigated tissue as the impact of field and coil inhomogeneities increase, which is more critical for abdominal imaging and surface coils than it is for brain imaging with birdcage coils. For abdominal MRI, it is highly dependent on the patient's abdomen's volume and shape. Previously, relative TSC was also considered in the abdomen, e.g. by Maril et al. who evaluated the medulla-to-cortex ratio in ^{23}Na MR images of the kidney [Mar+06] or by Haneder et al. who considered the renal to CSF ^{23}Na signal [Han+13]. Quantifying the TSC based on internal references, particularly those which are in spatial proximity to the ROI, could make results more stable and less prone to coil and field-induced inaccuracies.

The iliac- and the femoral blood vessels have a relatively large size (diameter of $\approx$ 10 mm in men) and are well distinguishable on an MR image of the prostate. In the human blood, a TSC of around 81 mM was found [OWB05; KS13; Lot+19], which is high compared to the sodium concentration within the tissue surrounding the blood vessels. Thus, blood might be of interest for consideration as reference for TSC

13 The Gleason score, or Gleason grading system, uses architectural patterns within the tissue for the prognosis of prostate cancer. It was introduced by Donald Gleason in 1966 [Gle66].

quantification.

In this thesis, a prospective in-vivo study was conducted, quantifying the TSC in the prostate of patients with suspected PCa. TSC was quantified based on the ^{23}Na MR image SI in the femoral blood vessel, thus, using references that are located within the immediate surrounding of the investigated tissue. The aim of the study was to investigate whether malignant tumors would present different TSC compared to benign tissue.

3

MATERIALS AND METHODS

The methodology described in this chapter was partially published in [Adl+21b] by Karger Publishers (subsection 3.2.2) and in [Adl+21a] by John Wiley & Sons Ltd (section 3.3), and the description of the corresponding methods are replicated here with permission.

3.1 IMAGE ACQUISITION AND PROCESSING

3.1.1 *MRI scanners and coils*

All in-vivo data of patients and healthy controls (HC) was acquired at clinical MRI scanners with a dual-tuned $^{1}H/^{23}Na$ coil.

MRI SCANNER Two different MRI scanners were used for the data acquisition:

1. MAGNETOM Trio
2. MAGNETOM Skyra

Both are 3 T scanners manufactured by Siemens Healthcare GmbH, Erlangen, Germany. They are located at the university hospital Mannheim. The scanner choice depended on the study and coil compatibility and is specified for each study in the respective section.

MRI COILS Two different MRI coils were used for the data acquisition in head or abdomen

1. Dual-tuned $^{1}H/^{23}Na$ birdcage head coil
2. Dual-tuned $^{1}H/^{23}Na$ body coil

Both radiofrequency (RF) coils are from Rapid Biomedical, Rimpar, Germany.

The head coil is 1Tx/1Rx, meaning that it contains one transmit channel (^{23}Na) and one ^{23}Na and ^{1}H receive channel. It is compatible with both MRI scanners. In this thesis, for all measurements with the birdcage head coil, the B_1^+-field was assumed to be homogeneous when the applied RF excitation pulse was $\alpha = 90°$. Analogue, the B_1^- field was also assumed to be homogeneous, as the principle of reciprocity applies [HR76; Hay+85]. Therefore, no B_1-field corrections were applied for measurements with the birdcage head coil.

The body coil consists of a circular ^{23}Na transmit coil within a fixed frame, which was also assumed to generate a homogeneous B_1^+ field, as is applicable for birdcage coils. For ^{1}H MRI, the transmit channel within the MRI scanner was used. Furthermore, the coil consists of 16 ^{23}Na receive channels and six ^{1}H receive channels on an array flex surface coil. It is compatible with the MAGNETOM Skyra but not with the MAGNETOM Trio. Here, the principle of reciprocity did not apply, requiring for corrections of B_1^- inhomogeneities.

3.1.2 *Sequence and reconstruction*

The sequence and reconstruction algorithm used for the ^{23}Na MR image acquisition were developed and published by Nagel et al. in 2009 [Nag+09].

3.1.2.1 *3D radial density-adapted ^{23}Na MRI Sequence*

The used sequence is an ultra-short echo time-sequence, which means that readout is shortly after signal excitation. Thus, TE was minimized, causing a suppression of the T2* contrast in the image, as is graphically explained in Figure 2.7. It used a 3D density-adapted radial k-space readout with half-projections, meaning that readout starts within the k-space center, which is graphically depicted in Figure 3.1.

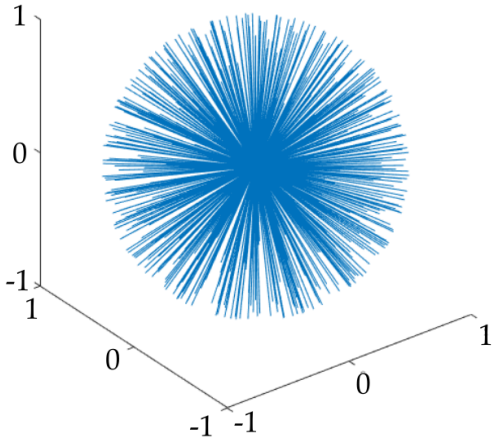

Figure 3.1: Graphical illustration of the radial k-space readout that was used by the 3D radial density-adapted ^{23}Na MRI sequence. In the figure, the lengths of the k-space spokes are normalized to 1.

Sampling occurred with a fixed time difference Δt between the sampling points. The distance between two sampled k-space points was Δk which can be calculated by

$$\Delta k = \frac{\gamma}{2\pi} G(t) \Delta t. \tag{3.1}$$

A radial readout starting in the k-space center over-samples the center region and relatively under-samples the peripheral k-space. A more homogeneous k-space sampling can reduce artifacts in the image, according to [Lia+97]. For a more homogeneous sampling, density-adapted radial readout was used, meaning that Δk was increased within the k-space center compared to the peripheral k-space. This was achieved by using a time-dependent gradient $G(t)$ that followed a rectangular 90° RF excitation pulse. G was applied in all three dimensions with

$$G = \sqrt{G_x^2 + G_y^2 + G_z^2} \tag{3.2}$$

and it was faster in the k-space center where readout was accelerated compared to the peripheral k-space region where the individual readout spokes were further apart. The sequence is graphically illustrated in Figure 3.2.

Sampling according to the Nyquist criterion requires a number of projections N. It depends on the distance of the k-space points k_{max} and $-k_{max}$, with the largest distance to k-space center, to their nearest-neighbor. It can be calculated based on the reconstructed field of view (FoV) with

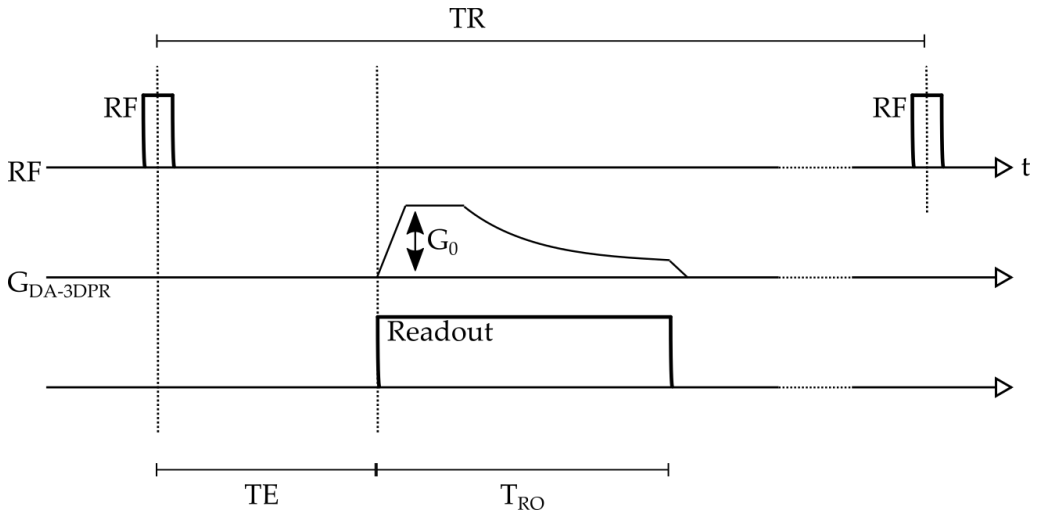

Figure 3.2: Sampling scheme of the 3D radial density-adapted ^{23}Na MRI sequence with the gradient $G_{DA-3DPR}$ being applied in all three dimensions. The sequence was developed by Nagel et al. and the figure was adapted from the original publication [Nag+09].

$$N = 4\pi \left(\frac{L}{\Delta x} \right)^2 \tag{3.3}$$

where L is the length of the image in one dimension, and Δx is the image's resolution.

The T1 contrast can be minimized by a relatively long TR, as is graphically explained in Figure 2.7. Thus, the resulting MR image can be considered to be ρ-weighted (or ^{23}Na-weighted), when TR is chosen to be sufficiently long, and TE is sufficiently short.

In the human brain, at clinically common field strength, the ^{23}Na T1 relaxation times are for white- and gray matter (WM, GM) in the range of $15-35$ ms and for the cerebrospinal fluid (CSF) around $50-55$ ms [MR13], which is why an ideal $TR \geqslant 5 \cdot T1_{max}$ would be set to ≈ 275 ms. As the measurement time linearly depends on TR and the most relevant regions for diagnoses are within the WM or GM ($TR \leqslant 35$ ms); it was usually set between 100 and 120 ms corresponding to $\approx 3-5 \cdot T1$ within the WM and GM, which allowed a T1 (longitudinal) relaxation – recovery of the magnetization in M_z direction – of $\approx 94-99\%$ within the brain matter.

The detailed sequence parameters that were used depended on the application and are mentioned within the corresponding sections.

3.1.2.2 *Reconstruction*

The image reconstruction was performed within MATLAB (The MathWorks, Inc., Natick, MA, USA). The Fast Fourier Transformation (FFT) was applied to the acquired MRI k-space data. The FFT requires equidistant data points for the translation from k-space data to image space. Therefore, regridding needed to be performed after radial data acquisition. The regridding algorithm transferred the acquired data points to a Cartesian grid via interpolation. It applied a Hanning filter with the purpose

of reducing Gibbs ringing artifacts [PGF87] in the resulting image. It further used a *Kaiser-Bessel window*[1] with a kernel width of $w = 4.0$.

During image reconstructions, a zero-filling factor of two was applied to increase the apparent image resolution by that factor without actually increasing the amount of available information. Eventually, k-space data was translated into image space through FFT.

3.1.3 *Co-registration and segmentation*

The quantitative evaluation of the individual parts of the human brain required image segmentation into these regions. Automatic segmentation of the human brain was performed with the statistical parametric mapping software SPM12 (Wellcome Trust Centre for Neuroimaging, London, UK) [Ash+14]. The software required an anatomical ^{1}H MR image for the automatic segmentation process. Therefore, evaluation of the separate tissues within the ^{23}Na MR image required image co-registration to a ^{1}H MR image of that patient or HC. Image co-registration was also performed with SPM12.

SPM12 SPM12 was used for image co-registration among sequences and image segmentation into WM, GM, and CSF. It was implemented in MATLAB.

The co-registration with SPM12 required one reference image onto which a separate source image was registered. The reference image was a T1w or T2w ^{1}H MR image based on which image segmentation was performed. The source image was a ^{23}Na MR image or another MR image. The source image was transformed to the same matrix and voxel size of the reference image. The software's default settings were used.

The image segmentation with SPM12 generated probability masks of WM, GM and CSF within the human brain. The probability masks included values between 0 and 255. A threshold was applied to obtain the tissue masks, which was set to 50%, meaning that the probability of the evaluated tissue belonging to that mask had to be above 50% to be considered. The image co-registration of the diffusion-weighted image (DWI), as the apparent diffusion concentration (ADC)-map, and of the ^{23}Na MR image to the same patient's ^{1}H turbo inversion recovery magnitude (T2-TIRM) with fluid attenuation (FLAIR) and the automatic segmentation into CSF, WM, and GM are depicted in Figure 3.3.

MANUAL SEGMENTATION Manual segmentation was implemented in MATLAB and was used to segment patient-specific pathologies or healthy-appearing regions (HR). It was based on MR images with different contrasts, e.g. T1w or ADC-map, which were considered slice-wise. It was performed by encircling the region of interest (ROI). Figure 3.3 depicts the manual segmentation of the stroke region based on the ADC-map of one patient with ischemic stroke.

1 The Kaiser-Bessel window is a filter function, which is commonly used in spectral analysis. It was developed by James Kaiser in 1980 [KS80]

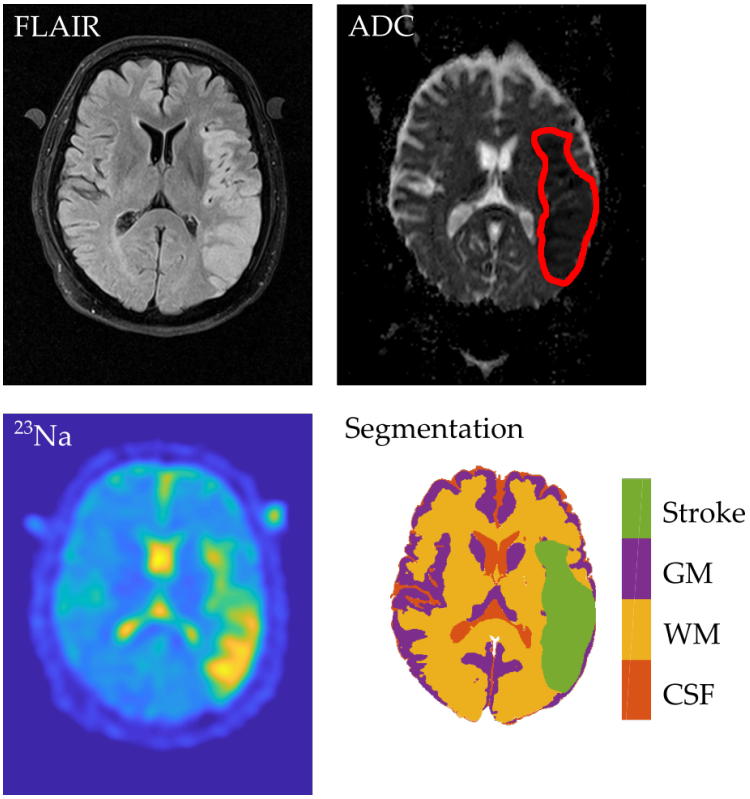

Figure 3.3: An exemplary transverse image slice of a ^{1}H FLAIR MR image (top left), the co-registered ADC-map (top right), and the co-registered ^{23}Na MR image (bottom left) of one patient with ischemic stroke with the corresponding segmentation map into CSF, WM, GM and the stroke region (bottom right). Co-registration and segmentation into CSF, WM, and GM was performed with SPM12. Segmentation of the stroke region was achieved through manual segmentation based on the co-registered ADC-map, as is depicted with the red line. The manual segmentation was performed by a neuroradiologist.

3.1.4 *TSC quantification*

RELATIVE TSC The relative TSC (rTSC) was calculated as the ratio of signal intensities (SI) to each other. Considering the fact that the used sequence was ρ- (and thus ^{23}Na)-weighted, the SI was proportional to the ^{23}Na concentration. According to the state of the art, the rTSC was calculated as the ratio of SI within the ROI to SI within the contra-lateral tissue, which is expressed as

$$\mathrm{rTSC} = \frac{\mathrm{SI(ROI)}}{\mathrm{SI(Contra)}}. \tag{3.4}$$

ABSOLUTE TSC The absolute TSC was calculated by obtaining the mean SI within three-dimensional ROIs with a known sodium concentration based on which the ^{23}Na MR image's SI of the rest of the image was normalized.

The normalization was performed based on a linear fit generating a linear polynomial curve based on one or more points of reference. If multiple references were available, their ratio determined the linear fit with an offset c by

$$TSC(Tissue) = (SI(Tissue) - c)\,\frac{TSC(Reference1) - TSC(Reference2)}{SI(Reference1) - SI(Reference2)}. \tag{3.5}$$

If only one reference point was available, an additional ROI was defined within the background region, which was set to be equivalent to 0 mM.

3.1.5 *Statistical analysis*

In this thesis, any TSC values will be given as full integer numbers with no decimal places. When considering any mean values – within patient cohorts or within individuals –, they will be given as mean ± standard deviation (sd).

Differences were evaluated for statistical significance for various data. Firstly, the one-sample Kolmogorov-Smirnov test was performed to evaluate whether normal distribution was present, verifying whether the student t-test was applicable. Which type of test was used is mentioned within the respective sections. A value of $p < 0.05$ was considered significant.

The correlations were evaluated using the Pearson correlation test or the Spearman correlation test, depending on the considered variables. Both tests were performed within MATLAB, using the corresponding pre-implemented functions. Which type of test was used is mentioned within the respective sections.

3.2 TSC QUANTIFICATION FOR "^{23}NA MRI IN ISCHEMIC STROKE"

In this thesis, data was used from a prospective study with the German title "Natrium (^{23}Na) MRT zur Diagnostik von ischämischem aber noch vitalem Hirngewebe bei Schlaganfallpatienten" (engl.: "Sodium (^{23}Na) MRI for the diagnosis of ischemic but still vital brain tissue of stroke patients", short: "^{23}Na MRI in ischemic stroke"). The study was conducted by the Department of Neuroradiology, the Department of Neurology and the Department of Computer Assisted Clinical Medicine, Medical Faculty Mannheim, Heidelberg University and it was funded by Dietmar-Hopp Stiftung under the project number 23014019.

3.2.1 *Data acquisition*

The data acquisition was performed between November 2016 and February 2019 at the university hospital Mannheim. A total of 62 patients was included who were admitted to the stroke center of the university hospital Mannheim. Out of those 62 patients, 28 were men and 34 were women. The patients had a mean age of 73 ± 13 years.

The study was approved by the local ethical review committee (Medizinische Ethik-Kommission II) with the approval number 2010-328N-MA. Written informed consent was obtained from all patients or an immediate family member.

The MRI data were acquired at the university hospital's MAGNETOM Trio with the dual-tuned ^{23}Na/^{1}H birdcage head coil; details are explained in subsection 3.1.1. Data acquisition was performed within the first 72 hours after the determined or estimated onset of symptoms.

MRI PROTOCOL The ^{23}Na MR images were acquired in addition to a standard MRI stroke protocol which comprised of the ^{1}H MRI DWI, generating an ADC-map, dynamic-susceptibility-contrast (DSC) perfusion imaging, and of a ^{1}H T2-TIRM FLAIR. The details of the protocol were described by Neumaier et al. [NP+15]. The entire protocol had a measurement time of 26 min and 56 sec, from which 10 min were the ^{23}Na MRI sequence.

The ^{23}Na MRI sequence and its reconstruction algorithm are explained in subsection 3.1.2. Reconstruction was performed in MATLAB 2015a. The sequence used TR = 100 ms, and TE = 0.2 ms. 6,000 equidistant spokes were acquired with 384 samples each (base resolution). The resulting measurement time was TA = 10 min, generating a 3D dataset with a nominal resolution of 4x4x4 mm^3. The reconstruction algorithm used a zero-filling factor of two to achieve a 3-dimensional image with an apparent resolution of 2x2x2 mm^3 and a FoV of 241x241x241 mm^3 for every patient. The detailed sequence and reconstruction parameters are listed in the appendix in Table A.1.

SEGMENTATION AND CO-REGISTRATION The ^{1}H FLAIR MR image served as the basis for automatic image segmentation into CSF, WM, and GM. The ADC-map was used for the manual image segmentation of the ischemic stroke region (stroke mask), which was performed by a neuroradiologist. The ischemic region was identified by a low ADC in correlation with a high SI on the ^{1}H FLAIR. The ^{23}Na MR image and the acquired ADC-maps were co-registered to the patients ^{1}H FLAIR MR image.

Automatic segmentation and co-registration were performed with SPM12, and the manual segmentation of the stroke region was performed in MATLAB, as was explained in subsection 3.1.3.

REFERENCE VIALS FOR TSC QUANTIFICATION For absolute TSC quantification, two reference phantoms were attached to the patient's head during data acquisition, and they were included in the FoV. The phantoms were cylindrical tubes of 14 ml with a diameter of 15 mm. They contained pure water with 2% agar and 50 mM NaCl (Phantom 1) or 100 mM NaCl (Phantom 2). Absolute TSC quantification was performed as is explained in subsection 3.1.4.

3.2.2 *Relative and absolute TSC quantification*

The methodology in this section was partially published in [Adl+21b], although, the methodology was marginally adjusted, which is described in detail.

Datasets from the study "^{23}Na MRI in ischemic stroke" were used to evaluate differences between and obtain information about the reliability of absolute and relative TSC quantification.

WHITE MATTER For all patients, the automatically segmented WM mask and the manually defined stroke mask were evaluated. The stroke mask was subtracted from the WM mask, and the outer 4 mm border of the resulting mask was removed to reduce potential partial volume effects (PVE). Mean absolute TSC in the WM was calculated within the resulting subtraction mask. Figure 3.4 depicts the ^{1}H FLAIR, the ADC-map, and the ^{23}Na MR image together with the corresponding masks of the WM from the automatic segmentation, the manually segmented stroke region

mask and the resulting subtraction mask of one representative, transverse image slice of one patient.

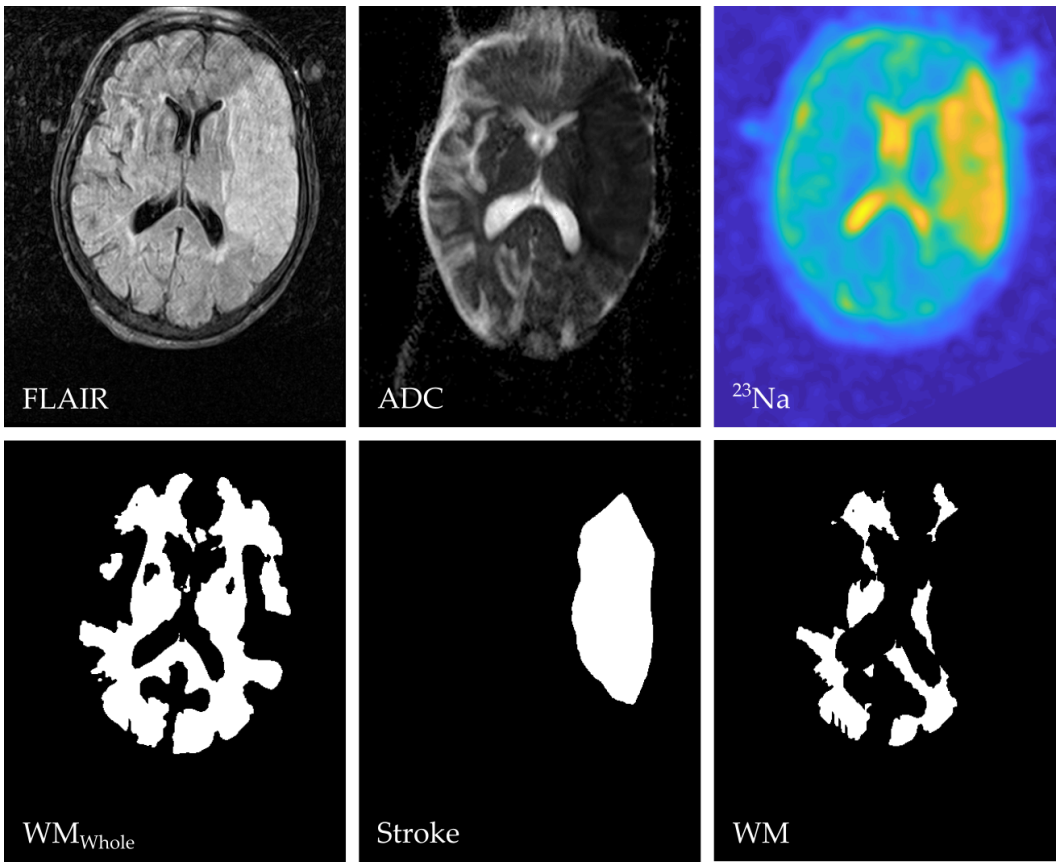

Figure 3.4: Top: One representative, transverse image slice of one patient with its ^{1}H FLAIR (left), the co-registered ^{1}H ADC-map (middle) and the co-registered ^{23}Na MR image (right). Bottom: The corresponding masks of the automatically segmented WM (WM_{whole}, left), the manually segmented stroke mask (middle) and the evaluated WM mask (right), which was calculated by subtraction of the two other masks with an additional cut-off of the outer 4 mm border.

Furthermore, a ROI was manually defined within the normal-appearing white matter (NAWM) and mean absolute TSC was evaluated within that ROI.

Some patients showed white matter lesions (WML), which were identified based on the ^{1}H FLAIR. The patients were graded according to the scale of Fazekas [Faz+87], based on the presence and severity of their WML, with:

Fazekas 0: No WML

Fazekas I: Mild WML

Fazekas II: Moderate WML

Fazekas III: Severe WML

The grading was performed by neuroradiologists.

STROKE After manual segmentation of the ischemic stroke region, its contra-lateral region was defined by mirroring at the central fissure, resulting in the same size and corresponding location compared to the defined stroke region.

Mean absolute TSC was calculated in both regions (stroke and contra-lateral) of all patients. Furthermore, the rTSC was calculated as the ratio between TSC in stroke and TSC in the contra-lateral brain tissue (see: Equation 3.4), thus

$$\mathrm{rTSC} = \frac{\mathrm{TSC}_{\mathrm{Stroke}}}{\mathrm{TSC}_{\mathrm{Contra}}} \tag{3.6}$$

Additionally, relative TSC was also calculated as the ratio between absolute TSC in the stroke region and absolute TSC within the NAWM, thus

$$\mathrm{rTSC}_{\mathrm{NAWM}} = \frac{\mathrm{TSC}_{\mathrm{Stroke}}}{\mathrm{TSC}_{\mathrm{NAWM}}} \tag{3.7}$$

The patients were further grouped, with

Group 1: No or mild white matter lesions (Fazekas grade 0 and I)

Group 2: Moderate or severe white matter lesions (Fazekas grade II and III)

STATISTICAL ANALYSIS Mean absolute TSC in WM and in the NAWM region was evaluated for all patients and compared between the patients with different Fazekas gradings. Mean intra-subject sd of absolute TSC in WM was also compared between the Fazekas gradings.

TSC in the stroke region was evaluated with its absolute TSC, the relative TSC (rTSC), and the relative TSC based on NAWM ($\mathrm{rTSC}_{\mathrm{NAWM}}$). Results were compared between patients in Group 1 and patients in Group 2.

The one-sample Kolmogorov-Smirnov test was performed and showed normal distribution for absolute TSC in WM, in the stroke region, in the contra-lateral stroke region and in the NAWM. Differences between absolute TSC within WM and NAWM and absolute and relative TSC within the stroke regions were compared between patients with different Fazekas gradings, and differences were evaluated using the two-sided student t-test.

Mean absolute TSC in WM and the extent of the WML (according to the Fazekas grade) were tested for correlation using the Spearman correlation test. Furthermore, the test was used to evaluate a possible correlation between the intra-subject sd of absolute TSC in WM and the Fazekas grade.

A multiple regression analysis was performed to investigate the impact of the patient's age, the time after the onset of the ischemic stroke and the extent of WML (Fazekas grade) on the mean absolute TSC in WM.

3.2.3 *Internal references for absolute TSC quantification*

The datasets from the study "^{23}Na MRI in ischemic stroke" were also used to evaluate the reliability of internal references (the cerebrospinal fluid or the vitreous humor) for absolute TSC quantification.

QUANTIFICATION Absolute TSC quantification based on SI within the reference vials ($\mathrm{TSC}_{\mathrm{Vials}}$) was used as baseline (ground truth) to further evaluate absolute TSC quantification based on other (internal) references. For $\mathrm{TSC}_{\mathrm{Vials}}$, no T1 or T2* corrections were performed, as the reference phantoms were composed of NaCl

with additional 2% agarose, resulting in a substance with similar relaxation times compared to brain tissue [Mit+86].

Two additional reference regions were defined as three dimensional ROIs, which were segmented within the patient's left vitreous humor (VH) and within the lateral ventricle (CSF) as is depicted in Figure 3.5. Thus, two additional TSC-maps were calculated based on SI within those reference regions, resulting in three TSC-maps per patient:

I. TSC_{Vials}: TSC quantification based on SI within the manually segmented region within the reference vials

II. TSC_{CSF}: TSC quantification based on SI within the manually segmented region within the cerebrospinal fluid

III. TSC_{VH}: TSC quantification based on SI within the manually segmented region within the vitreous humor

Assuming both internal reference regions to be entirely extra-cellular (as CSF and VH do not contain vital cells), their TSC was assumed to be equivalent to the patients' blood serum sodium concentration (SSC), when it was available. For the remaining patients, where no information about SSC was given, a mean SSC of 145 mM was assumed, corresponding to the extra-cellular sodium concentration [MR13; Pet+16b; Som04].

SI within CSF and VH was corrected for T1-weighting based on Equation 2.75 to

$$SI_{T1corr} = SI \frac{1}{1 - e^{-TR/T1}} \tag{3.8}$$

because of CSF having longer relaxation times compared to vital brain tissue ($T1(CSF) = 50$ ms) according to [MR13] and [Lom+16]. The T1 relaxation of VH was assumed to be equivalent to $T1(CSF)$ (thus: $T1(VH) = 50$ ms) as both do not contain cells and are purely extra-cellular fluids, justifying the assumption, which was previously suggested by Wenz et al. [Wen+18]. Thus, the same correction factor was used for both regions.

TSC-maps were calculated by

$$\begin{aligned} TSC_{CSF}(Tissue) &= SI(Tissue) \frac{SSC}{SI_{corr}(CSF)} \\ &= SI(Tissue) \frac{SSC \left(1 - e^{-TR/T1(CSF)}\right)}{SI(CSF)}) \\ &= SI(Tissue) \frac{SSC \cdot 0.8647}{SI(CSF)} \\ TSC_{VH}(Tissue) &= SI(Tissue) \frac{SSC}{SI_{corr}(VH)} \\ &= SI(Tissue) (\frac{SSC \cdot 0.8647}{SI(VH)} \end{aligned} \tag{3.9}$$

Correction for $T2^*$-weighting was not performed as a very short $TE = 0.2$ ms was used and mono-exponential $T2^*(CSF) \geqslant 55$ ms. Therefore, $T2^*$-weighting was

$$\begin{aligned} SI_{T2^*corr} &= SI \frac{1}{e^{-TE/T2^*}} \\ SI_{T2^*corr}(CSF, VH) &= SI(CSF, VH) \cdot 1.0036 \end{aligned} \tag{3.10}$$

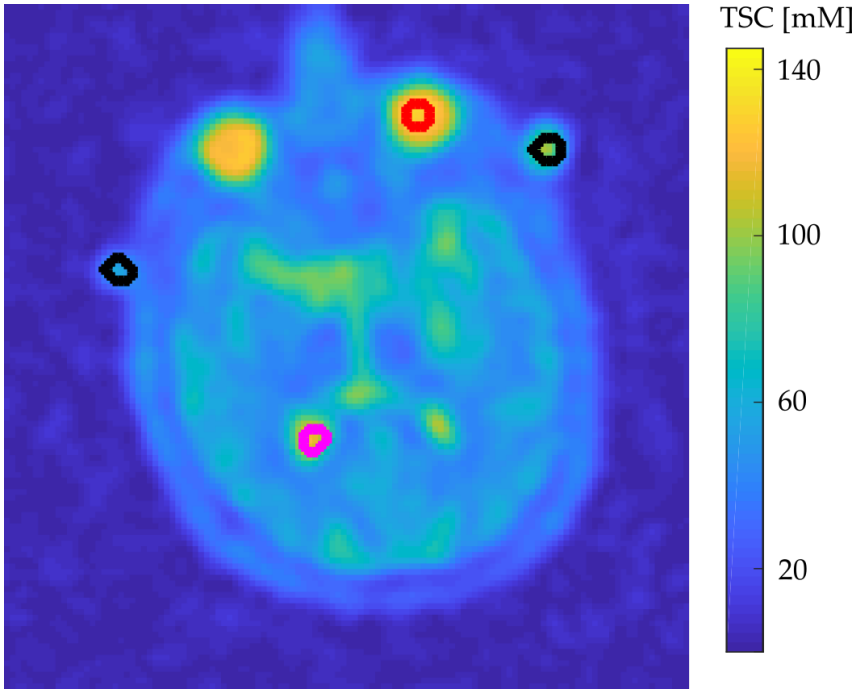

Figure 3.5: One representative transverse slice of the quantified ^{23}Na MR image of one patient with the segmentation of the different reference regions, which were used for the quantification methods. The reference region within both reference phantoms are encircled in black, the CSF reference region is encircled in magenta, and the VH reference region is encircled in red.

and the impact was, thus, below 1%.

Mean TSC in the whole brain (the mask was determined via thresholding) was evaluated for all three TSC maps (TSC_{Vials}, TSC_{VH}, TSC_{CSF}). Differences between the TSC_{Vials}-maps and the other two TSC-maps were evaluated by calculating the absolute TSC difference (in mM) voxel-wise for the whole brain region.

Mean TSC of the defined ROIs in VH and CSF was evaluated in the TSC_{Vials}-map. The T1 correction factor was applied for both regions.

Furthermore, the sd within the VH, the CSF and within one of the reference vials (100 mM) was calculated within their respective TSC-maps to evaluate and compare the stability of the quantification method.

Mean absolute TSC within the masks of WM, and GM, and within the mask of the stroke region were evaluated on all three TSC-maps. Again, the masks included a 4 mm (WM and GM) or a 2 mm (stroke) cut-off of the outer border to reduce PVE.

3.2.4 *Evaluation of quantification stability*

To evaluate the stability of quantification based on VH or CSF, one HC (male, 24 years old) was scanned three times over a span of six weeks (scan II was scheduled one week after scan I and scan III took place five weeks after scan II). A ^{23}Na MR image was acquired at all three time points, and an additional T1w ^{1}H MR image was acquired together with the first scan.

All three images were co-registered to the T1w ^{1}H MR image and, afterwards, the three ^{23}Na MR images were quantified based on SI within VH and CSF. No blood sample was available from the HC. Therefore, again, ESC was assumed to be 145 mM

within both reference regions. Due to the image co-registration, the same ROIs in CSF and VH were usable within all three ^{23}Na MR images. Image co-registration and automatic image segmentation into WM, GM, and CSF were performed with SPM12.

Absolute TSC was calculated within WM and GM on the TSC_{CSF}-map and on the TSC_{VH}-map from all three scans. Absolute TSC was compared voxel-wise within both tissues between all three measurements.

3.2.5 *Statistical analysis*

The paired student t-test was performed to evaluate whether TSC differences between the three absolute TSC quantification methods were statistically significant.

The correlation was tested between SSC and mean absolute TSC within VH and CSF on the TSC_{Vials}-map using the Pearson correlation test.

3.3 DATA ACQUISITION TIME REDUCTION BY APPLICATION OF A CNN

The methodology described in this section was partially (subsection 3.3.1 - subsection 3.3.3) published in [Adl+21a].

Convolutional neural networks (CNNs) were implemented, trained and tested using the datasets that were acquired within the study that was explained in section 3.2. A total of 46 out of 62 datasets from patients was initially included, which was afterwards expanded to 53 out of 62 datasets, whereas the remaining nine datasets had to be excluded because of data acquisition problems, e.g. abortion of the measurement.

3.3.1 *Data acquisition and processing*

UNDER-SAMPLING The Nyquist criterion requires the number of spokes (N_N) to be chosen depending on the length (L) of the image in one dimension and on the image resolution (distance of two neighbouring voxels, Δx). When calculating N_N while considering Equation 3.3 in section 3.1 and the parameters of the used ^{23}Na MRI sequence and the reconstruction algorithm, one derives

$$N_N = 4\pi \left(\frac{L}{\Delta x}\right)^2 = 4\pi \left(\frac{\lfloor \frac{241}{4.01} \rfloor}{2}\right)^2 = 11,310. \tag{3.11}$$

Thus, with the sequence using $N = 6,000$ spokes, the under-sampling factor R of a fully-reconstructed ^{23}Na MR image (Full Image, FI) can be calculated with

$$R_{FI} = \frac{N_N}{N_{FI}} = \frac{11,310}{6,000} = 1.885 \tag{3.12}$$

The term fully-reconstructed refers to the k-space data that was fully used for the reconstruction algorithm.

The aim was to prospectively shorten the measurement time TA, which can be achieved by increasing the under-sampling factor and thus reducing the number of acquired spokes N because TA linearly depends on N. A significant reduction of TA can therefore be achieved by under-sampling with different under-sampling factors R. However, in MRI, there is a common trade-off between image quality and measurement time. The loss in image quality, caused by R, can be evaluated based on the image's signal-to noise ratio (SNR).

For the training of a CNN, a large dataset is required. Therefore, the ^{23}Na MR images were used, which were available from the above introduced study about patients with ischemic stroke. The images were retrospectively, artificial under-sampled, resulting in simulated images that could have been acquired within a reduced measurement time (Reduced Image, RI). For that simulation – the generation of RI – the ^{23}Na MR image of each patient was reconstructed again but only using a fraction R of the acquired k-space data. Figure 3.6 depicts the reduced k-space schematically for $R = 4$.

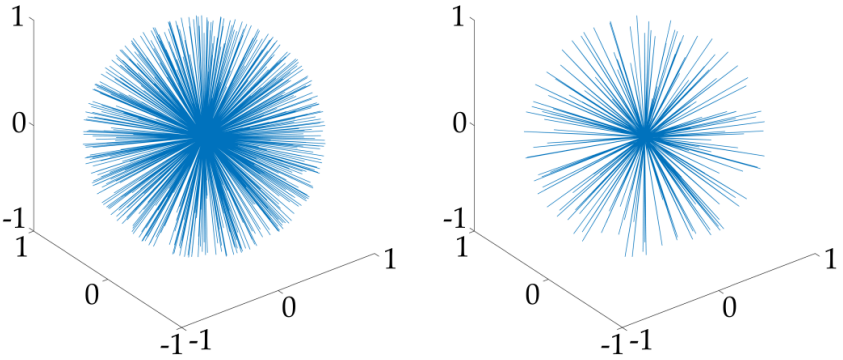

Figure 3.6: Schematic visualization of the full k-space that was used for the reconstruction of FI (left) and of the reduced k-space (here: $R = 4$) that was used for reconstruction of RI (right). Both k-space have equidistant spokes with the full k-space containing R-times the amount of spokes compared the k-space of RI. In the figure, the lengths of the k-space spokes are normalized to 1.

Thus, $N_{RI} = {}^{N_{FI}}/_{R}$ equidistant projections of every k-space dataset were chosen to achieve image information that could have been acquired with an acquisition time that was reduced by the factor R. The under-sampling factor of RI (R_{RI}) was therefore R-fold larger compared to R_{FI}. Taking, exemplary, $R = 4$, one yields

$$R_{RI} = \frac{N_N}{N_{RI}} = \frac{11,310}{\frac{6,000}{R}} = R \cdot 1.885. \tag{3.13}$$

To evaluate whether the artificial down-sampling was an appropriate approximation, ^{23}Na data was acquired from one HC (male, 28 years old). They were measured with the ^{23}Na MRI sequence as it was used for the patients with ischemic stroke. Acquired were FI (with $N = 6,000$) and real under-sampled MR image (rRI) with the same sequence but with a reduced N by $R = 2, 4, 5, 10$ ($N = 3,000, 1,500, 2,000, 600$). From FI, RI were generated via artificial down-sampling with the same R as rRI were acquired. SNR was compared between RI and rRI with the respective R. Based on the obtained results, all used datasets from the patients with ischemic stroke were artificially down-sampled, generating an RI for each patient. RI were used for the training of the CNN.

3.3.2 *CNN implementation and training*

A total of eight different network configurations with varying architectures and parameters and multiple loss functions each were implemented and compared. The CNNs were implemented in PyCharm 2018.3.3 (JetBrains, Prague, Czech Republic) using Tensorflow 1.10 (Google Brain, Mountain View, CA, USA).

The U-Net architecture [RFB15] included concatenated skip connections, and was implemented with additional residual connections. Furthermore, a ResNet [He+16] architecture was implemented that did not use those skip connections and concatenations. Figure 3.7 depicts both network architectures and illustrates the differences graphically. The implementations were introduced by Schnurr et al. [Sch+19].

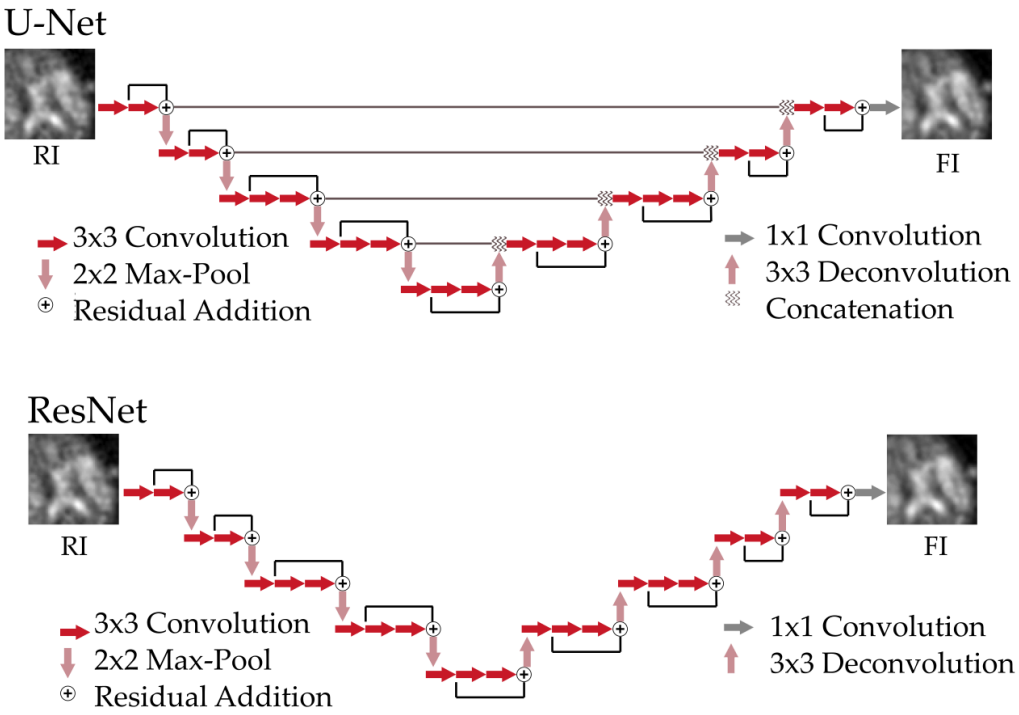

Figure 3.7: Graphical illustration of the implemented U-Net architecture with residual and skip connections and the ResNet architecture. The main differences between the two architectures are the U-Net's skip connections with concatenation which are not present in the ResNet architecture. This figure is reprinted with permission from [Adl+21a].

The amount of applied filters per block in each convolutional layer was varied and is referred to as number of filters. Here, 'Big' means the amount of filters per layer was doubled in comparison to 'Small' with the amount of filters being:

$$\begin{aligned} \text{Small} &: [16\ 32\ \ 64\ 128\ 256\ 128\ \ 64\ 32\ 16] \\ \text{Big} &: [32\ 64\ 128\ 256\ 512\ 256\ 128\ 64\ 32] \end{aligned} \tag{3.14}$$

Batch normalization was implemented and the impact was tested, with 'False' referring to no application of the batch normalization and 'True' meaning that batch normalization was applied.

Consequently, the parameters that differed between the eight CNNs were:

A. Architecture: U-Net and ResNet

B. Usage of batch normalization: False and True

C. Number of filters: Small and Big

All implemented CNNs carried the mutual parameters of using the Adam optimizer [KB14] and of consisting of four encoding- and four decoding stages. Each stage had two to three convolutional layers. The batch size was consistently set to eight, and the training ran for 20 epochs with a learning rate of 0.001.

The networks were trained and tested in image space after conventional image reconstruction. For the CNN training, the images were split into two-dimensional 64x64 voxel patches. Those patches were obtained from connected, transverse image slices as they are used for the examination by radiologists. For the network's training, RI were used as input and FI served as label and ground truth. The networks' outputs were the artificially up-sampled ^{23}Na MR image (CI). The methodology – including the artificial down-sampling and the training of the CNNs – is schematically illustrated in Figure 3.8.

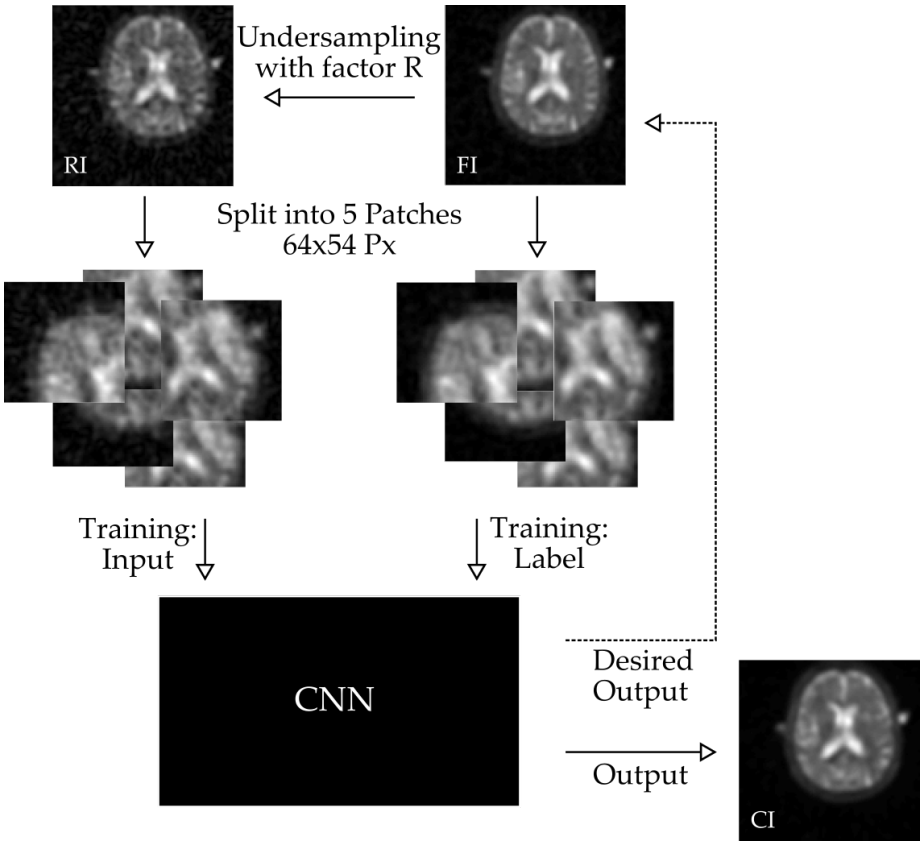

Figure 3.8: Schematic illustration of the workflow from a the fully reconstructed image (FI) to the artificially under-sampled image (RI) with both being split into five patches per transverse image slice. RI serving as training input and FI serving as training label for the convolutional neural network, generating its output image (CI).

For the initial network trainings and tests, datasets of 46 patients were included. They were split into 38 training- and eight test cases with no validation cases. The network required inputs with the size of a power of two. Therefore, a frame of zeros was added to the image slices resulting in input images with the size of 128x128 voxels per slice. Five random patches were dynamically sampled per image slice, and 50 (out of 120) central slices were considered per patient. This resulted in 250 samples per patient and, thus, a total of 9,500 training samples (with 64x64 voxels) per training epoch. The CNNs' test cases also included 50 full central slices (128x128 voxels) per test dataset resulting in 400 samples.

For the network evaluation, the loss functions L1 (absolute difference) and L2 (mean squared error) were considered. Later on, an additional loss function was tested for the best performing networks. The additional loss function used a gradient difference loss (GDL), which was supposed to improve edge accuracy and image sharpness. It was developed by Mathieu et al. [MCL15a] and can be described by

$$L_{GDL}(\hat{y}, y) = \sum_{i,j} \left| \left| |y_{i,j} - y_{i-1,j}| - |\hat{y}_{i,j} - \hat{y}_{i-1,j}| \right| \right|^2 + \left| \left| |y_{i,j} - y_{i,j-1}| - |\hat{y}_{i,j} - \hat{y}_{i,j-1}| \right| \right|^2, \tag{3.15}$$

with y being the network's label and $\hat{y}$ being the networks output. The indices i and j describe the observed pixel in x- and y-dimension, respectively.

The GDL was implemented with the weighting factor λ, in addition to L1 and L2, which resulted in the combined loss function:

$$\begin{aligned} L_A &= L1 + \lambda L_{GDL} \\ L_B &= L2 + \lambda L_{GDL} \end{aligned} \tag{3.16}$$

with λ being initially set to 0.5, whereas $\lambda = 0.2$ was considered within the later tests.

The first tests exclusively considered the under-sampling factor $R = 4$, whereas later on further factors were considered as is described in subsection 3.3.4.

3.3.3 *CNN performance evaluation*

The fully reconstructed ^{23}Na MR images, the artificially under-sampled images and the images obtained from CNN post-processing (FI, RI and CI) were evaluated and results were compared between each other.

SNR AND SSIM The ^{23}Na MR images were evaluated by calculating their SNR and their structural similarity index (SSIM) to FI.

SNR was calculated based on the masks of the patient's head (M_H) and of the image's background (M_{BG}) region. Both masks were calculated for each patient based on image segmentation via threshholding. SNR of the image (I) was defined as the fraction of mean (μ) signal intensity (SI) in the head and SI's sd (σ) in the background region:

$$SNR(I) = \frac{\mu(SI(M_H))}{\sigma(SI(M_{BG}))} \tag{3.17}$$

SSIM compares image degradation, luminance, and contrast between two images. The value can range between 0 and 1, where 1 represents an ideal equivalency between two images and 0 represents no similarities. It was calculated by using the pre-implemented MATLAB function [Wan+04].

TSC QUANTIFICATION ACCURACY TSC quantification was performed of the ^{23}Na MR images FI and RI and of CI from the best performing CNNs (according to the SSIM).

As was explained in section 3.2, two reference phantoms had been placed within the FoV for absolute TSC quantification. Here, a 3-point linear fit with SI of both phantoms and zero was performed; detail were described in subsection 3.1.4. The ROIs were exclusively defined within the homogeneous center region of the reference phantoms to minimize potential PVE.

Quantification was evaluated by calculating the TSC error, which was defined as the absolute TSC difference between the evaluated image and the FI that was considered as ground truth (ΔTSC). TSC error was calculated for the CI and it was compared to the TSC error of RI with the purpose of evaluating whether the CNN post-processing improved TSC quantification accuracy.

The evaluation of the TSC quantification accuracy was performed within CSF, WM, and GM tissue separately, which was possible due to image co-registration and automatic image segmentation as was explained in section 3.2 and subsection 3.1.3.

3.3.4 *Evaluation of different under-sampling factors*

The one best performing network was tested for its performance with different under-sampling factors of $R = 2, 3, 4, 5, 6, 8, 10$ for the optimization of measurement time reduction. The network was tested with the loss function L2 and L_B where $\lambda = 0.5$ and $\lambda = 0.2$ were considered.

Here, the datasets of 53 patients were included, which were split into 42 training-, eight test- and three validation datasets. Again, five random patches were dynamically sampled per image slice. An additional difference was that here all available 120 image slices were considered of each patient. Thus, it resulted in 600 samples per case, which was a total of $25,200$ training samples.

The networks' performance was evaluated via SNR and SSIM as described above (subsection 3.3.3).

3.3.5 *Application on real under-sampled data*

Eventually, the best performing network with the best performing loss function (considering the SSIM) was applied to real under-sampled data. For that purpose, one HC (male, 26 years old) was scanned with the same parameters as patients with ischemic stroke. The ^{23}Na MR image was acquired as FI ($N_{FI} = 6,000$, $TA = 10$ min) and it was also acquired as real under-sampled image (rRI) ($R = 4$, $N_{rRI} = 1,500$, $TA = 2.5$ min). The selected CNN was applied to rRI, generating an artificially up-sampled ^{23}Na MR image from real under-sampled data (rCI). During the measurement, again, two reference phantoms were attached to the HC's head based on which TSC quantification was performed. Additionally, the ^{1}H FLAIR from the MRI protocol was also acquired. It was used for image segmentation (with SPM12) and for image co-registration.

SNR of FI, rRI, and rCI, and SSIM to FI of rRI and rCI were calculated. Furthermore, quantification accuracy within CSF, WM, and GM was compared between the rRI and rCI.

3.3.6 *Statistical analysis*

Differences between SNR of CI and RI and their SSIM to FI were tested for statistical significance using the paired student t-test. The correlations between the under-sampling factor R and SNR and SSIM were evaluated using the Pearson correlation test.

3.4 PROSPECTIVE IN-VIVO STUDIES

3.4.1 *Evolution of TSC after stereotactic radiosurgery*

The one prospective in-vivo study that is presented in this thesis observed radiation-induced TSC changes within brain metastases (BM) and their surrounding peri-tumoral tissue. The data from that study was partially published in [Moh+21a]. However, that publication focused on TSC within the BM and their edemas, whereas, in this thesis, various ROIs, such as the areas within isodose lines were evaluated as is described in detail. Furthermore, additional patients are included in this thesis.

^{23}Na MR images were acquired of patients with BM, undergoing stereotactic radiosurgery (SRS) with the Leksell Gamma Knife Icon (Elekta AB, Stockholm, Sweden). ^{23}Na MR images were acquired once prior to irradiation with SRS (baseline) and twice after SRS.

All patients had one or multiple BM from differing primary tumors that were scheduled to be treated with the Leksell Gamma Knife with a single ablative dose. To be included in the study, the BM volume was required to be > 64 mm^3 because of the resolution of the ^{23}Na MR image. The local ethical review committee approved the study protocol with the approval number 2019-630N-MA, and written informed consent was obtained from all patients.

3.4.1.1 *Data acquisition*

Data acquisition was performed with the 3 T Magnetom Trio and the dual-tuned ^{1}H/^{23}Na head coil; details were introduced in subsection 3.1.1. The study protocol included a 3D ^{23}Na MR image, which was acquired additionally to all ^{1}H MR images that were required for SRS planning or post-treatment observations. The standard of care ^{1}H MR images were acquired with a twelve channel ^{1}H head coil, and the protocol included a T1w, T2w, and a contrast-enhanced T1w 3D magnetization prepared rapid gradient-echo sequence (MPRAGE).

By default, SRS radiation therapy planning was performed on the contrast-enhanced (Dotarem, 0.2 ml/kg body weight) MPRAGE, which was used for the localization and segmentation of the BM. The detailled sequence parameters are listed in the appendix in Table A.2.

The patients underwent ^{23}Na MRI scans at three different time points:

I. 2 days pre-SRS (baseline, $T = SRS - 2$ days): standard protocol + ^{23}Na MRI

II. 5 days post-SRS ($T = SRS + 5$ days): no standard protocol, ^{23}Na MRI

III. 40 days post-SRS ($T = SRS + 40$ days): standard protocol + ^{23}Na MRI

Measurement I and III were synchronized with the routine clinical appointments, and the standard of care protocol was conducted prior to the ^{23}Na measurements. An additional appointment was scheduled in between, which aimed to assess early TSC changes in response to SRS. ^{23}Na MR image acquisition was performed with the 3D radial density-adapted sequence [Nag+09]. The detailed sequence and reconstruction parameters are listed in the appendix in Table A.2. The reconstruction algorithm was performed with MATLAB 2018a; details were explained in subsection 3.1.2. All

^{23}Na MRI scans were performed after the administration of Dotarem, which has no significant impact on the TSC quantification according to Paschke et al. [Pas+18].

3.4.1.2 *Image processing and TSC quantification*

The university hospital's radiation oncology department calculated the radiation therapy treatment plan with the software Leksell GammaPlan. The plan was based on the pre-SRS contrast-enhanced ^{1}H MPRAGE. Radiation oncologists segmented all relevant BM with their gross tumor volume (GTV) and their planning target volumes. Additionally, organs at risk were segmented for the safest radiation exposure, which enabled the calculation of the radiation plan and thus all resulting isodose lines.

Furthermore, one radiation oncologist defined two regions (cylinders, height and diameter of 10 mm) within each patient's healthy-appearing brain matter (Healthy ROI, HR). All ROIs were exported from Leksell GammaPlan as DICOM RT files.

The DICOM RT structure files were imported into MATLAB with the Computational Environment for Radiological Research (CERR) [DBC03]. It allowed identifying the irradiated and segmented regions from Leksell GammaPlan on the ^{23}Na MR image and enabled evaluation of those regions within MATLAB.

The acquired and reconstructed ^{23}Na MR images were co-registered to the contrast-enhanced ^{1}H MPRAGE, which was used for the SRS planning with the aim of being able to transfer the ROIs (GTV, isodose lines and HR) to the ^{23}Na MR images of all time points. Therefore, all available ^{23}Na MR images of each patient were co-registered to the same MPRAGE from the first measurement session. Co-registration was performed with SPM12 as was explained in subsection 3.1.3. Furthermore, image segmentation into WM, GM, and CSF was performed for being able to exclusively evaluate brain matter with no CSF impingement.

Quantification was performed based on the SI within the patients' left VH through linear regression as was explained in subsection 3.1.4, including a correction of the T1-weighting within the VH. The parameters were chosen analogue to the TSC quantification in subsection 3.2.3.

The TSC-map was calculated as was shown in Equation 3.9. The ROIs within the VH were manually segmented within the MPRAGE, which was transferable to all three ^{23}Na MR images because of the image co-registration. The transfer of the reference ROI is depicted in a representative transverse slice of one patient in Figure 3.9.

The TSC was calculated within GTV, HR and the evaluated isodose areas, which were D = 2, 3, 4, 6, 8, 10, 12, and 18 Gray (Gy) on all ^{23}Na MR images of each patient. An isodose area was defined as the area enclosed by the corresponding isodose line with subtraction of the area enclosed by the preceding isodose line, as is visualized in Figure 4.13. The HR were evaluated to compare the TSC development within the irradiated regions to non-irradiated healthy-appearing tissue of the same patient at the same time points. The different isodose areas were evaluated to investigate the effect of radiation on healthy tissue, and the GTV were evaluated to investigate the effect of radiation on tumorous tissue. Potential CSF regions within the ROIs were subtracted. In this study, no outer border was cut-off from the ROIs because of the

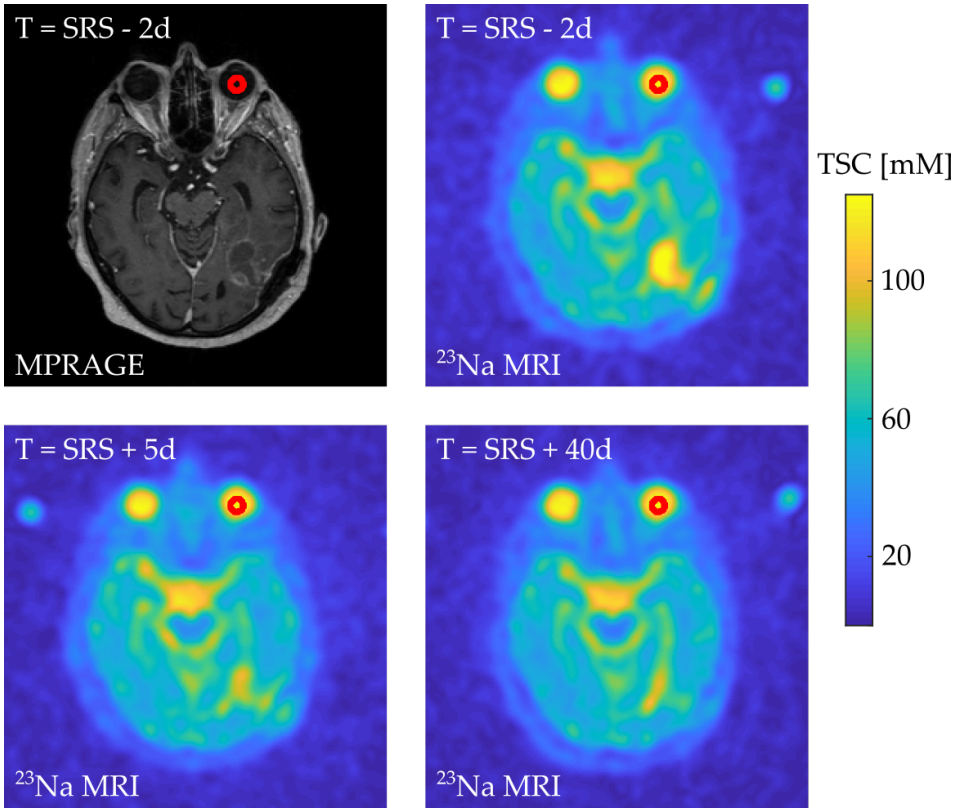

Figure 3.9: One slice of the MPRAGE and of the ^{23}Na MR images at all three time points from one representative patient. A red line encircles the reference in the VH that was used for the TSC quantification.

already relatively small size of GTV and the continuous (and not discrete) decrease of radiation within the isodose areas.

BM that presented tumor progression were evaluated individually.

3.4.1.3 *Statistical analysis*

The mean TSC within GTV, HR, and within all isodose areas was compared between measurements at time points I, II, and III. Differences were tested for statistical significance using the paired student t-test. The correlation was tested between the radiation doses D and the mean TSC within the corresponding isodose area using the Pearson correlation test.

3.4.2 *TSC in the human prostate with a suspected carcinoma*

The other prospective in-vivo study that is presented in this thesis investigated TSC within the male prostate. To be included in the study, the patient had to receive an MRI exam of the prostate to investigate a clinically *suspected prostate carcinoma*[2] (PCa). The data that is presented in this thesis was acquired between March 2020 and May 2021. The written informed consent was obtained from all patients. The study was approved by our local ethical review committee under the approval number 2016-631N-MA, and written informed consent was obtained from all patients.

2 Prostate carcinomas might be suspected because of, e.g., increased prostate-specific antigen values.

Prior to the study protocol, each patient underwent a standard multi-parametric magnetic resonance imaging (mpMRI) exam of the prostate according to the American College of Radiology PI-RADS guidelines [Wei+16]. During the measurements, a contrast agent was administered (Dotarem, 0.1 ml/kg body weight), with – again – no impact on the following TSC quantification [Pas+18].

3.4.2.1 *Data Acquisition*

The study protocol comprised of the ^{23}Na 3D radial density-adapted sequence (see: subsection 3.1.2) and a ^{1}H 2D T2w turbo-spin-echo (T2 TSE).

The ^{23}Na MRI sequence required a measurement time of 16 min per dataset to obtain an image with a FoV of 500x500x500 mm^3 with a nominal resolution of 5.01x5.01x5.01 mm^3. The detailed sequence parameters of the ^{1}H T2 TSE and of the ^{23}Na MRI sequence are listed in the appendix in Table A.3. Optimal reference amplitude was individual for each patient and was calculated via flip angle calibrations.

The study protocol was acquired after a coil change to the dual-tuned ^{1}H/^{23}Na body-coil, details are described in subsection 3.1.1.

Two radiologists segmented the whole prostate (WP) and its peripheral zone (PZ) based on the T2 TSE in MITK (German Cancer Research Center, Heidelberg, Germany). The subtraction of both masks resulted in the mask of the transitional zone (TZ). Image co-registration of the ^{23}Na MR image to the T2 TSE was performed by automatic slice positioning alignment and re-sampling of the ^{23}Na MR image to the T2 TSE's resolution with an additional anterior manual shift, which was required to achieve an optimal alignment. Therefore, the ROIs that were segmented on the T2 TSE were transferable to the ^{23}Na MR image.

3.4.2.2 *Data processing*

The ^{23}Na MR image reconstruction was performed in MATLAB 2018a with the algorithm that was explained in subsection 3.1.2. Image reconstruction resulted in an image with the size of 196x196x196 voxels, which had an apparent isotropic resolution of 2.55x2.55x2.55 mm^3 and, thus, a FoV of 500x500x500 mm^3.

The coil's 16 receive channels were reconstructed individually, resulting in 16 separate images, which were combined via adaptive coil combination (ACC), meaning that the channels were weighted during the reconstruction process, depending on their acquired SI, optimizing the resulting image for SNR [WGM00].

B_1^- CORRECTION Corrections were necessary for inhomogeneities within the coil's receive field B_1^-. The B_1^- correction was performed by application of a low-pass filter (LPF) to the ^{23}Na image (Na_{Im}). The methodology was performed similarly to the previously published method by Lachner et al. [Lac+20].

After image reconstruction and coil combination via ACC, the resulting Na_{Im} was low-pass filtered, generating Na_{LP}. The LPF was implemented with a Gaussian filter, using a cubic Gaussian kernel with the sd $\sigma_1 = 10$ voxels ≈ 25 mm and a filter size of 41 voxels.

A binary mask M was obtained by thresholding of Na_{LP}, with ones representing the object and zeros representing the background region. Again, a 3D cubic Gaussian filter was applied to the mask M, generating M_{LP}. Here, the Gaussian filter had a sd of $\sigma_2 = 20$ voxels ≈ 50 mm, and a filter size of 81 voxels. The B_1^- correction map

$B1^{-}_{corr}$ was then calculated by element-wise matrix division of $NaIm_{LP}$ and M_{LP} (analogue to the *Hadamard product*[3]), with

$$B1^{-}_{corr} = \frac{Na_{LP}}{M_{LP}}. \tag{3.18}$$

It was further normalized between 0 and 1 within the mask region and was set to 1 outside of the masks region. The B_1^--corrected ^{23}Na MR image Na_{B1corr} was eventually calculated with

$$Na_{B1corr} = \frac{NaIm}{B1^{-}_{corr}}. \tag{3.19}$$

The B_1^- correction algorithm is schematically illustrated in Figure 3.10.

No corrections were performed for the transmit field B_1^+, as homogeneity was assumed because of the birdcage structure of the transmit coil, as was explained in subsection 2.3.2 and subsection 3.1.1.

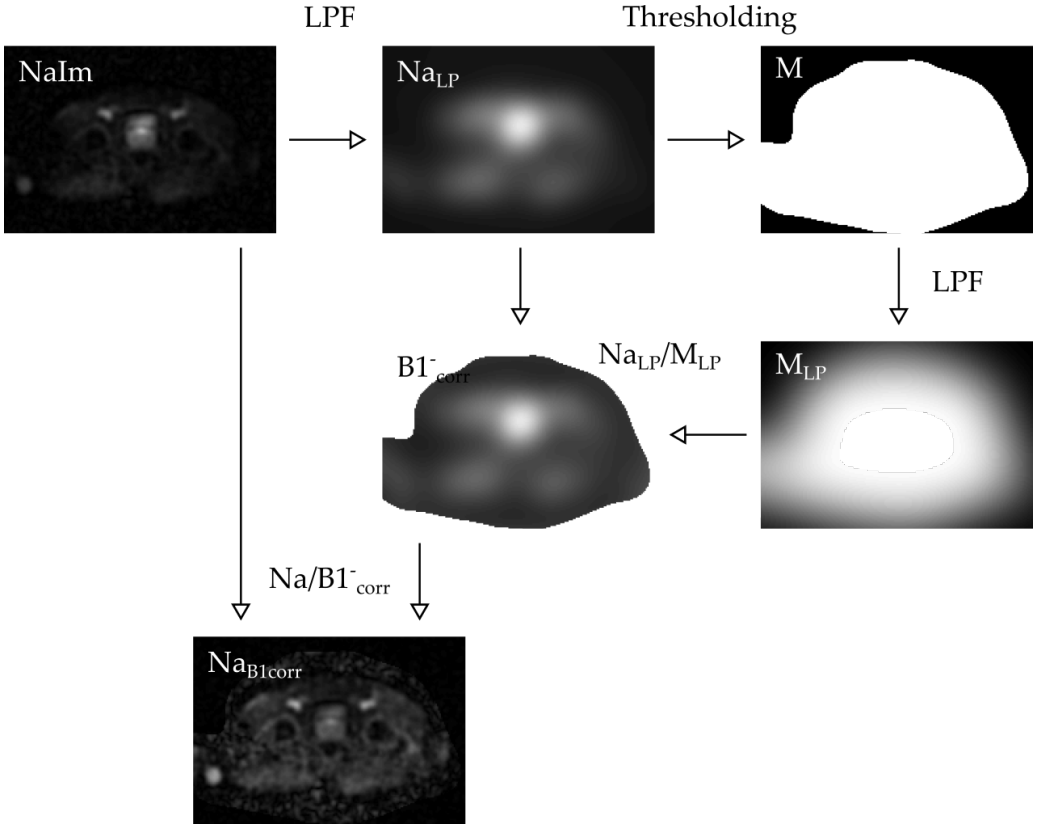

Figure 3.10: Schematic illustration of the B_1^- correction with a low-pass filter. The filter is applied to the image NaIm, generating Na_{LP} and a mask M is obtained via thresholding. Another low-pass filter is applied to M, calculating M_{LP}. The correction map $B1^{-}_{corr}$ is defined as the ratio of Na_{LP} and M_{LP}. Eventually, the B_1^--corrected image, Na_{B1corr}, is calculated by dividing NaIm and $B1^{-}_{corr}$. The algorithm was adapted from Lachner et al. [Lac+20].

TSC QUANTIFICATION For TSC quantification, the reference regions were chosen to be within the femoral blood vessels (FBV), where SI was high compared to the prostate tissue. The FBV were segmented within the region of the iliac-femoral blood

3 The Hadamard product is the element-wise multiplication of two matrices of the same size, generating a matrix with the same size. It was described by Jacques Salomon Hadamard.

vessel transition.TSC within the FBV was estimated to be $\approx$ 81 mM based on previous findings for blood sodium concentration [KS13; OWB05; Lot+19]. Three-dimensional ROIs were defined within the left and right FBV. Quantification was performed based on a linear fit of the mean SI within the ROIs as was explained in subsection 3.1.4, according to Equation 3.5.

SI within the FBV was corrected for T1- and for T2*-weighting based on the relaxation time of blood with $T1(\mathrm{Blood}) = 31.9$ ms, and mono-exponential $T2^*(\mathrm{Blood}) = 20.1$ ms according to Konstandin et al. [KS13]. However, this must be assumed an estimation as $T2^*$ further depends on the MR scanner specifics, such as B_0 inhomogeneities. The correction was performed with:

$$\begin{aligned} \mathrm{TSC}(\mathrm{Tissue}) &= \mathrm{SI}(\mathrm{Tissue}) \left(\frac{81\mathrm{mM}}{\mathrm{SI}_{\mathrm{corr}}(\mathrm{FBV})} \right) \\ &= \mathrm{SI}(\mathrm{Tissue}) \left(\frac{81\mathrm{mM} \left(1 - e^{-\mathrm{TR}/\mathrm{T1}(\mathrm{Blood})}\right) \left(e^{-\mathrm{TE}/\mathrm{T2}^*(\mathrm{Blood})}\right)}{\mathrm{SI}(\mathrm{FBV})} \right) \\ &= \mathrm{SI}(\mathrm{Tissue}) \left(\frac{81\mathrm{mM} \cdot 0.9768 \cdot 0.9420}{\mathrm{SI}(\mathrm{FBV})} \right) \\ &= \mathrm{SI}(\mathrm{Tissue}) \left(\frac{81\mathrm{mM} \cdot 0.9201}{\mathrm{SI}(\mathrm{FBV})} \right) \end{aligned} \tag{3.20}$$

For the calculation of the TSC-map, quantification was performed after B_1^--correction and after image co-registration to the T2 TSE. This was because the ROIs that needed to be segmented within the FBV were well-distinguishable within the T2 TSE, making segmentation more precise. TSC quantification with the marked reference regions of one representative patient is depicted in Figure 3.11.

Relaxation times of the prostate were assumed to be $T1(\mathrm{Prostate}) = 38.8$ ms, and $T2^*_f(\mathrm{Prostate}) = 6.8$ ms and $T2^*_s(\mathrm{Prostate}) = 14.8$ ms, as was estimated previously by Paschke [Pas20]. Therefore, relaxation time correction was performed within the WP according to Equation 2.75 with:

$$\begin{aligned} \mathrm{TSC}(WP)_{\mathrm{T1corr}} &= \mathrm{TSC}(WP) \left(\frac{1}{1 - e^{-\mathrm{TR}/\mathrm{T1}(\mathrm{Prostate})}} \right) \\ &= \mathrm{TSC}(\mathrm{PT}) \cdot 1.0475 \\ \mathrm{TSC}(\mathrm{PT})_{\mathrm{T2^*corr}} &= \mathrm{TSC}(\mathrm{PT}) \frac{1}{0.6e^{-\mathrm{TE}/\mathrm{T2}^*_f(\mathrm{Prostate})} + 0.4e^{-\mathrm{TE}/\mathrm{T2}^*_s(\mathrm{Prostate})}} \\ &= \mathrm{TSC}(\mathrm{PT}) \cdot 1.1471 \\ \mathrm{TSC}(\mathrm{PT})_{\mathrm{T1,T2^*corr}} &= \mathrm{TSC}(\mathrm{PT}) \cdot 1.2016 \end{aligned} \tag{3.21}$$

Mean TSC was calculated within PZ, TZ and WP, based on the radiologists' segmentation of the anatomical regions. As the segmentation was initially performed on the T2 TSE, TSC within the ROIs was evaluated after image co-registration.

Figure 3.12 shows one transverse slice of one representative patient with the quantified ^{23}Na MR image and the T2 TSE MR image, to which the ^{23}Na MR image was co-registered. On the ^{1}H MR image, the segmentation of PZ, TZ, and one lesion within the TZ, are depicted. The figure also shows the overlay of both MR images, including the segmentations.

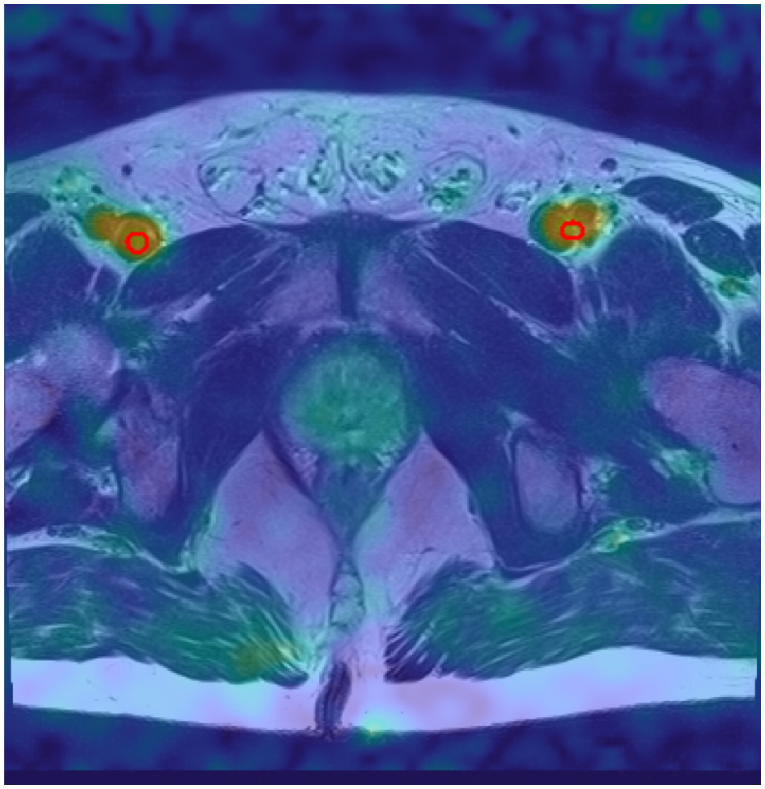

Figure 3.11: One transverse slice of the co-registered ^{23}Na MR image with the segmentation of the femoral blood vessels, which were used for the for the quantification. The ^{23}Na MR image is shown as an overlay over the T2 TSE and the segmented regions are encircled in red.

For comparison, mean ADC was calculated within the respective regions. For that purpose, ADC-maps were co-registered to the T2 TSE despite not being acquired with the dual-tuned coil but during the standard mpMRI protocol. Registration was performed via affine registration within MATLAB, using an initial radius of 0.0001, a growth factor of 1.05, and a maximal number of iterations of 1500.

For the evaluations, the outer border of the segmentation masks was cut-off. For the evaluation of TSC, this mainly served the purpose of avoiding potential PVE. For the ADC-map, the cut-off of the outer border was supposed to reduce any biases due to inaccuracies of the image co-registration, which is particularly challenging and prone to inaccuracies when using DWI. The cut-off was set to 5.2 mm – corresponding approximately to the ^{23}Na MR image's nominal resolution – for WP and TZ, but was reduced to 2.6 mm within PZ because of its already small volume.

Furthermore, TSC quantification was also performed within the ROIs that served as quantification references – within the FBV. Here, mainly the differences between both sides and sd within the FBV was of interest. The purpose was to evaluate the stability and reliability of the quantification method.

3.4.2.3 *Statistical analysis*

Differences between TSC in PZ, and TZ and between TSC in both segmented blood vessels of each patient were tested using the paired student t-test. The correlations

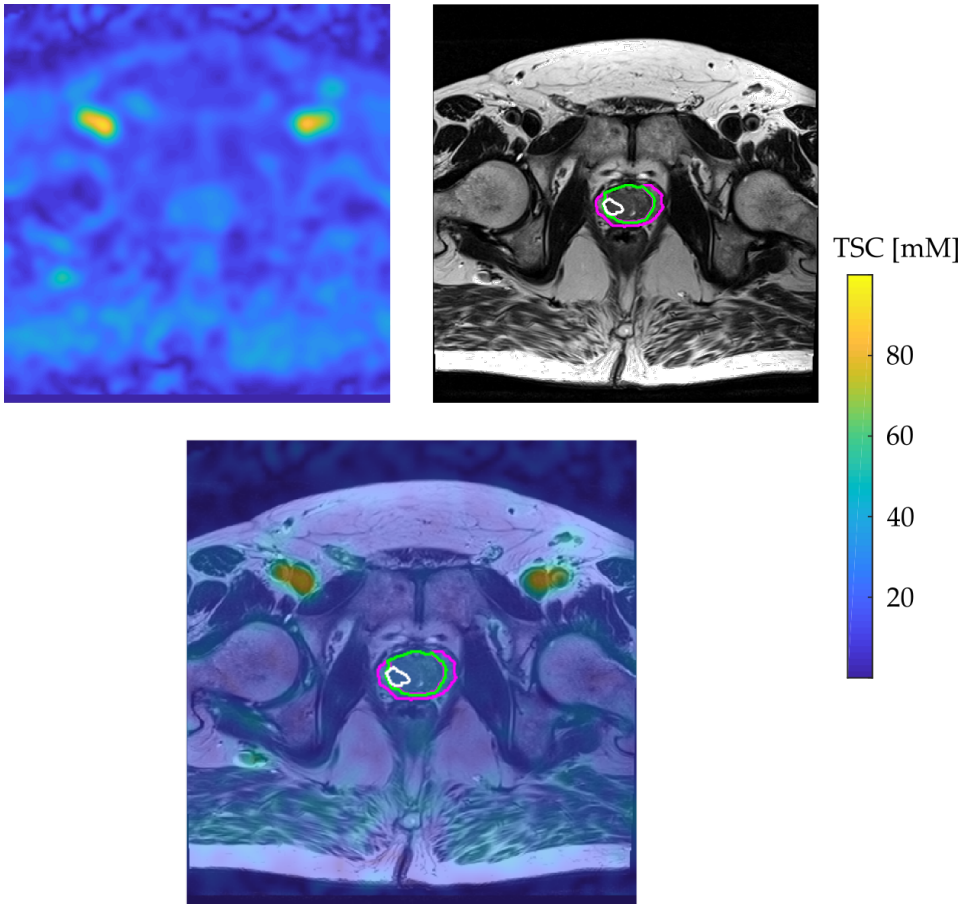

Figure 3.12: One transverse slice of the co-registered and quantified ^{23}Na MR image and the T2 TSE MR image with the segmentation of PZ, TZ, and one lesion within the TZ (top), and the overlay of both images, including the segmented regions (bottom).

between TSC and ADC values within WP, PZ and TZ were evaluated using the Pearson correlation test.

4 RESULTS

The results presented in this chapter were partially published in [Adl+21b] by Karger Publishers (subsection 4.1.1) and in [Adl+21a] by John Wiley & Sons Ltd (section 4.2), and the description of the corresponding results are replicated here with permission.

4.1 TSC QUANTIFICATION FOR "^{23}NA MRI IN ISCHEMIC STROKE"

The study "^{23}Na MRI in ischemic stroke" included a total of 62 patients. For evaluating absolute and relative TSC quantification (subsection 4.1.1), 42 out of the 62 patients were included. The remaining 20 patients were excluded because of movement artifacts or similar problems with the data acquisition of the ^{1}H MR image, because the patient aborted the measurements at some point, or because the data acquisition was unsuccessful and the ^{23}Na MR image was not or insufficiently quantifiable. A common problem was missing or misplaced reference vials, which were either forgotten to be placed within the FoV prior to the measurement or they were moved due to involuntary movements of the patient.

For the evaluation of internal references for the absolute TSC quantification (subsection 4.1.2), eight more patients (a total of 50 out of 62 patients) were included as acquisition problems with the ^{1}H MR image were no exclusion criterion whereas the remaining twelve patients were still excluded due to data acquisition problems with the ^{23}Na MR image.

4.1.1 *Relative and absolute TSC quantification*

The results presented in this section were partially published in [Adl+21b], although, a different sub-group of patients was included and the methodology was marginally adjusted, as was described in detail in subsection 3.2.2.

Three patients were rated with Fazekas grade 0, 23 patients with Fazekas grade I, seven patients with Fazekas grade II, and nine patients with Fazekas grade III. One transverse slice of one representative patient with each Fazekas grading is depicted in Figure 4.1.

The one-sample Kolmogorov-Smirnov test showed that absolute TSC in WM ($p = 0.90$), in the stroke region ($p = 0.61$), in the contra-lateral stroke region ($p = 0.92$), and in the NAWM ($p = 0.70$) followed a normal distribution. Therefore, the student t-test was applicable for TSC within all regions.

EVALUATION OF THE TISSUE SODIUM CONCENTRATION IN WHITE MATTER The evaluated WM was obtained by subtracting the stroke region from the automatically segmented WM mask with a cut-off of the outer 4 mm border. After subtractions, the remaining mean volume was 246 ± 125 cm^3.

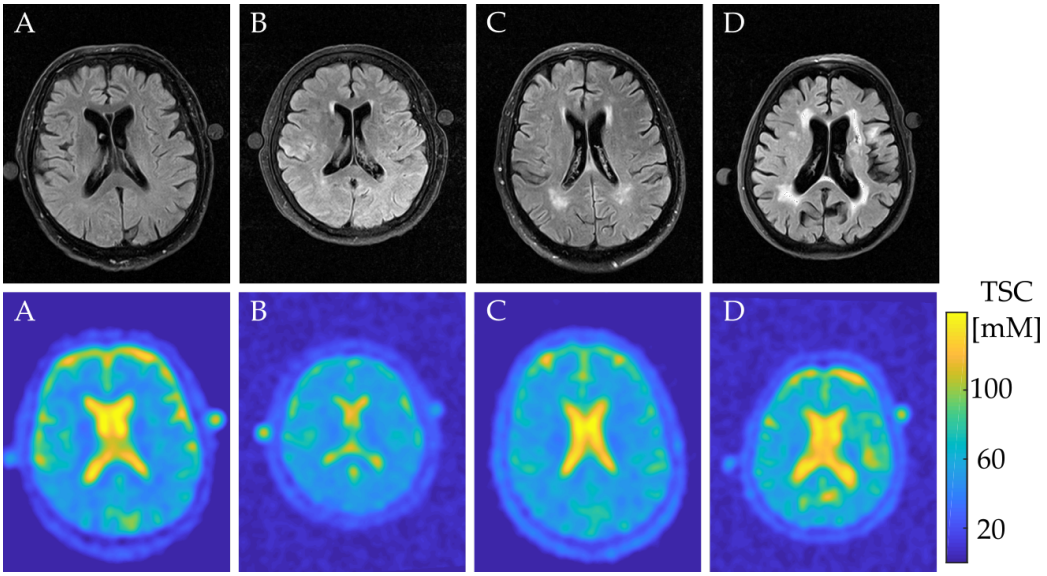

Figure 4.1: Transverse slice of the ^{1}H FLAIR and the co-registered quantified ^{23}Na MR images from a patient with A: Fazekas grade 0 (male, 80 years old), B: Fazekas grade I (female, 59 years old), C: Fazekas grade II (male, 77 years old), D: Fazekas grade III (female, 83 years old). This figure is adapted from [Adl+21b] with permission.

For all patients, absolute TSC in WM was between 36 and 74 mM with a mean of 52 ± 8 mM. The Spearman correlation test showed that there was a positive correlation between the TSC in WM and the Fazekas grade with $r = 0.43$ ($p = 0.0042$).

Considering patients with different Fazekas gradings separately, the patients with Fazekas grade 0 showed an absolute TSC in WM between 47 and 51 mM with a mean of 49 ± 2 mM and a mean intra-subject sd of 9 ± 1 mM.

The patients with Fazekas grade I showed an absolute TSC in WM between 37 and 63 mM with a mean of 50 ± 7 mM and a mean intra-subject sd of 10 ± 2 mM.

The patients with Fazekas grade II showed absolute TSC in WM between 36 and 59 mM with a mean of 49 ± 7 mM and a mean intra-subject sd of 11 ± 3 mM.

And the patients with Fazekas grade III showed absolute TSC in WM between 50 and 74 mM with a mean of 62 ± 7 mM and a mean intra-subject sd of 15 ± 4 mM.

Considering patients with Fazekas grade 0, mean absolute TSC in WM was not significantly different compared to mean absolute TSC in WM of patients with Fazekas grade I ($p = 0.82$) or grade II ($p = 0.92$), while it was significantly lower compared to mean absolute TSC in WM of patients with Fazeks grade III ($p = 0.0126$).

Mean absolute TSC in WM was not significantly different in patients with Fazekas grade I compared to patients with Fazekas grade II ($p = 0.76$).

Mean absolute TSC in WM was significantly lower in patients with Fazekas grade I and grade II than it was in patients with Fazekas grade III ($p = 0.0002$ and $p = 0.0036$, respectively).

There was a significant positive correlation (evaluated with the Spearman correlation test) between the Fazekas grade and the intra-subject sd of TSC within WM with $r = 0.49$ ($p = 0.0010$).

For all patients, the NAWM ROIs showed a mean absolute TSC of 47 ± 4 mM, which was significantly lower compared to the mean absolute TSC in the evaluated WM masks ($p < 0.0001$).

The patients with Fazekas grade 0 showed a mean absolute TSC within the NAWM of 45 ± 5 mM.

The patients with Fazekas grade I showed a mean absolute TSC within the NAWM of 47 ± 3 mM.

The patients with Fazekas grade II showed a mean absolute TSC within the NAWM of 45 ± 5 mM.

The patients with Fazekas grade III showed a mean absolute TSC within the NAWM of 48 ± 4 mM.

Mean absolute TSC within the NAWM was not significantly different between patients of different Fazekas grades (all $p > 0.2$).

The boxplots of absolute TSC in WM and in NAWM are depicted in Figure 4.2 for all Fazekas grades. The figure shows how TSC in NAWM was similar between patients with all Fazekas grades, whereas TSC in WM was different between patients with Fazekas grade III and patients with lower Fazekas grades.

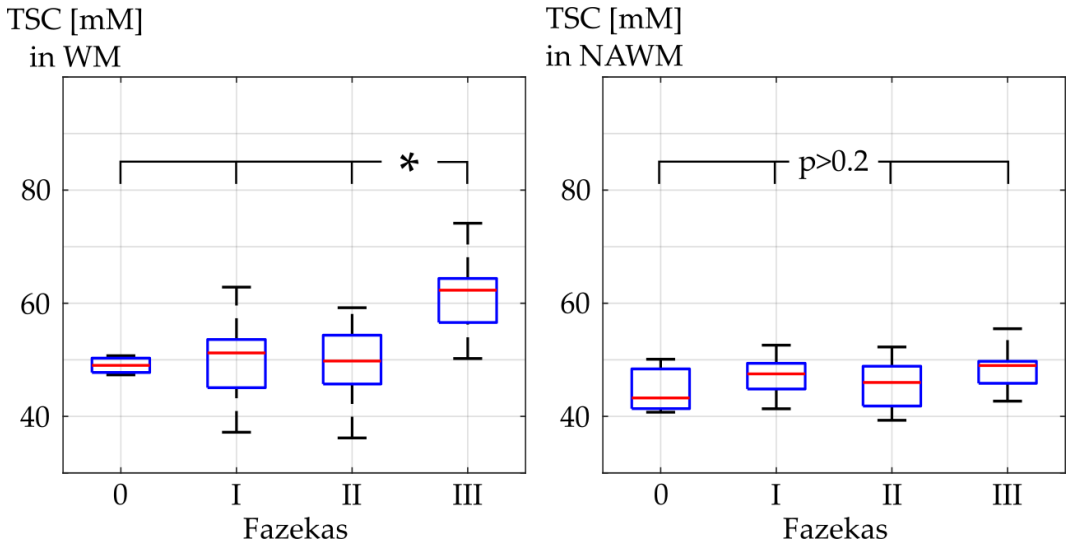

Figure 4.2: Mean absolute tissue sodium concentration (TSC) in white matter (WM, left) and normal-appearing white matter (NAWM, right), depicted as boxplots for Fazekas grades 0, I, II, and III. The red line in the box depicts the median value and the blue box' top and bottom edges represent the 25th and 75th percentiles of the data, respectively. The whiskers extend to the most extreme data points. Statistically significant differences are indicated with a $*$.

Table 4.1 lists the mean absolute TSC within WM and NAWM for all Fazekas grades.

The multiple regression analysis showed that patient's age, the time after onset of symptoms of the ischemic stroke and the Fazekas grade could significantly predict the absolute TSC in WM ($F = 45.74$, $p = 0.0024$) with the model explaining 31% of the variance. The time after onset of symptoms ($p = 0.18$) and the patients' age ($p = 0.21$) did not contribute significantly whereas the Fazekas grade's contribution was significant ($p = 0.0072$).

Table 4.1: Absolute tissue sodium concentration (TSC) in white matter (WM) and normal-appearing white matter (NAWM) within patients of all Fazekas grades. TSC in the stroke region as absolute TSC and relative TSC for both patient groups (Group 1: Fazekas 0 and I, Group 2: Fazekas II and III). The relative TSC as rTSC, which is relative to the contra-lateral tissue, and as $rTSC_{NAWM}$, which is relative to NAWM.

	Absolute TSC [mM]				
Patients	WM	NAWM	Stroke	rTSC	$rTSC_{NAWM}$
All	52 ± 8	47 ± 4	72 ± 15	1.27 ± 0.23	1.53 ± 0.34
Fazekas 0	49 ± 2	45 ± 5	74 ± 15	1.33 ± 0.22	1.57 ± 0.33
Fazekas I	50 ± 7	47 ± 3			
Fazekas II	49 ± 7	45 ± 5	67 ± 16	1.14 ± 0.19	1.43 ± 0.37
Fazekas III	62 ± 7	48 ± 4			

EVALUATION OF THE TISSUE SODIUM CONCENTRATION IN STROKE REGIONS

Out of the 42 patients, 35 presented with an ischemic stroke of which the stroke region was segmentable. In the remaining seven patients, no stroke area was segmented. The patients were grouped according to their Fazekas grade, with Fazekas grade 0 and I being Group 1 ($n = 24$), and Fazekas grade II and III being Group 2 ($n = 11$).

The manually segmented stroke regions had – after subtraction of the outer 2 mm border – a mean volume of 42 ± 61 cm^3.

For all patients, mean absolute TSC in the defined stroke region was between 36 and 109 mM with a mean of 72 ± 16 mM.

Mean absolute TSC in the stroke region was 74 ± 15 mM for patients in Group 1 (Fazekas grade 0 and I) and 67 ± 16 mM for patients in Group 2 (Fazekas grade II and III). Mean absolute TSC in the stroke region was not significantly different between both groups ($p = 0.25$).

For all patients, absolute TSC in the contra-lateral brain tissue was between 39 and 79 mM with a mean of 57 ± 9 mM.

For all patients, the relative TSC based on the contra-lateral brain tissue (rTSC) was 1.27 ± 0.23, and relative TSC based on the patient's NAWM ($rTSC_{NAWM}$) was significantly higher with 1.52 ± 0.34 ($p < 0.0001$).

For patients in Group 1, mean rTSC in the stroke region was 1.33 ± 0.22, and it was significantly lower for patients in Group 2 with 1.14 ± 0.19 ($p = 0.02$).

Mean $rTSC_{NAWM}$ in the stroke region was 1.57 ± 0.33 for patients in Group 1 and 1.43 ± 0.37 for patients in Group 2, which was not significantly different ($p = 0.28$).

The boxplots of absolute and relative TSC in the stroke region are depicted in Figure 4.3 for both Fazekas groups. The figure emphasizes the similarity of absolute TSC in the stroke region between both Fazekas groups and the difference of relative TSC in the stroke region between both Fazekas groups.

Mean absolute TSC and both mean relative TSC (rTSC and $rTSC_{NAWM}$) are listed in Table 4.1 for both groups.

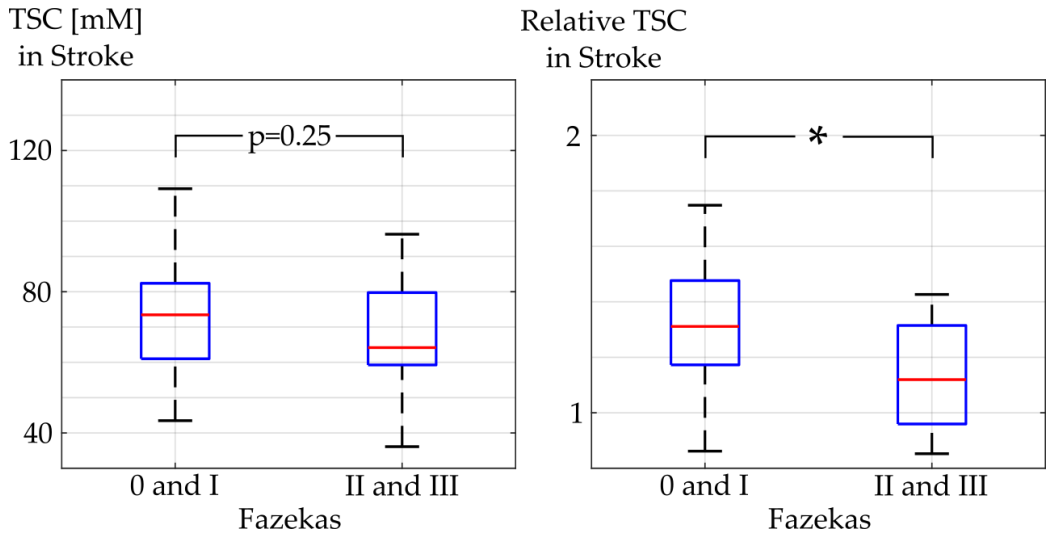

Figure 4.3: Mean absolute (left) and relative (right) tissue sodium concentration (TSC) in the stroke region, depicted in boxplots for Fazekas grade 0, I, II, and III. The red line in the box depicts the median value and the blue box' top and bottom edges represent the 25th and 75th percentiles of the data, respectively. The whiskers extend to the most extreme data points. Statistically significant differences are indicated with a $*$.

4.1.2 *Internal references for absolute TSC quantification*

For all included 50 patients, the absolute TSC quantification showed a mean of 42 ± 6 mM in the whole brain with the quantification method based on the SI within the reference vials (TSC_{Vials}).

Mean absolute TSC in the whole brain of all evaluated patients was 38 ± 3 mM with the quantification based on SI within the CSF region (TSC_{CSF}).

Mean absolute TSC in the whole brain of all evaluated patients was 35 ± 4 mM with the quantification based on SI within the VH region (TSC_{VH}).

Mean TSC_{CSF} and mean TSC_{VH} in the whole brain of all evaluated patients were both significantly lower compared to TSC_{Vials} (both $p < 0.0001$) and mean TSC_{VH} was significantly lower than mean TSC_{CSF} ($p < 0.0001$).

Mean absolute TSC in the whole brain of all evaluated patients are depicted as boxplots for TSC_{Vials}, TSC_{CSF}, and TSC_{VH} in Figure 4.4.

Mean absolute TSC differences (ΔTSC) between TSC_{CSF} and TSC_{Vials} within the whole brain of all evaluated patients was 6 ± 6 mM. Mean ΔTSC between TSC_{VH} and TSC_{Vials} within the whole brain of all evaluated patients was 8 ± 5 mM.

Mean ΔTSC of the TSC_{CSF}-map was significantly lower than mean ΔTSC of the TSC_{VH}-map ($p = 0.0019$).

ΔTSC of TSC_{CSF} and of TSC_{VH} within the whole brain of all evaluated patients are depicted as boxplots in Figure 4.5.

The SSC was available for 44 out of 50 patients. No information about SSC was available for $n = 6$ patients for whom ESC was thus assumed to be 145 mM. Considering those six patients, ΔTSC was 10 ± 9 mM within the TSC_{CSF}-map and 9 ± 6 mM within the TSC_{VH}-map. ΔTSC of that subgroup was not significantly different

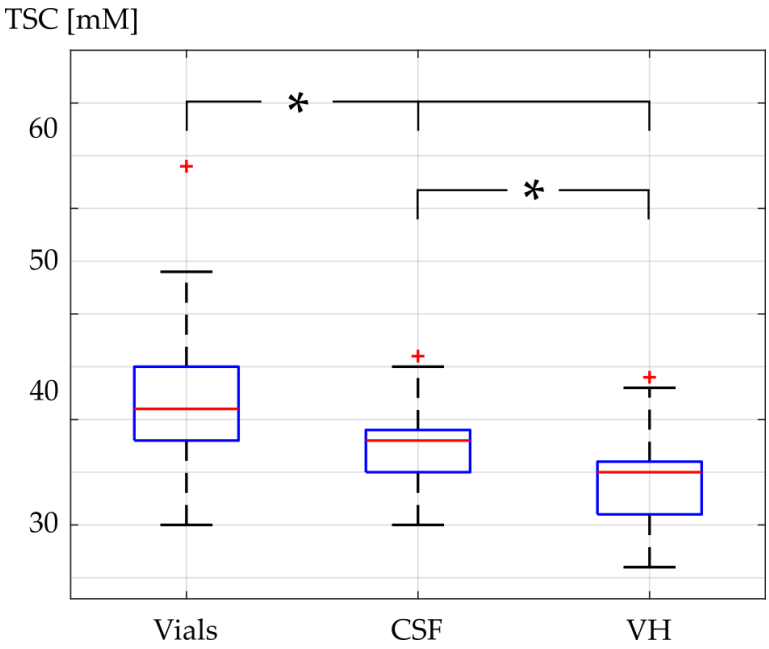

Figure 4.4: Boxplot of the mean absolute tissue sodium concentration (TSC) in the whole brain of all included patients. Evaluated within the TSC_{Vials}-map (left), TSC_{CSF}-map (middle), and the TSC_{VH}-map (right). The red line in the box depicts the median value and the blue box' top and bottom edges represent the 25th and 75th percentiles of the data, respectively. The whiskers extend to the most extreme data points, not considering outliers which are depicted as red +. Statistically significant differences are indicated with a $*$.

compared to ΔTSC of all patients within the respective TSC-map ($p = 0.14$ for TSC_{CSF} and $p = 0.40$ for TSC_{VH}).

On the TSC_{Vials}-map, after the introduction of the correction factor, mean absolute TSC within the manually defined CSF regions was 156 ± 27 mM, ranging between 111 and 265 mM. Mean absolute TSC within the manually defined VH regions was 171 ± 24 mM, ranging between 137 and 265 mM. Mean absolute TSC within the VH region was significantly higher than mean absolute TSC within the CSF region ($p < 0.0001$).

Mean absolute TSC within the manually defined CSF and VH regions are depicted as boxplots in Figure 4.6.

The evaluated regions within the reference vials (100 mM) had a mean size of 60 ± 33 voxel, the evaluated reference regions within CSF had a mean size of 35 ± 9 voxel, and the evaluated reference regions within VH had a mean size of 40 ± 7 voxel.

The sd within the reference vial of 100 mM was 6 ± 3 mM, sd within CSF region was 6 ± 2 mM, and sd in VH was 4 ± 2 mM. Sd within VH regions was significantly lower compared to sd within the reference vials ($p = 0.0063$) and CSF regions ($p = 0.0035$).

The Pearson correlation test showed a positive correlation between the mean absolute TSC within the CSF region on the TSC_{Vials}-map and the SSC with $r = 0.21$, which was not significant ($p = 0.18$).

The Pearson correlation test showed a positive correlation between the mean absolute TSC within the VH region on the TSC_{Vials}-map and the SSC with $r = 0.30$, which

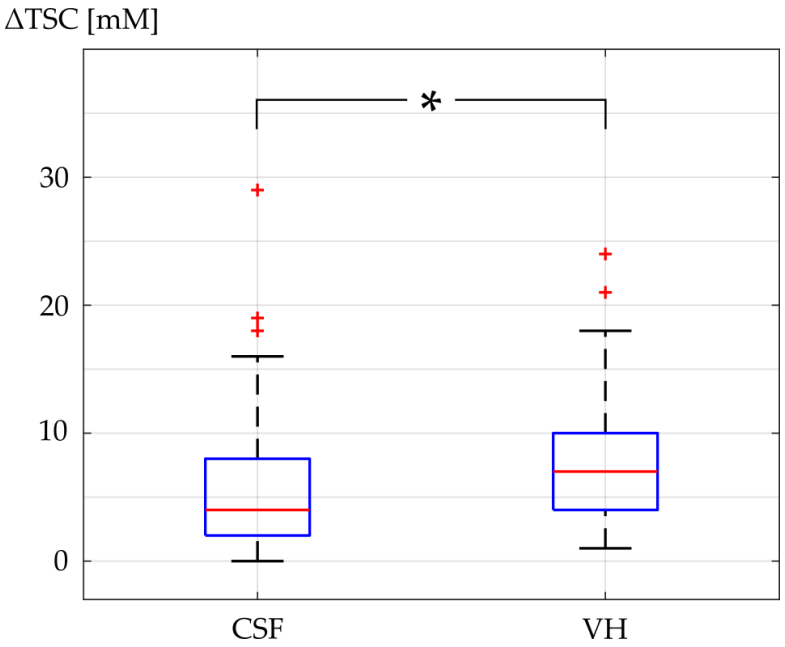

Figure 4.5: Boxplot of the mean absolute tissue sodium concentration differences (ΔTSC) in the whole brain of all evaluated patients between the TSC_{CSF}-map and the TSC_{Vials}-map (left) and between the TSC_{VH}-map and the TSC_{Vials}-map (right). The red line in the box depicts the median value and the blue box' top and bottom edges represent the 25th and 75th percentiles of the data, respectively. The whiskers extend to the most extreme data points, not considering outliers, which are depicted as red +. Statistically significant differences are indicated with a $*$.

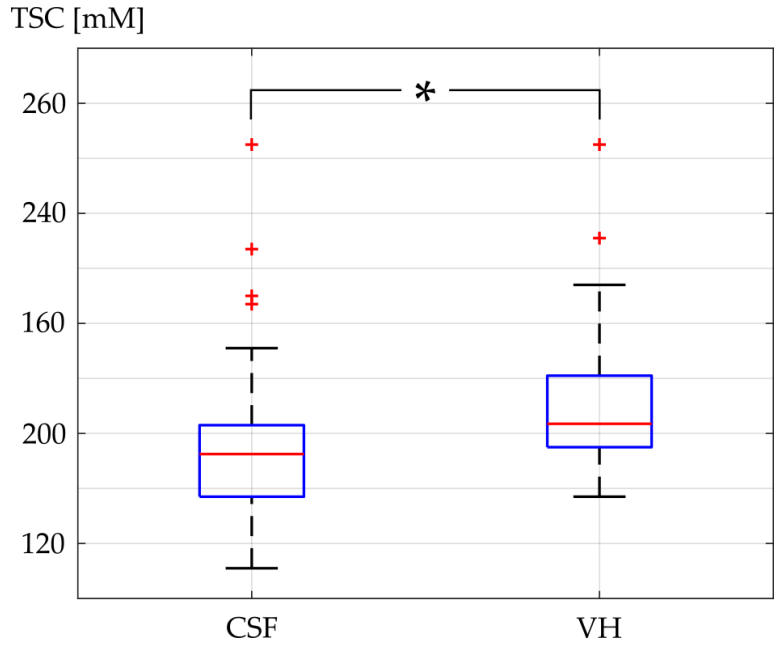

Figure 4.6: Boxplot of the mean absolute tissue sodium concentration (TSC) in the manually defined CSF (left) and VH (right) region within the TSC_{Vials}-map. The red line in the box depicts the median value and the blue box' top and bottom edges represent the 25th and 75th percentiles of the data, respectively. The whiskers extend to the most extreme data points, not considering outliers, which are depicted as red +. Statistically significant differences are indicated with a $*$.

was significant ($p = 0.0446$).

TSC QUANTIFICATION WITHIN TISSUES Mean absolute TSC was evaluated within the segmented masks – with subtraction of the outer border.

TSC_{Vials} showed a mean absolute TSC of 53 ± 9 mM in WM and 58 ± 8 mM in GM. Mean absolute TSC in the stroke region was 73 ± 16 mM.

TSC_{CSF} showed a mean absolute TSC of 48 ± 7 mM in WM and 53 ± 6 mM in GM. Mean absolute TSC in the stroke region was 66 ± 15 mM.

TSC_{VH} showed a mean absolute TSC of 44 ± 7 mM in WM and 48 ± 6 mM in GM. Mean absolute TSC in the stroke region was 60 ± 12 mM.

Mean absolute TSC within the stroke region was significantly higher compared to mean absolute TSC in WM and GM on all three TSC-maps (all $p < 0.0001$). Mean absolute TSC within GM was significantly higher compared to mean absolute TSC in WM on all three TSC-maps (all $p < 0.0001$).

Mean TSC values in WM, GM, and stroke region on all three TSC-maps are listed in Table 4.2, the corresponding boxplots are depicted in Figure 4.7. The figure visualizes how differentiation of TSC within the different tissues is possible on all the three TSC-maps.

Table 4.2: Mean absolute tissue sodium concentration (TSC) in white matter (WM), grey matter (GM), and in the stroke region on the three TSC-maps: TSC_{Vials}, TSC_{CSF}, and TSC_{VH}.

Tissue	TSC_{Vials}	TSC_{CSF}	TSC_{VH}
WM	53 ± 9	48 ± 7	44 ± 7
GM	58 ± 8	53 ± 6	48 ± 6
Stroke	73 ± 16	66 ± 15	60 ± 12

4.1.3 *Evaluation of quantification stability*

TSC quantification based on SI within CSF and VH was performed on three MRI scans of the same HC over a time span of a total of six weeks, which were all co-registered to the same ^{1}H MR image.

On the TSC_{CSF}-map, mean absolute TSC was 56 ± 6 mM, 58 ± 6 mM, and 57 ± 7 mM in WM, and 65 ± 8 mM, 65 ± 9 mM, and 66 ± 9 mM in GM. Mean absolute TSC differences between the three scans were 4 ± 3 mM between all three scans in WM, and they were 5 ± 3 mM between scan I and II, 5 ± 4 mM between scan II and III and 4 ± 3 between scan I and III in GM.

On the TSC_{VH}-map, mean absolute TSC was 43 ± 5 mM, 45 ± 5 mM, and 46 ± 5 mM in WM, and 50 ± 6 mM, 51 ± 7 mM, and 53 ± 7 mM in GM, on the TSC_{VH}-map. Mean absolute TSC differences between the three scans were 3 ± 2 mM between scan I and II and between II and III, and 3 ± 3 mM between scan I and II in WM, and they were 4 ± 3 mM between all three scans in GM.

All Δ, within both tissue types and within both TSC-maps, were within the sd of the respective tissue. The TSC_{VH}-map showed substantially lower values than the

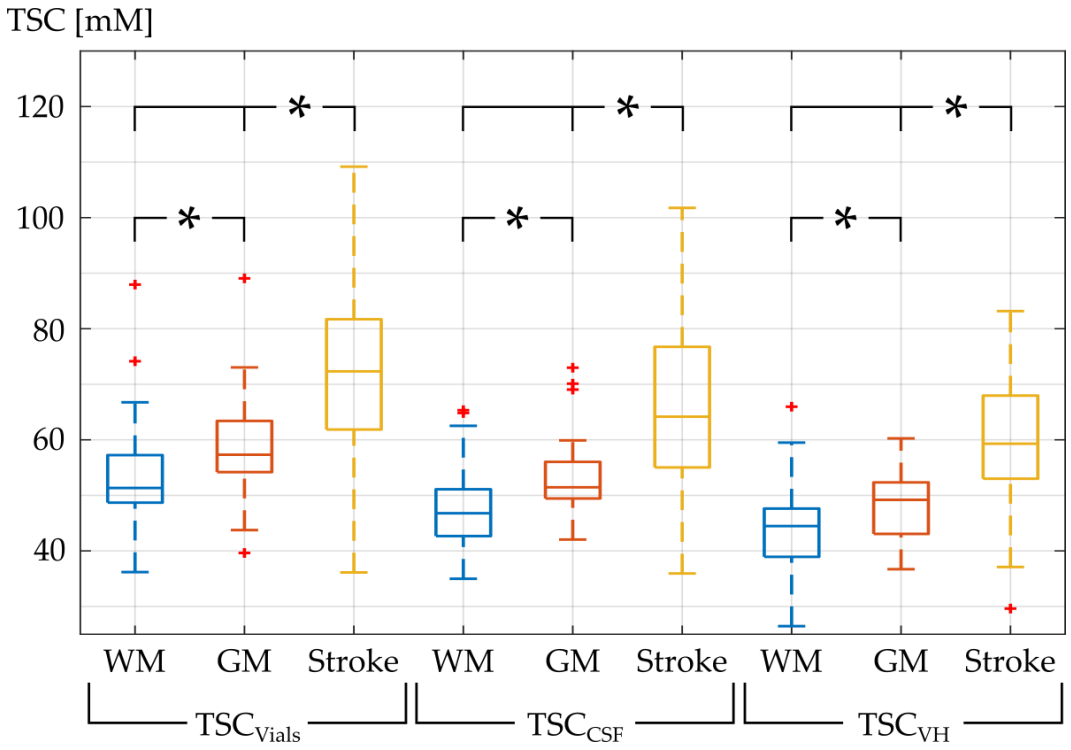

Figure 4.7: Boxplots of the mean absolute tissue sodium concentration (TSC) in white matter (WM, blue), grey matter (GM, red), and in the stroke region (Stroke, yellow) on the three TSC-maps: TSC$_{Vials}$, TSC$_{CSF}$, and TSC$_{VH}$. The middle line in the box depicts the median value and the blue box' top and bottom edges represent the 25th and 75th percentiles of the data, respectively. The whiskers extend to the most extreme data points, not considering outliers, which are depicted as red $+$. Statistically significant differences are indicated with a $*$.

TSC$_{CSF}$-map.

Mean absolute TSC in WM and GM on TSC$_{CSF}$, and on TSC$_{VH}$ at all three measurement points, as well as mean absolute TSC differences (Δ) between the three measurement points are listed in Table 4.3.

Figure 4.8 shows two transverse slices of the ^{23}Na MR image from scan I. The reference regions within CSF and VH are encircled in magenta (CSF) and red (VH).

Table 4.3: Mean absolute tissue sodium concentration (TSC) within white matter (WM) and grey matter (GM) in one healthy control at three measurement points, including the mean voxel-wise differences Δ between the three measurements within both tissue types. TSC quantification based on SI within cerebrospinal fluid and vitreous humor.

		TSC [mM]	
Tissue	Scan(s)	TSC_{CSF}	TSC_{VH}
WM	I	56 ± 6	43 ± 5
	II	58 ± 6	45 ± 5
	III	57 ± 7	46 ± 5
	Δ (I-II)	4 ± 3	3 ± 2
	Δ (II-III)	4 ± 3	3 ± 3
	Δ (I-III)	4 ± 3	3 ± 2
GM	I	65 ± 8	50 ± 6
	II	65 ± 9	51 ± 7
	III	66 ± 9	53 ± 7
	Δ (I-II)	5 ± 3	4 ± 3
	Δ (II-III)	5 ± 4	4 ± 3
	Δ (I-III)	4 ± 3	4 ± 3

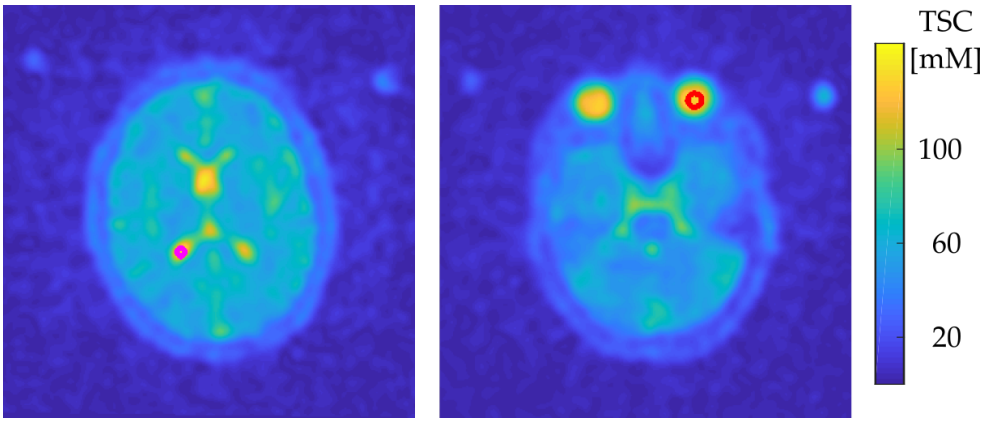

Figure 4.8: ^{23}Na MR image of one healthy control (male, 24 years old) from scan I with two transverse slices. The reference regions (for the quantification of the tissue sodium concentration) within cerebrospinal fluid (magenta) and vitreous humor (red) are encircled.

4.2 DATA ACQUISITION TIME REDUCTION BY APPLICATION OF CNN

The results presented in this section were partially (subsection 4.2.2 and subsection 4.2.3) published in [Adl+21a].

CNNs were implemented, trained and tested with the purpose to perspectively shorten the measurement time of ^{23}Na MRI.

4.2.1 *Verification of artificial under-sampling*

The ^{23}Na MR image of one HC showed an SNR of 25.51 in the fully sampled image FI. The under-sampled ^{23}Na MR images – that were acquired with a reduced measurement time by $R = 2, 4, 5, 10$ – showed an SNR of 15.27, 11.33, 10.09, 7.29, respectively. The artificially under-sampled ^{23}Na MR image showed an SNR of 16.28, 10.60, 9.57, 7.00. SNR of the artificially under-sampled data and the real under-sampled data were not significantly different ($p = 0.79$). They are listed in Table 4.4. These results justified the artificial under-sampling as a simulation of data with reduced measurement time. Figure 4.9 shows one representative transverse slice of the ^{23}Na MR images with each under-sampling factor of the real under-sampled images and of the artificially under-sampled images. The figure shows the decreasing image quality with increasing R and the similarity between the real under-sampled ^{23}Na MR images and the artificially under-sampled ones.

Table 4.4: SNR of under-sampled ^{23}Na MR images with the under-sampling factor $R = 2, 4, 5$, and 10.

	SNR	
Under-sampling Factor	Real Under-sampling	Artificial Under-sampling
1	25.51	
2	15.27	16.28
4	11.33	10.60
5	10.09	9.57
10	7.29	7.00

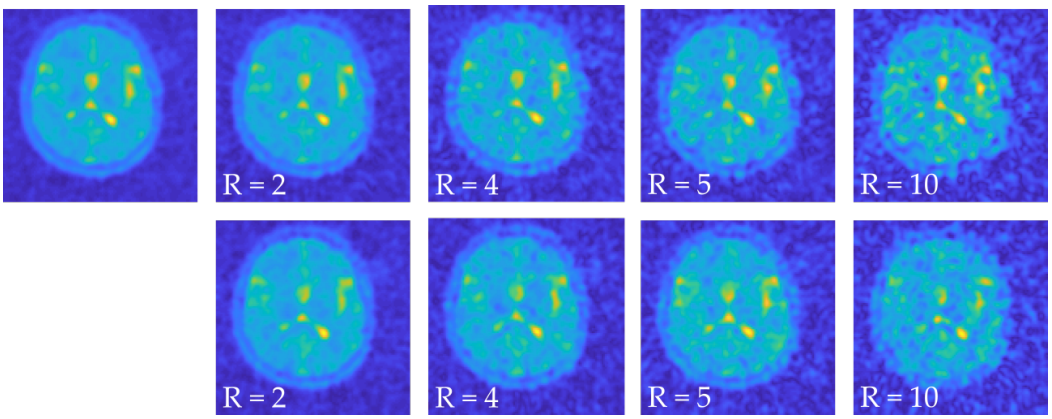

Figure 4.9: ^{23}Na MR image of one HC (male, 28 years old) with different artificial and real under-sampling factors. The top row shows the acquired images with the respective under-sampling factors. The bottom row shows the artificially under-sampled ^{23}Na MR images, generated from the fully-sample image.

4.2.2 *Evaluation of SNR and SSIM*

All CNNs increase the image's SNR. The U-Net-based networks were also able to improve the SSIM to FI.

Mean SNR of FI was 21.72 ± 2.75, and mean SNR of RI ($R = 4$) was 10.16 ± 0.96, which is less than half of FI's SNR and significantly lower with $p < 0.001$. Table 4.5 lists SNR and SSIM to FI of FI, RI, and of CI from networks where improvement of SSIM was significant. In the appendix, Table B.1 lists the respective results of all evaluated CNN output images. SNR and SSIM are given as mean and sd values across all eight test datasets. The network training took between 1.5 and 4.5 hours for every CNN configuration. After the networks were trained, the additional CNN post-processing took approximately 20 seconds for the full dataset of one patient, which is in addition to the time of the traditional image reconstruction.

L1 AND L2 Considering only the CNNs with loss functions L1 and L2, the SNR of the U-Net-based architectures was between 35.24 ± 7.08 and 59.12 ± 10.99, with a mean of 43.99. For ResNet-based architectures, SNR was between 15.48 ± 2.23 and 69.88 ± 12.11, with a mean of 35.31, which was significantly lower with $p < 0.001$.

The mean SSIM between RI and FI was 0.87 ± 0.03, whereas it was between 0.69 ± 0.05 (CNN 8 L1) and 0.90 ± 0.03 (CNN 1 L2, CNN 2 L2) for CI. Improvement in SSIM was only observed for CNNs with U-Net architectures. The network configurations with the number of filters 'Big' (independent of batch normalization) and with the number of filters 'Small' without batch normalization improved the SSIM. Improvement was significant with $p < 0.05$ for CNN 1 with L1 and L2, CNN 2 with L2, and CNN 3 with L1 and L2, but not for CNN 2 with L1 ($p = 0.0946$). Therefore, CNN 1 to 3 were further evaluated and tested with the additional GDL loss function. The other network configurations deteriorated the structural similarity to FI. CNNs with ResNet-based architectures caused a loss of accuracy in anatomical structures, and checkerboard artifacts were introduced.

Figure 4.10 shows one transverse slice for each test dataset in the form of FI, RI, and CI from CNN 2 with L1, L2, L_A, and L_B (each $\lambda = 0.5$) and from CNN 6 with L1, and L2. The figure shows the results of the CNN post-processing for the different network architecture and parameter combinations with loss functions. The checkerboard artifacts, introduced by CNN 6, can be identified.

GRADIENT DIFFERENCE LOSS The additional application of the GDL loss function deteriorated the mean SNR for the U-Net-based networks to 34.73. At the same time, L_{GDL} improved the image similarity to FI when added to L1, but not when added to L2. Maximal SSIM of 0.91 was achieved by adding L_{GDL} to L1 (L_A) in CNN 2 (U-Net, big number of filters, batch normalization) and CNN 3 (U-Net, small number of filters, no batch normalization). The improvements compared to SSIM from RI were significant ($p < 0.01$).

4.2.3 *Evaluation of TSC quantification accuracy*

TSC quantification of the ^{23}Na MR images showed that additional CNN post-processing after conventional reconstruction was able to decrease the TSC error (ΔTSC) in CSF, GM, and WM. Table 4.6 lists the absolute TSC error for RI and CI

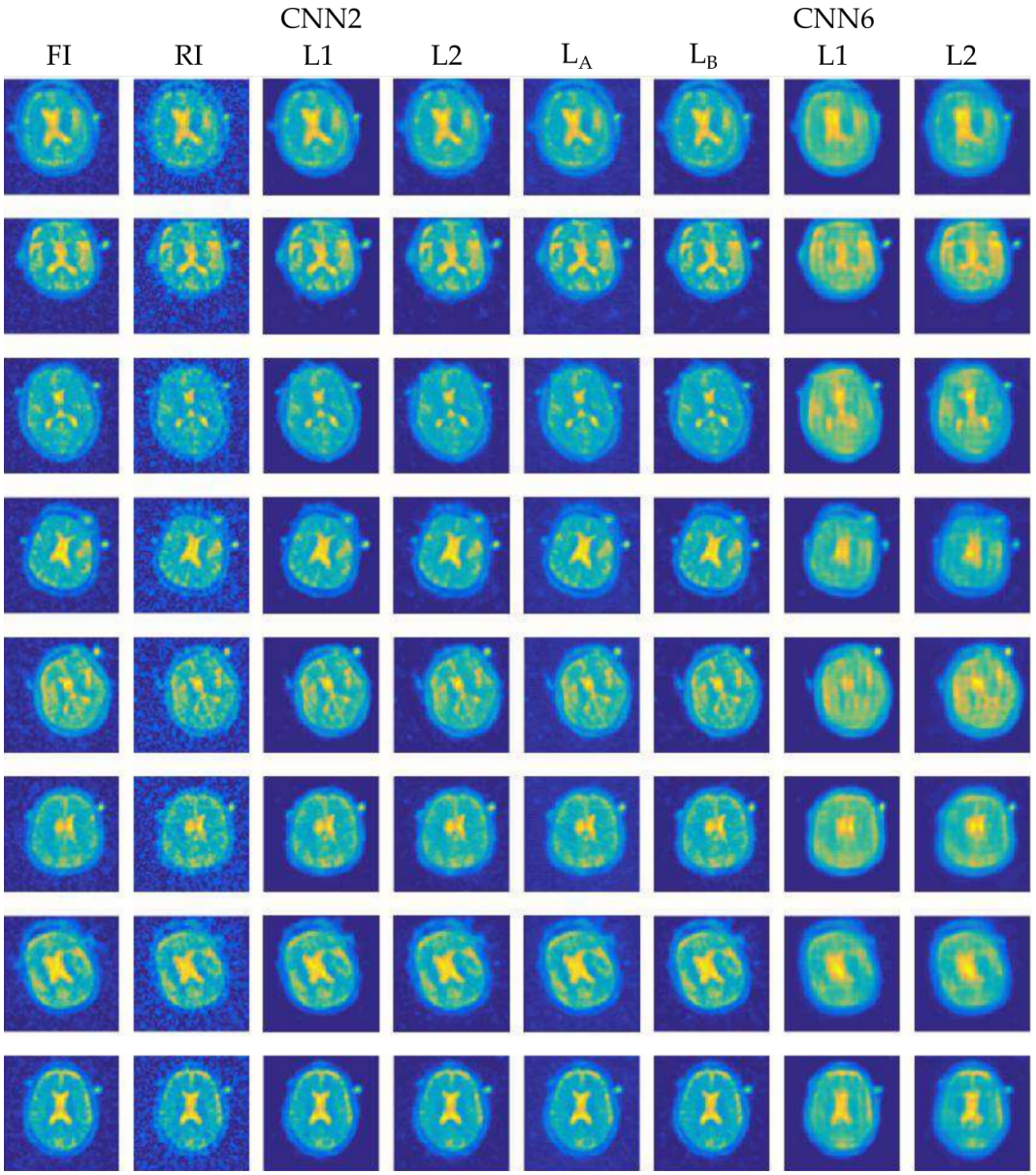

Figure 4.10: The figure shows one representative transverse slice of one ^{23}Na MR image per test dataset in the versions of the fully-sampled original image (FI), the artificially under-sampled image (RI), and the image after CNN post-processing (CI) of the networks CNN 2 (with L1, L2, L_A, and L_B) and CNN 6 (with L1 and L2). This figure is reproduced with permission from [Adl+21a].

of the CNNs, which improved TSC quantification accuracy compared to RI. In the appendix, Table B.2 lists the respective results for all evaluated CNNs.

In WM, ΔTSC was reduced by all CNNs except for CNN 1 with L1. In GM, the ΔTSC was also decreased by all CNNs except for CNN 1 with L1 (deterioration in GM and WM) and CNN 3 with L1 (improvement in WM only). ΔTSC in CSF was decreased with L2 by CNN 1, 2 and 3, but was increased by all CNNs with L1. The additional L_{GDL} decreased the ΔTSC in CSF when being applied to CNN 2 with L1 and L2 and when being applied to CNN 3 with L2. Overall, the addition of L_{GDL} to L1 or L2 had no significant impact on TSC error reduction.

Reduction of ΔTSC in WM was significant with CNN 3 with L2 ($p = 0.0058$), and with L_B ($p = 0.0441$). In GM, the improvement was significant with CNN 3 with L2

Table 4.5: List of the generated signal-to-noise ratio (SNR, mean ± sd) and structural similarity index (SSIM, mean ± sd) of the fully reconstructed image FI, the artificially under-sampled image RI and the image after CNN-post-processing CI. Significant ($p < 0.05$) improvements compared to RI are marked with *. The table only considers CNNs where improvement of SSIM was significant. The CNNs generating the best results of SSIM are printed in bold.

					SNR ($\mu \pm \sigma$)	SSIM ($\mu \pm \sigma$)
FI					21.72 ± 2.75	1.00
RI					10.16 ± 0.96	0.87 ± 0.03
CNN	Architecture	Filters	Batch Norm.	Loss		
1	U-Net	Big	False	L1	$35.24^* \pm 07.08$	$0.89^* \pm 0.03$
	U-Net	Big	False	L2	$36.67^* \pm 07.42$	$0.90^* \pm 0.03$
2	U-Net	Big	True	L2	$35.33^* \pm 05.54$	$0.90^* \pm 0.03$
3	U-Net	Small	False	L1	$45.02^* \pm 07.75$	$0.89^* \pm 0.03$
	U-Net	Small	False	L2	$41.31^* \pm 07.91$	$0.89^* \pm 0.03$
1	U-Net	Big	False	L_A	$32.19^* \pm 05.98$	$0.90^* \pm 0.03$
	U-Net	Big	False	L_B	$41.32^* \pm 07.60$	$0.89^* \pm 0.03$
2	**U-Net**	**Big**	**True**	L_A	$34.10^* \pm 04.72$	$0.91^* \pm 0.02$
	U-Net	Big	True	L_B	$36.64^* \pm 06.33$	$0.89^* \pm 0.03$
3	**U-Net**	**Small**	**False**	L_A	$23.55^* \pm 03.13$	$0.91^* \pm 0.02$
	U-Net	Small	False	L_B	$40.55^* \pm 06.74$	$0.89^* \pm 0.03$

($p = 0.0045$) and CNN 2 with L1 ($p = 0.0336$). The improvements in the CSF were non-significant with $p > 0.05$ for all CNNs.

Thus, CNN 3 (U-Net, small number of filters, no batch normalization) with L2 was the only network that decreased TSC quantification error significantly for both tissue types (WM and GM). It also decreased the TSC quantification error in CSF from a mean of 4.21 mM to a mean of 3.94 mM, although the improvement was non-significant with $p = 0.0782$. The reduction of ΔTSC relative to the ΔTSC in RI was 15.27% in WM, 14.89% in GM and 6.41% in CSF. CNN 3 with L2 plus L_{GDL} (L_B with $\lambda = 0.5$) also decreased ΔTSC in WM, GM and CSF. Here, error reduction was significant in WM (9.51%, $p = 0.0441$) and non-significant in GM (8.44%, $p = 0.0882$) and in CSF (0.05%, $p = 0.9030$). Its' training took 1 hour and 55 minutes.

4.2.4 *Evaluation of different under-sampling factors*

Only the best-performing CNN (CNN 3) was further tested for the optimization of the under-sampling factor R, which was previously set to $R = 4$ and was further tested with $R = 2, 3, 4, 5, 6, 8, 10$. The network architecture used the U-Net design, no batch-normalization and the number of filters 'Small'.

Table 4.7 lists FI, RI and CI with the best-performing loss function for each R (according to the SSIM) with their SNR and SSIM to FI for all evaluated R. In the appendix, Table B.3 lists the respective results of all evaluated loss functions for all evaluated R.

Table 4.6: Mean absolute tissue sodium concentration difference to FI (ΔTSC) of RI and CI from CNNs which improved TSC quantification in WM, GM, and CSF. Networks performing significantly ($p < 0.05$) better are marked with *. The network where improvements were significant in WM and GM is printed in bold.

					ΔTSC [mM]		
					WM	GM	CSF
RI					4.52	4.50	4.21
CNN	Architecture	Filters	Batch Norm.	Loss			
1	U-Net	Big	False	L2	4.09	4.08	4.05
2	U-Net	Big	True	L2	4.48	4.11	4.00
3	**U-Net**	**Small**	**False**	L2	3.83*	3.83*	3.94
2	U-Net	Big	True	L_A	3.98	3.90*	3.88
	U-Net	Big	True	L_B	4.10	3.97	3.82
3	U-Net	Small	False	L_B	4.09*	4.12	4.19

Table 4.7: List of FI and RI from all evaluated under-sampling factors R with CI from the single best-performing loss function (according to SSIM) with their generated signal to noise ratio (SNR, mean ± sd) and structural similarity index (SSIM, mean ± sd) to FI. Networks performing significantly ($p < 0.05$) better are marked with *.

		SNR	SSIM
	($\mu \pm \sigma$)	($\mu \pm \sigma$)	
FI		24.60 ± 1.81	1

Under-sampling factor	Loss	λ		
Half	RI		18.32 ± 1.53	0.9886 ± 0.0045
	L2		38.28 ± 2.57	$0.9900^* \pm 0.0042$
Third	RI		14.31 ± 1.20	0.9761 ± 0.0085
	L_B	0.5	41.89 ± 3.39	$0.9810^* \pm 0.0073$
Quarter	RI		11.83 ± 1.19	0.9630 ± 0.0135
	L_B	0.5	36.32 ± 4.48	$0.9740^* \pm 0.0095$
Fifth	RI		10.43 ± 0.96	0.9531 ± 0.0171
	L_B	0.2	58.71 ± 7.94	$0.9663^* \pm 0.0138$
Sixth	RI		9.36 ± 0.90	0.9437 ± 0.0188
	L_B	0.5	54.36 ± 7.66	$0.9620^* \pm 0.0143$
Eighth	RI		7.96 ± 0.79	0.9235 ± 0.0222
	L2		53.35 ± 7.14	$0.9496^* \pm 0.0190$
Tenth	RI		7.21 ± 0.69	$0.9169 \pm 0,0250$
	L_B	0.5	52.29 ± 9.61	$0.9446^* \pm 0.0182$

The Pearson correlation test showed a negative correlation of $r = -0.91$ between the under-sampling factor R and SNR of RI, which was significant with $p = 0.0041$.

The Pearson correlation test showed no significant correlation between the under-sampling factor R and SNR of CI with L2, which was $r = 0.48$ with $p = 0.27$, whereas a significant positive correlation was shown for R and SNR of CI with L_B with $\lambda = 0.5$ and $\lambda = 0.2$ and the respective correlation factors were $r = 0.76$, and $r = 0.93$ with $p = 0.0446$ and $p = 0.0025$.

Figure 4.11 shows one representative transverse slice of one patient with $R = 2, 4, 10$ as RI and as CI with loss L2. The figure shows the image noise to increase with an increasing R, which is present for RI but not for CI.

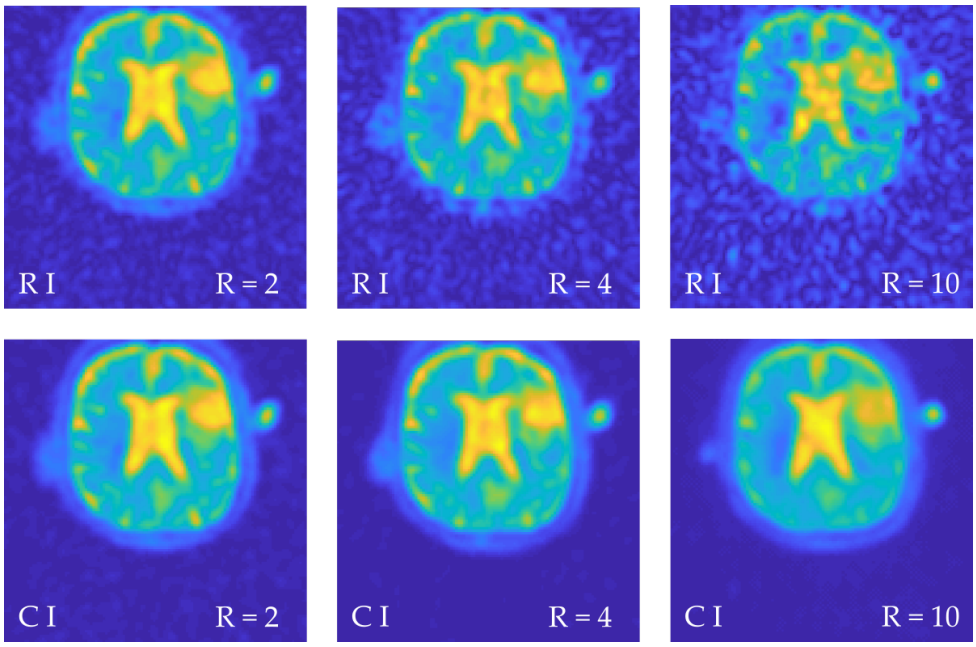

Figure 4.11: One representative, transverse slice of one patient with under-sampling factor $R = 2, 4, 10$ as RI and as the network generated CI with loss function L2.

The Pearson correlation test showed a negative correlation of $r = -0.99$ between the under-sampling factor R and SSIM of RI to FI, which was significant with $p = 0.0001$.

The Pearson correlation test also showed a negative correlation between the under-sampling factor R and SSIM of CI to FI with L2 and L_B with $\lambda = 0.5$ and $\lambda = 0.2$ with the respective correlation factors of $r = -0.98$, $r = 0.98$, and $r > 0.99$, which were all significant with $p = 0.0001$, $p = 0.0002$, and $p < 0.0001$.

Considering the SSIM, loss function L2 showed the highest SSIM (best improvement of the SSIM) for $R = 2$ (error decreased by 12%) and $R = 8$ (24%), L_B with $\lambda = 0.5$ showed the highest SSIM for $R = 3$ (21%), $R = 4$ (30%), $R = 6$ (33%), and $R = 10$ (33%), and L_B with $\lambda = 0.2$ showed the highest SSIM for $R = 5$ (28%).

4.2.4.1 *Application on real under-sampled data*

The acquired ^{23}Na MRI data with $R = 4$ from one HC was post-processed with CNN 3 (U-Net architecture, no batch-normalization, and small number of filters) with loss function L_B with $\lambda = 0.5$, which had generated the best results regarding SSIM for the respective under-sampling factor.

SNR of FI was 18.95, and SNR of the real under-sampled MR image (rRI) was 11.32, whereas SNR of rCI was higher with 27.25. SSIM to FI was 0.9084 for rRI and 0.9240

for rCI (inaccuracy decreased by 17%). One representative, transverse slice of FI, rRI and rCI is depicted in Figure 4.12.

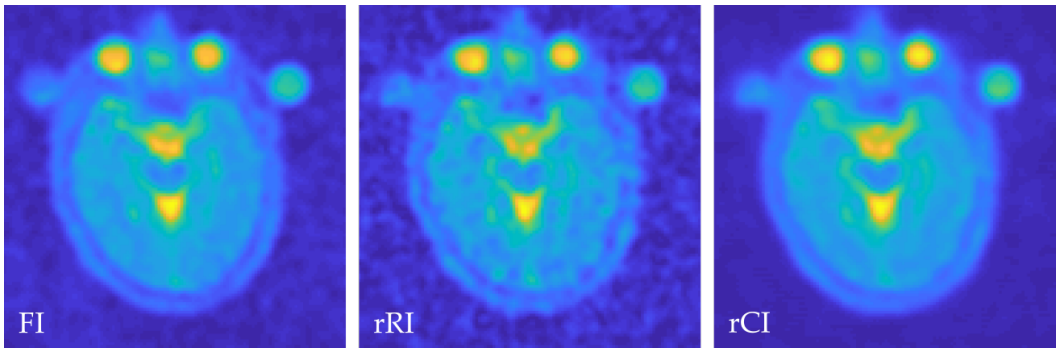

Figure 4.12: One transverse slice of the ^{23}Na MR images of one HC (male, 26 years old) as fully sampled image (FI), under-sampled image after conventional reconstruction only (rRI), and under-sampled image after CNN post-processing of the under-sampled image (rCI).

Mean ΔTSC of rRI was 4.82 mM in the whole brain, which consisted of a mean ΔTSC = 4.78 mM in WM, ΔTSC = 5.00 mM in GM, and ΔTSC = 4.70 mM in CSF. Mean ΔTSC of rCI was 4.09 mM in the whole brain, which consisted of a mean ΔTSC = 3.79 mM in WM, ΔTSC = 4.06 mM in GM, and ΔTSC = 6.40 mM in CSF. The results are listed in Table 4.8.

Table 4.8: Signal-to-noise ratio, structural similarity index (SSIM), and absolute TSC quantification error ΔTSC of the fully sampled ^{23}Na MR image (FI), the under-sampled image after conventional reconstruction only (rRI), and the under-sampled image after CNN post-processing (rCI).

	FI	rRI	rCI
SNR	18.95	11.32	27.25
SSIM		0.9084	0.9240
ΔTSC			
WM		4.78	3.79
GM		5.00	4.06
CSF		4.70	6.40

4.3 PROSPECTIVE IN-VIVO STUDIES

4.3.1 *Evolution of TSC after stereotactic radiosurgery*

The data from the here presented study was partially published in [Moh+21a]. However, that publication was limited to the evaluation of TSC within BM and their edemas and it did not consider ROIs such as the isodose areas, which were evaluated within this thesis. Furthermore, additional patients were included in this thesis.

The data of 12 patients with a total of 14 BM was evaluated. The inclusion criteria involved a sufficient size of the BM, which was required to be > 64 mm^3.

Out of those 12 patients, five were men, and seven were women who had a mean age of 63 ± 14 years. Nine patients (11 BM) underwent all three scheduled MRI measurements, one patient (1 BM) only underwent the first MRI measurement successfully, and two patients (2 BM) only underwent the first two MRI measurements.

Out of the included fourteen BM, two showed local tumor progression (non-responders), which was defined as a progressing lesion with overlap with the planning target volume at some point during follow-up examination. The remaining twelve patients (responders) did not show a local progression of the BM at any follow-up exam.

Figure 4.13 shows one representative transverse slice of the MPRAGE and of the three ^{23}Na MR images of one patient (responder) with the GTV, and the isodose areas regions being visualized within the MPRAGE.

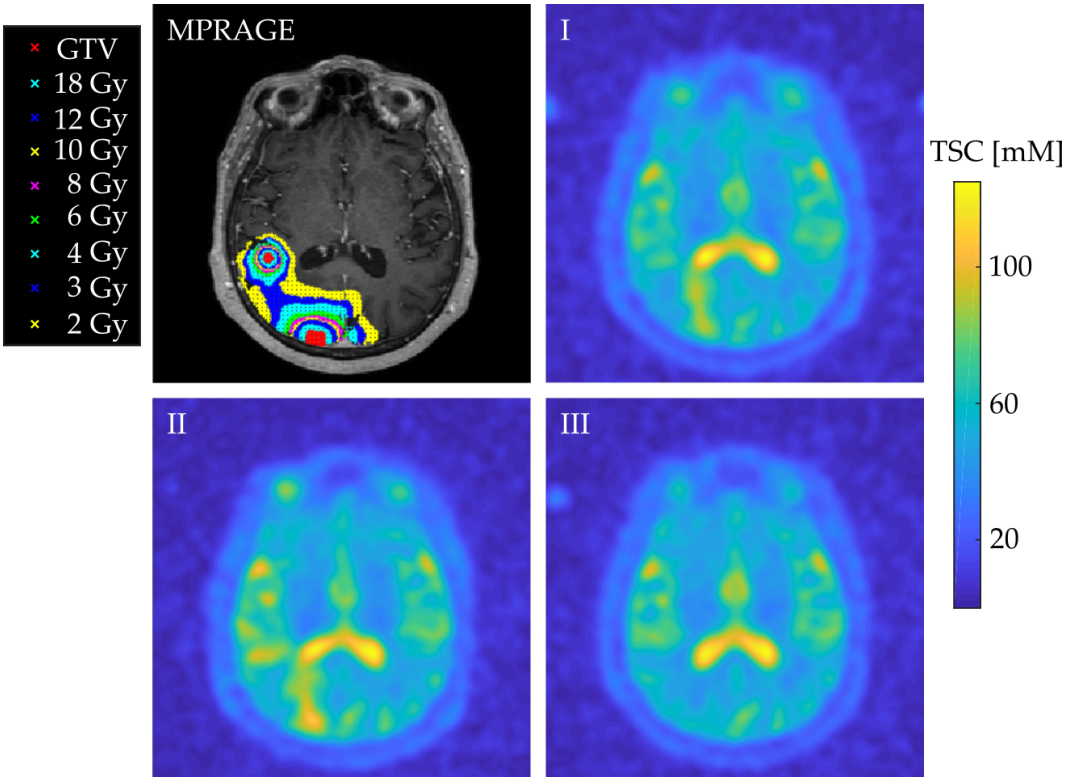

Figure 4.13: One representative transverse slice of one patient's (responder) MPRAGE and the co-registered ^{23}Na of all three measurements: I – t = SRS − 2days, II – t = SRS + 5days, and III – t = SRS + 40days. The isodose areas and the GTV are visualized within the MPRAGE as color-coded regions.

The one-sample Kolmogorov-Smirnov test showed that mean absolute TSC in GTV ($p = 0.90$, $p = 0.92$, $p = 1.0$), HR ($p = 0.70$, $p = 0.93$, $p = 0.65$), and all evaluated isodose areas (all: $p \geqslant 0.3$) followed a normal distribution at all three time points. Therefore, the student t-test was applicable for mean absolute TSC within all regions.

The mean absolute TSC within all GTV, HR, and the isodose areas of D = 2, 3, 4, 6, 8, 10, 12, 18 at all three measurements (I, II, and III) are listed in Table 4.9.

At baseline (MRI scan at time point I, t = SRS − 2days), mean absolute TSC in all 14 GTV was 61 ± 10 mM. MRI scan at time point II (t = SRS + 5days) showed a mean absolute TSC of 68 ± 9 mM in the remaining 13 GTV. MRI scan at time point

Table 4.9: Mean absolute tissue sodium concentration (TSC) within all gross tumor volumes (GTV), healthy-appearing brain matter (HR), and isodose areas at all three measurements.

	TSC [mM]		
Region	Scan I	Scan II	Scan III
	$t = SRS - 2days$	$t = SRS + 5days$	$t = SRS + 40days$
GTV	61 ± 10	68 ± 9	58 ± 9
HR	45 ± 5	45 ± 5	44 ± 5
Isodose Area			
18 Gy	60 ± 10	65 ± 10	54 ± 7
12 Gy	58 ± 10	62 ± 10	52 ± 6
10 Gy	57 ± 9	61 ± 10	51 ± 6
8 Gy	58 ± 9	61 ± 10	51 ± 6
6 Gy	57 ± 8	59 ± 10	51 ± 5
4 Gy	55 ± 7	57 ± 9	51 ± 5
3 Gy	54 ± 6	56 ± 8	51 ± 5
2 Gy	53 ± 5	54 ± 6	51 ± 5

III ($t = SRS + 40days$) showed a mean absolute TSC of 58 ± 9 mM in the evaluated 11 GTV.

Mean absolute TSC in GTV was significantly lower at baseline compared to scan II ($p = 0.0076$) and it was higher compared to scan III, but differences were not significant ($p = 0.27$). Mean absolute TSC in GTV was significantly higher at scan II compared to scan III ($p = 0.0214$).

At baseline, mean absolute TSC in all HR was 45 ± 5 mM. At scan II, mean absolute TSC in HR was 45 ± 5 mM. At scan III, mean absolute TSC in HR was 44 ± 5 mM. Mean absolute TSC in HR was not significantly different at baseline, scan II or scan III ($p = 0.81$, $p = 0.74$, $p = 0.99$).

Mean TSC in HR was significantly lower than mean TSC in GTV at all three time points (all $p < 0.0001$).

Figure 4.14 depicts the mean absolute TSC in GTV and HR at all three measurements as boxplots for all patients, including responders and non-responders. The figure shows the significantly higher TSC within GTV compared to HR and it also shows how TSC within GTV evolves whereas it remains relatively constant within HR.

The two progressing BM showed, within the GTV, a mean TSC of 50 ± 3 mM (non-responder 1) and 48 ± 2 mM (non-responder 2) at baseline, which evolved to 53 ± 5 mM and 53 ± 3 mM at scan II, and to 71 ± 5 mM and 50 ± 3 mM at scan III. The TSC evolution within both progressive GTV is depicted in Figure 4.15 separately. The figure shows a substantially different TSC evolution of non-responder 1 (left) compared to the mean TSC evolution with all GTV.

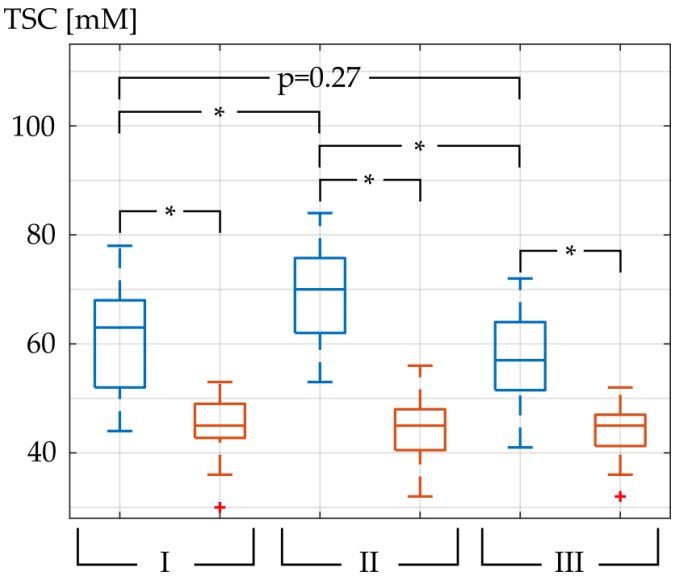

Figure 4.14: Boxplot of the mean absolute tissue sodium concentration (TSC) within all gross tumor volumes (blue), and all healthy-appearing brain matter regions (red) at the three measurements: I – t = SRS − 2days, II – t = SRS + 5days, and III – t = SRS + 40days. The middle line in the box depicts the median value and the box' top and bottom edges represent the 25th and 75th percentiles of the data, respectively. The whiskers extend to the most extreme data points, not considering outliers, which are depicted by +. Statistically significant differences are indicated with a ∗.

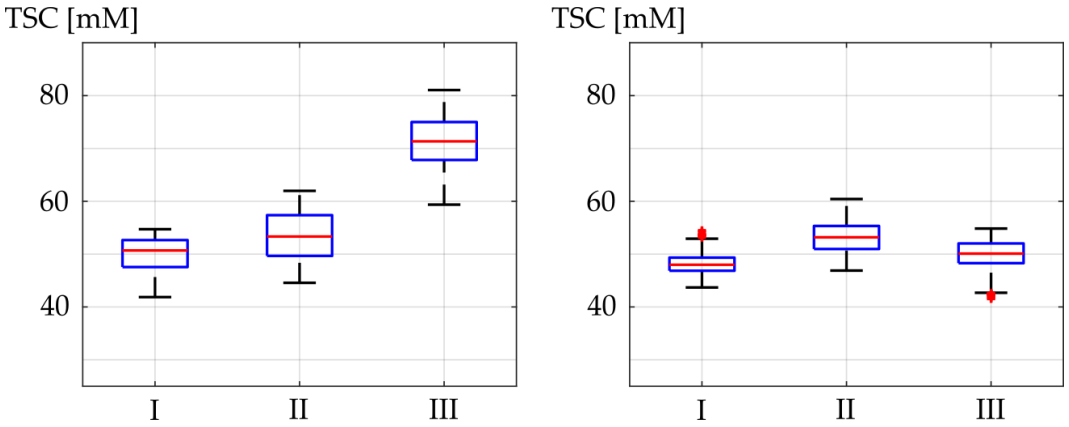

Figure 4.15: Left: Non-responder 1. Right: Non-responder 2. Boxplots of the absolute tissue sodium concentration (TSC) within the gross tumor volumes of both progressive brain metastases at all three measurements: I – t = SRS − 2days, II – t = SRS + 5days, and III – t = SRS + 40days. The middle line in the box depicts the median value and the box' top and bottom edges represent the 25th and 75th percentiles of the data, respectively. The whiskers extend to the most extreme data points, not considering outliers, which are depicted by +.

Considering all patients, the mean absolute TSC within isodose areas of D = 2, 3, 4, 6, 8, 10, 12, 18 was lower at baseline compared to scan II for all isodose areas and differences were significant for isodose areas D = 18, 12, 10, and 8 ($p = 0.0132$, $p = 0.0202$, $p = 0.0352$, and $p = 0.0364$) but not for isodose areas D = 6, 4, 3, and 2 ($p = 0.05$, $p = 0.07$, $p = 0.18$, and $p = 0.27$).

Comparing mean absolute TSC within the isodose areas between baseline and scan III; it was higher at baseline within all isodose areas and differences were significant for D = 18, 12, 10, 8, 6, 4, 3 Gy (p = 0.0257, p = 0.0180 p = 0.0134, p = 0.0092, p = 0.0081, p = 0.0156, and p = 0.0032) but not for D = 2 Gy (p = 0.06).

Comparing mean absolute TSC within the isodose areas between scans II and III; it was higher at II for all isodose areas and differences were significant for D = 18, 12, 10, 8, 6, 4, 3 Gy (p = 0.0079, p = 0.0068, p = 0.0062, p = 0.0058, p = 0.0089, p = 0.0140, and p = 0.0161) but not for D = 2 Gy (p = 0.13).

Figure 4.16 depicts the mean absolute TSC of all patients within the isodose areas D = 2, D = 10, and D = 18 Gy at all three measurements as boxplots. The figures illustrates how TSC within the higher isodose areas was significantly different between the the measurements, whereas TSC within the lowest observed isodose area did not change significantly.

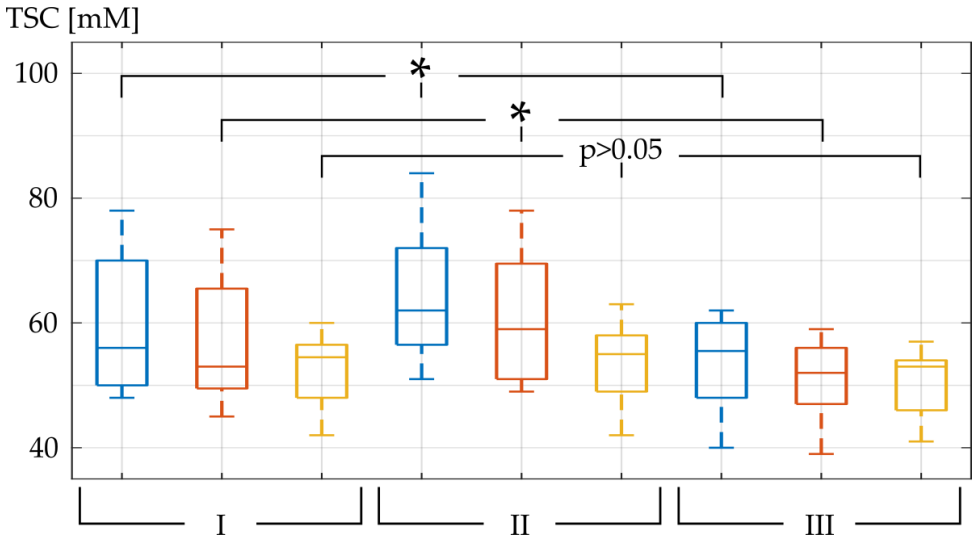

Figure 4.16: Boxplot of the mean absolute tissue sodium concentration (TSC) within the isodose areas D = 18 (blue), D = 10 (red), and D = 2 Gy (yellow) of all patients at all three measurements: I – t = SRS − 2days, II – t = SRS + 5days, and III – t = SRS + 40days. The middle line in the box depicts the median value and the box' top and bottom edges represent the 25th and 75th percentiles of the data, respectively. The whiskers extend to the most extreme data points. Statistically significant differences are indicated with a ∗.

Considering all patients, mean absolute TSC within isodose area D = 18 Gy was significantly higher than mean absolute TSC within isodose area D = 12 Gy at beaseline (p = 0.0076), II (p = 0.0006), and III (p = 0.0294).

Mean absolute TSC within isodose area D = 12 Gy was higher than mean absolute TSC within isodose area D = 10 Gy, which was significant at beaseline (p = 0.0014), and II (p = 0.0004), but not at III (p = 0.06).

Mean absolute TSC within isodose area D = 10 Gy was similar to mean absolute TSC within isodose area D = 8 Gy with no significant differences between any time points (p = 0.73, p = 0.86, and p = 0.07).

Mean absolute TSC within isodose area D = 8 Gy was significantly higher than mean absolute TSC within isodose area D = 6 Gy at baseline and at II (p = 0.0451 and p = 0.0148) but not at III (p = 0.41). The same was applicable for isodose area

$D = 6$ Gy compared to $D = 4$ Gy ($p = 0.0250$, $p = 0.0097$, and $p = 0.81$), and for $D = 4$ Gy compared to $D = 3$ Gy ($p = 0.0122$, $p = 0.0027$, and $p = 0.91$).

Differences between isodode areas $D = 3$ Gy and $D = 2$ Gy were only significant at II ($p = 0.0308$) but not at baseline or III ($p = 0.0642$ and $p = 0.57$).

The Pearson correlation test showed a significant, positive correlation between the radiation dose D and the mean absolute TSC within the corresponding isodose area at all three scans. Correlation between D and mean absolute TSC was $r = 0.92$ ($p = 0.0011$) at baseline (I), $r = 0.96$ ($p = 0.0001$) five days after SRS (II), and $r = 0.86$ ($p = 0.0061$) 40 days after SRS (III).

Mean absolute TSC within the isodose areas of all patients who did not show progression (reponders) and their ratio between each other at all three scans are depicted in Figure 4.17. The figure shows a decreasing TSC with a decreasing isodose area (increasing distance to the tumorous tissue) and overall a higher TSC at II and a lower TSC at III, compared to baseline (I).

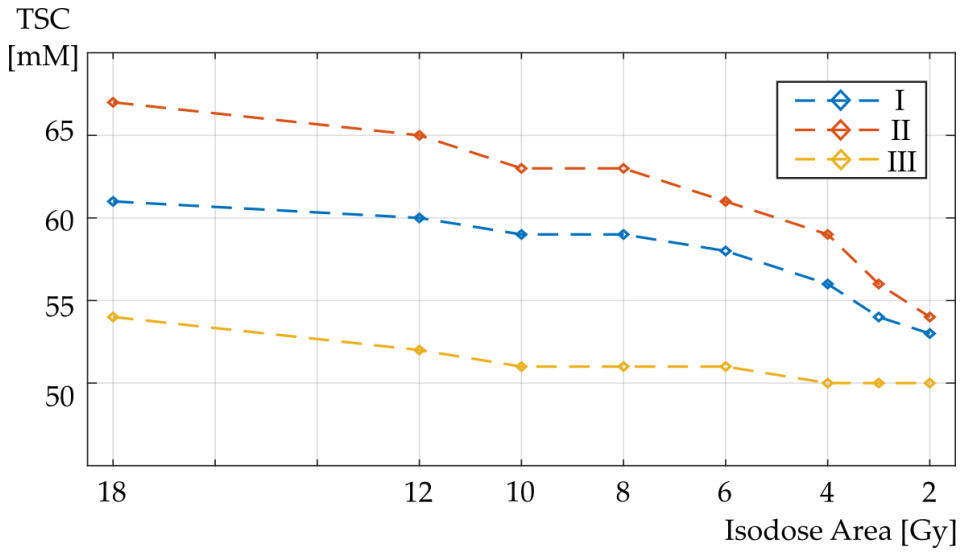

Figure 4.17: Plot of the mean absolute tissue sodium concentration (TSC) within the observed isodose areas of all included brain metastases, which did not show progression (responders) at all three measurements: I – t = SRS − 2days (blue), II – t = SRS + 5days (red), and III – t = SRS + 40days (yellow).

Considering only the two progressing BM: At baseline, mean TSC within all isodose areas was between 48 and 50 mM (non-responder 1) and between 51 and 54 mM (non-responder 2). At scan II, it was between 50 and 52 mM and between 48 and 51 mM. At scan III, it increased substantially for non-responder 1 where it was between 51 and 60 mM, with a tendency of higher TSC values within the higher isodose areas. Isodose areas of the other progressing BM (non-responder 2) remained similar and between 48 and 53 mM.

The TSC evolution of the isodose areas of both progressing BM is depicted in Figure 4.18. The figure shows a relatively constant TSC over all isodose areas at scan I and II. An increased TSC is observed within higher isodose areas of one of the BM at scan III.

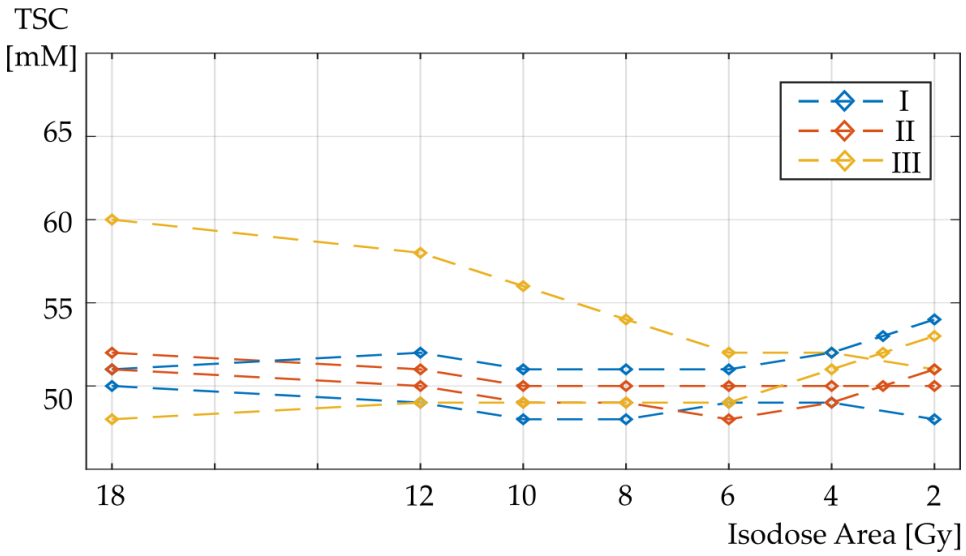

Figure 4.18: Plot of the mean absolute tissue sodium concentration (TSC) within the observed isodose areas of both progressing brain metastases at all three measurements: I – t = SRS − 2days (blue), II – t = SRS + 5days (red), and III – t = SRS + 40days (yellow).

4.3.2 *TSC in the human prostate with a suspected carcinoma*

A total of 37 male patients with a clinically suspected PCa was included in the study. The data of *29* patients was analyzed who had a mean age of 67 ± 8 years. The remaining eight patients were excluded due to failure of data acquisition ($n = 3$), abortion of the measurement due to discomfort of the patient ($n = 2$), or because the patient had a hip implant on one side and the resulting artifacts were too severe for reliable image analysis ($n = 3$). Of those *29* patients, six were rated with a PI-RADS 5 lesion, three with a PI-RADS 4 lesion, and the remaining 20 patients were rated with lower ranking lesions or did not show any. Of those patients who received a prostatectomy, ten patients had a Gleason score of $\geqslant 3+3$. Within those were all six patients with a PI-RADS 5 lesion (two Gleason $3+4$, one Gleason $4+3$, three Gleason $4+5$) and one had a PI-RADS 4 lesion (Gleason $3+3$). It also included two patients who had only a PI-RADS 2 lesion (both Gleason $3+3$), and one of those patients presented a PI-RADS 1 (also Gleason $3+3$).

Segmentation of the lesions was performed for the six patients with a PI-RADS 5 lesion and for the one patient with a PI-RADS 4 lesion. Two patients with PI-RADS 5 lesions had their lesion within the TZ (Gleason $3+4$ and $4+3$) and four patients with PI-RADS 5 and one patient PI-RADS 4 lesion had their lesions within the PZ, with one patient presenting multifocal PCa with two segmentable lesions (PI-RADS 5, Gleason $3+4$).

Absolute TSC quantification was performed for all *29* patients based on SI within the FBV.

The one-sample Kolmogorov-Smirnov test showed that absolute TSC in the WP ($p = 0.17$), the PZ ($p = 0.47$), within the TZ ($p = 0.67$), and within the FBV ($p = 0.87$) followed a normal distribution. Therefore, the student t-test was applicable for TSC within all regions.

Within the WP, all evaluated patients showed a mean absolute TSC between 30 and 52 mM, with a mean of 40 ± 5 mM.

In the PZ, all patients showed a mean absolute TSC between 29 and 56 mM with a mean of 41 ± 6 mM, and in the TZ, all patients showed a mean absolute TSC between 26 and 48 mM with a mean of 38 ± 6 mM.

Mean absolute TSC of all patients was significantly higher in the PZ than in the TZ ($p = 0.0048$), by a mean of 3 ± 15 mM.

Mean absolute TSC in the WP, PZ, and TZ of all evaluated patients are depicted as boxplots in Figure 4.19. The figure shows the significant differences between TSC in PZ and TZ.

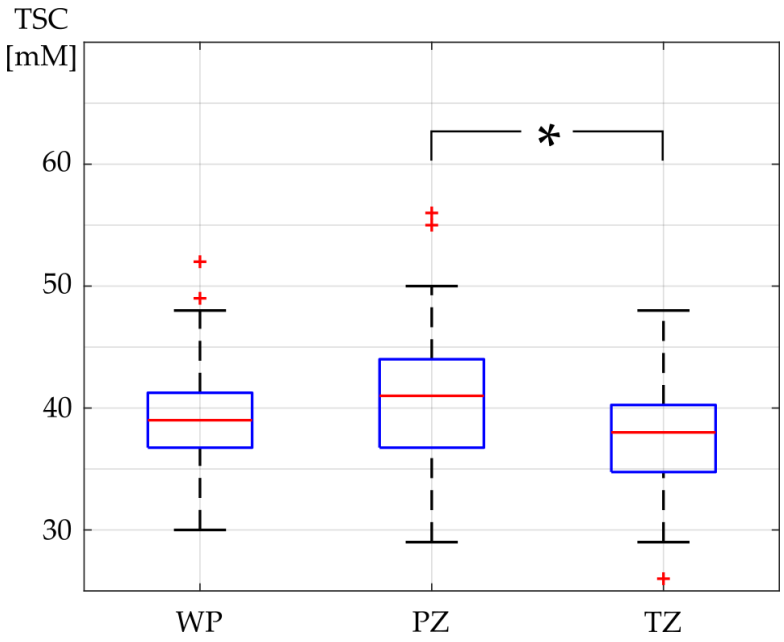

Figure 4.19: Mean absolute tissue sodium concentration (TSC) in the whole prostate (WP), peripheral zone (PZ), and transitional zone (TZ). The red line in the box depicts the median value and the blue box' top and bottom edges represent the 25th and 75th percentiles of the data, respectively. The whiskers extend to the most extreme data points. Statistically significant differences are indicated with a $*$.

Evaluation of the ROIs within the FBV – which served as TSC quantification references and were set to a mean absolute TSC of 81 mM – showed a mean absolute TSC of 80.4 ± 2.0 mM on the left side and a mean absolute TSC of 81.6 ± 2.0 mM on the right side.

Mean sd within the left FBV was 3.0 ± 1.4 mM and mean sd in the right FBV was 4.1 ± 1.6 mM. Considering both FBV, mean sd of TSC within the whole evaluated blood vessel regions was at 4.3 ± 1.3 mM. Mean absolute TSC differences between both sides was 3.5 ± 2.3 mM. There were no significant differences between absolute TSC within the FBV on the left side compared to the mean absolute TSC within the FBV on the right side ($p = 0.16$).

Considering the six segmented lesions in the PZ, they all showed mean absolute TSC values of 24 to 43 mM with a mean of 31 ± 6 mM within the segmented lesion(s).

For every patient ($n = 5$), mean absolute TSC within the lesion(s) was lower than mean absolute TSC within the patient's PZ.

Evaluating the PZ of all patients with an identified lesion (Gleason $\geqslant 3+3$) within the PZ ($n = 6$) and comparing the TSC within their PZ to the TSC within the PZ of all other patients ($n = 23$), the TSC was significantly lower within the PZ of patients, where lesions were identified (37 ± 4 mM compared to 43 ± 6 mM, $p = 0.0331$). Considering only the three patients with a $4+5$ Gleason score, who all presented their lesion within the PZ, TSC within the whole PZ of those patients was lower in PZ than in the TZ for two patients (by 2 mM and by 5 mM). For the third patient, TSC within PZ was higher than in TZ by 1 mM.

The segmented PZ, TZ and lesions within PZ are depicted on one slice of the T2 TSE and on the quantified ^{23}Na MR image of two patients in Figure 4.20.

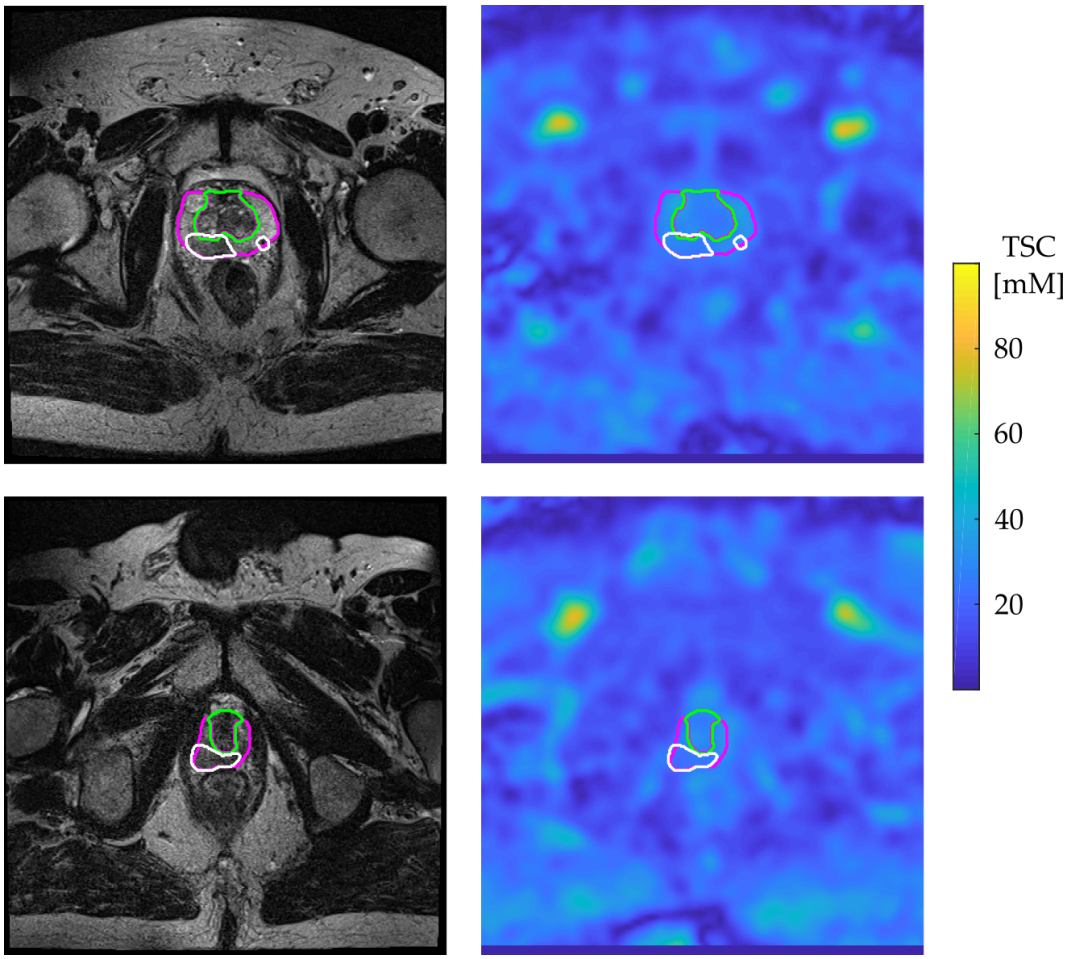

Figure 4.20: One transverse slice of MR images of two patients with one (bottom) or two (top) lesions in the peripheral zone of their prostate. Their T2 TSE is on the left, including the segmentation of the peripheral zone (pink), transitional zone (green) and lesions (white), and their co-registered and quantified ^{23}Na MR image is on the right, including the transferred segmentation masks of the regions of interest.

The two segmented lesions within TZ showed mean TSC values of 37 ± 4 mM and 36 ± 3 mM, which was lower than mean TSC within the healthy TZ for one patient

(mean TSC with TZ was 40 ± 5) but higher than mean TSC within the TZ of the other patient (mean TSC was 31 ± 6 mM).

Evaluating the TZ of all patients with an identified lesion (Gleason $\geqslant 3+3$) within the TZ ($n = 3$) and comparing the TSC within their TZ to the TSC within the TZ of all other patients ($n = 26$), the TSC was lower within the TZ of patients, where lesions were identified (36 ± 4 mM compared to 38 ± 6 mM) but differences were not significant ($p = 0.53$).

Table 4.10 lists the mean absolute TSC values within WP, PZ, TZ and possible lesions of patients with a Gleason lower than $3+3$, patients with a Gleason $\geqslant 3+3$ in the PZ and patients with a Gleason $\geqslant 3+3$ in the TZ.

Table 4.10: Mean absolute tissue sodium concentration (TSC) within the whole prostate (WP), its peripheral -, its transitional zone (PZ, TZ), and within segmented lesions. Values are given for all patients and are separated between patients with no identified lesions with a Gleason score of $\geqslant 3+3$ (No lesions), with identified lesions within PZ (Lesions in PZ) and with identified lesions within TZ (Lesions in TZ).

	TSC [mM]			
Patients	WP	PZ	TZ	Lesion
All	40 ± 5	41 ± 6	38 ± 6	33 ± 6
No lesions	41 ± 6	43 ± 6	40 ± 6	–
Lesions in PZ	36 ± 2	37 ± 4	34 ± 3	31 ± 6
Lesions in TZ	38 ± 3	40 ± 3	36 ± 4	37 ± 0

Regarding the patients' ADC-maps; image co-registration was not successful for $n = 2$ patients but was considered for $n = 27$ patients. A positive correlation (evaluated with the Pearson correlation test) was found between ADC and TSC values within WP ($r = 0.35$), PZ ($r = 0.50$) and TZ ($r = 0.22$), although, correlation was only significant within PZ ($p = 0.0078$) but not within WP ($p = 0.08$) or TZ ($p = 0.28$).

5 DISCUSSION

This chapter discusses the methodologies and results presented in this thesis. The different methods for the quantification of tissue sodium concentration (TSC) in the human brain of patients with ischemic stroke are evaluated, with the first part already being published in [Adl+21b] by Karger Publishers. The impact of ^{23}Na MR image post-processing with a convolutional neural network (CNN) is discussed, with parts of it already being published in [Adl+21a] by John Wiley & Sons Ltd. The results of both conducted prospective in-vivo studies are analyzed.

5.1 TSC QUANTIFICATION FOR "^{23}NA MRI IN ISCHEMIC STROKE"

The ^{23}Na MRI data from patients with ischemic stroke was used to evaluate different TSC quantification methods.

Absolute TSC quantification based on the signal intensity (SI) within external reference phantoms, which are placed within the field of view (FoV) during the MRI measurements, is common practice and currently considered as state of the art [Boa+94; Thu+99; MR13; Thu18]. However, different quantification methods, like the relative TSC based on the contra-lateral brain tissue or the cerebrospinal fluid (CSF), have also been evaluated previously, despite being rather described as semi-quantitative parameters [WAH12; Han+13; NP+15].

In this thesis, absolute and relative TSC quantification methods were compared in the human brain of patients with ischemic stroke. Absolute TSC was calculated based on the SI within reference vials (TSC_{Vials}) with a known sodium concentration. Relative TSC quantification was performed based on SI within the contra-lateral brain tissue (rTSC). Furthermore, absolute TSC quantification was also performed based on SI within internal references, where a constant extra-cellular sodium concentration (ESC) was assumed: the cerebrospinal fluid (TSC_{CSF}), and the vitreous humor (TSC_{VH}). On the one hand, results indicated that rTSC might be influenced by potential pre-existing small vessel diseases within the white matter (WM), which appeared to have an impact on the contra-lateral TSC. On the other hand, absolute TSC quantification based on CSF or VH did not seem to suffer from such systematic errors. However, the quantification based on SI within CSF, particularly of younger patients, seemed to suffer from partial volume effects (PVE). TSC quantification based on the SI within the VH was considered as reliable method.

5.1.1 *Relative and absolute TSC quantification*

The TSC was evaluated within the WM of patients with ischemic stroke. In the healthy human WM, previous studies reported TSC to be between 20 and 60 mM [MR13]. In the here presented study, the manually segmented normal-appearing white matter (NAWM) regions of all patient groups showed a TSC of 45 ± 5 mM, which is within that range, supporting the findings.

Small vessel diseases can cause white matter lesions (WML), which present themselves as white matter hyperintensities (WMH) on T2w MR images [Pan10; DM10; WSD13; Man+15]. WML are usually caused by changes in the water content or changes in the overall white matter integrity, consequently indicating changes in the cell viability and vitality [WVHMM15; Man+15; MC19], which might manifest itself by cognitive impairment or different neuro-pathological diseases, such as dementia, or depression [Faz+93; Bok+06; YHK08; PS15].

With TSC being highly sensitive to changes in extra- and intra-cellular volume fraction (IVF/EVF) [Thu18], such changes of the vascularization will also lead to alterations in TSC. This was previously observed for multiple sclerosis lesions, which were reported to present increased absolute TSC values [Zaa+12; Eis+16; Pet+16a; Pet+16c; Don+19; Web+21].

The scale of Fazekas was used to rate and quantify WMH in the evaluated patients, indicating their white matter disease severity.

Considering patients with Fazekas grade 0 or I (no or mild WML), mean absolute TSC within WM was between 37 and 63 mM, with a mean of 49 ± 2, and 50 ± 7, respectively. The results are within the global range of previously reported results [MR13], although being at the upper limit with some individual patients even exceeding maximal previously reported values. One possible explanation of the rather high results could be the effect of the ischemic area – even after its subtraction from the WM mask – with PVE possibly having an impact on the TSC in the surrounding area, which was classified as healthy tissue. However the effect was reduced by the cut-off of the outer border.

Considering patients with Fazekas grade III (extensive WML), mean absolute TSC in WM was between 50 and 74 mM, exceeding even the upper limits for TSC in healthy WM from the above mentioned literature values by up to 23%. It is hypothesized that the increased TSC might arise from the WML, which indicate axonal loss and thus an increase in EVF.

The intra-subject standard deviation (sd) of absolute TSC in WM was higher in patients with Fazekas grade III than it was in patients with Fazekas grades 0, I, or II. A significant positive correlation was shown between the Fazekas grade and the intra-subject sd. This indicates higher variations of TSC within the WM of patients with an increased Fazekas grade, which might thus be caused by the higher TSC in WML. A more homogeneous TSC was present in the WM of patients with lower Fazekas grades, who presented less WML.

After subtraction of the area that was affected by ischemic stroke, the un-affected WM area had a mean size of 246 ± 125 cm^3, which is smaller than previously reported WM volumes, which were between 420 and 508 cm^3 [LSJ02; Tak+11], and therefore $\approx 40 - 50\%$ larger. The difference might be caused by subtraction of the stroke area and cut-off of the outer 4 mm border that was performed with the purpose of reducing PVE. The cut-off was chosen to be 4 mm as it corresponds to the nominal resolution of the ^{23}Na MR image and thus the equivalent of one voxel – as it was on the original ^{23}Na MR image – was subtracted.

Evaluation of the patient's age and the time after the onset of symptoms of the ischemic stroke showed that both factors did not contribute significantly to the patient's absolute TSC in WM. The Fazekas grade was the only significant contributor to

TSC in WM. The influence of gender and possible differences between both genders were not evaluated but would be of high interest for future investigations.

The ischemic stroke region was defined as presenting lowered values on the apparent diffusion concentration (ADC)-map. The contra-lateral stroke region was defined by mirroring the stroke region on the middle fissure. Again, the outer border of the region of interest (ROI) was subtracted. The mean absolute TSC in the stroke region was 72 ± 16 mM with a wide range of 36 to 109 mM. The contra-lateral stroke region also presented a wide range of 39 to 79 mM with a mean of 57 ± 9 mM. Mean absolute TSC within the stroke region was within the range of previously reported values [Thu+05; Hus+09; Wet+12]. However, mean TSC within the contra-lateral stroke region of some patients exceeded even the upper limit of previously reported TSC values in healthy brain matter substantially [MR13].

Mean TSC in the stroke region was – with the absolute quantification – 74 ± 15 mM in Group 1 (Fazekas grade 0 and I) and 67 ± 16 mM in Group 2 (Fazekas grade II and III) with the differences not being significant. The relative quantification based on the NAWM showed – again – that no significant differences of TSC within the stroke were present between both groups. However, when using the relative TSC quantification based on the contra-lateral stroke region, differences of TSC in WM between both groups were significant. The apparent differences in relative TSC between both groups are thus assumed to be primarily caused by TSC differences in the contra-lateral brain tissue, which were influenced by WML.

Consequently, absolute TSC quantification is warranted and provides more reliable results than relative quantification, which might be influenced by, e.g., pre-existing small vessel diseases – resulting in WML.

5.1.2 *Absolute TSC quantification with internal references*

Different absolute TSC quantification methods were performed with datasets from patients with ischemic stroke. The absolute TSC quantification was based on the SI within references vials (TSC_{Vials}), which is being considered as state of the art and it is broadly used within and beyond applications in the human brain [Ouw11; MR13; Hu+20]. However, usage of reference phantoms is prone to human errors. Their proper placement is crucial and they might get displaced by just small and potentially involuntary movements of the patient – particularly when considering patients with ischemic stroke. In hectic or stressful situations, their placement might even be forgotten entirely.

Therefore, additionally to TSC_{Vials}, two other, less established, absolute quantification methods were performed for comparison. Quantification was based on internal quantification references: the cerebrospinal fluid (CSF) and the vitreous humor (VH). Previously, it had been suggested to evaluate the sodium concentration relative to other organs or tissues [Mar+06; Han+13]. CSF and VH, do not contain vital cells and a stable sodium concentration, strongly linked to the blood serum sodium concentration (SSC), was found within both [OR55; Har+10; SLG20; Pig+20], motivating the consideration of either region as potential reference for the absolute TSC quantification. In the presented study, TSC in VH and in CSF were assumed to be equivalent to SSC, which was thus used for the quantification if the value was available. It was assumed to be 145 mM, corresponding to previously reported ESC

[SE92; Som02], if SSC was not available.

On the one hand, overall, the results of all three quantification methods were within the range of previously reported values [MR13], particularly when considering that WM TSC might be elevated because of the above-discussed WML. Image segmentation allowed for TSC evaluation within WM, GM and stroke region separately. The results showed mean absolute TSC values of 53 ± 9 mM (TSC_{Vials}), 48 ± 7 mM (TSC_{CSF}), and 44 ± 7 mM (TSC_{VH}) in the WM, and 58 ± 8 mM (TSC_{Vials}), 53 ± 6 mM (TSC_{CSF}), and 48 ± 6 (TSC_{VH}) in GM.

On all three TSC-maps, the stroke regions presented with significantly higher TSC values than WM and GM, and TSC within WM was lower than TSC within GM. Both tendencies, which were present with all three quantification methods, were similar to previously reported findings [Lin+01; Hus+09; Mad+12a; NP+15; Maa+17; Rid+18; Lia+19].

On the other hand, TSC_{CSF} and TSC_{VH} showed lower TSC values in the whole brain than TSC_{Vials} and the TSC_{VH}-map showed lower values than the TSC_{CSF}-map. The manually segmented regions within CSF and VH showed mean absolute TSC values of 156 ± 27 mM (CSF) and 171 ± 24 mM (VH) on the TSC_{Vials}-map. This is generally high, and $n = 4$ outliers even presented values above 200 mM, which is far above previously reported or physiologically reasonable values [SE92; Fal+94; Som02; Som04].

The size of the used reference vials was rather small, with a volume of 14 ml and a diameter of 15 mm, making them sensitive to PVE. The introduction of PVE especially from surrounding air, would decrease the SI within reference vials and consequently increase values on the TSC_{Vials}-map. Misplacement of the vials, e.g. not parallel to the image plane, could potentially increase the impact, which might explain the outliers. Larger reference vials, particularly in diameter, might help to increase the accuracy of a TSC_{Vials}-map.

Furthermore, TSC within VH was higher than TSC within CSF; despite the sodium concentration of both being strongly linked (or equilibrated) with ESC [OR55; Har+10; SLG20; Pig+20]. The VH is a spherical body with a diameter of $\approx$ 16 mm, which remains relatively stable in adulthood [RWB06]. CSF expands with age, and ventricles are significantly larger in older patients [Mat+96; Zha+05]. Figure 4.1 shows one transverse slice of four patients with different Fazekas grading. The figure illustrates how CSF in the ventricles is more prominent on the ^{23}Na MR image of the older patients (Fazekas grade 0, II, and III, age between 77 and 83 years old) compared to the substantially younger patient (Fazaks grade I, 59 years old). Smaller ventricles make the manual definition of a CSF region more challenging. Thus, CSF in younger patients is more prone to the introduction of PVE compared to the easier segmentable regions within VH with its stable size.

The impact was further explored by considering the sd of TSC within the segmented regions of one of the reference phantoms, the CSF, and the VH. Sd was significantly lower within VH than within the two other regions, which emphasizes the homogeneity of the TSC in VH. Thus, making the TSC quantification based on the SI within the VH more stable and robust.

Figure 3.5 illustrates the three different regions that were considered as references for the TSC quantification on a transverse image slice of one representative patient. The figure might visualize why PVE are differently prominent within the three re-

gions.

A significant positive correlation was found between SSC and TSC in VH whereas the correlation between SSC and TSC in CSF was not significant. However, for TSC_{VH} and for TSC_{CSF}, TSC differences to TSC_{Vials} was not significantly different between patients where SSC was available and those where an ESC was estimated to be 145 mM within CSF and VH. This is despite the fact that the estimation must be considered highly simplified, as SSC might fluctuate – even if only marginally – and, especially for patients with the risk of an ischemic stroke, altered SSC levels were found previously [Wan+94]. However, apparently, even with no SSC available, the TSC quantification accuracy did not seem to suffer substantially.

Those results justify a TSC quantification based on internal references even if no blood sample of the patient is available.

EVALUATION OF QUANTIFICATION STABILITY To evaluate the absolute TSC quantification stability, three ^{23}Na MRI were acquired of one healthy control (HC) over a time span of six weeks. TSC quantification was performed based on SI within CSF and VH. Again, TSC_{VH} showed lower values than TSC_{CSF}. Here, PVE within CSF were especially prominent because of the the HC's small ventricles. They are visible in Figure 4.8, and can be explained by the young age (24 years) of the HC. Results within WM and GM on both TSC-maps show values, which were within the range of literate values [MR13]. However, for TSC_{CSF}, they are at the upper limit, whereas the results within the TSC_{VH}-map were more similar to the globally reported values [Ouw+03; Ouw11; Zaa+12; Nie+15; Eis+19; Lia+19; Web+21]. TSC differences between the three measurements were below the sd within the respective tissues. Thus, the results indicate high quantification stability. The TSC differences between scans were lower on the TSC_{VH}-map than on the TSC_{CSF}-map.

Overall, the VH appeared as reliable reference for the TSC quantification. Quantification based on SI within VH seemed to be more robust than quantification based on SI within CSF. This is despite the fact that the TSC_{VH}-map of the patients with ischemic stroke presented higher TSC differences to the TSC_{Vials}-map compared to the TSC_{CSF}-map. It is justified, on the one side, because of the low differences between the TSC_{VH}-maps of scans at different time points, and, on the other side, because of the great variations in ventricle size and shape.

Consequently, TSC quantification based on SI within the VH was chosen for the prospective in-vivo study investigating TSC evolution within patients who underwent stereotactic radiosurgery, which is discussed in subsection 5.3.1.

5.2 DATA ACQUISITION TIME REDUCTION BY APPLICATION OF A CNN

The aim was to prospectively reduce ^{23}Na MRI data acquisition time for patients with ischemic stroke.

Data acquisition of ^{23}Na MRI takes substantially longer compared to ^{1}H MRI, requiring a measurement time of at least $\approx$ 10 min, according to the current state of the art. This is caused by the substantially lower natural abundance of ^{23}Na MRI and its less favorable NMR properties compared to ^{1}H. Furthermore, the resulting images have a relatively low signal-to-noise ratio (SNR) because of the trade-off between measurement time and SNR.

At the same time, measurement time is a crucial parameter for the decision of whether a sequence can be used in the clinical routine. Particularly when considering acute diseases, such as the ischemic stroke, fast treatment decisions are warranted, which do not allow for for long MRI protocols. Furthermore, patients might experience discomfort during the MRI because of the restricted space and exposure to noise.

To reduce the ^{23}Na MRI data acquisition time, ^{23}Na MRI data from patients with ischemic stroke was artificially under-sampled and the resulting images were used to test and train a CNN with various architectures and parameters. The purpose was to be able to use a multiple-fold measurement time reduction without increasing the image's noise and while maintaining TSC quantification accuracy, which was supposed to achieved by image post-processing with the CNN. Different CNN configurations were implemented with varying loss functions. Initially, the simulated under-sampling factor was set to $R = 4$.

Overall, CNNs with U-Net architecture, including skip connections, performed better than CNNs with ResNet architecture, that did not contain skip connections. The other parameters that were considered (number of filters, batch normalization, and loss function) individually did not have a prominent impact on the network's performance but were rather dependent on their deployment and combinations. The preliminary results indicated that artifacts from under-sampling were reduced with the application of a properly adjusted U-Net.

A U-Net architecture with the smaller number of filters, which did not use batch normalization, and was trained with the L2 loss function (possibly complemented with a gradient loss function, L_{GDL}) showed the best results. This CNN was further implemented and trained with varying under-sampling factors ($R = 2, 3, 4, 5, 6, 8, 10$), and different weightings of the L_{GDL} ($\lambda = 0.2$, and $\lambda = 0.5$).

The results suggest that post-processing with CNNs might be able to reduce artifacts from high under-sampling of ^{23}Na MRI.

5.2.1 *SNR and SSIM*

All evaluated CNNs increased the SNR of the highly under-sampled image (RI). The relative improvement was between 55% and more than an eight-fold improvement. The significant improvement of SNR – even compared to the image that was reconstructed using the full k-space data (FI) – might be due to the networks' recognition and elimination of background noise. CNNs have already previously been used for image de-noising [Zha+17; Kop+19], which has been applied to different medical imaging modalities [Hig+19]. According to the SSIM, CNNs (U-Nets) with some parameter configuration increased the image's similarity to FI, whereas the index decreased for CNNs (mostly ResNets) with other parameter configurations. An increased SSIM indicates an improvement in image quality and accuracy in the relevant region of the image: the patient's brain.

Only U-Net-based networks increased the SSIM. Thus, the additional skip connections in the U-Net architecture were considered essential for the accurate maintenance of the location information. The addition of L_{GDL} increased the SSIM, which is a parameter that depends on image degradation and contrast [Wan+04]. Consequently, it is hypothesized that L_{GDL} improves edge accuracy, which was also observed previously and was intended [MCL15b]. The improvements in edge accuracy might

be highly valuable for future applications when aiming to define strongly affected regions within the ischemic stroke – particularly when considering the relatively low resolution of ^{23}Na MR images.

The three networks with the best improvement of the SSIM were chosen for an in-depth evaluation, and their TSC quantification accuracy was evaluated.

5.2.2 *TSC quantification*

The accurate quantification of ^{23}Na MR images is crucial as TSC provides valuable information about cell vitality and viability, which can be of high relevance for patients with ischemic stroke [Thu+05]. Prospectively, a possible application might be an onset time prediction for wake-up stroke patients [LaV+09; NP+15], although its reliability has been discussed and results are pending. Other possible applications include a more precise definition of the stroke's penumbra [Wet+15]. Considering the initially trained CNNs (using ^{23}Na MRI data with $R = 4$) for which TSC quantification was performed: All three CNNs that were evaluated in-depth were able to decrease quantification error (ΔTSC) of the artificially up-sampled ^{23}Na MRI (CI) compared to ΔTSC of RI, which was reconstructed traditionally without application of a CNN.

The regions of WM and GM can both be affected by ischemic strokes. CNNs decreased ΔTSC in both tissues significantly below a mean of 4 mM, which is below the sd within the respective tissues, as was discussed in subsection 5.1.2.

For patients with ischemic stroke, it has been suggested that tissue with an increased TSC by more than 50% might be non-reversibly damaged [MR13]. The large range of TSC values in healthy tissue, and the high increase in TSC that is necessary for indicating permanent tissue (brain) damage, suggest that a 4 mM variation might not be of high relevance. Thus, an error of $\leqslant 4$ mM would still allow for a sufficiently accurate TSC quantification to determine whether non-reversible damage occurred within the affected brain region.

Because of its high SI and its stable sodium concentration, CSF is a valuable marker within ^{23}Na MR images. ΔTSC in CSF was similar compared to ΔTSC in WM and GM and it was also reduced to below 4 mM. However, here, the improvements were not statistically significant. These results indicate that CI's accuracy does not suffer with high SI regions. This is in contrast to compressed sensing, which is another technique that was previously used for k-space under-sampling of ^{23}Na MR images and its measurement time reduction [Utz+20; Lac+21]. However, compressed sensing has been proven to be a robust technique and it does not carry the risk of introducing false information, which is an advantage over CNN-based post-processing techniques. At the same time, quantification accuracy seemed to be lowered in tissues with high SI when using compressed sensing [Mad+12b; Gna+14]. This issue was not present in the ^{23}Na MR images that were artificially up-sampled with CNNs. This can be considered an important advantage of CNN-based post-processing techniques compared to the previously investigated techniques. It is especially important when considering the fact that the region of most interest is the region affected by ischemic stroke, which presents itself by elevated SI. The relatively fast reconstruction times with CNN-based post-processing were an additional advantage compared to compressed sensing methods for k-space under-sampling [Mad+12b; Gna+14].

The addition of L_{GDL} enhanced the quantification accuracy for some of the observed network architecture and loss function combinations. Considering the overall

best performing CNN architecture; improvement of the TSC quantification accuracy was present in all evaluated regions, although it was only significant within the WM but not in GM or CSF. It is hypothesized that the positive impact on edge accuracy from L_{GDL} [MCL15a], which was observed with the SSIM, might mainly improve contours (influencing SSIM) but has no to little impact on the overall SI, which defines the TSC. This might explain the improved SSIM when introducing L_{GDL} whilst maintaining a similar TSC quantification where only mean values of larger regions were considered.

5.2.3 *Evaluation of different under-sampling factors*

As the results were promising for under-sampling with $R = 4$, the best-performing CNN was further trained and tested, trying out various under-sampling factors of $R = 2, 3, 4, 5, 6, 8, 10$.

As mentioned above, the results from using the L_{GDL} loss function were promising as the additionally introduced maintenance of edge accuracy is of high value for ^{23}Na MR images, where resolution is generally low. Therefore, different weightings of the loss function ($\lambda = 0.5$, and $\lambda = 0.2$) were considered to evaluate whether overall performance might increase further.

The evaluations of RI showed a negative correlation between the under-sampling factor R and SNR and between R and SSIM to FI, implying that image quality and accuracy decreased with an increasing under-sampling factor; as was expected.

Considering CI, no correlation was found between R and SNR of CI with loss function L2 and a positive correlation was found between R and SNR of CI with the loss function including L_{GDL} (for both λ). This was not expected but could be explained by the strong de-noising that was introduced by the CNN, which becomes more obvious when regarding the absolute SNR values, which were elevated even far above the SNR of FI. SNR of RI was significantly lower than SNR of CI with all loss functions, regarding all under-sampling factors.

Results also showed a negative correlation between R and SSIM to FI for CI with all loss functions, demonstrating that the structural accuracy remained dependent on the initially available amount (or quality) of data; even after CNN-processing, independently of the chosen CNN parameters.

SSIM was significantly increased by CNN post-processing, for all under-sampling factors. Overall, considering the SSIM to FI, differences were low between the results of the three considered loss functions. For different under-sampling factors, different loss functions performed best.

The improvements in SSIM were particularly prominent for higher R. Considering $R = 10$, CNN post-processing increased SSIM to up to 0.9446 ± 0.0182, which is similar to SSIM of RI with $R = 6$ (0.9437 ± 0.0188). The results indicate that CNN post-processing of a ^{23}Na MR image that was acquired with a ten-fold under-sampling generates an image with an accuracy that is comparable to a ^{23}Na MR image that was acquired with six-fold under-sampling.

5.2.4 *Application on real under-sampled data*

The CNN architecture that generated the best results for $R = 4$ was applied to one dataset of one HC, from whom real under-sampled MR images (rRI) were acquired. SNR of FI and rRI was similar compared to SNR of FI and RI of patients with ischemic stroke. SNR of the CNN-generated rCI was also improved beyond FI's SNR, indicating a similar effect compared to the test datasets.

SSIM to FI of rRI and of rCI from the HC were lower compared to SSIM of RI and CI from the patients with ischemic stroke. This might be explained by having performed two different measurements with the HC. For in-vivo measurements, this will always involve small movements and consequently displacements in between the scans, leading to a lower structural similarity between the images. At the same time, SSIM was – again – improved by the CNN post-processing.

Quantification and segmentation showed that CNN post-processing introduced an improvement in TSC accuracy in WM and GM but a decrease in TSC accuracy in CSF. For patients with ischemic stroke, TSC quantification accuracy in CSF, with its high SI, was already worse than TSC quantification accuracy in WM and GM, but CNN post-processing had still yielded improvements. The here presented decrease in TSC quantification accuracy might be influenced by the young age of the HC (26 years old) compared to the group of patients with ischemic stroke based on which the CNN was trained. This could explain the lowered accuracy in CSF, considering the fact that ventricles change (grow significantly) with an increasing age [Mat+96; Zha+05].

Overall, the results obtained from the HC measurements and data processing indicate that the implemented and trained CNN might be of value beyond the application for patients with ischemic stroke, although accuracy might decrease with decreasing age, particularly in the area of the CSF. Therefore, additional training datasets – particularly from a younger age group – would be of high interest.

5.3 PROSPECTIVE IN-VIVO STUDIES

5.3.1 *Evolution of TSC after stereotactic radiosurgery*

A prospective study was conducted, aiming to evaluate the TSC changes in brain metastases (BM) and their surrounding tissue (peritumoral tissue, PTT).

^{23}Na MR images were acquired from patients undergoing stereotactic radiosurgery (SRS), with data acquisition pre- and post-SRS. The TSC quantification was performed based on SI within the VH. The stability of the TSC quantification method was validated by the HC measurements, which were presented in subsection 4.1.2 and discussed in subsection 5.1.2.

Considering all 14 BM, mean absolute TSC was elevated within the evaluated gross tumor volumes (GTV) compared to the considered healthy-appearing ROI (HR), which is in alignment with previously reported findings about TSC in brain tumors [Has+91; Thu+99; Ouw+03; Reg+20]. Brain tumors were found to show elevated TSC values compared to healthy tissue. It is hypothesised that the increased TSC derives from an increased intra-cellular sodium concentration (ISC) because of altered cell metabolism in tumorous tissue [Cam+80; Ign83; Ouw+07]. Further interpretations

involve tumor angiogenesis, increasing the tumor's vascularisation, to increase TSC [Ouw07; Jac+10; Dri+20].

Shortly after SRS, mean TSC within GTV increased further. SRS aims for ablative radiation therapy, causing vascular damage and cell apoptosis within the tumor and its PTT [Par+12; Sia+20], as was previously observed with other MRI modalities [Jak+15; Win+18]. The increase in TSC might, thus, be introduced by cellular damage and excessive cell death, consequently increasing the EVF, as was observed in other pathologies, e.g. the ischemic stroke or MS lesions, previously [Lin+01; NP+15; Web+21]. The increase in TSC in PTT might be further induced by peritumoral edemas, which have been found to grow shortly after SRS [Sch+17b; Tra+19]. The alterations in TSC in the peritumoral edemas of a subgroup of the here presented patients was published by Mohamed et al. [Moh+21a]. Previous studies have already indicated that early radiation-induced changes in the tissue, shortly after SRS, might be detectable with MRI and could be used as an indicator for the long-term tumor response [Des+17; Sha+21]. Recently, Lewis et al. have published the effect of SRS on TSC in the vestibular schwannoma microenvironment, who found SRS to cause a long-term increase in TSC [Lew+21]. However, their scans were scheduled at different time points compared to the here presented study.

At the third measurement, almost six weeks after SRS, TSC was observed to have decreased below TSC values from before irradiation. Mean TSC within the irradiated GTV became more similar to healthy tissue values. However, it remained significantly higher than TSC in HR. The decrease in TSC might be physiologically explainable because of tissue regeneration, despite a smaller fraction of remaining tumor cells within the GTV [Oh+07; BCS12; Oft+21].

Regarding the PTT, TSC increased shortly after SRS within isodose areas $D \geqslant 8$ Gy but not (significantly) for lower isodose areas. These findings were in alignment with previous studies, that reported radiation doses higher than 8 to 10 Gy might cause vascular damage, resulting in apoptosis of, e.g., endothelial cells whereas less long-term harm was observed for exposure with lower radiation dosages [Lju+91; PFK00; GB+03; Par+12; Son+20].

Like in the GTV, TSC in all isodose areas had also decreased after an initial increase. However, at $D = 2$ Gy, no significant changes were observed at any time point, which could thus be hypothesized as not having induced any vascular changes or damage. Dosages below 1 or 2 Gy are often referred to as low or moderate doses and are also used as low-dose radiation therapy for benign diseases [Wun+15; Ott+14]. A threshold – for the otherwise assumed to be linear carcinogenicity of radiation – has been hypothesised [HL98; Coh08; Mul+09].

TSC was overall higher within higher isodose areas than within the lower isodose areas pre-SRS and five days after SRS. At the third measurement, the mean TSC was more similar between the isodose areas. These results support the hypothesis of tissue regeneration some weeks after SRS [Oh+07; BCS12; Oft+21]. However, a positive correlation between radiation dose and mean absolute TSC within the corresponding isodose areas was found at pre- and post-SRS, at all measurements.

Considering the two BM that showed tumor progression; at baseline, mean TSC within GTV was low compared to the other BM. Instead, mean TSC within GTV of those two BM was closer to healthy tissue TSC. In 2016, Schepkin found gliomas

in rats with little resistance to chemotherapy to contain the highest sodium concentrations, whereas he found chemotherapy-resistant cells to contain much lower sodium concentrations, rather in the area of healthy tissue values [Sch+05]. Obtaining information about similar tendencies when considering potential radiation-resistance would be of high interest, and the here presented findings might point in that direction. However, there have also been multiple previous studies showing a positive correlation of tumor malignancy and sodium concentration, indicating that ^{23}Na MRI might increase the accuracy of tumor classifications [Cam+80; Ign83; Nag+83; Mad+14; Bil+16].

Five days after SRS, mean TSC increased within GTV of both progressing BM, although the increase was less sharp than it was in all GTV on average. The third ^{23}Na MR image showed that mean TSC had dropped within one GTV but had remained above baseline TSC. Mean TSC within the other GTV had even increased further, which was contrary to the mean trend of all GTV.

Overall, the TSC evolution within GTV of one of the BM with progression was substantially different from the mean TSC evolution of all (mostly responders) GTV. TSC evolution within GTV of the other progressing BM was similar to the mean TSC evolution of all GTV, although the trend was less prevalent and TSC was substantially lower. Paech et al. have investigated TSC evolution within glioblastomas after chemoradiotherapy over a similar timespan compared to the here presented study. They have found a trend towards a stronger TSC increase in tumors with early progression [Pae+21], which aligns with the results of one of the here presented BM with progression.

Regarding the isodose areas of the progressing BM, mean TSC was similar in all isodose areas pre-SRS and five days post-SRS. The third measurement revealed that it had remained similar for one of the progressing BM in all isodose areas but for the other progressing BM it had increased within higher isodose areas ($D \geqslant 8$ Gy).

The little to no changes in TSC within GTV and PTT of the progressing BM might have already indicated early on that less tissue response occurred.

5.3.2 *TSC in the human prostate with a suspected carcinoma*

A prospective study was conducted, investigating the TSC in the human prostate of patients with a suspected prostate carcinoma. The study showed differences in TSC of segmented cancerous lesions and TSC in healthy prostate tissue. Patients were included who received a standard multi-parametric MRI (mpMRI) exam of the prostate for the diagnosis of a clinically suspected prostate carcinoma. After the mpMRI protocol, additional ^{23}Na MR images were acquired. After image post-processing, including the correction of the coil's receive field (B_1^-), TSC quantification was performed based on the SI within blood vessels.

TSC quantification in the abdomen is – analogue to the TSC quantification in the head – most commonly performed based on reference phantoms, placed within the FoV. Within the patient's abdomen this causes additional inaccuracies, which are less prevalent in head scans [Isa+90; Pas20]. The multi-channel abdominal coil that was used for the abdominal ^{23}Na MRI had a less homogeneous B_1-field than the birdcage head coil, and the principle of reciprocity did not apply [HR76], which required corrections [Roe+90; Gio+02; She+10]. The impact was reduced by using an adaptive coil combination, reducing the influence of channels with a weaker signal.

B_1^- corrections were performed by using a low-pass filter, which was applied onto the acquired image and onto a generated mask of the ROI (the patient's body), smoothing the image signal [Lac+20]. No B_1^+ corrections were performed because they would have required additional scans, lasting for several minutes for every patient, which was not justifiable. The assumption of a relatively homogeneous B_1^+-field was legit because of the birdcage structure of the circular transmit coil. Still, particularly in the peripheral FoV, inhomogeneities might remain.

Because of the introduced signal smoothing by the LPF from the B_1^- correction, which potentially increased PVE, and because of the lack of a B_1^+ correction; reference phantoms outside of the patient, distant to the investigated tissue, were not considered appropriate for the TSC quantification.

Using, instead, the femoral blood vessels (FBV) as quantification references carries the great advantage of being less prone to be impacted by inaccuracies caused by B_1 inhomogeneities because of their spatial proximity to the investigated tissue. At the same time, this approach introduces an additional confounder into the TSC quantification, and makes it dependent on the patient's physiology. The sodium concentration in blood does not only depend on the SSC (as it was assumed for the sodium concentration in the VH) but it also depends on the patient's red blood cell percentage (hematocrit), ranging for healthy men between $\approx 40-50\%$, which can be further influenced by pathologies such as renal dysfunctions [Bil90; Hsu+01].

Areas were segmented within the left and right FBV. Results showed that the sd of TSC was low within those areas. No significant differences were found between TSC within the left and right FBV. This indicated a high stability for the quantification method.

^{23}Na MRI has shown TSC levels in the blood to be between 71 and 85 mM [OWB05; KS13; Lot+19], with the most recent results from Lott et al. [Lot+19], who reported 81 ± 7 mM, which is why it was assumed to be 81 mM in every patient.

Literature about ^{23}Na MRI in the human prostate in general, and in prostate cancer in particular, is limited.

Considering studies examining the healthy prostate tissue, in 2012 Hausmann et al. have found TSC to be between 24 and 70 mM in the peripheral zone (PZ) and between 34 and 85 mM in the transitional zone (TZ) [Hau+12], whereas in 2015 Farag et al. have found values between 51 and 92 mM in PZ and between 72 and 98 mM in TZ [Far+15].

In more recent studies, TSC was also investigated within prostate carcinomas. Studies from Barrett et al. in 2018 and 2020 showed TSC values of ≈ 33 and 34 mM in TZ and 39 mM in PZ, and they found, on average, an elevated TSC within the prostate carcinomas (mean TSC of 42 and 43.1 mM) [Bar+18; Bar+20]. Broeke et al. published a study in 2019 that also found elevated TSC values within prostate carcinomas compared to healthy prostate tissue, particularly when considering high Gleason scores [Bro+19].

The results that were presented in this thesis showed mean absolute TSC values of all patients to be 40 ± 5 mM in the WP, and suggested that, overall, TSC within the PZ was with 41 ± 6 mM significantly higher than TSC in the TZ, where mean TSC was 38 ± 6 mM. The here presented results are within the very broad range of previously reported values. They are similar to Barrett et al.'s findings and at the lower end of findings from Hausmann et al., although they are substantially

lower than the values that Farag et al. have reported [Hau+12; Bar+18; Bar+20]. However, one aspect where all previous findings are in alignment with each other is that TSC within PZ was commonly reported to be higher than TSC in TZ [Hau+12; Far+15; Pas+17; Bar+18; Bar+20]. The same was applicable for the data that was presented in this thesis, where differences between TSC in PZ and TZ were significant.

Regarding the TSC in the segmented lesions; they were found to be lower than TSC within the healthy prostate tissue, which was applicable for all identified lesions within the PZ and for one out of two identified lesions in the TZ.

Additionally, regarding exclusively the patients who were identified with a $4+5$ Gleason score (meaning high aggressiveness of the tumor) within the PZ ($n = 3$); two of them showed lower TSC values in the PZ than in the TZ. This was opposite to the mean of all patients. The third patient showed a higher TSC in PZ than in TZ but differences were smaller than the mean difference of all patients. Those results are not in alignment with previously reported findings. Barret et al. and Broeke et al. have both reported elevated TSC within cancerous lesions in the prostate [Bar+18; Bro+19; Bar+20], which is opposite to the tendency of the here reported results. Overall, so far, TSC was reported to be elevated within tumorous tissue within various regions of the body [Ouw+07; Jac+10; Pok+21]. This is hypothesized to derive from an increased ISC, caused by the increased cell metabolism in tumor cells, and by the increased vascularization of tumors. However, tumors also present a higher cell density, thus decreasing the EVF, which might offer an explanation for decreased TSC values. Furthermore, it remains questionable whether the here reported results can be properly compared to results that were previously reported by Farag et al. (about healthy prostate tissues) [Far+15] or Barret et al. and Broeke et al. (about healthy and cancerous prostate tissue) [Bar+18; Bro+19; Bar+20] because of substantial differences in the measurement setup. They used endorectal receive coils, whereas, in this thesis, a surface receive coil was used, which can be assumed to reduce inconveniences for the patient substantially.

The positive correlation between ADC and TSC values, which was reported for the here presented findings, was another indicator for a robust TSC quantification. However, the correlation was only present within PZ and not within TZ. ADC values represent the tissue's diffusion and, consequently, decrease with an increasing cell density. The same is applicable for TSC values, which also decrease with increasing cell density because of the lower ISC compared to ESC.

5.4 LIMITATIONS

The results presented in this thesis were obtained within studies carrying various limitations. Some of the limitations applied to all obtained data:

The resolution of ^{23}Na MR images is low compared to most ^{1}H MR images. The low resolution makes ^{23}Na images prone to PVE, as one image voxel might contain more than one million cells [BSJ19], which are all influencing the voxels' SI. Thus, PVE are a common and crucial problem when aiming to quantify TSC [Thu+99; Ouw+03]. The problem was addressed – if possible – by cut-off of the outer borders of the considered ROIs. However, this technique reduces the considered volumes and increases the problem of not being able to evaluate smaller ROIs. There are also methods for minimizing PVE within the images. Usage of a geometric transfer matrix

correction [Nie+15] or a voxel-wise linear regression [Kim+21] have been proposed and should be further explored.

Furthermore, the repetition time was set to values, which were below $5 \cdot T1$ of all tissues so that T1-weighting effects must be expected within certain areas with relatively long T1. However, correction for T1-weighting were performed if possible. The measurement parameters were chosen such that the data acquisition time of the ^{23}Na MR image was still appropriate for the respective application and further increasing TR would have exceeded an acceptable measurement time for the patients.

Automatic image co-registration and segmentation of the head were performed with SPM12. The software is well-established and has shown high accuracy [Fel+15; Hin+18]. Even though, inaccuracies might occur, e.g. the underestimation of tissue volumes compared to manual segmentation [Mal+15]. Additionally, any image co-registration – particularly when involving re-sampling, which might introduce misalignments, and will enhance the already existing PVE – must be considered a limitation.

Manual image segmentation, which was performed for the stroke region (based on the ADC-map, performed by neuroradiologists) and for the segmentation of the prostate (segmentation of WP, PZ, and possible lesions, based on T2 TSE, performed by radiologists) always carries the risk of subjectivity and depends on the person performing the segmentation.

Further limitations were specific to the respective studies.

5.4.1 *TSC quantification for "^{23}Na MRI in ischemic stroke"*

The different quantification methods that were applied to the data of the study "^{23}Na MRI in ischemic stroke" all carried various different limitations.

The reference vials were rather small with a volume of 14 ml and a diameter of 15 mm, thus, carrying an increased risk of PVE, especially if correct placement was impaired by, e.g., involuntary movements of the patient. Consequently, the validation of both other quantification methods – based on SI with CSF and VH – lacked comparison to a robust and reliable ground truth.

Quantification based on CSF and VH were based on SSC, which was not available for all patients, warranting for the assumption of an ESC of 145 mM, despite various pathologies possibly impairing ESC.

The resolution of the ^{23}Na MR image is a multiple-fold lower than the resolution of the T2 FLAIR, to which it was registered and based on which the WM mask was generated. It is also lower than the ADC-map's resolution based on which the stroke mask was defined. This must be considered a limitation of the study as it causes inaccuracies of the image co-registrations and PVE within the co-registered ^{23}Na MR image [Nie+15; Mal+15; Hin+18]. However, inaccuracies were reduced by the cut-off of the outer-boarder of the WM mask.

5.4.2 *Data acquisition time reduction by application of a CNN*

The introduced methodology of using a CNN for ^{23}Na MRI post-processing carried the limitations of using FI as label and ground truth, as well as the limited size and

homogeneity of the datasets.

FI already carried an under-sampling factor of $R_{FI} = 1.885$. However, image quality was still considered sufficient by the neuroradiologists. The CNNs were exclusively trained and tested with datasets from patients with acute ischemic stroke who were 73 ± 13 years old. Training datasets from patients from a more heterogeneous age group and with different pathologies are warranted to apply the implemented method more globally, which should be investigated in the future.

The network was trained and tested with images of a relatively low resolution (apparent resolution of 2x2x2 mm^3), whereas higher resolutions would be of high interest. At this point, no predictions of the network's performance for images with higher resolutions can be made. However, it would be challenging to obtain a sufficient amount of higher resolution ^{23}Na MRI datasets.

Furthermore, the networks' training and testing used DICOM data in image space. Thus, only the image's magnitude but not its phase were used, implying that parts of the available information were neglected. Therefore, further improvement of the performance might be possible when using the complex MRI data (including magnitude and phase) as it was already suggested and implemented previously for ^{1}H MRI [Wan+16; HSY19].

Image evaluation – particularly of the TSC quantification – depends on the ^{23}Na MR image co-registration to the T2 FLAIR and segmentation into GM, WM and CSF; both were performed with SPM12 and its possible issues were discussed above.

Another crucial drawback of all CNN-based post-processing techniques is the potential introduction of false information into the image. Here, the issue was addressed by the quantified comparison of the CNN output images with FI.

5.4.3 *Evolution of TSC after stereotactic radiosurgery*

The presented prospective study investigating TSC within BM and their PTT, undergoing SRS, only included a small number of patients and BMs. Particularly results from more patients who presented with tumor progression would be of interest as well as evaluating the differences for BM deriving from different primary tumor. Further studies, including more patients, would be necessary to verify the preliminary results.

Additionally, the TSC quantification based on SI within the VH carries the risk of being influenced by patient-specific (patho-)physiological variances, as was discussed in depth.

Furthermore, the image co-registration might have introduced additional inaccuracies, as all ^{23}Na MR images were co-registered to the MPRAGE from the pre-SRS measurement. The registration of the later scans – particularly the third one – might have suffered because of pathophysiological and structural changes following SRS [Oh+07; Par+12; Sha+14; Sha+14; Hin+18].

5.4.4 *TSC in the human prostate with a suspected carcinoma*

The prospective study investigating TSC in the human prostate of patients with a suspected prostate carcinoma carried the great limitation of a small number of included

patients with an identified cancerous lesion, which made the results unstable and sensitive to outliers. This is particularly prevalent as only two lesions were segmented within TZ. It requires the results to be considered preliminary. At the same time, the substantially higher number of included patients where no lesion was identified, and whose results were in alignment with previously reported findings, might support the validity of the methodology.

Another major limitation of the study is the assumption of TSC in the blood to be at 81 mM for every patient, despite it being dependent on various patient-specific physiological factors [Bil90; Hsu+01]. In the future, additional information about the patient's SSC and relative hematocrit level would be of high interest, requiring a blood sample obtained from patient shortly before or after the MRI examination. At the same time, a differing sodium concentration in blood would have impacted the absolute TSC values in the whole image but not the ratio of absolute TSC within healthy prostate tissue and identified lesions. Thus, this limitation might indicate that the results should be rather considered semi-quantitative (an expression that was previously suggested by Haneder et al. who investigated TSC within the human kidney [Han+13]) but it does not influence the here presented tendencies of lower mean TSC values within the segmented lesions than within the entire organ.

Additional limitations include the RF coil and its B_1 inhomogeneities. B_1^- inhomogeneities were corrected but minor differences might remain [Roe+90; BLH02; She+10]. More elaborate B_1^- corrections, as were suggested by Paschke [Pas20] would be of high interest to increase accuracy. B_1^+ corrections were not performed because it would have required measurement time in addition to the already relatively long sequence protocol, which was justified because of the coil's optimized transmit field by using a birdcage geometry [Isa+90; Ibr+01].

6 CONCLUSION AND OUTLOOK

This thesis aimed to provide a contribution to make quantitative ^{23}Na magnetic resonance imaging (MRI) more efficient by enabling faster data acquisition and an easier measurement setup. This could perspectively lead to the establishment of ^{23}Na MRI in clinical applications.

This thesis evaluated methods for the quantification of tissue sodium concentration (TSC) in the human head. It was investigated whether ^{23}Na MRI could be simplified by using internal instead of external quantification references. Additionally, a convolutional neural network (CNN) was optimized for the application of allowing shorter ^{23}Na image data acquisition times.

Moreover, two prospective in-vivo studies were conducted to gain further insight into TSC's significance for clinical applications. In one study, TSC changes following irradiation with stereotactic radiosurgery were observed in the brain of patients with brain metastases. In the other study, TSC was investigated within the healthy and the cancerous prostate tissue.

6.1 CONCLUSION

TSC quantification was performed in the human brain of patients with ischemic stroke and brain metastases and in the male pelvis of patients with suspected prostate carcinoma.

TSC was quantified in the brain of patients with ischemic stroke by using quantification references corresponding to the current state of the art: external reference vials for the absolute TSC quantification and contra-lateral brain tissue for the relative TSC quantification. Additionally, internal references with an apparently stable sodium concentration – the cerebrospinal fluid and the vitreous humor – were considered as references for the absolute TSC quantification.

The results indicated the additional accuracy obtained from the absolute TSC quantification compared to the relative TSC, with the relative TSC being highly dependent on pre-existing (small vessel) diseases.

Comparing the three different references for the absolute TSC quantification, the results showed a high similarity between all three references. However, especially the results of the vitreous humor as quantification reference indicated high quantification stability and robustness.

Using internal instead of external quantification references would allow for an easier setup of the ^{23}Na MRI and could eliminate various hazards, such as misplacement of references or forgetting them entirely. Furthermore, it would decrease the currently required additional effort for quantitative ^{23}Na MRI compared to conventional ^{1}H MRI.

In the second part of this thesis, a CNN was optimized, trained, and tested that improved signal-to-noise ratio and structural accuracy of multiple-fold under-

sampled ^{23}Na MR images. The images required a fraction of previously used measurement times.

The CNN that generated the best results used a U-Net architecture with additional residual connections. Its parameters were optimized for the application on under-sampled ^{23}Na MR images.

It was shown that high under-sampling of ^{23}Na MR images is feasible and that a good signal-to-noise ratio, a high edge accuracy and a stable TSC quantification can be maintained by application of a tuned CNN in the post-processing algorithm.

Exemplary, this was demonstrated for patients with an acute ischemic stroke. Patients with such acute diseases require immediate treatment, emphasizing the importance of fast diagnosis. Thus, data acquisition time is a crucial parameter for determining whether a sequence can be added to the MRI protocol.

The here presented results suggest that using an appropriately designed and trained CNN is feasible for generating accurate and quantifiable ^{23}Na MR images from highly under-sampled data. It allows for shorter data acquisition times and might increase the acceptance of ^{23}Na MRI in the clinical routine for the diagnosis of an ischemic stroke.

The two prospective in-vivo studies allowed for further insights into TSC alterations in specific pathologies:

The one prospective in-vivo study investigated TSC within brain metastases and their surrounding peritumoral tissue. The study showed that detecting radiation-induced pathophysiological changes in brain metastases and healthy brain tissue with ^{23}Na MRI is possible. Furthermore, differences were observed between the TSC evolution within brain metastases that responded to radiation therapy and those that progressed and therefore appeared to be higher radiation-resistant. Thus, the absolute TSC might be able to quantify radiation-induced tissue damage, which could prospectively lead to a more precise prognosis of treatment response. It may allow for earlier adaptations of the treatment plan – if necessary.

The other prospective in-vivo study investigated TSC within the human prostate with suspected prostate carcinoma. It showed significant differences between the mean absolute TSC in patients with diagnosed cancerous lesions and the mean absolute TSC in the prostate of patients with clinically inconspicuous findings. ^{23}Na MRI might allow, prospectively, for a more reliable diagnosis of prostate cancer. ^{23}Na MRI might become a valuable addition to the current state of the art multi-parametric MRI protocol for the diagnosis of prostate carcinomas.

6.2 OUTLOOK AND APPLICATION

The suggested ^{23}Na MRI data acquisition and post-processing techniques can be applied at any 3 T MRI scanner, which is enabled for ^{23}Na MRI. These methods allow for further applying ^{23}Na MRI to explore TSC as a potential biomarker for tissue viability and cell vitality in various pathologies.

The additional, valuable information that TSC can provide was demonstrated exemplary for brain metastases and prostate carcinomas.

Prospectively, for quantitative abdominal ^{23}Na MRI, obtaining a blood sample from the patient in addition to the MRI examination, and measuring the blood sodium

concentration, would be of high interest for making the quantification based on internal references (within blood vessels) more reliable and robust. For quantitative ^{23}Na MRI in the head, internal quantification references could already be applied with no further patient-specific information being required. A convolutional neural network could prospectively be broadly applied to the post-processing of ^{23}Na MR images of the human head, allowing for shorter data acquisition times.

In the future, the here presented findings could make ^{23}Na MRI faster and allow for an easier measurement setup whilst allowing for precise TSC quantification. They might decrease the threshold for implementing ^{23}Na MRI in clinics.

^{23}Na MRI could – if established – have a beneficial impact on diagnoses and therapy decisions of various pathologies.

BIBLIOGRAPHY

[Adl+21a] Anne Adlung, Nadia K Paschke, Alena-Kathrin Golla, Dominik Bauer, Sherif A Mohamed, Melina Samartzi, Marc Fatar, Eva Neumaier-Probst, Frank G Zöllner, and Lothar R Schad. "23Na MRI in ischemic stroke: Acquisition time reduction using postprocessing with convolutional neural networks." In: *NMR in Biomedicine* 34.4 (2021), e4474 (cit. on pp. 4, 39, 50, 52, 65, 74, 77, 91).

[Adl+21b] Anne Adlung, Melina Samartzi, Lothar R Schad, Eva Neumaier-Probst, Marc Fatar, and Sherif A Mohamed. "Tissue Sodium Concentration within White Matter Correlates with the Extent of Small Vessel Disease." In: *Cerebrovascular Diseases* 50.3 (2021), pp. 347–355 (cit. on pp. 4, 39, 45, 65, 66, 91).

[AM20] Abhinav Agrawal and Namita Mittal. "Using CNN for facial expression recognition: a study of the effects of kernel size and number of filters on accuracy." In: *The Visual Computer* 36.2 (2020), pp. 405–412 (cit. on p. 32).

[Ash+14] John Ashburner, Gareth Barnes, Chun-Chuan Chen, Jean Daunizeau, Guillaume Flandin, Karl Friston, Stefan Kiebel, James Kilner, Vladimir Litvak, Rosalyn Moran, et al. "SPM12 manual." In: *Wellcome Trust Centre for Neuroimaging, London, UK* 2464 (2014) (cit. on p. 42).

[ASS81] Jens Astrup, Bo K Siesjö, and Lindsay Symon. "Thresholds in cerebral ischemia – the ischemic penumbra." In: *Stroke* 12.6 (1981), pp. 723–725 (cit. on p. 34).

[Ayd+12] Hasan Aydin, Volkan Kizilgöz, Idil Günes Tatar, Çagr Damar, Ali Riza Ugan, Irem Paker, and Baki Hekimoglu. "Detection of prostate cancer with magnetic resonance imaging: optimization of T1-weighted, T2-weighted, dynamic-enhanced T1-weighted, diffusion-weighted imaging apparent diffusion coefficient mapping sequences and MR spectroscopy, correlated with biopsy and histopathological findings." In: *Journal of computer assisted tomography* 36.1 (2012), pp. 30–45 (cit. on p. 1).

[Bab+05] Andriy M Babsky, Shahryar K Hekmatyar, Hong Zhang, James L Solomon, and Navin Bansal. "Application of 23Na MRI to monitor chemotherapeutic response in RIF-1 tumors." In: *Neoplasia* 7.7 (2005), pp. 658–666 (cit. on p. 34).

[Bab+07] Andriy M Babsky, Hong Zhang, Shahryar K Hekmatyar, Gary D Hutchins, and Navin Bansal. "Monitoring chemotherapeutic response in RIF-1 tumors by single-quantum and triple-quantum-filtered 23Na MRI, 1H diffusion-weighted MRI and PET imaging." In: *Magnetic resonance imaging* 25.7 (2007), pp. 1015–1023 (cit. on p. 34).

[Bai+18] Ruiliang Bai, Charles S Springer Jr, Dietmar Plenz, and Peter J Basser. "Fast, Na+/K+ pump driven, steady-state transcytolemmal water exchange in neuronal tissue: A study of rat brain cortical cultures." In: *Magnetic resonance in medicine* 79.6 (2018), pp. 3207–3217 (cit. on p. 27).

[BCS12] Ehsan H Balagamwala, Samuel T Chao, and John H Suh. "Principles of radiobiology of stereotactic radiosurgery and clinical applications in the central nervous system." In: *Technology in cancer research & treatment* 11.1 (2012), pp. 3–13 (cit. on p. 100).

[Ban12] Peter A Bandettini. "Twenty years of functional MRI: the science and the stories." In: *Neuroimage* 62.2 (2012), pp. 575–588 (cit. on p. 1).

[Ban07] Peter Bandettini. "Functional MRI today." In: *International Journal of Psychophysiology* 63.2 (2007), pp. 138–145 (cit. on p. 1).

[Bar+18] Tristan Barrett, Frank Riemer, Mary A McLean, Josh Kaggie, Fraser Robb, James S Tropp, Anne Warren, Ola Bratt, Nimish Shah, Vincent J Gnanapragasam, Fiona J Gilbert, Martin J Graves, and Ferdia A Gallagher. "Quantification of total and intracellular sodium concentration in primary prostate cancer and adjacent normal prostate tissue with magnetic resonance imaging." In: *Investigative radiology* 53.8 (2018), pp. 450–456 (cit. on pp. 36, 102, 103).

[Bar+20] Tristan Barrett, Frank Riemer, Mary A McLean, Joshua D Kaggie, Fraser Robb, Anne Y Warren, Martin J Graves, and Ferdia A Gallagher. "Molecular imaging of the prostate: Comparing total sodium concentration quantification in prostate cancer and normal tissue using dedicated 13C and 23Na endorectal coils." In: *Journal of Magnetic Resonance Imaging* 51.1 (2020), pp. 90–97 (cit. on pp. 36, 102, 103).

[Bau+21] Dominik F Bauer, Anne Adlung, Irène Brumer, Alena-Kathrin Golla, Tom Russ, Eva Oelschlegel, Fabian Tollens, Sven Clausen, Philipp Aumüller, Lothar R Schad, Dominik Nörenberg, and Frank G Zöllner. "An anthropomorphic pelvis phantom for MR-guided prostate interventions." In: *Magnetic Resonance in Medicine* (2021) (cit. on p. 30).

[BBN14] Nadia Benkhedah, Peter Bachert, and Armin M Nagel. "Two-pulse biexponential-weighted 23Na imaging." In: *Journal of Magnetic Resonance* 240 (2014), pp. 67–76 (cit. on p. 29).

[Ben+13] Nadia Benkhedah, Peter Bachert, Wolfhard Semmler, and Armin M Nagel. "Three-dimensional biexponential weighted 23Na imaging of the human brain with higher SNR and shorter acquisition time." In: *Magnetic resonance in medicine* 70.3 (2013), pp. 754–765 (cit. on pp. 1, 29).

[Ben+16] Nadia Benkhedah, Stefan H Hoffmann, Armin Biller, and Armin M Nagel. "Evaluation of adaptive combination of 30-channel head receive coil array data in 23 N a MR imaging." In: *Magnetic resonance in medicine* 75.2 (2016), pp. 527–536 (cit. on p. 29).

[Ber+19] Jose Bernal, Kaisar Kushibar, Daniel S Asfaw, Sergi Valverde, Arnau Oliver, Robert Martí, and Xavier Lladó. "Deep convolutional neural networks for brain image analysis on magnetic resonance imaging: a review." In: *Artificial intelligence in medicine* 95 (2019), pp. 64–81 (cit. on pp. 2, 30, 31).

[BKZ04] Matt A Bernstein, Kevin F King, and Xiaohong Joe Zhou. *Handbook of MRI pulse sequences*. Elsevier, 2004 (cit. on p. 1).

[Bil+16] Armin Biller, Stephanie Badde, Armin M Nagel, Jan-Oliver Neumann, Wolfgang Wick, Anne Hertenstein, Martin Bendszus, Felix Sahm, Nadia Benkhedah, and Jens P Kleesiek. "Improved brain tumor classification by sodium MR imaging: prediction of IDH mutation status and tumor progression." In: *American Journal of Neuroradiology* 37.1 (2016), pp. 66–73 (cit. on pp. 34, 101).

[Bil90] Henny H Billett. "Hemoglobin and hematocrit." In: *Clinical Methods: The History, Physical, and Laboratory Examinations. 3rd edition* (1990) (cit. on pp. 102, 106).

[Blo46] Felix Bloch. "Nuclear induction." In: *Physical review* 70.7-8 (1946), p. 460 (cit. on p. 7).

[BPP48] Nicolaas Bloembergen, Edward M Purcell, and Robert V Pound. "Relaxation effects in nuclear magnetic resonance absorption." In: *Physical review* 73.7 (1948), p. 679 (cit. on pp. 15, 19).

[Boa+94] Fernando E Boada, James D Christensen, Frank R Huang-Hellinger, Timothy G Reese, and Keith R Thulborn. "Quantitative in vivo tissue sodium concentration maps: the effects of biexponential relaxation." In: *Magnetic resonance in medicine* 32.2 (1994), pp. 219–223 (cit. on pp. 2, 27, 91).

[Boa+97a] Fernando E Boada, Joseph S Gillen, Douglas C Noll, Gary X Shen, and Keith R Thulborn. "Data acquisition and postprocessing strategies for fast quantitative sodium imaging." In: *International journal of imaging systems and technology* 8.6 (1997), pp. 544–550 (cit. on p. 26).

[Boa+97b] Fernando E Boada, Joseph S Gillen, Gary X Shen, Sam Y Chang, and Keith R Thulborn. "Fast three dimensional sodium imaging." In: *Magnetic resonance in medicine* 37.5 (1997), pp. 706–715 (cit. on pp. 2, 26, 29).

[Boa+04] Fernando E Boada, Costin Tanase, Denise Davis, K Walter, Alejandro Torres-Trejo, M Couce, R Hamilton, Douglas Kondziolka, Walter S Bartynski, and Frank S Lieberman. "Non-invasive assessment of tumor proliferation using triple quantum filtered ^{23}Na MRI: technical challenges and solutions." In: *The 26th Annual International Conference of the IEEE Engineering in Medicine and Biology Society*. Vol. 2. IEEE. 2004, pp. 5238–5241 (cit. on p. 34).

[Boe04] Chris Boesch. "Nobel Prizes for nuclear magnetic resonance: 2003 and historical perspectives." In: *Journal of Magnetic Resonance Imaging: An Official Journal of the International Society for Magnetic Resonance in Medicine* 20.2 (2004), pp. 177–179 (cit. on p. 7).

[Bok+06] Hirokazu Bokura, Shotai Kobayashi, Shuhei Yamaguchi, Kenichi Iijima, Atsushi Nagai, Genya Toyoda, Hiroaki Oguro, and Kazuo Takahashi. "Silent brain infarction and subcortical white matter lesions increase the risk of stroke and mortality: a prospective cohort study." In: *Journal of stroke and cerebrovascular diseases* 15.2 (2006), pp. 57–63 (cit. on pp. 34, 92).

[Bri+14] Leslie R Bridges, Joycelyn Andoh, Andrew J Lawrence, Cheryl HL Khoong, Wayne W Poon, Margaret M Esiri, Hugh S Markus, and Atticus H Hainsworth. "Blood-brain barrier dysfunction and cerebral small vessel disease (arteriolosclerosis) in brains of older people." In: *Journal of Neuropathology & Experimental Neurology* 73.11 (2014), pp. 1026–1033 (cit. on p. 34).

[Bro+19] Nolan C Broeke, Justin Peterson, Joseph Lee, Peter R Martin, Adam Farag, Jose A Gomez, Madeleine Moussa, Mena Gaed, Joseph Chin, Stephen E Pautler, Aaron Ward, Glenn Bauman, Robert Bartha, and Timothy J Scholl. "Characterization of clinical human prostate cancer lesions using 3.0-T sodium MRI registered to Gleason-graded whole-mount histopathology." In: *Journal of Magnetic Resonance Imaging* 49.5 (2019), pp. 1409–1419 (cit. on pp. 36, 102, 103).

[BB00] Thomas Brott and Julien Bogousslavsky. "Treatment of acute ischemic stroke." In: *New England Journal of Medicine* 343.10 (2000), pp. 710–722 (cit. on pp. 3, 33).

[Bro+16] Paul D Brown, Kurt Jaeckle, Karla V Ballman, Elana Farace, Jane H Cerhan, S Keith Anderson, Xiomara W Carrero, Fred G Barker, Richard Deming, Stuart H Burri, et al. "Effect of radiosurgery alone vs radiosurgery with whole brain radiation therapy on cognitive function in patients with 1 to 3 brain metastases: a randomized clinical trial." In: *Jama* 316.4 (2016), pp. 401–409 (cit. on p. 35).

[BSJ19] Deborah Burstein and Charles S Springer Jr. "Sodium MRI revisited." In: *Magnetic resonance in medicine* 82.2 (2019), pp. 521–524 (cit. on pp. 1, 26, 27, 32, 103).

[BLH02] Mark Bydder, David J Larkman, and Joseph V Hajnal. "Combination of signals from array coils using image-based estimation of coil sensitivity profiles." In: *Magnetic Resonance in Medicine: An Official Journal of the International Society for Magnetic Resonance in Medicine* 47.3 (2002), pp. 539–548 (cit. on pp. 29, 106).

[Cam+80] Ivan L Cameron, Nancy KR Smith, Thomas B Pool, and Rodney L Sparks. "Intracellular concentration of sodium and other elements as related to mitogenesis and oncogenesis in vivo." In: *Cancer research* 40.5 (1980), pp. 1493–1500 (cit. on pp. 34, 99, 101).

[Cha+07] Julio A Chalela, Chelsea S Kidwell, Lauren M Nentwich, Marie Luby, John A Butman, Andrew M Demchuk, Michael D Hill, Nicholas Patronas, Lawrence Latour, and Steven Warach. "Magnetic resonance imaging and computed tomography in emergency assessment of patients with suspected acute stroke: a prospective comparison." In: *The Lancet* 369.9558 (2007), pp. 293–298 (cit. on pp. 1, 34).

[Cha+09] Eric L Chang, Jeffrey S Wefel, Kenneth R Hess, Pamela K Allen, Frederick F Lang, David G Kornguth, Rebecca B Arbuckle, J Michael Swint, Almon S Shiu, Moshe H Maor, et al. "Neurocognition in patients with brain metastases treated with radiosurgery or radiosurgery plus whole-brain irradiation: a randomised controlled trial." In: *The lancet oncology* 10.11 (2009), pp. 1037–1044 (cit. on p. 35).

[Che+17] Zengai Chen, Jinyan Zu, Xiaojie Lu, Jianming Ni, Jianrong Xu, et al. "Assessment of stereotactic radiosurgery treatment response for brain metastases using MRI based diffusion index." In: *European journal of radiology open* 4 (2017), pp. 84–88 (cit. on p. 35).

[Coh08] Bernard L Cohen. "The linear no-threshold theory of radiation carcinogenesis should be rejected." In: *J Am Physicians Surg* 13.3 (2008), pp. 70–76 (cit. on p. 100).

[Con+00] Chris D Constantinides, Joseph S Gillen, Fernando E Boada, Martin G Pomper, and Paul A Bottomley. "Human skeletal muscle: sodium MR imaging and quantification—potential applications in exercise and disease." In: *Radiology* 216.2 (2000), pp. 559–568 (cit. on p. 27).

[DS+09] Arnaldo Neves Da Silva, Kazuki Nagayama, David Schlesinger, and Jason P Sheehan. "Early brain tumor metastasis reduction following Gamma Knife surgery." In: *Journal of neurosurgery* 110.3 (2009), pp. 547–552 (cit. on p. 35).

[Dam71] Raymond Damadian. "Tumor detection by nuclear magnetic resonance." In: *Science* 171.3976 (1971), pp. 1151–1153 (cit. on p. 19).

[DV+10] Pieter J De Visschere, Gert O De Meerleer, Jurgen J Futterer, and Geert M Villeirs. "Role of MRI in follow-up after focal therapy for prostate carcinoma." In: *American Journal of Roentgenology* 194.6 (2010), pp. 1427–1433 (cit. on p. 36).

[DBC03] Joseph O Deasy, Angel I Blanco, and Vanessa H Clark. "CERR: a computational environment for radiotherapy research." In: *Medical physics* 30.5 (2003), pp. 979–985 (cit. on p. 57).

[DM10] Stéphanie Debette and HS Markus. "The clinical importance of white matter hyperintensities on brain magnetic resonance imaging: systematic review and meta-analysis." In: *Bmj* 341 (2010) (cit. on pp. 34, 92).

[Dee+19] Surrin S Deen, Frank Riemer, Mary A McLean, Andrew B Gill, Joshua D Kaggie, James T Grist, Robin Crawford, John Latimer, Peter Baldwin, Helena M Earl, et al. "Sodium MRI with 3D-cones as a measure of tumour cellularity in high grade serous ovarian cancer." In: *European journal of radiology open* 6 (2019), pp. 156–162 (cit. on p. 36).

[Des+17] Kimberly L Desmond, Hatef Mehrabian, Sofia Chavez, Arjun Sahgal, Hany Soliman, Radoslaw Rola, and Greg J Stanisz. "Chemical exchange saturation transfer for predicting response to stereotactic radiosurgery in human brain metastasis." In: *Magnetic resonance in medicine* 78.3 (2017), pp. 1110–1120 (cit. on pp. 35, 100).

[Dev12] Slobodan Devic. "MRI simulation for radiotherapy treatment planning." In: *Medical physics* 39.11 (2012), pp. 6701–6711 (cit. on pp. 1, 35).

[Dic+11] Louise Dickinson, Hashim U Ahmed, Clare Allen, Jelle O Barentsz, Brendan Carey, Jurgen J Futterer, Stijn W Heijmink, Peter J Hoskin, Alex Kirkham, Anwar R Padhani, et al. "Magnetic resonance imaging for the detection, localisation, and characterisation of prostate cancer: recommendations from a European consensus meeting." In: *European urology* 59.4 (2011), pp. 477–494 (cit. on pp. 1, 35).

[Don+19] Maxime Donadieu, Yann Le Fur, Adil Maarouf, Soraya Gherib, Ben Ridley, Lauriane Pini, Stanislas Rapacchi, Sylviane Confort-Gouny, Maxime Guye, Lothar R Schad, Andrew A Maudsley, Jean Pelletier, Bertrand Audoin, Wafaa Zaaraoui, and Jean-Philippe Ranjeva. "Metabolic counterparts of sodium accumulation in multiple sclerosis: a whole brain 23Na-MRI and fast 1H-MRSI study." In: *Multiple Sclerosis Journal* 25.1 (2019), pp. 39–47 (cit. on p. 92).

[Dri+20] Ian D Driver, Robert W Stobbe, Richard G Wise, and Christian Beaulieu. "Venous contribution to sodium MRI in the human brain." In: *Magnetic resonance in medicine* 83.4 (2020), pp. 1331–1338 (cit. on p. 100).

[Ege+02] Lars Egevad, T Granfors, L Karlberg, A Bergh, and Per Stattin. "Prognostic value of the Gleason score in prostate cancer." In: *BJU international* 89.6 (2002), pp. 538–542 (cit. on p. 36).

[Eis+16] Philipp Eisele, Simon Konstandin, Martin Griebe, Kristina Szabo, Marc E Wolf, Angelika Alonso, Anne Ebert, Julia Serwane, Christina Rossmanith, Michael G Hennerici, Lothar R Schad, and Achim Gass. "Heterogeneity of acute multiple sclerosis lesions on sodium (23Na) MRI." In: *Multiple Sclerosis Journal* 22.8 (2016), pp. 1040–1047 (cit. on p. 92).

[Eis+19] Philipp Eisele, Simon Konstandin, Kristina Szabo, Anne Ebert, Christina Roßmanith, Nadia Paschke, Martin Kerschensteiner, Michael Platten, Stefan O Schoenberg, Lothar R Schad, and Achim Gass. "Temporal evolution of acute multiple sclerosis lesions on serial sodium (23Na) MRI." In: *Multiple sclerosis and related disorders* 29 (2019), pp. 48–54 (cit. on p. 95).

[Eis+21] Philipp Eisele, Matthias Kraemer, Andreas Dabringhaus, Claudia E Weber, Anne Ebert, Michael Platten, Lothar R Schad, and Achim Gass. "Characterization of chronic active multiple sclerosis lesions with sodium (23Na) magnetic resonance imaging—preliminary observations." In: *European Journal of Neurology* (2021) (cit. on p. 27).

[Ell+14] Benjamin M Ellingson, Martin Bendszus, A Gregory Sorensen, and Whitney B Pope. "Emerging techniques and technologies in brain tumor imaging." In: *Neuro-oncology* 16.suppl_7 (2014), pp. vii12–vii23 (cit. on p. 34).

[Eo+18] Taejoon Eo, Yohan Jun, Taeseong Kim, Jinseong Jang, Ho-Joon Lee, and Dosik Hwang. "KIKI-net: cross-domain convolutional neural networks for reconstructing undersampled magnetic resonance images." In: *Magnetic resonance in medicine* 80.5 (2018), pp. 2188–2201 (cit. on p. 30).

[Fal+94] Jacques Falciola, Bernard Volet, Rolf M Anner, Marlis Moosmayer, Danielle Lacotte, and Beatrice M Anner. "Role of cell membrane Na, K-ATPase for survival of human lymphocytes in vitro." In: *Bioscience reports* 14.4 (1994), pp. 189–204 (cit. on pp. 1, 2, 26, 94).

[Far+15] Adam Farag, Justin Charles Peterson, Trevor Szekeres, Glenn Bauman, Joseph Chin, Cesare Romagnoli, Robert Bartha, and Timothy J Scholl. "Unshielded asymmetric transmit-only and endorectal receive-only radiofrequency coil for 23Na MRI of the prostate at 3 tesla." In: *Journal of Magnetic Resonance Imaging* 42.2 (2015), pp. 436–445 (cit. on pp. 32, 102, 103).

[Faz+87] Franz Fazekas, John B Chawluk, Abass Alavi, Howard I Hurtig, and Robert A Zimmerman. "MR signal abnormalities at 1.5 T in Alzheimer's dementia and normal aging." In: *American journal of roentgenology* 149.2 (1987), pp. 351–356 (cit. on p. 46).

[Faz+93] Franz Fazekas, Reinhold Kleinert, Hans Offenbacher, Reinhold Schmidt, Gertrude Kleinert, Franz Payer, Herbert Radner, and Helmut Lechner. "Pathologic correlates of incidental MRI white matter signal hyperintensities." In: *Neurology* 43.9 (1993), pp. 1683–1683 (cit. on pp. 34, 92).

[Fel+15] Iven Fellhauer, Frank G Zöllner, Johannes Schröder, Christina Degen, Li Kong, Marco Essig, Philipp A Thomann, and Lothar R Schad. "Comparison of automated brain segmentation using a brain phantom and patients with early Alzheimer's dementia or mild cognitive impairment." In: *Psychiatry Research: Neuroimaging* 233.3 (2015), pp. 299–305 (cit. on p. 104).

[Fie+13] Daniel P Fiege, Sandro Romanzetti, Christian C Mirkes, Daniel Brenner, and N Jon Shah. "Simultaneous single-quantum and triple-quantum-filtered MRI of 23Na (SISTINA)." In: *Magnetic resonance in medicine* 69.6 (2013), pp. 1691–1696 (cit. on p. 29).

[Fou22] Jean Baptiste Joseph Fourier. *Théorie analytique de la chaleur*. Chez Firmin Didot, père et fils, 1822 (cit. on p. 20).

[FA+18] Maayan Frid-Adar, Idit Diamant, Eyal Klang, Michal Amitai, Jacob Goldberger, and Hayit Greenspan. "GAN-based synthetic medical image augmentation for increased CNN performance in liver lesion classification." In: *Neurocomputing* 321 (2018), pp. 321–331 (cit. on pp. 2, 30).

[Fuk88] Kunihiko Fukushima. "Neocognitron: A hierarchical neural network capable of visual pattern recognition." In: *Neural networks* 1.2 (1988), pp. 119–130 (cit. on p. 30).

[Gao+17] Shouguo Gao, Xiangqin Cui, Xujing Wang, Maurice B Burg, and Natalia I Dmitrieva. "Cross-sectional positive association of serum lipids and blood pressure with serum sodium within the normal reference range of 135–145 mmol/L." In: *Arteriosclerosis, thrombosis, and vascular biology* 37.3 (2017), pp. 598–606 (cit. on p. 33).

[GB+03] Monica Garcia-Barros, Francois Paris, Carlos Cordon-Cardo, David Lyden, Shahin Rafii, Adriana Haimovitz-Friedman, Zvi Fuks, and Richard Kolesnick. "Tumor response to radiotherapy regulated by endothelial cell apoptosis." In: *Science* 300.5622 (2003), pp. 1155–1159 (cit. on pp. 35, 100).

[Ger+20] Teresa Gerhalter, Lena V Gast, Benjamin Marty, Michael Uder, Pierre G Carlier, and Armin M Nagel. "Assessing the variability of 23Na MRI in skeletal muscle tissue: Reproducibility and repeatability of tissue sodium concentration measurements in the lower leg at 3 T." In: *NMR in Biomedicine* 33.5 (2020), e4279 (cit. on p. 27).

[GS24] Walther Gerlach and Otto Stern. "Ueber die Richtungsquantelung im Magnetfeld." In: *Annalen der Physik* 379.16 (1924), pp. 673–699 (cit. on p. 7).

[Gib99] Josiah W Gibbs. "Fourier's series." In: *Nature* 59.1539 (1899), pp. 606–606 (cit. on p. 30).

[GNM17] Alina Gilles, Armin M Nagel, and Guillaume Madelin. "Multipulse sodium magnetic resonance imaging for multicompartment quantification: proof-of-concept." In: *Scientific reports* 7.1 (2017), pp. 1–19 (cit. on p. 33).

[Gio+02] Giulio Giovannetti, Luigi Landini, Maria Filomena Santarelli, and Vincenzo Positano. "A fast and accurate simulator for the design of birdcage coils in MRI." In: *Magnetic Resonance Materials in Physics, Biology and Medicine* 15.1 (2002), pp. 36–44 (cit. on pp. 28, 101).

[Gle66] Donald F Gleason. "Classification of prostatic carcinomas." In: *Cancer Chemother. Rep.* 50 (1966), pp. 125–128 (cit. on p. 36).

[Gle92] Donald F Gleason. "Histologic grading of prostate cancer: a perspective." In: *Human pathology* 23.3 (1992), pp. 273–279 (cit. on p. 36).

[GM74] Donald F Gleason and George T Mellinger. "Prediction of prognosis for prostatic adenocarcinoma by combined histological grading and clinical staging." In: *The Journal of urology* 111.1 (1974), pp. 58–64 (cit. on p. 36).

[Gna+14] Christine Gnahm, Michael Bock, Peter Bachert, Wolfhard Semmler, Nicolas GR Behl, and Armin M Nagel. "Iterative 3D projection reconstruction of 23Na data with an 1H MRI constraint." In: *Magnetic resonance in medicine* 71.5 (2014), pp. 1720–1732 (cit. on p. 97).

[GN15] Christine Gnahm and Armin M Nagel. "Anatomically weighted second-order total variation reconstruction of 23Na MRI using prior information from 1H MRI." In: *Neuroimage* 105 (2015), pp. 452–461 (cit. on p. 29).

[Goe+20] Eric A Goethe, Ganesh Rao, Adrian Harvey, Fassil B Mesfin, Miao Li, Anita Mahajan, Jiabu Ye, and Dima Suki. "Temporal change in tumor volume following stereotactic radiosurgery to a single brain metastasis." In: *World neurosurgery* 136 (2020), e328–e333 (cit. on p. 35).

[Gon06] R Gilberto Gonzalez. "Imaging-guided acute ischemic stroke therapy: from "time is brain" to "physiology is brain"." In: *American Journal of Neuroradiology* 27.4 (2006), pp. 728–735 (cit. on pp. 3, 34).

[GBC16] Ian Goodfellow, Yoshua Bengio, and Aaron Courville. *Deep learning*. MIT press, 2016 (cit. on p. 30).

[Gra+13] Andreas Graessl, Anjuli Ruehle, Wolfgang Renz, Lukas Winter, Harald Pfeiffer, Jan Ruff, Jan Rieger, and Thoralf Niendorf. "Sodium imaging of the heart at 7T: design, evaluation and application of a four-channel transmit/receive surface coil array." In: *Journal of Cardiovascular Magnetic Resonance* 15.1 (2013), W14 (cit. on p. 27).

[Gra14] Benjamin Graham. "Fractional max-pooling." In: *arXiv preprint arXiv:1412.6071* (2014) (cit. on p. 31).

[Gra+19] Aude-Marie Grapperon, Ben Ridley, Annie Verschueren, Adil Maarouf, Sylviane Confort-Gouny, Etienne Fortanier, Lothar Schad, Maxime Guye, Jean-Philippe Ranjeva, Shahram Attarian, and Wafaa Zaaraoui. "Quantitative brain sodium MRI depicts corticospinal impairment in amyotrophic lateral sclerosis." In: *Radiology* 292.2 (2019), pp. 422–428 (cit. on p. 27).

[GP95] Hákon Gudbjartsson and Samuel Patz. "The rician distribution of noisy mri data." In: *Magnetic Resonance in Medicine* 34.6 (1995), pp. 910–914 (cit. on p. 23).

[GG82] Raj K Gupta and Pratima Gupta. "Direct observation of resolved resonances from intra-and extracellular sodium-23 ions in NMR studies of intact cells and tissues using dysprosium (III) tripolyphosphate as paramagnetic shift reagent." In: *Journal of Magnetic Resonance (1969)* 47.2 (1982), pp. 344–350 (cit. on p. 27).

[GHN06] Paul T Gurney, Brian A Hargreaves, and Dwight G Nishimura. "Design and analysis of a practical 3D cones trajectory." In: *Magnetic Resonance in Medicine: An Official Journal of the International Society for Magnetic Resonance in Medicine* 55.3 (2006), pp. 575–582 (cit. on pp. 2, 29).

[Haa+99] E Mark Haacke, Robert W Brown, Michael R Thompson, and Ramesh Venkatesan. *Magnetic Resonance Imaging: Physical Principles and Sequence Design*. John Wiley & Sons, 1999, p. 944. ISBN: 9780471351283 (cit. on pp. 1, 7).

[Hae+20] Alexa Haeger, Arthur Coste, Cécile Lerman-Rabrait, Julien Lagarde, Jörg B Schulz, Alexandre Vignaud, Marie Sarazin, Michel Bottlaender, Kathrin Reetz, Sandro Romanzetti, and Fawzi Boumezbeur. "Quantitative sodium imaging using ultra-high field magnetic resonance imaging in patients with Alzheimer's disease: Neuroimaging/Op-

timal neuroimaging measures for tracking disease progression." In: *Alzheimer's & Dementia* 16 (2020), e042107 (cit. on p. 27).

[Hah50] Erwin L Hahn. "Spin echoes." In: *Physical review* 80.4 (1950), p. 580 (cit. on p. 15).

[HSY19] Yoseo Han, Leonard Sunwoo, and Jong Chul Ye. "K-Space Deep Learning for Accelerated MRI." In: *IEEE transactions on medical imaging* 39.2 (2019), pp. 377–386 (cit. on p. 105).

[Han+15] Stefan Haneder, Johannes Michael Budjan, Stefan Oswald Schoenberg, Simon Konstandin, Lothar Rudi Schad, Ralf Dieter Hofheinz, Veronika Gramlich, Frederik Wenz, Frank Lohr, and Judit Boda-Heggemann. "Dose-dependent changes in renal 1 H-/23 Na MRI after adjuvant radiochemotherapy for gastric cancer." In: *Strahlentherapie und Onkologie* 191.4 (2015), pp. 356–364 (cit. on p. 35).

[Han+11] Stefan Haneder, Simon Konstandin, John N Morelli, Armin M Nagel, Frank G Zoellner, Lothar R Schad, Stefan O Schoenberg, and Henrik J Michaely. "Quantitative and qualitative 23Na MR imaging of the human kidneys at 3 T: before and after a water load." In: *Radiology* 260.3 (2011), pp. 857–865 (cit. on p. 2).

[Han+13] Stefan Haneder, Simon Konstandin, John N Morelli, Lothar R Schad, Stefan O Schoenberg, and Henrik J Michaely. "Assessment of the renal corticomedullary 23Na gradient using isotropic data sets." In: *Academic radiology* 20.4 (2013), pp. 407–413 (cit. on pp. 33, 36, 91, 93, 106).

[Han+14] Stefan Haneder, Henrik J Michaely, Simon Konstandin, Lothar R Schad, John N Morelli, Bernhard K Krämer, Stefan O Schoenberg, and Alexander Lammert. "3T Renal 23 Na-MRI: effects of desmopressin in patients with central diabetes insipidus." In: *Magnetic Resonance Materials in Physics, Biology and Medicine* 27.1 (2014), pp. 47–52 (cit. on p. 27).

[Har+10] Michael G Harrington, Ronald M Salomon, Janice M Pogoda, Elena Oborina, Neil Okey, Benjamin Johnson, Dennis Schmidt, Alfred N Fonteh, and Nathan F Dalleska. "Cerebrospinal fluid sodium rhythms." In: *Cerebrospinal fluid research* 7.1 (2010), pp. 1–9 (cit. on pp. 33, 93, 94).

[Har+01] Robin K Harris, Edwin D Becker, Sonia M Cabral De Menezes, Robin Goodfellow, and Pierre Granger. "NMR nomenclature. Nuclear spin properties and conventions for chemical shifts (IUPAC Recommendations 2001)." In: *Pure and Applied Chemistry* 73.11 (2001), pp. 1795–1818 (cit. on pp. 16, 17).

[Has+91] Takahiro Hashimoto, Hiroo Ikehira, Hiroshi Fukuda, Akira Yamaura, Osamu Watanabe, Yukio Tateno, Ryouichi Tanaka, and Howard E Simon. "In vivo sodium-23 MRI in brain tumors: evaluation of preliminary clinical experience." In: *American journal of physiologic imaging* 6.2 (1991), pp. 74–80 (cit. on pp. 34, 99).

[Hau+12] Daniel Hausmann, Simon Konstandin, Friedrich Wetterling, Stefan Haneder, Armin M Nagel, Dietmar J Dinter, Stefan O Schönberg, Frank G Zöllner, and Lothar R Schad. "Apparent diffusion coefficient and sodium concentration measurements in human prostate tissue via hydrogen-1 and sodium-23 magnetic resonance imaging in a clinical setting at 3 T." In: *Investigative radiology* 47.12 (2012), pp. 677–682 (cit. on pp. 32, 36, 102, 103).

[Haw+97] Hans Hawighorst, Marco Essig, Jürgen Debus, Michael V Knopp, Rita Engenhart-Cabilic, SO Schönberg, Gunnar Brix, Ivan Zuna, and Gerhard van Kaick. "Serial MR imaging of intracranial metastases after radiosurgery." In: *Magnetic resonance imaging* 15.10 (1997), pp. 1121–1132 (cit. on p. 35).

[Hay+85] Cecil E Hayes, William A Edelstein, John F Schenck, Otward M Mueller, and Matthew Eash. "An efficient, highly homogeneous radiofrequency coil for whole-body NMR imaging at 1.5 T." In: *Journal of Magnetic Resonance (1969)* 63.3 (1985), pp. 622–628 (cit. on p. 39).

[HZ12] Caroline Hayhurst and Gelareh Zadeh. "Tumor pseudoprogression following radiosurgery for vestibular schwannoma." In: *Neuro-oncology* 14.1 (2012), pp. 87–92 (cit. on p. 35).

[He+16] Kaiming He, Xiangyu Zhang, Shaoqing Ren, and Jian Sun. "Deep residual learning for image recognition." In: *Proceedings of the IEEE conference on computer vision and pattern recognition*. 2016, pp. 770–778 (cit. on pp. 31, 52).

[Hig+19] Toru Higaki, Yuko Nakamura, Fuminari Tatsugami, Takeshi Nakaura, and Kazuo Awai. "Improvement of image quality at CT and MRI using deep learning." In: *Japanese journal of radiology* 37.1 (2019), pp. 73–80 (cit. on p. 96).

[Hil+85] Sadek K Hilal, Andrew A Maudsley, Jong Beom Ra, Howard E Simon, Peter Roschmann, Stefan Wittekoek, ZH Cho, and SK Mun. "In vivo NMR imaging of sodium-23 in the human head." In: *Journal of computer assisted tomography* 9.1 (1985), pp. 1–7 (cit. on pp. 1, 26, 32).

[Hin+18] Walter A Hinds, Amrit Misra, Michael R Sperling, Ashwini Sharan, Joseph I Tracy, and Karen A Moxon. "Enhanced co-registration methods to improve intracranial electrode contact localization." In: *NeuroImage: Clinical* 20 (2018), pp. 398–406 (cit. on pp. 104, 105).

[HL98] David G Hoel and Ping Li. "Threshold models in radiation carcinogenesis." In: *Health physics* 75.3 (1998), pp. 241–250 (cit. on p. 100).

[HSR20] Michaela AU Hoesl, Lothar R Schad, and Stanislas Rapacchi. "Efficient 23Na triple-quantum signal imaging on clinical scanners: Cartesian imaging of single and triple-quantum 23Na (CRISTINA)." In: *Magnetic resonance in medicine* 84.5 (2020), pp. 2412–2428 (cit. on p. 29).

[Hou00] David I Hoult. "The principle of reciprocity in signal strength calculations—a mathematical guide." In: *Concepts in Magnetic Resonance: An Educational Journal* 12.4 (2000), pp. 173–187 (cit. on p. 28).

[HR76] David I Hoult and RE Richards. "The signal-to-noise ratio of the nuclear magnetic resonance experiment." In: *Journal of Magnetic Resonance (1969)* 24.1 (1976), pp. 71–85 (cit. on pp. 16, 28, 39, 101).

[Hsu+01] Chi-Yuan Hsu, David W Bates, Gilad J Kuperman, and Gary C Curhan. "Relationship between hematocrit and renal function in men and women." In: *Kidney international* 59.2 (2001), pp. 725–731 (cit. on pp. 102, 106).

[Hu+20] Ruomin Hu, Dennis Kleimaier, Matthias Malzacher, Michaela AU Hoesl, Nadia K Paschke, and Lothar R Schad. "X-nuclei imaging: current state, technical challenges, and future directions." In: *Journal of Magnetic Resonance Imaging* 51.2 (2020), pp. 355–376 (cit. on pp. 1, 2, 26–29, 32, 93).

[Hua+17] Jonathan Huang, Vivek Rathod, Chen Sun, Menglong Zhu, Anoop Korattikara, Alireza Fathi, Ian Fischer, Zbigniew Wojna, Yang Song, Sergio Guadarrama, et al. "Speed/accuracy trade-offs for modern convolutional object detectors." In: *Proceedings of the IEEE conference on computer vision and pattern recognition*. 2017, pp. 7310–7311 (cit. on p. 30).

[HW62] David H Hubel and Torsten N Wiesel. "Receptive fields, binocular interaction and functional architecture in the cat's visual cortex." In: *The Journal of physiology* 160.1 (1962), pp. 106–154 (cit. on p. 30).

[Hus+09] Muhammad S Hussain, Robert W Stobbe, Yusuf A Bhagat, Derek Emery, Kenneth S Butcher, Dulka Manawadu, Nasir Rizvi, Perkash Maheshwari, James Scozzafava, Ashfaq Shuaib, and Christian Beaulieu. "Sodium imaging intensity increases with time after human ischemic stroke." In: *Annals of Neurology: Official Journal of the American Neurological Association and the Child Neurology Society* 66.1 (2009), pp. 55–62 (cit. on pp. 27, 34, 93, 94).

[Ibr+01] Tamer S Ibrahim, Robert Lee, Brian A Baertlein, and Pierre-Marie L Robitaille. "B1 field homogeneity and SAR calculations for the birdcage coil." In: *Physics in Medicine & Biology* 46.2 (2001), p. 609 (cit. on pp. 28, 106).

[Ign83] Ronald J Ignelzi. "An analysis of the nuclear sodium content of human normal glia as well as tumors of glial and nonglial origin." In: *Neurological research* 5.2 (1983), pp. 79–84 (cit. on pp. 34, 99, 101).

[Ioa+15] Yani Ioannou, Duncan Robertson, Jamie Shotton, Roberto Cipolla, and Antonio Criminisi. "Training cnns with low-rank filters for efficient image classification." In: *arXiv preprint arXiv:1511.06744* (2015) (cit. on p. 32).

[IS15] Sergey Ioffe and Christian Szegedy. "Batch normalization: Accelerating deep network training by reducing internal covariate shift." In: *International conference on machine learning*. PMLR. 2015, pp. 448–456 (cit. on p. 31).

[Isa+90] Gamaliel Isaac, Mitchell D Schnall, Robert E Lenkinski, and Katherine Vogele. "A design for a double-tuned birdcage coil for use in an integrated MRI/MRS examination." In: *Journal of Magnetic Resonance (1969)* 89.1 (1990), pp. 41–50 (cit. on pp. 28, 101, 106).

[Jab+20] Paola Anna Jablonska, Diego Serrana Tejero, Alfonso Calvo González, Marta Gimeno Morales, Leire Arbea Moreno, Marta Moreno-Jiménez, Alejandro García-Consuegra, Santiago M Martín Pastor, Pablo D Domínguez Echavarri, Ignacio Gil-Bazo, Luis I Ramos García, and Javier J Aristu. "Repeated stereotactic radiosurgery for recurrent brain metastases: An effective strategy to control intracranial oligometastatic disease." In: *Critical Reviews in Oncology/Hematology* 153 (2020), p. 103028 (cit. on p. 35).

[Jac+10] Michael A Jacobs, Vered Stearns, Antonio C Wolff, Katarzyna Macura, Pedram Argani, Nagi Khouri, Theodore Tsangaris, Peter B Barker, Nancy E Davidson, Zaver M Bhujwalla, David A Bluemke, and Ronald Ouwerkerk. "Multiparametric magnetic resonance imaging, spectroscopy and multinuclear (23Na) imaging monitoring of preoperative chemotherapy for locally advanced breast cancer." In: *Academic radiology* 17.12 (2010), pp. 1477–1485 (cit. on pp. 27, 100, 103).

[Jak+15] Raphael Jakubovic, Arjun Sahgal, Mark Ruschin, Ana Pejović-Milić, Rachael Milwid, and Richard I Aviv. "Non tumor perfusion changes following stereotactic radiosurgery to brain metastases." In: *Technology in cancer research & treatment* 14.4 (2015), pp. 497–503 (cit. on pp. 35, 100).

[Jam+15] Judy R James, Anshuman Panda, Chen Lin, Ulrike Dydak, Brian M Dale, and Navin Bansal. "In vivo sodium MR imaging of the abdomen at 3T." In: *Abdominal imaging* 40.7 (2015), pp. 2272–2280 (cit. on p. 27).

[Jen+02] Dominique Jennings, B Nicholas Hatton, Jingyu Guo, Jean-Philippe Galons, Theodore P Trouard, Natarajan Raghunand, James Marshall, and Robert J Gillies. "Early response of prostate carcinoma xenografts to docetaxel chemotherapy monitored with diffusion MRI." In: *Neoplasia* 4.3 (2002), pp. 255–262 (cit. on p. 36).

[JL89] Peter M Joseph and Dongfeng Lu. "A technique for double resonant operation of birdcage imaging coils." In: *IEEE transactions on medical imaging* 8.3 (1989), pp. 286–294 (cit. on pp. 1, 28).

[KS80] James F Kaiser and Ronald W Schafer. "On the use of the I 0-sinh window for spectrum analysis." In: *IEEE Transactions on Acoustics, Speech, and Signal Processing* 28.1 (1980), pp. 105–107 (cit. on p. 42).

[Kan+10] Hideyuki Kano, Douglas Kondziolka, Javier Lobato-Polo, Oscar Zorro, John C Flickinger, and L Dade Lunsford. "T1/T2 matching to differentiate tumor growth from radiation effects after stereotactic radiosurgery." In: *Neurosurgery* 66.3 (2010), pp. 486–492 (cit. on pp. 1, 35).

[Kar+99] Jari O Karonen, Ritva L Vanninen, Yawu Liu, Leif Østergaard, Jyrki T Kuikka, Juho Nuutinen, Esko J Vanninen, PL Kaarina Partanen, Pauli A Vainio, Katja Korhonen, Jussi Perkiö, Reina Roivainen, Juhani Sivenius, and Hannu J Aronen. "Combined diffusion and perfusion MRI with correlation to single-photon emission CT in acute ischemic stroke: ischemic penumbra predicts infarct growth." In: *Stroke* 30.8 (1999), pp. 1583–1590 (cit. on p. 34).

[KJS17] Baris Kayalibay, Grady Jensen, and Patrick van der Smagt. "CNN-based segmentation of medical imaging data." In: *arXiv preprint arXiv:1701.03056* (2017) (cit. on pp. 2, 30).

[Ken+18] Alexander P Kenigsberg, Tsutomu Tamada, Andrew B Rosenkrantz, Elton Llukani, Fang-Ming Deng, Jonathan Melamed, Ming Zhou, and Herbert Lepor. "Multiparametric magnetic resonance imaging identifies significant apical prostate cancers." In: *BJU international* 121.2 (2018), pp. 239–243 (cit. on pp. 3, 35).

[Kid+13] Chelsea S Kidwell, Max Wintermark, Deidre A De Silva, Timothy J Schaewe, Reza Jahan, Sidney Starkman, Tudor Jovin, Jason Hom, Mouhammad Jumaa, Jeffrie Schreier, Jeffrey Gornbein, David S Liebeskind, Jeffry R Alger, and Jeffrey L Saver. "Multiparametric MRI and CT models of infarct core and favorable penumbral imaging patterns in acute ischemic stroke." In: *Stroke* 44.1 (2013), pp. 73–79 (cit. on p. 34).

[Kim+14] Bum Joon Kim, Hyun Goo Kang, Hye-Jin Kim, Sung-Ho Ahn, Na Young Kim, Steven Warach, and Dong-Wha Kang. "Magnetic resonance imaging in acute ischemic stroke treatment." In: *Journal of stroke* 16.3 (2014), p. 131 (cit. on pp. 27, 34).

[Kim+21] Sang-Young Kim, Junghyun Song, Jong-Hyun Yoon, Kyoung-Nam Kim, Jun-Young Chung, and Young Noh. "Voxel-wise partial volume correction method for accurate estimation of tissue sodium concentration in 23Na-MRI at 7 T." In: *NMR in Biomedicine* 34.2 (2021), e4448 (cit. on pp. 29, 104).

[KB14] Diederik P Kingma and Jimmy Ba. "Adam: A method for stochastic optimization." In: *arXiv preprint arXiv:1412.6980* (2014) (cit. on p. 53).

[Koh+15] Myeong Ju Koh, Ho Sung Kim, Choong Gon Choi, and Sang Joon Kim. "Which is the best advanced MR imaging protocol for predicting recurrent metastatic brain tumor following gamma-knife radiosurgery: focused on perfusion method." In: *Neuroradiology* 57.4 (2015), pp. 367–376 (cit. on p. 35).

[Kok+16] Jan Kokavec, San H Min, Mei H Tan, Jagjit S Gilhotra, Henry S Newland, Shane R Durkin, John Grigg, and Robert J Casson. "Biochemical analysis of the living human vitreous." In: *Clinical & experimental ophthalmology* 44.7 (2016), pp. 597–609 (cit. on pp. 32, 33).

[Kol+87] Nancy H Kolodny, Evangelos S Gragoudas, Donald J D'amico, Susan J Kohler, Johanna M Seddon, Elizabeth J Murphy, Christina Yun, and Daniel M Albert. "Proton and sodium 23 magnetic resonance imaging of human ocular tissues: a model study." In: *Archives of ophthalmology* 105.11 (1987), pp. 1532–1536 (cit. on p. 26).

[KN14] Simon Konstandin and Armin M Nagel. "Measurement techniques for magnetic resonance imaging of fast relaxing nuclei." In: *Magnetic Resonance Materials in Physics, Biology and Medicine* 27.1 (2014), pp. 5–19 (cit. on p. 29).

[KS13] Simon Konstandin and Lothar R Schad. "Two-dimensional radial sodium heart MRI using variable-rate selective excitation and retrospective electrocardiogram gating with golden angle increments." In: *Magnetic resonance in medicine* 70.3 (2013), pp. 791–799 (cit. on pp. 32, 36, 61, 102).

[KS14] Simon Konstandin and Lothar R Schad. "30 years of sodium/X-nuclei magnetic resonance imaging." In: *Magnetic Resonance Materials in Physics, Biology and Medicine* 27.1 (2014), pp. 1–4 (cit. on pp. 1, 2, 26, 28, 32).

[Kop+19] Simon Koppers, Edouard Coussoux, Sandro Romanzetti, Kathrin Reetz, and Dorit Merhof. "Sodium image denoising based on a convolutional denoising autoencoder." In: *Bildverarbeitung für die Medizin 2019*. Springer, 2019, pp. 98–103 (cit. on p. 96).

[Kur+08] John Kurhanewicz, Daniel Vigneron, Peter Carroll, and Fergus Coakley. "Multiparametric magnetic resonance imaging in prostate cancer: present and future." In: *Current opinion in urology* 18.1 (2008), p. 71 (cit. on p. 35).

[Kur+14] Goldie Kurtz, Gelareh Zadeh, Geneviève Gingras-Hill, Barbara-Ann Millar, Normand J Laperriere, Mark Bernstein, Haiyan Jiang, Cynthia Ménard, and Caroline Chung. "Salvage radiosurgery for brain metastases: prognostic factors to consider in patient selection." In: *International Journal of Radiation Oncology* Biology* Physics* 88.1 (2014), pp. 137–142 (cit. on p. 35).

[LaV+09] George C LaVerde, Charles A Jungreis, Edwin Nemoto, and Fernando E Boada. "Sodium time course using 23Na MRI in reversible focal brain ischemia in the monkey." In: *Journal of Magnetic Resonance Imaging: An Official Journal of the International Society for Magnetic Resonance in Medicine* 30.1 (2009), pp. 219–223 (cit. on p. 97).

[Lac+20] Sebastian Lachner, Laurent Ruck, Sebastian C Niesporek, Matthias Utzschneider, Johanna Lott, Bernhard Hensel, Arnd Dörfler, Michael Uder, and Armin M Nagel. "Comparison of optimized intensity correction methods for 23Na MRI of the human brain using a 32-channel phased array coil at 7 Tesla." In: *Zeitschrift für Medizinische Physik* 30.2 (2020), pp. 104–115 (cit. on pp. 29, 59, 60, 102).

[Lac+21] Sebastian Lachner, Matthias Utzschneider, Olgica Zaric, Lenka Minarikova, Laurent Ruck, Štefan Zbýň, Bernhard Hensel, Siegfried Trattnig, Michael Uder, and Armin M Nagel. "Compressed sensing and the use of phased array coils in 23Na MRI: a comparison of a SENSE-based and an individually combined multi-channel reconstruction." In: *Zeitschrift für Medizinische Physik* 31.1 (2021), pp. 48–57 (cit. on p. 97).

[Lau73] Paul C Lauterbur. "Image formation by induced local interactions: examples employing nuclear magnetic resonance." In: *nature* 242.5394 (1973), pp. 190–191 (cit. on p. 19).

[Lee+14] Cheng-Chia Lee, Max Wintermark, Zhiyuan Xu, Chun-Po Yen, David Schlesinger, and Jason P Sheehan. "Application of diffusion-weighted magnetic resonance imaging to predict the intracranial metastatic tumor response to gamma knife radiosurgery." In: *Journal of neuro-oncology* 118.2 (2014), pp. 351–361 (cit. on p. 35).

[LHC86] SW Lee, Sadek K Hilal, and ZH Cho. "A multinuclear magnetic resonance imaging technique-simultaneous proton and sodium imaging." In: *Magnetic resonance imaging* 4.4 (1986), pp. 343–350 (cit. on p. 26).

[LP86] Wai Hung Lee and MILTON Packer. "Prognostic importance of serum sodium concentration and its modification by converting-enzyme inhibition in patients with severe chronic heart failure." In: *Circulation* 73.2 (1986), pp. 257–267 (cit. on p. 33).

[Lef+20] Avigdor Leftin, Jens T Rosenberg, Xuegang Yuan, Teng Ma, Samuel C Grant, and Lucio Frydman. "Multiparametric classification of subacute ischemic stroke recovery with ultrafast diffusion, 23Na, and MPIO-labeled stem cell MRI at 21.1 T." In: *NMR in Biomedicine* 33.2 (2020), e4186 (cit. on p. 27).

[Lek83] Lars Leksell. "Stereotactic radiosurgery." In: *Journal of Neurology, Neurosurgery & Psychiatry* 46.9 (1983), pp. 797–803 (cit. on pp. 3, 35).

[Levo8] Malcolm H Levitt. *Spin Dynamics: Basics of Nuclear Magnetic Resonance*. 2nd ed. John Wiley & Sons, 2008, p. 740. ISBN: 9780470511176 (cit. on pp. 1, 7).

[Lew+21] Daniel Lewis, Damien J McHugh, Ka-loh Li, Xiaoping Zhu, Catherine Mcbain, Simon K Lloyd, Alan Jackson, Omar N Pathmanaban, Andrew T King, and David J Coope. "Detection of early changes in the post-radiosurgery vestibular schwannoma microenvironment using multinuclear MRI." In: *Scientific reports* 11.1 (2021), pp. 1–13 (cit. on pp. 34, 100).

[Lia+97] Jan-Ray Liao, John M Pauly, Thomas J Brosnan, and Norbert J Pelc. "Reduction of motion artifacts in cine MRI using variable-density spiral trajectories." In: *Magnetic resonance in medicine* 37.4 (1997), pp. 569–575 (cit. on p. 40).

[Lia+19] Yupeng Liao, Nazim Lechea, Arthur W Magill, Wieland A Worthoff, Vincent Gras, and N Jon Shah. "Correlation of quantitative conductivity mapping and total tissue sodium concentration at 3T/4T." In: *Magnetic resonance in medicine* 82.4 (2019), pp. 1518–1526 (cit. on pp. 32, 94, 95).

[LC16] Zhibin Liao and Gustavo Carneiro. "On the importance of normalisation layers in deep learning with piecewise linear activation units." In: *2016 IEEE Winter Conference on Applications of Computer Vision (WACV)*. IEEE. 2016, pp. 1–8 (cit. on p. 31).

[Lin+15] Nancy U Lin, Eudocia Q Lee, Hidefumi Aoyama, Igor J Barani, Daniel P Barboriak, Brigitta G Baumert, Martin Bendszus, Paul D Brown, D Ross Camidge, Susan M Chang, et al. "Response assessment criteria for brain metastases: proposal from the RANO group." In: *The lancet oncology* 16.6 (2015), e270–e278 (cit. on p. 35).

[Lin+01] Shao-Pow Lin, Sheng-Kwei Song, J Philip Miller, Joseph JH Ackerman, and Jeffrey J Neil. "Direct, longitudinal comparison of 1H and 23Na MRI after transient focal cerebral ischemia." In: *Stroke* 32.4 (2001), pp. 925–932 (cit. on pp. 27, 34, 94, 100).

[Lin21] Grace W Lindsay. "Convolutional neural networks as a model of the visual system: Past, present, and future." In: *Journal of cognitive neuroscience* 33.10 (2021), pp. 2017–2031 (cit. on p. 30).

[Lju+91] NV Ljubimova, M Kh Levitman, ED Plotnikova, and L Kh Eidus. "Endothelial cell population dynamics in rat brain after local irradiation." In: *The British journal of radiology* 64.766 (1991), pp. 934–940 (cit. on p. 100).

[LAr90] Jay S Loeffler and Eben Alexander 3rd. "The role of stereotactic radiosurgery in the management of intracranial tumors." In: *Oncology (Williston Park, NY)* 4.3 (1990), pp. 21–31 (cit. on p. 35).

[Lom+16] Jonathan Lommen, Simon Konstandin, Philipp Krämer, and Lothar R Schad. "Enhancing the quantification of tissue sodium content by MRI: time-efficient sodium B1 mapping at clinical field strengths." In: *NMR in Biomedicine* 29.2 (2016), pp. 129–136 (cit. on p. 48).

[LSD15] Jonathan Long, Evan Shelhamer, and Trevor Darrell. "Fully convolutional networks for semantic segmentation." In: *Proceedings of the IEEE conference on computer vision and pattern recognition*. 2015, pp. 3431–3440 (cit. on p. 31).

[Lot+19] Johanna Lott, Tanja Platt, Sebastian C Niesporek, Daniel Paech, Nicolas GR Behl, Thoralf Niendorf, Peter Bachert, Mark E Ladd, and Armin M Nagel. "Corrections of myocardial tissue sodium concentration measurements in human cardiac 23Na MRI at 7 Tesla." In: *Magnetic resonance in medicine* 82.1 (2019), pp. 159–173 (cit. on pp. 2, 32, 36, 61, 102).

[Lu+10] Aiming Lu, Ian C Atkinson, Theodore C Claiborne, Frederick C Damen, and Keith R Thulborn. "Quantitative sodium imaging with a flexible twisted projection pulse sequence." In: *Magnetic Resonance in Medicine: An Official Journal of the International Society for Magnetic Resonance in Medicine* 63.6 (2010), pp. 1583–1593 (cit. on pp. 2, 29).

[Lu+05] Hanzhang Lu, Lidia M Nagae-Poetscher, Xavier Golay, Doris Lin, Martin Pomper, and Peter CM Van Zijl. "Routine clinical brain MRI sequences for use at 3.0 Tesla." In: *Journal of Magnetic Resonance Imaging: An Official Journal of the International Society for Magnetic Resonance in Medicine* 22.1 (2005), pp. 13–22 (cit. on p. 1).

[LSJ02] Eileen Lüders, Helmuth Steinmetz, and Lutz Jäncke. "Brain size and grey matter volume in the healthy human brain." In: *Neuroreport* 13.17 (2002), pp. 2371–2374 (cit. on p. 92).

[LRD20] Roberta Lugano, Mohanraj Ramachandran, and Anna Dimberg. "Tumor angiogenesis: causes, consequences, challenges and opportunities." In: *Cellular and Molecular Life Sciences* 77.9 (2020), pp. 1745–1770 (cit. on p. 34).

[LL19] Alexander Selvikvåg Lundervold and Arvid Lundervold. "An overview of deep learning in medical imaging focusing on MRI." In: *Zeitschrift für Medizinische Physik* 29.2 (2019), pp. 102–127 (cit. on pp. 2, 30).

[Lup+09] Mihaela Lupu, Carole D Thomas, Philippe Maillard, Bernard Loock, Benoit Chauvin, Isabelle Aerts, Alain Croisy, Elodie Belloir, Andreas Volk, and Joel Mispelter. "23Na MRI longitudinal follow-up of PDT in a xenograft model of human retinoblastoma." In: *Photodiagnosis and photodynamic therapy* 6.3-4 (2009), pp. 214–220 (cit. on p. 34).

[Maa+17] Adil Maarouf, Bertrand Audoin, Fanelly Pariollaud, Soraya Gherib, Audrey Rico, Elisabeth Soulier, Sylviane Confort-Gouny, Maxime Guye, Lothar Schad, Jean Pelletier, Jean-Philippe Ranjeva, and Wafaa Zaaraoui. "Increased total sodium concentration in gray matter better explains cognition than atrophy in MS." In: *Neurology* 88.3 (2017), pp. 289–295 (cit. on p. 94).

[Mac96] Albert Macovski. "Noise in MRI." In: *Magnetic Resonance in Medicine* 36.3 (1996), pp. 494–497 (cit. on p. 23).

[Mad+12a] Vince I Madai, Federico C von Samson-Himmelstjerna, Miriam Bauer, Katharina L Stengl, Matthias A Mutke, Elena Tovar-Martinez, Jens Wuerfel, Matthias Endres, Thoralf Niendorf, and Jan Sobesky. "Ultrahigh-field MRI in human ischemic stroke–a 7 tesla study." In: *PLoS One* 7.5 (2012), e37631 (cit. on pp. 1, 94).

[Mad+12b] Guillaume Madelin, Gregory Chang, Ricardo Otazo, Alexej Jerschow, and Ravinder R Regatte. "Compressed sensing sodium MRI of cartilage at 7T: preliminary study." In: *Journal of magnetic resonance* 214 (2012), pp. 360–365 (cit. on p. 97).

[Mad+14] Guillaume Madelin, Richard Kline, Ronn Walvick, and Ravinder R Regatte. "A method for estimating intracellular sodium concentration and extracellular volume fraction in brain in vivo using sodium magnetic resonance imaging." In: *Scientific reports* 4.1 (2014), pp. 1–7 (cit. on pp. 33, 34, 101).

[MR13] Guillaume Madelin and Ravinder R Regatte. "Biomedical applications of sodium MRI in vivo." In: *Journal of Magnetic Resonance Imaging* 38.3 (2013), pp. 511–529 (cit. on pp. 1, 2, 17, 26, 27, 29, 32, 33, 36, 41, 48, 91–95, 97).

[MMI16] Hitoshi Maeda, Tomomi Michiue, and Takaki Ishikawa. "Postmortem Changes: Postmortem Electrolyte Disturbances." In: *Encyclopedia of Forensic and Legal Medicine (Second Edition)*. Second Edition. Elsevier, 2016, pp. 32–42 (cit. on p. 33).

[Mag+18] Francesca Maggiorelli, Alessandra Retico, E Boskamp, F Robb, Angelo Galante, Marco Fantasia, Marcello Alecci, Michela Tosetti, and Gianluigi Tiberi. "Double Tuned 1 H-23 Na Birdcage Coils for MRI at 7 T: Performance evaluation through electromagnetic simulations." In: *2018 IEEE International Symposium on Medical Measurements and Applications (MeMeA)*. IEEE. 2018, pp. 1–6 (cit. on pp. 1, 28).

[Mal+15] Ian B Malone, Kelvin K Leung, Shona Clegg, Josephine Barnes, Jennifer L Whitwell, John Ashburner, Nick C Fox, and Gerard R Ridgway. "Accurate automatic estimation of total intracranial volume: a nuisance variable with less nuisance." In: *Neuroimage* 104 (2015), pp. 366–372 (cit. on p. 104).

[Mal+19a] Matthias Malzacher, Jorge Chacon-Caldera, Nadia Paschke, and Lothar R Schad. "Feasibility study of a double resonant (1H/23Na) abdominal RF setup at 3 T." In: *Zeitschrift für Medizinische Physik* 29.4 (2019), pp. 359–367 (cit. on pp. 1, 27, 28).

[Mal+19b] Matthias Malzacher, Jorge Chacon-Caldera, Nadia Paschke, and Lothar R Schad. "Feasibility study of a double resonant 8-channel 1H/8-channel 23Na receive-only head coil at 3 Tesla." In: *Magnetic resonance imaging* 59 (2019), pp. 97–104 (cit. on pp. 1, 28).

[Man+15] Susana Muñoz Maniega, Maria C Valdés Hernández, Jonathan D Clayden, Natalie A Royle, Catherine Murray, Zoe Morris, Benjamin S Aribisala, Alan J Gow, John M Starr, Mark E Bastin, Ian J Dearyce, and Joanna M Wardlawabc. "White matter hyperintensities and normal-appearing white matter integrity in the aging brain." In: *Neurobiology of aging* 36.2 (2015), pp. 909–918 (cit. on pp. 34, 92).

[MG73] Peter Mansfield and Peter K Grannell. "NMR diffraction in solids?" In: *Journal of Physics C: solid state physics* 6.22 (1973), p. L422 (cit. on p. 19).

[Mar+06] Nimrod Maril, Yael Rosen, Glenn H Reynolds, Alex Ivanishev, Long Ngo, and Robert E Lenkinski. "Sodium MRI of the human kidney at 3 Tesla." In: *Magnetic Resonance in Medicine: An Official Journal of the International Society for Magnetic Resonance in Medicine* 56.6 (2006), pp. 1229–1234 (cit. on pp. 36, 93).

[MC19] Miguel Alejandro Marin and S Thomas Carmichael. "Mechanisms of demyelination and remyelination in the young and aged brain following white matter stroke." In: *Neurobiology of disease* 126 (2019), pp. 5–12 (cit. on pp. 34, 92).

[MCL15a] Michael Mathieu, Camille Couprie, and Yann LeCun. "Deep multi-scale video prediction beyond mean square error." In: *arXiv preprint arXiv:1511.05440* (2015) (cit. on pp. 54, 98).

[MCL15b] Michael Mathieu, Camille Couprie, and Yann LeCun. "Deep multi-scale video prediction beyond mean square error." In: *arXiv preprint arXiv:1511.05440* (2015) (cit. on p. 96).

[Mat+96] Mitsunori Matsumae, Ron Kikinis, István A Mórocz, Antonio V Lorenzo, Tamás Sándor, Marilyn S Albert, Peter McL Black, and Ferenc A Jolesz. "Age-related changes in intracranial compartment volumes in normal adults assessed by magnetic resonance imaging." In: *Journal of neurosurgery* 84.6 (1996), pp. 982–991 (cit. on pp. 33, 94, 99).

[MJU17] Michael T McCann, Kyong Hwan Jin, and Michael Unser. "Convolutional neural networks for inverse problems in imaging: A review." In: *IEEE Signal Processing Magazine* 34.6 (2017), pp. 85–95 (cit. on p. 30).

[McK+16] Will H McKay, Emory R McTyre, Catherine Okoukoni, Natalie K Alphonse-Sullivan, Jimmy Ruiz, Michael T Munley, Shadi Qasem, Hui-Wen Lo, Fei Xing, Adrian W Laxton, et al. "Repeat stereotactic radiosurgery as salvage therapy for locally recurrent brain metastases previously treated with radiosurgery." In: *Journal of neurosurgery* 127.1 (2016), pp. 148–156 (cit. on p. 35).

[Meh+19] Hatef Mehrabian, Jay Detsky, Hany Soliman, Arjun Sahgal, and Greg J Stanisz. "Advanced magnetic resonance imaging techniques in management of brain metastases." In: *Frontiers in oncology* 9 (2019), p. 440 (cit. on p. 35).

[Mil+21] Michael T Milano, Jimm Grimm, Andrzej Niemierko, Scott G Soltys, Vitali Moiseenko, Kristin J Redmond, Ellen Yorke, Arjun Sahgal, Jinyu Xue, Anand Mahadevan, et al. "Single-and multifraction stereotactic radiosurgery dose/volume tolerances of the brain." In: *International Journal of Radiation Oncology* Biology* Physics* 110.1 (2021), pp. 68–86 (cit. on pp. 3, 35).

[Mit+86] Matthew D Mitchell, Harold L Kundel, Leon Axel, and Peter M Joseph. "Agarose as a tissue equivalent phantom material for NMR imaging." In: *Magnetic resonance imaging* 4.3 (1986), pp. 263–266 (cit. on pp. 30, 48).

[MA14] Amirreza Modarreszadeh and Omid Abouali. "Numerical simulation for unsteady motions of the human vitreous humor as a viscoelastic substance in linear and non-linear regimes." In: *Journal of Non-Newtonian Fluid Mechanics* 204 (2014), pp. 22–31 (cit. on p. 33).

[Moh+21a] Sherif A Mohamed, Anne Adlung, Arne M Ruder, Michaela AU Hoesl, Lothar Schad, Christoph Groden, Frank A Giordano, and Eva Neumaier-Probst. "MRI Detection of Changes in Tissue Sodium Concentration in Brain Metastases after Stereotactic Radiosurgery: A Feasibility Study." In: *Journal of Neuroimaging* 31.2 (2021), pp. 297–305 (cit. on pp. 2, 56, 81, 100).

[Moh+21b] Sherif A Mohamed, Katrin Herrmann, Anne Adlung, Nadia Paschke, Lucrezia Hausner, Lutz Frölich, Lothar Schad, Christoph Groden, and Hans Ulrich Kerl. "Evaluation of Sodium (23Na) MR-imaging as a Biomarker and Predictor for Neurodegenerative Changes in Patients With Alzheimer's Disease." In: *in vivo* 35.1 (2021), pp. 429–435 (cit. on p. 27).

[Mul+09] Leon Mullenders, Mike Atkinson, Herwig Paretzke, Laure Sabatier, and Simon Bouffler. "Assessing cancer risks of low-dose radiation." In: *Nature Reviews Cancer* 9.8 (2009), pp. 596–604 (cit. on p. 100).

[Mur+13] Gillian Murphy, Masoom Haider, Sangeet Ghai, and Boraiah Sreeharsha. "The expanding role of MRI in prostate cancer." In: *American Journal of Roentgenology* 201.6 (2013), pp. 1229–1238 (cit. on p. 36).

[MB97] Kieran J Murphy and James A Brunberg. "Adult claustrophobia, anxiety and sedation in MRI." In: *Magnetic resonance imaging* 15.1 (1997), pp. 51–54 (cit. on p. 28).

[MP14] Naila Murray and Florent Perronnin. "Generalized max pooling." In: *Proceedings of the IEEE conference on computer vision and pattern recognition*. 2014, pp. 2473–2480 (cit. on p. 31).

[Nag+11] Armin M Nagel, Michael Bock, Christian Hartmann, Lars Gerigk, Jan-Oliver Neumann, Marc-André Weber, Martin Bendszus, Alexander Radbruch, Wolfgang Wick, Heinz-Peter Schlemmer, Wolfhard Semmler, and Armin Biller. "The potential of relaxation-weighted sodium magnetic resonance imaging as demonstrated on brain tumors." In: *Investigative radiology* 46.9 (2011), pp. 539–547 (cit. on p. 34).

[Nag+09] Armin M Nagel, Frederik B Laun, Marc-André Weber, Christian Matthies, Wolfhard Semmler, and Lothar R Schad. "Sodium MRI using a density-adapted 3D radial acquisition technique." In: *Magnetic Resonance in Medicine: An Official Journal of the International Society for Magnetic Resonance in Medicine* 62.6 (2009), pp. 1565–1573 (cit. on pp. 2, 29, 40, 41, 56).

[Nag+83] Imre Zs Nagy, György Lustyik, Géza Lukács, Valéria Zs Nagy, and György Balázs. "Correlation of malignancy with the intracellular Na+: K+ ratio in human thyroid tumors." In: *Cancer research* 43.11 (1983), pp. 5395–5402 (cit. on pp. 34, 101).

[Nel11] Sarah J Nelson. "Assessment of therapeutic response and treatment planning for brain tumors using metabolic and physiological MRI." In: *NMR in biomedicine* 24.6 (2011), pp. 734–749 (cit. on p. 1).

[NP+15] Eva Neumaier-Probst, Simon Konstandin, Judith Ssozi, Christoph Groden, Michael Hennerici, Lothar R Schad, and Marc Fatar. "A double-tuned 1H/23Na resonator allows 1H-guided 23Na-MRI in ischemic stroke patients in one session." In: *International Journal of Stroke* 10.SA100 (2015), pp. 56–61 (cit. on pp. 28, 30, 34, 45, 91, 94, 97, 100).

[NV+07] Sònia Nielles-Vallespin, Marc-André Weber, Michael Bock, André Bongers, Peter Speier, Stephanie E Combs, Johannes Wöhrle, Frank Lehmann-Horn, Marco Essig, and Lothar R Schad. "3D radial projection technique with ultrashort echo times for sodium MRI: clinical applications in human brain and skeletal muscle." In: *Magnetic Resonance in Medicine: An Official Journal of the International Society for Magnetic Resonance in Medicine* 57.1 (2007), pp. 74–81 (cit. on pp. 2, 29).

[Nie+15] Sebastian C Niesporek, Stefan H Hoffmann, Moritz C Berger, Nadia Benkhedah, Aaron Kujawa, Peter Bachert, and Armin M Nagel. "Partial volume correction for in vivo 23Na-MRI data of the human brain." In: *Neuroimage* 112 (2015), pp. 353–363 (cit. on pp. 29, 95, 104).

[Not+15] Mark Notley, Jinxing Yu, Ann S Fulcher, Mary Ann Turner, Charles H Cockrell, and Don Nguyen. "Diagnosis of recurrent prostate cancer and its mimics at multiparametric prostate MRI." In: *The British journal of radiology* 88.1054 (2015), p. 20150362 (cit. on p. 36).

[Now+16] Johannes Nowak, Uwe Malzahn, Alexander DJ Baur, Uta Reichelt, Tobias Franiel, Bernd Hamm, and Tahir Durmus. "The value of ADC, T2 signal intensity, and a combination of both parameters to assess Gleason score and primary Gleason grades in patients with known prostate cancer." In: *Acta Radiologica* 57.1 (2016), pp. 107–114 (cit. on p. 36).

[Nyq32] Harry Nyquist. "Regeneration theory." In: *Bell system technical journal* 11.1 (1932), pp. 126–147 (cit. on p. 22).

[Oft+21] Dominik Oft, Manuel Alexander Schmidt, Thomas Weissmann, Johannes Roesch, Veit Mengling, Siti Masitho, Christoph Bert, Sebastian Lettmaier, Benjamin Frey, Luitpold Valentin Distel, Rainer Fietkau1, and Florian Putz1. "Volumetric regression in brain metastases after stereotactic radiotherapy: Time course, predictors, and significance." In: *Frontiers in Oncology* (2021), p. 3011 (cit. on p. 100).

[Oga+90] Seiji Ogawa, Tso-Ming Lee, Alan R Kay, and David W Tank. "Brain magnetic resonance imaging with contrast dependent on blood oxygenation." In: *proceedings of the National Academy of Sciences* 87.24 (1990), pp. 9868–9872 (cit. on p. 1).

[Oh+07] Bryan C Oh, Paul G Pagnini, Michael Y Wang, Charles Y Liu, Paul E Kim, Cheng Yu, and Michael LJ Apuzzo. "Stereotactic radiosurgery: Adjacent tissue injury and response afterhigh-dose single fraction radiation: Part i—histology, imaging, and molecularevents." In: *Neurosurgery* 60.1 (2007), pp. 31–45 (cit. on pp. 100, 105).

[OR55] Norman S Olsen and Guilford G Rudolph. "Transfer of sodium and bromide ions between blood, cerebrospinal fluid and brain tissue." In: *American Journal of Physiology-Legacy Content* 183.3 (1955), pp. 427–432 (cit. on pp. 33, 93, 94).

[Osa+19] Kazuki Osawa, Siddharth Swaroop, Anirudh Jain, Runa Eschenhagen, Richard E Turner, Rio Yokota, and Mohammad Emtiyaz Khan. "Practical deep learning with Bayesian principles." In: *arXiv preprint arXiv:1906.02506* (2019) (cit. on p. 31).

[Ott+14] Oliver J Ott, S Hertel, Udo S Gaipl, Benjamin Frey, M Schmidt, and Rainer Fietkau. "The Erlangen Dose Optimization trial for low-dose radiotherapy of benign painful elbow syndrome." In: *Strahlentherapie und Onkologie* 190.3 (2014), p. 293 (cit. on p. 100).

[Ouw07] Ronald Ouwerkerk. "Sodium magnetic resonance imaging: from research to clinical use." In: *Journal of the American College of Radiology* 4.10 (2007), pp. 739–741 (cit. on pp. 34, 100).

[Ouw11] Ronald Ouwerkerk. "Sodium mri." In: *Magnetic resonance neuroimaging*. Springer, 2011, pp. 175–201 (cit. on pp. 32, 33, 93, 95).

[Ouw+03] Ronald Ouwerkerk, Karen B Bleich, Joseph S Gillen, Martin G Pomper, and Paul A Bottomley. "Tissue sodium concentration in human brain tumors as measured with 23Na MR imaging." In: *Radiology* 227.2 (2003), pp. 529–537 (cit. on pp. 2, 27, 32, 34, 95, 99, 103).

[Ouw+07] Ronald Ouwerkerk, Michael A Jacobs, Katarzyna J Macura, Antonio C Wolff, Vered Stearns, Sarah D Mezban, Nagi F Khouri, David A Bluemke, and Paul A Bottomley. "Elevated tissue sodium concentration in malignant breast lesions detected with non-invasive 23 Na MRI." In: *Breast cancer research and treatment* 106.2 (2007), pp. 151–160 (cit. on pp. 2, 27, 34, 99, 103).

[OWB05] Ronald Ouwerkerk, Robert G Weiss, and Paul A Bottomley. "Measuring human cardiac tissue sodium concentrations using surface coils, adiabatic excitation, and twisted projection imaging with minimal T2 losses." In: *Journal of Magnetic Resonance Imaging: An Official Journal of the International Society for Magnetic Resonance in Medicine* 21.5 (2005), pp. 546–555 (cit. on pp. 32, 36, 61, 102).

[Ozt+20] Murat Alp Oztek, Christina L Brunnquell, Michael N Hoff, Daniel J Boulter, Mahmud Mossa-Basha, Luke H Beauchamp, David L Haynor, and Xuan V Nguyen. "Practical considerations for radiologists in implementing a patient-friendly MRI experience." In: *Topics in Magnetic Resonance Imaging* 29.4 (2020), pp. 181–186 (cit. on p. 28).

[Pae+21] Daniel Paech, Sebastian Regnery, Tanja Platt, Nicolas GR Behl, Nina Weckesser, Paul Windisch, Katerina Deike-Hofmann, Wolfgang Wick, Martin Bendszus, Stefan Rieken, Laila König, Mark E Ladd, Heinz-Peter Schlemmer, Jürgen Debus, and Sebastian Adeberg. "Assessment of Sodium MRI at 7 Tesla as Predictor of Therapy Response and Survival in Glioblastoma Patients." In: *Frontiers in neuroscience* 15 (2021) (cit. on pp. 34, 101).

[Pan10] Leonardo Pantoni. "Cerebral small vessel disease: from pathogenesis and clinical characteristics to therapeutic challenges." In: *The Lancet Neurology* 9.7 (2010), pp. 689–701 (cit. on pp. 34, 92).

[Par+97] Todd B Parish, David S Fieno, Steven W Fitzgerald, and Robert M Judd. "Theoretical basis for sodium and potassium MRI of the human heart at 1.5 T." In: *Magnetic resonance in medicine* 38.4 (1997), pp. 653–661 (cit. on pp. 2, 29).

[Par+12] Heon Joo Park, Robert J Griffin, Susanta Hui, Seymour H Levitt, and Chang W Song. "Radiation-induced vascular damage in tumors: implications of vascular damage in ablative hypofractionated radiotherapy (SBRT and SRS)." In: *Radiation research* 177.3 (2012), pp. 311–327 (cit. on pp. 35, 100, 105).

[PGF87] Dennis L Parker, Grant T Gullberg, and Philip R Frederick. "Gibbs artifact removal in magnetic resonance imaging." In: *Medical physics* 14.4 (1987), pp. 640–645 (cit. on pp. 30, 42).

[Pas20] Nadia K Paschke. "Quantifizierungsgenauigkeit in der humanen 23Na-Magnetresonanztomographie." PhD thesis. 2020 (cit. on pp. 28, 32, 61, 101, 106).

[Pas+17] Nadia K Paschke, Daniel Hausmann, Lothar R Schad, Stefan O Schönberg, and Frank G Zöllner. "Multi-Parametric/-Nuclear 1H/23Na Clinical Protocol of the Prostate at 3T using a Double Resonant Coil." In: *Proceedings of the 25th annual meeting of ISMRM*. 2017, p. 1016 (cit. on p. 103).

[Pas+18] Nadia K Paschke, Wiebke Neumann, Tanja Uhrig, Manuel Winkler, Eva Neumaier-Probst, Marc Fatar, Lothar R Schad, and Frank G Zoellner. "Influence of Gadolinium-Based Contrast Agents on Tissue Sodium Quantification in Sodium Magnetic Resonance Imaging." In: *Invest Radiol* 53.9 (2018), pp. 555–562 (cit. on pp. 57, 59).

[Pat+11] Toral R Patel, Brian J McHugh, Wenya L Bi, Frank J Minja, Jonathan PS Knisely, and Veronica L Chiang. "A comprehensive review of MR imaging changes following radiosurgery to 500 brain metastases." In: *American journal of neuroradiology* 32.10 (2011), pp. 1885–1892 (cit. on p. 35).

[Pau25] Wolfgang Pauli. "Über den Zusammenhang des Abschlusses der Elektronengruppen im Atom mit der Komplexstruktur der Spektren." In: *Zeitschrift für Physik* 31.1 (1925), pp. 765–783 (cit. on p. 7).

[PFK00] Louis A Pena, Zvi Fuks, and Richard N Kolesnick. "Radiation-induced apoptosis of endothelial cells in the murine central nervous system: protection by fibroblast growth factor and sphingomyelinase deficiency." In: *Cancer research* 60.2 (2000), pp. 321–327 (cit. on p. 100).

[Per+86] William H Perman, Patrick A Turski, Lanning W Houston, Gary H Glover, and Cecil E Hayes. "Methodology of in vivo human sodium MR imaging at 1.5 T." In: *Radiology* 160.3 (1986), pp. 811–820 (cit. on p. 26).

[Pet+16a] Maria Petracca, Lazar Fleysher, Niels Oesingmann, and Matilde Inglese. "Sodium MRI of multiple sclerosis." In: *NMR in Biomedicine* 29.2 (2016), pp. 153–161 (cit. on p. 92).

[Pet+16b] Maria Petracca, Roxana O Vancea, Lazar Fleysher, Laura E Jonkman, Niels Oesingmann, and Matilde Inglese. "Brain intra-and extracellular sodium concentration in multiple sclerosis: a 7 T MRI study." In: *Brain* 139.3 (2016), pp. 795–806 (cit. on p. 48).

[Pet+16c] Maria Petracca, Roxana O Vancea, Lazar Fleysher, Laura E Jonkman, Niels Oesingmann, and Matilde Inglese. "Brain intra-and extracellular sodium concentration in multiple sclerosis: a 7 T MRI study." In: *Brain* 139.3 (2016), pp. 795–806 (cit. on p. 92).

[Pig+20] Nicola Pigaiani, Anna Bertaso, Elio Franco De Palo, Federica Bortolotti, and Franco Tagliaro. "Vitreous humor endogenous compounds analysis for post-mortem forensic investigation." In: *Forensic science international* 310 (2020), p. 110235 (cit. on pp. 33, 93, 94).

[Pip+11] James G Pipe, Nicholas R Zwart, Eric A Aboussouan, Ryan K Robison, Ajit Devaraj, and Kenneth O Johnson. "A new design and rationale for 3D orthogonally oversampled k-space trajectories." In: *Magnetic resonance in medicine* 66.5 (2011), pp. 1303–1311 (cit. on pp. 2, 29).

[Ple+12] Esben Plenge, Dirk HJ Poot, Monique Bernsen, Gyula Kotek, Gavin Houston, Piotr Wielopolski, Louise van der Weerd, Wiro J Niessen, and Erik Meijering. "Super-resolution methods in MRI: can they improve the trade-off between resolution, signal-to-noise ratio, and acquisition time?" In: *Magnetic resonance in medicine* 68.6 (2012), pp. 1983–1993 (cit. on p. 30).

[Pok+21] Linda Osei Poku, M Phil, Yongna Cheng, Kai Wang, and Xilin Sun. "23Na-MRI as a Noninvasive Biomarker for Cancer Diagnosis and Prognosis." In: *Journal of Magnetic Resonance Imaging* 53.4 (2021), pp. 995–1014 (cit. on pp. 27, 34, 36, 103).

[PS15] Niels D Prins and Philip Scheltens. "White matter hyperintensities, cognitive impairment and dementia: an update." In: *Nature Reviews Neurology* 11.3 (2015), pp. 157–165 (cit. on pp. 34, 92).

[PTP46] Edward M Purcell, Henry C Torrey, and Robert V Pound. "Resonance Absorption by Nuclear Magnetic Moments in a Solid." In: *Physical Review* 69.1-2 (1946). PR, pp. 37–38 (cit. on p. 7).

[RHO89] Jong Beom Ra, SK Hilal, and CH Oh. "An algorithm for MR imaging of the short T2 fraction of sodium using the FID signal." In: *Journal of computer assisted tomography* 13.2 (1989), pp. 302–309 (cit. on p. 26).

[RC33] Isidor I Rabi and Victor W Cohen. "The Nuclear Spin of Sodium." In: *Physical Review* 43.7 (1933), pp. 582–583 (cit. on p. 7).

[RW17] Waseem Rawat and Zenghui Wang. "Deep convolutional neural networks for image classification: A comprehensive review." In: *Neural computation* 29.9 (2017), pp. 2352–2449 (cit. on p. 30).

[Red98] Thomas William Redpath. "Signal-to-noise ratio in MRI." In: *The British journal of radiology* 71.847 (1998), pp. 704–707 (cit. on p. 1).

[Reg+20] Sebastian Regnery, Nicolas GR Behl, Tanja Platt, Nina Weinfurtner, Paul Windisch, Katerina Deike-Hofmann, Felix Sahm, Martin Bendszus, Jürgen Debus, Mark E Ladd, et al. "Ultra-high-field sodium MRI as biomarker for tumor extent, grade and IDH mutation status in glioma patients." In: *NeuroImage: Clinical* 28 (2020), p. 102427 (cit. on pp. 34, 99).

[Ren+08] Jing Ren, Yi Huan, He Wang, HaiTao Zhao, YaLi Ge, YingJuan Chang, and Ying Liu. "Diffusion-weighted imaging in normal prostate and differential diagnosis of prostate diseases." In: *Abdominal imaging* 33.6 (2008), pp. 724–728 (cit. on p. 36).

[Ric44] Stephen O Rice. "Mathematical analysis of random noise." In: *The Bell System Technical Journal* 23.3 (1944), pp. 282–332 (cit. on p. 23).

[Rid+18] Ben Ridley, Armin M Nagel, Mark Bydder, Adil Maarouf, Jan-Patrick Stellmann, Soraya Gherib, Jeremy Verneuil, Patrick Viout, Maxime Guye, Jean-Philippe Ranjeva, and Wafaa Zaaraoui. "Distribution of brain sodium long and short relaxation times and concentrations: a multi-echo ultra-high field 23 Na MRI study." In: *Scientific reports* 8.1 (2018), pp. 1–12 (cit. on pp. 33, 94).

[Roe+90] Peter B Roemer, William A Edelstein, Cecil E Hayes, Steven P Souza, and Otward M Mueller. "The NMR phased array." In: *Magnetic resonance in medicine* 16.2 (1990), pp. 192–225 (cit. on pp. 29, 101, 106).

[RFB15] Olaf Ronneberger, Philipp Fischer, and Thomas Brox. "U-net: Convolutional networks for biomedical image segmentation." In: *International Conference on Medical image computing and computer-assisted intervention*. Springer. 2015, pp. 234–241 (cit. on pp. 31, 52).

[Roo+15] William D Rooney, Xin Li, Manoj K Sammi, Dennis N Bourdette, Edward A Neuwelt, and Charles S Springer Jr. "Mapping human brain capillary water lifetime: high-resolution metabolic neuroimaging." In: *NMR in Biomedicine* 28.6 (2015), pp. 607–623 (cit. on p. 27).

[RS91] William D Rooney and Charles S Springer. "A comprehensive approach to the analysis and interpretation of the resonances of spins 3/2 from living systems." In: *NMR Biomed* 4.5 (1991), pp. 209–226 (cit. on pp. 17, 18).

[RWB06] Alan J Ruby, George A Williams, and MS Blumenkranz. "Vitreous humor." In: *Anonymous. Lippincott Williams & Wilkins* (2006) (cit. on pp. 33, 94).

[Sah18] Sumit Saha. "A comprehensive guide to convolutional neural networks—the ELI5 way." In: *Towards data science* 15 (2018) (cit. on p. 30).

[SSZ14] Roberto Sampaolesi, Juan Roberto Sampaolesi, and Jorge Zárate. "Aqueous Humor: Physiology of the Aqueous Humor." In: *The Glaucomas*. Springer, 2014, pp. 85–97 (cit. on p. 33).

[Sav06] Jeffrey L Saver. "Time is brain —- quantified." In: *Stroke* 37.1 (2006), pp. 263–266 (cit. on pp. 3, 34).

[Saw+19] Vijay Sawlani, Nigel Davies, Markand Patel, Robert Flintham, Charles Fong, Geoff Heyes, Garth Cruickshank, Neil Steven, Andrew Peet, Andrew Hartley, Helen Benghiat, Sara Meade, and Paul Sanghera. "Evaluation of response to stereotactic radiosurgery in brain metastases using multiparametric magnetic resonance imaging and a review of the literature." In: *Clinical Oncology* 31.1 (2019), pp. 41–49 (cit. on p. 35).

[Sch19] Victor D Schepkin. "Statistical tensor analysis of the MQ MR signals generated by weak quadrupole interactions." In: *Zeitschrift für Medizinische Physik* 29.4 (2019), pp. 326–336 (cit. on p. 29).

[Sch+05] Victor D Schepkin, Brian D Ross, Thomas L Chenevert, Alnawaz Rehemtulla, Surabhi Sharma, Mahesh Kumar, and Jadranka Stojanovska. "Sodium magnetic resonance imaging of chemotherapeutic response in a rat glioma." In: *Magnetic Resonance in Medicine: An Official Journal of the International Society for Magnetic Resonance in Medicine* 53.1 (2005), pp. 85–92 (cit. on pp. 34, 101).

[SMB10] Dominik Scherer, Andreas Müller, and Sven Behnke. "Evaluation of pooling operations in convolutional architectures for object recognition." In: *International conference on artificial neural networks*. Springer. 2010, pp. 92–101 (cit. on p. 30).

[Sch+93] Mark L Schiebler, Mitchell D Schnall, Howard M Pollack, Robert E Lenkinski, John E Tomaszewski, Alan J Wein, Richard Whittington, Wolfgang Rauschning, and Herbert Y Kressel. "Current role of MR imaging in the staging of adenocarcinoma of the prostate." In: *Radiology* 189.2 (1993), pp. 339–352 (cit. on p. 36).

[Sch+17a] Jo Schlemper, Jose Caballero, Joseph V Hajnal, Anthony Price, and Daniel Rueckert. "A deep cascade of convolutional neural networks for MR image reconstruction." In: *International Conference on Information Processing in Medical Imaging*. Springer. 2017, pp. 647–658 (cit. on pp. 2, 30).

[Sch+04] Franz Schmitt, Daniel Grosu, Cecil Mohr, David Purdy, K Salem, KT Scott, and B Stoeckel. "3 Tesla MRI: successful results with higher field strengths." In: *Der Radiologe* 44.1 (2004), pp. 31–47 (cit. on p. 1).

[Sch+17b] Tanja Schneider, Jan Felix Kuhne, Paul Bittrich, Julian Schroeder, Tim Magnus, Malte Mohme, Malte Grosser, Gerhard Schoen, Jens Fiehler, and Susanne Siemonsen. "Edema is not a reliable diagnostic sign to exclude small brain metastases." In: *PloS one* 12.5 (2017), e0177217 (cit. on p. 100).

[Sch+19] Alena-Kathrin Schnurr, Khanlian Chung, Tom Russ, Lothar R Schad, and Frank G Zoellner. "Simulation-based deep artifact correction with convolutional neural networks for limited angle artifacts." In: *Zeitschrift für Medizinische Physik* 29.2 (2019), pp. 150–161 (cit. on p. 52).

[Sch+13] Stefanie Schreiber, Celine Zoe Bueche, Cornelia Garz, and Holger Braun. "Blood brain barrier breakdown as the starting point of cerebral small vessel disease?-New insights from a rat model." In: *Experimental & translational stroke medicine* 5.1 (2013), pp. 1–8 (cit. on p. 34).

[Sha+21] Akash Deelip Shah, Amaresha Shridhar Konar, Ramesh Paudyal, Jung Hun Oh, Eve LoCastro, David Aramburu Nuñez, Nathaniel Swinburne, Behroze Vachha, Gary A Ulaner, Robert J Young, et al. "Diffusion and Perfusion MRI Predicts Response Preceding and Shortly After Radiosurgery to Brain Metastases: A Pilot Study." In: *Journal of Neuroimaging* 31.2 (2021), pp. 317–323 (cit. on pp. 35, 100).

[SWL16] N Jon Shah, Wieland A Worthoff, and Karl-Josef Langen. "Imaging of sodium in the brain: a brief review." In: *NMR in Biomedicine* 29.2 (2016), pp. 162–174 (cit. on pp. 1, 26).

[Sha+02] Erik M Shapiro, Arijitt Borthakur, Alexander Gougoutas, and Ravinder Reddy. "23Na MRI accurately measures fixed charge density in articular cartilage." In: *Magnetic Resonance in Medicine: An Official Journal of the International Society for Magnetic Resonance in Medicine* 47.2 (2002), pp. 284–291 (cit. on p. 27).

[Sha+17] Mayur Sharma, Xuefei Jia, Manmeet Ahluwalia, Gene H Barnett, Michael A Vogelbaum, Samuel T Chao, John H Suh, Erin S Murphy, Jennifer S Yu, Lilyana Angelov, et al. "First follow-up radiographic response is one of the predictors of local tumor progression and radiation necrosis after stereotactic radiosurgery for brain metastases." In: *Cancer medicine* 6.9 (2017), pp. 2076–2086 (cit. on p. 35).

[Sha+14] Suzanne R Sharpton, Eric K Oermann, Dominic T Moore, Eric Schreiber, Riane Hoffman, David E Morris, and Matthew G Ewend. "The volumetric response of brain metastases after stereotactic radiosurgery and its post-treatment implications." In: *Neurosurgery* 74.1 (2014), pp. 9–16 (cit. on p. 105).

[She+10] Huajun She, Rong-Rong Chen, Dong Liang, Yuchou Chang, and Leslie Ying. "Image reconstruction from phased-array MRI data based on multichannel blind deconvolution." In: *2010 IEEE International Symposium on Biomedical Imaging: From Nano to Macro*. IEEE. 2010, pp. 760–763 (cit. on pp. 29, 101, 106).

[SNS93] T Shimizu, Hiroyuki Naritomi, and Tohru Sawada. "Sequential changes on 23 Na MRI after cerebral infarction." In: *Neuroradiology* 35.6 (1993), pp. 416–419 (cit. on pp. 27, 34).

[Sia+20] Joseph Sia, Radoslaw Szmyd, Eric Hau, and Harriet E Gee. "Molecular mechanisms of radiation-induced cancer cell death: a primer." In: *Frontiers in cell and developmental biology* 8 (2020), p. 41 (cit. on pp. 35, 100).

[SE12] Jennifer H Siggers and C Ross Ethier. "Fluid mechanics of the eye." In: *Annual Review of Fluid Mechanics* 44 (2012), pp. 347–372 (cit. on p. 33).

[SE92] Jens Christian Skou and Mikael Esmann. "The na, k-atpase." In: *Journal of bioenergetics and biomembranes* 24.3 (1992), pp. 249–261 (cit. on pp. 1, 2, 26, 94).

[SLG20] David W Smith, Chang-Joon Lee, and Bruce S Gardiner. "No flow through the vitreous humor: How strong is the evidence?" In: *Progress in retinal and eye research* 78 (2020), p. 100845 (cit. on pp. 33, 93, 94).

[Som02] George G Somjen. "Ion regulation in the brain: implications for pathophysiology." In: *The Neuroscientist* 8.3 (2002), pp. 254–267 (cit. on pp. 1, 2, 26, 33, 94).

[Som04] George G Somjen. *Ions in the brain: normal function, seizures, and stroke*. Oxford University Press, 2004 (cit. on pp. 1, 2, 26, 48, 94).

[Son+20] Chang W Song, Stephanie Terezakis, Bahman Emami, Robert J Griffin, Paul W Sperduto, Mi-Sook Kim, and L Chinsoo Cho. "Indirect cell death and the LQ model in SBRT and SRS." In: *Journal of Radiosurgery and SBRT* 7.1 (2020), p. 1 (cit. on pp. 35, 100).

[Sto+12] Abigail L Stockham, Andrew L Tievsky, Shlomo A Koyfman, Chandana A Reddy, John H Suh, Michael A Vogelbaum, Gene H Barnett, and Samuel T Chao. "Conventional MRI does not reliably distinguish radiation necrosis from tumor recurrence after stereotactic radiosurgery." In: *Journal of neuro-oncology* 109.1 (2012), pp. 149–158 (cit. on p. 35).

[Sug+00] Takeshi Sugahara, Yukunori Korogi, Seiji Tomiguchi, Yoshinori Shigematsu, Ichiro Ikushima, Tomohiro Kira, Luxia Liang, Yukitaka Ushio, and Mutsumasa Takahashi. "Posttherapeutic intraaxial brain tumor: the value of perfusion-sensitive contrast-enhanced MR imaging for differentiating tumor recurrence from nonneoplastic contrast-enhancing tissue." In: *American Journal of Neuroradiology* 21.5 (2000), pp. 901–909 (cit. on p. 35).

[Tak+11] Yasuyuki Taki, Shigeo Kinomura, Kazunori Sato, Ryoi Goto, Kai Wu, Ryuta Kawashima, and Hiroshi Fukuda. "Correlation between gray/white matter volume and cognition in healthy elderly people." In: *Brain and cognition* 75.2 (2011), pp. 170–176 (cit. on p. 92).

[Tau+18] Neil K Taunk, Jung Hun Oh, Amita Shukla-Dave, Kathryn Beal, Behroze Vachha, Andrei Holodny, and Vaios Hatzoglou. "Early posttreatment assessment of MRI perfusion biomarkers can predict long-term response of lung cancer brain metastases to stereotactic radiosurgery." In: *Neuro-oncology* 20.4 (2018), pp. 567–575 (cit. on p. 35).

[The+08] Jens M Theysohn, Stefan Maderwald, Oliver Kraff, Christoph Moenninghoff, Mark E Ladd, and Susanne C Ladd. "Subjective acceptance of 7 Tesla MRI for human imaging." In: *Magnetic Resonance Materials in Physics, Biology and Medicine* 21.1-2 (2008), p. 63 (cit. on p. 1).

[Thu18] Keith R Thulborn. "Quantitative sodium MR imaging: A review of its evolving role in medicine." In: *Neuroimage* 168 (2018), pp. 250–268 (cit. on pp. 1, 26, 32, 91, 92).

[Thu+99] Keith R Thulborn, Denise Davis, Holly Adams, Tatyana Gindin, and Joe Zhou. "Quantitative tissue sodium concentration mapping of the growth of focal cerebral tumors with sodium magnetic resonance imaging." In: *Magnetic Resonance in Medicine: An Official Journal of the International Society for Magnetic Resonance in Medicine* 41.2 (1999), pp. 351–359 (cit. on pp. 2, 26, 27, 32, 91, 99, 103).

[Thu+05] Keith R Thulborn, Denise Davis, James Snyder, Howard Yonas, and Amin Kassam. "Sodium MR imaging of acute and subacute stroke for assessment of tissue viability." In: *Neuroimaging Clinics* 15.3 (2005), pp. 639–653 (cit. on pp. 27, 34, 93, 97).

[Tol+21] Fabian Tollens, Niklas Westhoff, Jost von Hardenberg, Sven Clausen, Michael Ehmann, Frank Zöllner, Anne Adlung, Dominik F Bauer, Stefan O Schoenberg, and Dominik Nörenberg. "MRT-gestützte minimalinvasive Therapie des Prostatakarzinoms." In: *Der Radiologe* 61.9 (2021), pp. 829–838 (cit. on pp. 3, 35).

[Tra+19] Thuy T Tran, Amit Mahajan, Veronica L Chiang, Sarah B Goldberg, Don X Nguyen, Lucia B Jilaveanu, and Harriet M Kluger. "Perilesional edema in brain metastases: potential causes and implications for treatment with immune therapy." In: *Journal for immunotherapy of cancer* 7.1 (2019), pp. 1–8 (cit. on p. 100).

[TSB12] Adrian Tsang, Robert W Stobbe, and Christian Beaulieu. "Triple-quantum-filtered sodium imaging of the human brain at 4.7 T." In: *Magnetic resonance in medicine* 67.6 (2012), pp. 1633–1643 (cit. on p. 32).

[Tur+10] Baris Turkbey, Peter A Pinto, Haresh Mani, Marcelino Bernardo, Yuxi Pang, Yolanda L McKinney, Kiranpreet Khurana, Gregory C Ravizzini, Paul S Albert, Maria J Merino, et al. "Prostate cancer: value of multiparametric MR imaging at 3 T for detection—histopathologifc correlation." In: *Radiology* 255.1 (2010), pp. 89–99 (cit. on p. 36).

[Utz+20] Matthias Utzschneider, Nicolas GR Behl, Sebastian Lachner, Lena V Gast, Andreas Maier, Michael Uder, and Armin M Nagel. "Accelerated quantification of tissue sodium concentration in skeletal muscle tissue: quantitative capability of dictionary learning compressed sensing." In: *Magnetic Resonance Materials in Physics, Biology and Medicine* (2020), pp. 1–11 (cit. on p. 97).

[VG12] J Thomas Vaughan and John R Griffiths. *RF coils for MRI*. John Wiley & Sons, 2012 (cit. on p. 28).

[VR17] Pedro Vilela and Howard A Rowley. "Brain ischemia: CT and MRI techniques in acute ischemic stroke." In: *European journal of radiology* 96 (2017), pp. 162–172 (cit. on p. 34).

[WGM00] David O Walsh, Arthur F Gmitro, and Michael W Marcellin. "Adaptive reconstruction of phased array MR imagery." In: *Magnetic Resonance in Medicine: An Official Journal of the International Society for Magnetic Resonance in Medicine* 43.5 (2000), pp. 682–690 (cit. on pp. 29, 59).

[Wan+18] Weitao Wan, Yuanyi Zhong, Tianpeng Li, and Jiansheng Chen. "Rethinking feature distribution for loss functions in image classification." In: *Proceedings of the IEEE conference on computer vision and pattern recognition*. 2018, pp. 9117–9126 (cit. on p. 31).

[Wan+16] Shanshan Wang, Zhenghang Su, Leslie Ying, Xi Peng, Shun Zhu, Feng Liang, Dagan Feng, and Dong Liang. "Accelerating magnetic resonance imaging via deep learning." In: *2016 IEEE 13th international symposium on biomedical imaging (ISBI)*. IEEE. 2016, pp. 514–517 (cit. on p. 105).

[Wan+04] Zhou Wang, Alan C Bovik, Hamid R Sheikh, and Eero P Simoncelli. "Image quality assessment: from error visibility to structural similarity." In: *IEEE transactions on image processing* 13.4 (2004), pp. 600–612 (cit. on pp. 54, 96).

[Wan+94] Goya Wannamethee, Peter H Whincup, A Gerald Shaper, and Anthony F Lever. "Serum sodium concentration and risk of stroke in middle-aged males." In: *Journal of hypertension* 12.8 (1994), pp. 971–979 (cit. on pp. 33, 95).

[War+03] Joanna M Wardlaw, Peter AG Sandercock, Martin S Dennis, and John M Starr. "Is breakdown of the blood-brain barrier responsible for lacunar stroke, leukoaraiosis, and dementia?" In: *Stroke* 34.3 (2003), pp. 806–812 (cit. on p. 34).

[WSD13] Joanna M Wardlaw, Colin Smith, and Martin Dichgans. "Mechanisms of sporadic cerebral small vessel disease: insights from neuroimaging." In: *The Lancet Neurology* 12.5 (2013), pp. 483–497 (cit. on pp. 34, 92).

[WVHMM15] Joanna M Wardlaw, Maria C Valdés Hernández, and Susana Muñoz-Maniega. "What are white matter hyperintensities made of? Relevance to vascular cognitive impairment." In: *Journal of the American Heart Association* 4.6 (2015), e001140 (cit. on pp. 34, 92).

[Web+21] Claudia E Weber, Katja Nagel, Anne Ebert, Christina Roßmanith, Nadia Paschke, Anne Adlung, Michael Platten, Lothar R Schad, Achim Gass, and Philipp Eisele. "Diffusely appearing white matter in multiple sclerosis: Insights from sodium (23Na) MRI." In: *Multiple Sclerosis and Related Disorders* 49 (2021), p. 102752 (cit. on pp. 27, 92, 95, 100).

[Web+11] Marc-André Weber, Armin M Nagel, Karin Jurkat-Rott, and Frank Lehmann-Horn. "Sodium (23Na) MRI detects elevated muscular sodium concentration in Duchenne muscular dystrophy." In: *Neurology* 77.23 (2011), pp. 2017–2024 (cit. on p. 27).

[Wei+16] Jeffrey C Weinreb, Jelle O Barentsz, Peter L Choyke, Francois Cornud, Masoom A Haider, Katarzyna J Macura, Daniel Margolis, Mitchell D Schnall, Faina Shtern, Clare M Tempany, et al. "PI-RADS prostate imaging–reporting and data system: 2015, version 2." In: *European urology* 69.1 (2016), pp. 16–40 (cit. on pp. 3, 35, 59).

[WB+19] Jeffrey C Weinreb, Jelle O Barentsz, et al. "PI-RADS Prostate Imaging - Reporting and Data System: 2019, Version 2.1." In: (2019) (cit. on p. 35).

[Wen+18] Daniel Wenz, Andre Kuehne, Till Huelnhagen, Armin M Nagel, Helmar Waiczies, Oliver Weinberger, Celal Oezerdem, Oliver Stachs, Soenke Langner, Erdmann Seeliger, Bert Flemming, Russell Hodge, and Thoralf Niendorf. "Millimeter spatial resolution in vivo sodium MRI of the human eye at 7 T using a dedicated radiofrequency transceiver array." In: *Magnetic resonance in medicine* 80.2 (2018), pp. 672–684 (cit. on pp. 32, 33, 48).

[WT18] Catherine Westbrook and John Talbot. *MRI in Practice*. John Wiley & Sons, 2018 (cit. on p. 1).

[WAH12] Friedrich Wetterling, Saema Ansar, and Eva Handwerker. "Sodium-23 magnetic resonance imaging during and after transient cerebral ischemia: multinuclear stroke protocols for double-tuned 23Na/1H resonator systems." In: *Physics in Medicine & Biology* 57.21 (2012), p. 6929 (cit. on pp. 30, 91).

[Wet+12] Friedrich Wetterling, Lindsay Gallagher, I Mhairi Macrae, Sven Junge, and Andrew J Fagan. "Regional and temporal variations in tissue sodium concentration during the acute stroke phase." In: *Magnetic resonance in medicine* 67.3 (2012), pp. 740–749 (cit. on p. 93).

[Wet+15] Friedrich Wetterling, Lindsay Gallagher, Jim Mullin, William M Holmes, Chris McCabe, I Mhairi Macrae, and Andrew J Fagan. "Sodium-23 magnetic resonance imaging has potential for improving penumbra detection but not for estimating stroke onset time." In: *Journal of Cerebral Blood Flow & Metabolism* 35.1 (2015), pp. 103–110 (cit. on pp. 34, 97).

[WBL16] Graham C Wiggins, Ryan Brown, and Karthik Lakshmanan. "High-performance radiofrequency coils for 23Na MRI: brain and musculoskeletal applications." In: *NMR in Biomedicine* 29.2 (2016), pp. 96–106 (cit. on p. 28).

[Win90] Stefan S Winkler. "Sodium-23 magnetic resonance brain imaging." In: *Neuroradiology* 32.5 (1990), pp. 416–420 (cit. on p. 26).

[Win+18] Jeff D Winter, Fabio Y Moraes, Caroline Chung, and Catherine Coolens. "Detectability of radiation-induced changes in magnetic resonance biomarkers following stereotactic radiosurgery: A pilot study." In: *PloS one* 13.11 (2018), e0207933 (cit. on pp. 35, 100).

[Win+07] Max Wintermark, Reto Meuli, Patrick Browaeys, Marc Reichhart, Julien Bogousslavsky, Pierre Schnyder, and Patrik Michel. "Comparison of CT perfusion and angiography and MRI in selecting stroke patients for acute treatment." In: *Neurology* 68.9 (2007), pp. 694–697 (cit. on pp. 1, 34).

[Wol+21] Michael Woletz, Sigrun Roat, Allan Hummer, Martin Tik, and Christian Windischberger. "Human tissue-equivalent MRI phantom preparation for 3 and 7 Tesla." In: *Medical Physics* (2021) (cit. on p. 30).

[Wol13] Matthew B Wolf. "Whole body acid-base and fluid-electrolyte balance: a mathematical model." In: *American Journal of Physiology-Renal Physiology* 305.8 (2013), F1118–F1131 (cit. on p. 33).

[WK04] C Shun Wong and Albert J Van der Kogel. "Mechanisms of radiation injury to the central nervous system: implications for neuroprotection." In: *Molecular interventions* 4.5 (2004), p. 273 (cit. on pp. 3, 35).

[WG07] H Bart Van der Worp and Jan van Gijn. "Acute ischemic stroke." In: *New England Journal of Medicine* 357.6 (2007), pp. 572–579 (cit. on pp. 3, 33).

[Wun+15] Roland Wunderlich, Anne Ernst, Franz Rödel, Rainer Fietkau, Oliver S Ott, Kirsten Lauber, Benjamin Frey, and Udo S Gaipl. "Low and moderate doses of ionizing radiation up to 2 Gy modulate transmigration and chemotaxis of activated macrophages, provoke an anti-inflammatory cytokine milieu, but do not impact upon viability and phagocytic function." In: *Clinical & Experimental Immunology* 179.1 (2015), pp. 50–61 (cit. on p. 100).

[Yam+14] Masaaki Yamamoto, Toru Serizawa, Takashi Shuto, Atsuya Akabane, Yoshinori Higuchi, Jun Kawagishi, Kazuhiro Yamanaka, Yasunori Sato, Hidefumi Jokura, Shoji Yomo, et al. "Stereotactic radiosurgery for patients with multiple brain metastases (JLGK0901): a multi-institutional prospective observational study." In: *The Lancet Oncology* 15.4 (2014), pp. 387–395 (cit. on p. 35).

[Yos+08] Kengo Yoshimitsu, Keijiro Kiyoshima, Hiroyuki Irie, Tsuyoshi Tajima, Yoshiki Asayama, Masakazu Hirakawa, Kousei Ishigami, Seiji Naito, and Hiroshi Honda. "Usefulness of apparent diffusion coefficient map in diagnosing prostate carcinoma: correlation with stepwise histopathology." In: *Journal of Magnetic Resonance Imaging: An Official Journal of the International Society for Magnetic Resonance in Medicine* 27.1 (2008), pp. 132–139 (cit. on p. 36).

[YHK08] Vanessa G Young, Glenda M Halliday, and Jillian J Kril. "Neuropathologic correlates of white matter hyperintensities." In: *Neurology* 71.11 (2008), pp. 804–811 (cit. on pp. 34, 92).

[Zaa+12] Wafaa Zaaraoui, Simon Konstandin, Bertrand Audoin, Armin M Nagel, Audrey Rico, Irina Malikova, Elisabeth Soulier, Patrick Viout, Sylviane Confort-Gouny, Patrick J Cozzone, Jean Pelletier, Lothar R Schad, and Jean-Philippe Ranjeva. "Distribution of brain sodium accumulation correlates with disability in multiple sclerosis: a cross-sectional 23Na MR imaging study." In: *Radiology* 264.3 (2012), pp. 859–867 (cit. on pp. 2, 27, 92, 95).

[ZB97] Pieter Zeeman and Maxime Bôcher. "Zeeman effect." In: *Nature* 55.1424 (1897), p. 347 (cit. on p. 8).

[Zha+05] Jing Zhang, David R Goodlett, Elaine R Peskind, Joseph F Quinn, Yong Zhou, Qin Wang, Catherine Pan, Eugene Yi, Jimmy Eng, Ruedi H Aebersold, et al. "Quantitative proteomic analysis of age-related changes in human cerebrospinal fluid." In: *Neurobiology of aging* 26.2 (2005), pp. 207–227 (cit. on pp. 33, 94, 99).

[Zha+17] Kai Zhang, Wangmeng Zuo, Yunjin Chen, Deyu Meng, and Lei Zhang. "Beyond a gaussian denoiser: Residual learning of deep cnn for image denoising." In: *IEEE transactions on image processing* 26.7 (2017), pp. 3142–3155 (cit. on p. 96).

[Zha+16] Hang Zhao, Orazio Gallo, Iuri Frosio, and Jan Kautz. "Loss functions for image restoration with neural networks." In: *IEEE Transactions on computational imaging* 3.1 (2016), pp. 47–57 (cit. on p. 31).

[ZAP16] Hao Zhou, Jose M Alvarez, and Fatih Porikli. "Less is more: Towards compact cnns." In: *European Conference on Computer Vision*. Springer. 2016, pp. 662–677 (cit. on p. 32).

APPENDIX

A

MAGNETIC RESONANCE IMAGING: SEQUENCE PARAMETERS

Table A.1: MRI sequence parameters and reconstruction details as used for all patients with ischemic stroke.

Parameter	Value
^{1}H FLAIR Sequence	
Acquisition Time (TA)	4 min 50 s
Repetition Time (TR)	9000 ms
Echo Time (TE)	93 ms
Inversion Time (TI)	2500 ms
Flip Angle	130°
Resolution	0.47x0.47 mm^2
Slice Thickness	5.0 mm
Number of Slices	24
Field of View	195x240 mm^2
^{1}H DWI Sequence	
Acquisition Time (TA)	1 min 40 s
Repetition Time (TR)	6700 ms
Echo Time (TE)	152 ms
Flip Angle	90°
b Value	0 & 1000 s/mm^2
Resolution	1.25x1.25 mm^2
Slice Thickness	5.0 mm
Number of Slices	24
Field of View	240x240 mm^2
3D radial density-adapted ^{23}Na MRI Sequence	
Acquisition Time (TA)	10 min
Repetition Time (TR)	100 ms
Echo Time (TE)	0.2 ms
Flip Angle	90°
Number of Spokes (N)	6,000
Samples per Spoke	384
Gradient Amplitude	4.6 mT/m
Slew Rate	170 T/(m · s)
Resolution	4.01x4.01x4.01 mm^3
Bandwidth	50 Hz/Pixel
Reconstruction	
Zero-filling	2
Field of View	241x241x241 mm^3
Matrix	120x120x120 voxel^3

Table A.2: MRI sequence parameters and reconstruction details as used for all patients undergoing stereotactic radiosurgery.

Parameter	Value
^{1}H MPRAGE	
Sequence	
Acquisition Time (TA)	4 min 18 s
Repetition Time (TR)	1900 ms
Echo Time (TE)	2.52 ms
Flip Angle	9°
Resolution	1x1x1 mm^3
Phase Resolution	96 %
Field of View	250x250x250 mm^3
3D radial density-adapted ^{23}Na MRI	
Sequence	
Acquisition Time (TA)	15 min
Repetition Time (TR)	100 ms
Echo Time (TE)	0.4 ms
Flip Angle	90°
Number of Spokes (N)	9000
Samples per Spoke	200
Gradient Amplitude	5.8 mT/m
Slew Rate	170 T/(m · s)
Resolution	4.01x4.01x4.01 mm^3
Bandwidth	100 Hz/Pixel
Reconstruction	
Zero-filling	2
Field of View	300x300x300 mm^3
Matrix	150x150x150 voxel^3

Table A.3: MRI sequence parameters and reconstruction details of the T2 TSE and of the ^{23}Na MRI, as they were used for all patients with a suspected prostate carcinoma.

Parameter	Value
^{1}H 2D T2w TSE Sequence	
Acquisition Time (TA)	3 min 57 s
Repetition Time (TR)	4710 ms
Echo Time (TE)	108 ms
Flip Angle	160°
Resolution	0.7x0.7 mm^2
Slice Thickness	3.0 mm
Number of Slices	34
Field of View	250x250 mm^2
3D radial density-adapted ^{23}Na MRI Sequence	
Acquisition Time (TA)	16 min
Repetition Time (TR)	120 ms
Echo Time (TE)	1.2 ms
Flip Angle	90°
Number of Spokes (N)	8000
Samples per Spoke	384
Gradient Amplitude	3.6 mT/m
Slew Rate	170 T/(m · s)
Resolution	5.1x5.1x5.1 mm^3
Bandwidth	50 Hz/Pixel
Reconstruction	
Zero-filling	2
Field of View	500x500x500 mm^3
Matrix	196x196x196 voxel^3

B

RESULTS: PERFORMANCE OF CONVOLUTIONAL NEURAL NETWORKS

Table B.1: List of FI, RI and CI from all CNNs with their generated signal to noise ratio (SNR, mean ± sd) and structural similarity index (SSIM, mean pm sd) to FI. Networks performing significantly ($p < 0.05$) better than RI are marked with *. The CNNs generating the best results of SSIM are printed in bold.

					SNR ($\mu \pm \sigma$)	SSIM ($\mu \pm \sigma$)
FI					21.72 ± 2.75	1.00
RI					10.16 ± 0.96	0.87 ± 0.03
CNN	Architecture	Filters	Batch Norm.	Loss		
1	U-Net	Big	False	L1	$35.24^* \pm 07.08$	$0.89^* \pm 0.03$
	U-Net	Big	False	L2	$36.67^* \pm 07.42$	$0.90^* \pm 0.03$
2	U-Net	Big	True	L1	$59.12^* \pm 10.99$	0.88 ± 0.03
	U-Net	Big	True	L2	$35.33^* \pm 05.54$	$0.90^* \pm 0.03$
3	U-Net	Small	False	L1	$45.02^* \pm 07.75$	$0.89^* \pm 0.03$
	U-Net	Small	False	L2	$41.31^* \pm 07.91$	$0.89^* \pm 0.03$
4	U-Net	Small	True	L1	$49.26^* \pm 08.80$	0.85 ± 0.04
	U-Net	Small	True	L2	$49.97^* \pm 07.19$	0.86 ± 0.04
5	ResNet	Big	False	L1	$29.11^* \pm 05.24$	0.73 ± 0.03
	ResNet	Big	False	L2	$25.63^* \pm 04.63$	0.72 ± 0.03
6	ResNet	Big	True	L1	$52.98^* \pm 10.49$	0.74 ± 0.04
	ResNet	Big	True	L2	$32.51^* \pm 04.20$	0.75 ± 0.04
7	ResNet	Small	False	L1	$30.80^* \pm 06.39$	0.73 ± 0.04
	ResNet	Small	False	L2	$20.14^* \pm 02.43$	0.70 ± 0.04
8	ResNet	Small	True	L1	$75.51^* \pm 14.36$	0.69 ± 0.05
	ResNet	Small	True	L2	$15.77^* \pm 02.60$	0.74 ± 0.03
1	U-Net	Big	False	L_A	$32.19^* \pm 05.98$	$0.90^* \pm 0.03$
	U-Net	Big	False	L_B	$41.32^* \pm 07.60$	$0.89^* \pm 0.03$
2	**U-Net**	**Big**	**True**	L_A	$34.10^* \pm 04.72$	$0.91^* \pm 0.02$
	U-Net	Big	True	L_B	$36.64^* \pm 06.33$	$0.89^* \pm 0.03$
3	**U-Net**	**Small**	**False**	L_A	$23.55^* \pm 03.13$	$0.91^* \pm 0.02$
	U-Net	Small	False	L_B	$40.55^* \pm 06.74$	$0.89^* \pm 0.03$

Table B.2: Mean absolute TSC difference to FI (ΔTSC) of RI and CI from CNNs which improved TSC quantification in WM, GM, and CSF. Significance was calculated with the paired student t-test and p-values are given for the networks that reduced ΔTSC compared to RI. Networks performing significantly ($p < 0.05$) better are marked with *. The network where improvements were significant in WM and GM is printed in bold.

					WM		GM		CSF	
					ΔTSC [mM]	p-value	ΔTSC [mM]	p-value	ΔTSC [mM]	p-value
RI					4.52		4.50		4.21	
CNN	Architecture	Filters	Batch Norm.	Loss						
1	U-Net	Big	False	L1	4.82		4.92		6.28	
	U-Net	Big	False	L2	4.09	0.1383	4.08	0.2487	4.05	0.4602
2	U-Net	Big	True	L1	4.11	0.1512	4.01	0.0638	4.82	
	U-Net	Big	True	L2	4.48	0.9055	4.11	0.1705	4.00	0.2112
3	U-Net	Small	False	L1	4.48	0.8798	4.60		6.12	
	U-Net	**Small**	**False**	L2	3.83	0.0058*	3.83	0.0045*	3.94	0.0782
1	U-Net	Big	False	L_A	4.10	0.1512	4.19	0.2533	4.40	
	U-Net	Big	False	L_B	4.35	0.6176	4.30	0.5511	4.33	
2	U-Net	Big	True	L_A	3.98	0.0625	3.90	0.0336*	3.88	0.1872
	U-Net	Big	True	L_B	4.10	0.1339	3.97	0.0511	3.82	0.0507
3	U-Net	Small	False	L_A	4.25	0.3333	4.20	0.2718	4.41	
	U-Net	Small	False	L_B	4.09	0.0441*	4.12	0.0822	4.19	0.9030

Table B.3: List of FI, RI and CI from all evaluated under-sampling factors R and different loss functions with their generated signal to noise ratio (SNR, mean ± sd) and structural similarity index (SSIM, mean ± sd) to FI. Networks performing significantly ($p < 0.05$) better are marked with *.

			SNR	SSIM
		($\mu \pm \sigma$)	($\mu \pm \sigma$)	
	FI		24.60 ± 1.81	1
Under-sampling factor	Loss	λ		
Half	RI		18.32 ± 1.53	0.9886 ± 0.0045
	L2		38.28 ± 2.57	$0.9900^* \pm 0.0042$
	L_B	0.5	34.54 ± 2.77	$0.9892^* \pm 0.0045$
	L_B	0.2	32.52 ± 2.58	0.9886 ± 0.0054
Third	RI		14.31 ± 1.20	0.9761 ± 0.0085
	L2		50.27 ± 4.36	$0.9790^* \pm 0.0080$
	L_B	0.5	41.89 ± 3.39	$0.9810^* \pm 0.0073$
	L_B	0.2	48.89 ± 4.75	$0.9813^* \pm 0.0072$
Quarter	RI		11.83 ± 1.19	0.9630 ± 0.0135
	L2		54.58 ± 8.29	$0.9734^* \pm 0.0108$
	L_B	0.5	36.32 ± 4.48	$0.9740^* \pm 0.0095$
	L_B	0.2	45.74 ± 4.80	$0.9734^* \pm 0.0101$
Fifth	RI		10.43 ± 0.96	0.9531 ± 0.0171
	L2		76.26 ± 14.52	$0.9644^* \pm 0.0142$
	L_B	0.5	51.57 ± 5.53	$0.9662^* \pm 0.0137$
	L_B	0.2	58.71 ± 7.94	$0.9663^* \pm 0.0138$
Sixth	RI		9.36 ± 0.90	0.9437 ± 0.0188
	L2		70.98 ± 10.62	$0.9595^* \pm 0.0148$
	L_B	0.5	54.36 ± 7.66	$0.9620^* \pm 0.0143$
	L_B	0.2	49.55 ± 4.62	$0.9597^* \pm 0.0148$
Eighth	RI		7.96 ± 0.79	0.9235 ± 0.0222
	L2		53.35 ± 7.14	$0.9496^* \pm 0.0190$
	L_B	0.5	50.77 ± 5.88	$0.9448^* \pm 0.0178$
	L_B	0.2	70.48 ± 12.28	$0.9475^* \pm 0.0186$
Tenth	RI		7.21 ± 0.69	$0.9169 \pm 0,0250$
	L2		64.15 ± 11.58	$0.9439^* \pm 0.0182$
	L_B	0.5	52.29 ± 9.61	$0.9446^* \pm 0.0182$
	L_B	0.2	103.76 ± 22.64	$0.9363^* \pm 0.0256$

PUBLICATIONS

A

PEER-REVIEWED JOURNAL ARTICLES

[1] **Anne Adlung**, Nadia K Paschke, Alena-Kathrin Golla, Dominik F Bauer, Sherif A Mohamed, Melina Samartzi, Marc Fatar, Eva Neumaier Probst, Frank G Zöllner and Lothar R Schad. 23Na MRI in ischemic stroke: Acquisition time reduction using postprocessing with convolutional neural networks. NMR Biomed, 34 (4), p.e4474 (2021).

[2] **Anne Adlung**, Melina Samartzi, Lothar R Schad, Eva Neumaier-Probst, Marc Fatar and Sherif A Mohamed. Tissue sodium concentration within white matter correlates with the extent of small vessel disease. Cerebrovasc Dis, 50, pp.347-355 (2021).

[3] Dominik F Bauer, **Anne Adlung**, Irène Brumer, Alena-Kathrin Golla, Tom Russ, Eva Oelschlegel, Fabian Tollens, Sven Clausen, Philipp Aumüller, Lothar R Schad, Dominik Nörenberg and Frank G Zöllner. An anthropomorphic pelvis phantom for MR-guided prostate interventions. Magn Reson Med, p.in Press (2021).

[4] Sherif A Mohamed, Katrin Herrmann, **Anne Adlung**, Nadia K Paschke, Lucrezia Hausner, Lutz Frölich, Lothar R Schad, Christoph Groden and Hans U Kerl. Evaluation of sodium (23Na) MR-imaging as a biomarker and predictor for neurodegenerative changes in patients with Alzheimer Disease. In Vivo, 35 (1), pp.429-435 (2021).

[5] Fabian Tollens, Niklas Westhoff, Jost von Hardenberg, Sven Clausen, Michael Ehmann, Frank G Zöllner, **Anne Adlung**, Dominik F Bauer, Stefan O Schoenberg and Dominik Nörenberg. MRI-guided minimally invasive treatment of prostate cancer. Der Radiologe, 61 (9), pp.829-838 (2021).

[6] Claudia E Weber, Katja Nagel, Anne Ebert, Christina Roßmanith, Nadia K Paschke, **Anne Adlung**, Michael Platten, Lothar R Schad, Achim Gass and Philipp Eisele. Diffusely appearing white matter in multiple sclerosis: insights from sodium (23Na) MRI. Multiple Sclerosis and Related Disorders, 49, p.102752 (2021).

[7] Sherif A Mohamed, **Anne Adlung**, Arne M Ruder, Michaela Hoesl, Lothar R Schad, Christoph Groden, Frank A Giordano and Eva Neumaier Probst. MRI Detection of changes in tissue sodium concentration in brain metastases after stereotactic radiosurgery: A feasibility study. Journal of Neuroimaging, 31 (2), pp.297-305 (2020).

B

CONFERENCE CONTRIBUTIONS

[1] **Anne Adlung**, Nadia Paschke, Alena-Katrin Golla, Dominik F Bauer, Sherif A Mohamed, Melina Samartzi, Marc Fatar, Eva Neumaier Probst, Frank G Zöllner, Lothar R Schad. Accuracy of quantified 23Na MRI in ischemic stroke with varying undersampling factors and CNN postprocessing. Proc. ISMRM Annual Meeting, Virutal Meeting, (2021) 29.

[2] **Anne Adlung**, Sherif A Mohamed, Nadia K Paschke, Mara Berger, Melina Samartzi, Marc Fatar, Achim Gass, Eva Neumaier Probst, Lothar R Schad. Evaluation of different references for the quantification of tissue sodium concentration in patients with ischemic stroke. Proc. ISMRM Annual Meeting, Virtual Meeting, (2021) 29.

[3] **Anne Adlung**, Fabian Tollens, Nadia K Paschke, Jennifer Hümsch, Niklas Westhoff, Daniel Hausmann, Lothar R Schad, Dominik Nörenberg, Frank G Zöllner. 23Na MRI in patients with suspected prostate cancer: External and internal References for quantification of tissue sodium concentration. Proc. ISMRM Annual Meeting, Virutal Meeting, (2021) 29.

[4] **Anne Adlung**, Nadia K Paschke, Alena-Katrin Schnurr, Sherif A Mohamed, Victor Saase, Melina Samartzi, Marc Fatar, Eva Neumaier Probst and Lothar R Schad. CNNs improve tissue sodium concentration accuracy in white and grey matter from stroke patients at 3T 23Na MRI. Proc. ISMRM Annual Meeting, (2020) 28.

[5] **Anne Adlung**, Michaela Hoesl, Sherif A Mohamed, Arne M Ruder, Frank A Giordano, Eva Neumaier Probst and Lothar R Schad. Evolution of the tissue sodium concentration in brain metastases undergoing stereotactical radiosurgery: a feasilbility study. Proc. ISMRM Annual Meeting, Virutal Meeting, (2020) 28.

[6] **Anne Adlung**, Nadia K Paschke, Alena-Katrin Schnurr, Eva Neumaier Probst, Sherif A Mohamed, Melina Samartzi, Marc Fatar and Lothar R Schad. Can a Convolutional neural network reduce the measurement time for 23Na quantification?. Proc. ESMRMB Congress, Rotterdam, NL, (2019) 36.

[7] Dominik Bauer, Eva Oelschläger, Alena-Katrin Golla, **Anne Adlung**, Tom Russ, Ingo Hermann, Irène Brumer, J. Rosenkranz, Fabian Tollens, Sven Clausen, Philipp Aumüller, Lothar R Schad, Dominik Nörenberg and Frank G Zöllner. An anthropomorphic pelvis phantom for prostate brachytherapy. Proc. ISMRM Annual Meeting, Virtual Meeting, (2021) 29.

[8] Dominik Bauer, Irène Brumer, **Anne Adlung**, Alena-Katrin Golla, Tom Russ, Eva Oelschlegel, Fabian Tollens, Sven Clausen, Philipp Aumüller, Lothar R Schad, Dominik Nörenberg and Frank G Zöllner. An anthropomorphic pelvis phantom for MR-guided prostate biopsy. Proc. 5th Conference on Image-Guided Interventions, Virtual Meeting, (2021) 29.

[9] Felix Schuler, Irène Brumer, **Anne Adlung**, Tim P Pusch, Marius Siegfarth, Pierre Renaud and Michael de Wild. MRI compatibility of additive manufactured auxetic NiTi parts. Proc. [MEET THE EXPERT] Implants, (2021).

[10] Melina Samartzi, Sherif A Mohamed, **Anne Adlung**, Lothar R Schad, Eva Neumaier Probst, Michael Platten, Marc Fatar. 23Na-MRT: Veränderung der Natriumgewebekonzentration im Infarktkern nach Akuttherapie bei ischämischem Schlaganfall. Proc. DGN Kongress, Virtual Meeting, (2020) 93.

[11] Irène Brumer, **Anne Adlung**, Wiebke Neumann, Tanja Uhrig, Matthias Malzacher, Lothar R Schad and Frank G Zöllner. Novel pixel-based approach for artifact evaluation of passive implants in MRI validated on intrauterine devices at 3T. Proc. ESMRMB Congress, Rotterdam, NL, (2019) 36.

[12] Jorge Chacon-Caldera, **Anne Adlung**, Nadia K Paschke, Ruomin Hu and Lothar R Schad. T1 bias reduction in the quantification of tissue sodium concentration using flip angle sweep. Proc. ESMRMB Congress, Rotterdam, NL, (2019) 36.

ACKNOWLEDGMENTS

First and foremost I would like to express my gratitude towards my thesis supervisor, Prof. Lothar Schad, for his continuous support and valuable advice regarding my research. Furthermore, I also want to express how very thankful I am for the support and guidance that I have received from Prof. Frank Zöllner and Dr. Nadia Paschke.

This thesis would not have been possible without fruitful collaborations, for which I am particularly thankful to PD Dr. Eva Neumaier Probst and Dr. Sherif A. Mohamed from the department of neroradiology, PD Dr. Dominik Nörenberg and Dr. Fabian Tollens from the department of radiology, Prof. Achim Gass, Prof. Philipp Eisele, Prof. Marc Fatar, and Melina Samartzi from the department of neurology, and Prof. Frank Giordano and Dr. Arne Ruder from the department of radiation oncology. I also want to thank the Dietmar-Hopp Stiftung for funding the study "^{23}Na MRI in ischemic stroke".

I am extremely grateful for my wonderful colleagues at the Chair of Computer Assisted Clinical Medicine. It is wonderful how welcoming and supportive our institute is! Very special thanks go to my colleagues Valerie Klein, Safa Özdemir, and Efe Ilicak. Valerie was an amazing office mate and without her the the writing process of this dissertation would have double as hard and half the fun. Efe's visits to our office were a constant supply of laughters. Safa was the most reliable source for advice and provided an indefinite repository of nerve-strengthening chocolate.

My colleagues, friends and family members have helped me finishing this thesis by proof-reading some chapters or sections. Thank you, Dennis Kleimaier, Simon Reichert, Dominik Bauer, Steffen Albert, Valerie Klein, Safa Özdemir, Janek Salatzki, and Kerrin and Sönke Adlung.

I also want to express my gratitude for the support that I have received from my friends, my family, and from my boyfriend. Thank you very much for your helpful advice and the encouragement to pursue science and academia.